NORTHWESTERN UNIVERSITY

Engineering DNA-Based Materials for the Analysis of Live Single Cells

A DISSERTATION

SUBMITTED TO THE GRADUATE SCHOOL

IN PARTIAL FULLFILLMENT OF THE REQUIREMENTS

for the degree

DOCTOR OF PHILOSOPHY

Field of Chemical Engineering

By

Sasha Brian Ebrahimi

EVANSTON, ILLINOIS

September 2021

ABSTRACT

Engineering DNA-Based Materials for the Analysis of Live Single Cells

Cells are primarily comprised of metal ions, small molecules, proteins, lipids, and nucleic acids. The ability to probe these molecules in single living cells can shed new light on chemical processes inside of cells or allow disease diagnosis based on molecular profiling. However, there exists a lack of tools that allow one to monitor and analyze these molecules dynamically in live cells. Although genetically-encoded fluorescent tags have transformed live-cell protein analysis, there is a deficiency of robust techniques for studying other molecules. In this regard, probes based on nucleic acids have recently emerged as powerful tools for studying intracellular processes. Their biocompatibility, amenability to genetic encoding, low cost, ease of synthesis, modular structure, and ability to be chemically modified in a sequence-defined manner make them especially useful in sensing applications. By tuning their sequence, nucleic acids can be designed to recognize a wide range of molecules including other nucleic acids, proteins, ions, and small molecules.

The earliest analysis techniques based on DNA, such as *in situ* hybridization and polymerase chain reaction (PCR), required the fixation and lysis of cells, respectively, preventing their use for live-cell analysis. The introduction of linear DNA probes that can study events in live cells, such as molecular beacons, helped to expand the capabilities in the field. However, such DNA probes do not efficiently cross the cell membrane without the use of transfection reagents, and they are susceptible to rapid nuclease degradation in the cellular environment. To overcome these challenges, NanoFlares were developed in 2007 as a new tool for live-cell analysis. NanoFlares are comprised of a gold core functionalized with recognition strands (hybridization-based, aptamer, DNAzyme, or aptazyme) for a target of interest. These recognition strands are hybridized

to short fluorophore-labeled flare strands. Close proximity between the gold nanoparticle and the fluorophore quenches the fluorescence. When the target is present and binds to the recognition strand, the flare strand is displaced, separating the fluorophore and gold, and turning on fluorescence. Owing to the dense orientation of DNA on the nanoparticle surface in a spherical nucleic acid (SNA) architecture, NanoFlares exhibit high cellular uptake without the need for transfection reagents, display enhanced resistance to nuclease degradation in comparison to free nucleic acid probes, have enhanced target recognition and binding, and exhibit little immunogenicity or toxicity. To date, NanoFlares have been used in over 50 studies for studying various targets including mRNA, small molecules, ions, and proteins. Although NanoFlares constituted the first platform for live intracellular analysis at single-cell resolution, challenges still exist. These challenges include false-positive signal due to non-specific separation of the fluorophore and gold nanoparticle quencher, limited quantitative capabilities, inability to spatiotemporally track analytes, kinetically slow responses due to partial blocking of the recognition strand, and the restriction that only targets with known nucleic acid-based recognition sequences can be detected. My dissertation research seeks to alleviate these challenges through the development of next generation SNA constructs for live cell chemical analysis. In Chapter 2, a new class of quencher free signaling aptamers called Forced-intercalation aptamers (FIT-aptamers) are introduced. It is shown that FIT-aptamers offer several advantages over state-of-the-art transduction methods, and enable study of important analytes such as markers of cancer, thrombosis, and heavy metal poisoning in complex media. Chapter 3 explores the leveraging of these advantageous properties to design the first fluorogenic aptamers capable of sensing steroid hormones in clinical serum samples. Chapter 4 reports the development of a new class of live cell

probes based on protein spherical nucleic acids (ProSNAs). ProSNAs are able to recognize analytes using either DNA-based or protein-based recognition, ultimately enabling false-positive resistant measurement of analytes in living cells. Finally, Chapter 5 discusses the outlook and future directions for the work covered in this thesis.

Acknowledgements

The most important part of the completion of any endeavor is acknowledging those who made it possible. This thesis is first and foremost a testament to all the people who have pushed me to be the best person I can be. I first thank my thesis advisor, Professor Chad Mirkin, who gave me the opportunity to pursue exciting research questions. Chad's guidance, willingness to challenge me, and endless support made this thesis possible. I also thank my committee, Professors Josh Leonard, Nathan Gianneschi, and Bill Miller, for their invaluable advice, insights, and suggestions. To the Mirkin office, Elizabeth, Sara, Pam, and Tanushri, thank you for your endless kindness and help each and every day for the past five years. To all those in the Mirkin lab, who will now be lifelong friends, thank you. Thank you for making me feel part of the family from day one. Thank you to my direct collaborators, who I learned so much from, including Edmund Cheng, Caroline Kusmierz, Benjamin Partridge, Peter Mirau, and Jorge Chávez. Thank you to Devleena Samanta, one of the most brilliant scientists and kindest people I have met, for your endless mentorship. It transformed my thesis into something it never could have been without you. I'm an only child, and I always tell my closest friends that I consider them my siblings. To my siblings, thank you. As my first gift to you, I am not going to embarrass you by naming you here. You know who you are, and as you know having you in my life makes every day "thankful Thursday." Last but not least, I thank my family. In particular, this thesis is more a testament to my mom's and dad's, Haleh's and Nader's, parenting than to my scientific prowess. From the first day of school two decades ago to this thesis, they have been my biggest cheerleaders through all the struggles and challenges that life brings. I am incredibly grateful.

Contents

List of Figures

Figure 1.5.1-1. Common gold nanoparticle-based hybridization probes. (A) In the off state of a NanoFlare, a fluorophore-labeled flare strand is hybridized to a gold-bound recognition strand, allowing for gold to quench fluorescence. Target binding to the recognition strand displaces the flare sequence, separates it from gold, and turns on fluorescence.[43] (B) In the StickyFlare construct, the fluorophore-labeled strand is designed to be complementary to the target. Therefore, upon probe-target binding, the target can be monitored, providing valuable spatiotemporal information about its dynamics.[133] (C) Gold MBs consist of fluorophore-labeled hairpin ONTs conjugated to the surface of gold nanoparticles. The principle of action is the same as that of MBs, except the central gold nanoparticle acts as a quencher.[97] (D) As opposed to chemical conjugation, fluorophore-labeled ONTs may also be adsorbed onto surface-coated gold nanoparticles. For example, as depicted in the figure, fluorophore-tagged hairpin ONTs can be adsorbed onto polydopamine (colored black)-coated gold nanoparticles.[166,167] Polydopamine acts as a further source of quenching and can be utilized in photothermal therapy due its ability to absorb NIR light. (E) Anisotropic gold nanoparticles have also been used as cores. For example, a gold nanorod (functionalized with the recognition strand) that acts as a quencher can be attached to a gold nanocross (functionalized with a complementary fluorophore-labeled strand). Upon target binding, the fluorophore-labeled strand attached to the nanocross is released, inducing fluorescence turn on. The presence of the nanocross further enhances the fluorescence due to surface enhanced resonance.[168] 73

Figure 1.5.1-2. Selected upconverting nanoparticle-based hybridization probes. (A) A dual gold nanoparticle/upconversion system that allows for simultaneous monitoring of luminescent and

List of Tables

CHAPTER ONE

1. Introduction

1.1. Nucleic acids as live cell probes

Cells are primarily composed of metal ions, small molecules, proteins, lipids, and nucleic acids.[1] Over the past few decades, numerous methods have been developed for monitoring these analytes and correlating their abundances to fate and health status of the cells. Techniques ranging from microscopy and mass spectrometry to assays such as enzyme-linked immunosorbent assay (ELISA) and reverse transcription polymerase chain reaction (RT-PCR) have vastly improved our understanding of fundamental processes associated with cells.[2–5]

Many techniques for cellular analysis such as northern blotting, western blotting, fluorescence in situ hybridization (FISH), RT-PCR, DNA microarrays, and electron microscopy rely on the fixation or lysis of cells.[5–11] Moreover, as the amount of material from one cell is often insufficient for accurate analysis, a bulk population of cells is used for methods that analyze cell lysates. Information about dynamics of various molecules inside cells and cell-to-cell heterogeneity is often lost in such cases due to ensemble averaging.

The ability to track molecules in live cells is important from a fundamental perspective as it can enable one to determine how the spatial distribution of cellular analytes impacts cellular function, monitor transient processes, and study the evolution of chemical signatures associated with the progression of disease. To highlight this point, Lichtman and Fraser have put forth a useful sports analogy: reconstructing a game of American football and identifying its rules from a series of still snapshots taken at different timepoints from separate games would be a near impossible task.[12]

An indispensable tool for visualizing live cells is light microscopy.[13] However, as methods based on fluorescence typically have greater sensitivity than those based on absorbance, numerous fluorescent tools have been developed for analysis of cellular analytes in live cells.[14] For example, a prominent "zinc spark," associated with the fertilization of human eggs, could be detected only because of advances in live cell imaging with fluorophore reporters.[15] Conventional light microscopes provide resolution down to 250 nm, while ~50 nm resolution is regularly achieved using super-resolution techniques.[16] These capabilities allow one to not only observe sub-cellular organelles, but also can provide resolution down to the single-molecule level.[17]

Recently, nucleic acid-based probes have gained popularity for visualizing intracellular analytes due to several advantageous properties (listed in section 1.1.1). Through judicious selection of sequences, a wide variety of targets ranging from nucleic acids to ions, small molecules, and proteins inside living cells can be visualized.

1.1.1. Why nucleic acid-based probes?

Nucleic acid-based probes are desirable because of their programmable nature, a property that has led to key advances in several areas of nanotechnology.[18–21] DNA and RNA oligonucleotides (ONTs) can be synthesized across different length scales (1-1,000,000 nt) at relatively low cost, either through chemical or enzymatic processes.[22] Moreover, these probes are amenable to chemical modifications (e.g. with fluorescent tags or custom bases with specific functionalities) at any desired site. Single-stranded probes can be designed to detect other nucleic acids through complementary interactions (hybridization-based probes). They can also be evolved through combinatorial selection techniques such that they bind to any target molecule of interest (aptamers) or catalyze specific reactions (DNAzymes).[23–25] Importantly, these probes, being biopolymers,

are biocompatible and non-toxic to cells. Finally, they can be assembled into spherical nucleic acids (SNAs) and taken into cells without the need for transfection agents, which are often toxic.[26] Taken together, these features make nucleic acids particularly attractive as probes.

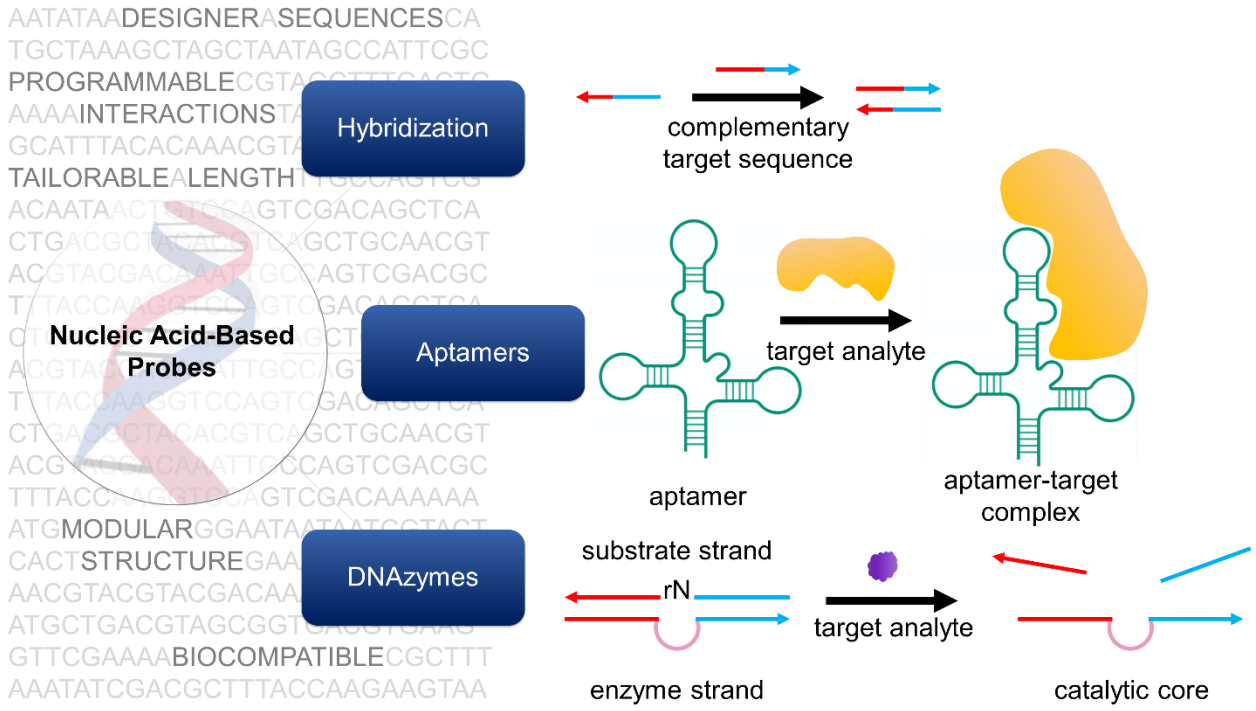

Figure 1.1.1-1. Nucleic acid-based probes can be broadly classified into three types: (i) hybridization-based probes, (ii) aptamers, and (iii) DNAzymes. Hybridization-based probes are single-stranded and recognize complementary targets through Watson-Crick base pairing. For ease of identification, complementary regions are colored the same in this figure. Aptamers are oligonucleotides evolved through combinatorial selection strategies that can bind to analytes of interest including ions, small molecules, and proteins. Aptamers often adopt complex tertiary structures that enable target recognition. Alternately, target binding can induce conformational changes in their structure. DNAzymes consist of a substrate strand and an enzyme strand (containing a catalytic core) hybridized to each other. The substrate strand contains a single RNA nucleotide which can be catalytically cleaved in the presence of a target.

1.1.2. The nucleic acid structure

Nucleic acids are anionic polymers composed of nucleotide building blocks. Each nucleotide consists of three subunits: a nitrogenous base, a five-carbon sugar moiety, and a phosphate "backbone" (Figure 1.1.2-1). In this section, we briefly describe the common modifications that are made to nucleotides in the context of generating improved sensors (Figure 1.1.2-1).

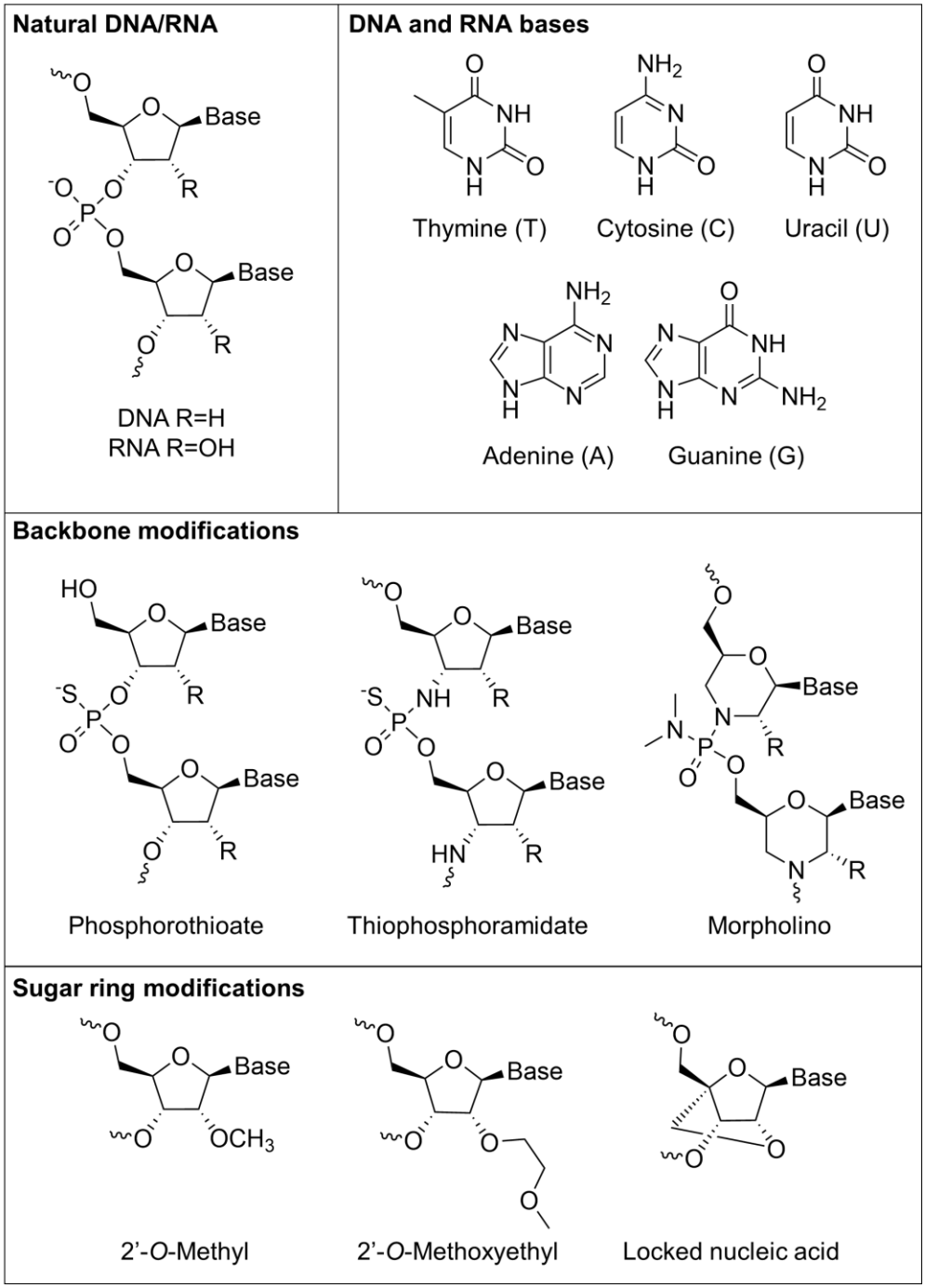

Figure 1.1.2-1. The nucleic acid structure and common modifications to it. Adapted with permission from Springer Nature.[27] Copyright (2013)

Base modifications

Five bases form the foundational alphabet of genetic codes: adenine (A), thymine (T), uracil (U), cytosine (C) and guanine (G). These bases interact with each other through hydrogen bonds, resulting in specific and highly programmable interactions. In classical Watson-Crick base-pairing, A pairs with T while C pairs with G. In RNA, T is substituted by U. Several types of modifications can be made to these standard bases with the goal of increasing stability or functionality. For example, Lannes et al. demonstrated that i-motifs, which have pH-dependent secondary structures, can be engineered to switch their conformation at more acidic or more basic pH by replacing cytosine bases with 5-methylcytosines and 5-bromocytosines, respectively.[28]

Sugar ring modifications

In unmodified RNA, the 2' position on the sugar is hydroxylated, but in DNA it is not (Figure 1.1.2-1). To impart nuclease resistance, the 2' position is often modified.[29] Most commonly used modifications include the use of 2'-O-methyl (2'-OMe), 2'-O-methoxyethyl derivatives, and locked nucleic acids (LNAs).[30–32] These modifications can also impact the melting temperature (T_m) of the nucleic acid duplexes. For example, LNAs have been used in developing probes that bind more strongly to their target nucleic acids.[33]

Backbone modifications

Phosphorothioates (PS), thiophosphoramidates, morpholinos, and peptide nucleic acids (PNAs) are common backbone-modified nucleic acids (Figure 1.1.2-1).[34–37] These modifications influence the thermal and enzymatic stability as well as solubility of the probes. For example, morpholino-based probes for messenger RNA (mRNA) detection afford greater nuclease resistance and higher specificity towards their target, albeit at the cost of reduced solubility.[36,38]

1.1.3. Types of nucleic acid-based probes

Nucleic acid-based probes can be broadly classified into three groups: (i) hybridization-based probes, (ii) aptamers, and (iii) DNAzymes (Figure 1.1.1-1).

Hybridization-based probes are designed by leveraging Watson-Crick base pairing to detect complementary sequences. Therefore, these probes are used in the detection of nucleic acids including mRNA, microRNA, and non-coding RNA.[39–41] Examples of this type of probe include those used with FISH, molecular beacons (MBs), and NanoFlares.[42–44]

Aptamers are ONT sequences that can be designed to bind to any target of interest. These ONTs are generated through an *in vitro* process called systematic evolution of ligands by exponential enrichment (SELEX).[23] Aptamers are nucleic acid analogues of antibodies, and recent studies have shown that their performance (in terms of binding affinities, detection limits), in several cases rivals that of antibodies at reduced cost and greater stability.[45] Moreover, aptamers can be evolved using secondary structures alone, without having detailed knowledge of tertiary folding. To date, over 500 aptamers have been generated for more than 100 different targets ranging from ions, small molecules, proteins, to whole cells.[46]

DNAzymes are synthetic DNA structures that can catalyze chemical reactions.[24] So far, no naturally occurring DNAzyme has been identified.[47] However, DNAzymes are obtained through an *in vitro* combinatorial process by screening a large library of ONTs containing up to 10^{15} distinct sequences.[48,49] These sequences can be evolved as long single-stranded ONTs to bind specific substrates and subsequently catalyze chemical reactions. The single-stranded ONT is then converted into a two-stranded catalyst. One strand (the substrate strand) consists of a single

ribonucleotide and other (the enzyme strand) contains the catalytic core. These two strands are hybridized together through complementary binding arms on either side of the ribonucleotide/catalytic core (Figure 1.1.1-1). The ribonucleotide can be catalytically cleaved, typically, in the presence of specific metal ions. DNAzymes have been used to detect a wide variety of metals,[22] although recent work has focused on detecting other analytes such as RNA.[50]

Combining the advantages of two or more of these classes of probes, hybrid probes can also be generated. Probes termed as **aptazymes** have been designed wherein a DNAzyme is activated only upon aptamer-ligand binding.[51] We further note that the reporting mechanism of a few select nucleic acid-based probes solely take advantage of the nanostructures formed by DNA and cannot be categorized into any of the above mentioned categories. For example, fluorophore-labeled dextran molecules encapsulated within DNA icosahedrons enable the imaging of specific endocytic pathways as the icosahedrons are taken up by the anionic ligand binding receptor pathway.[52] For the purposes of this review, the probes reported in literature have been classified into one of the three broad categories described above based on our perspective of where the design can be most effectively described for the reader to follow.

In **Error! Reference source not found.**, I list selected structures/specific sub-classes of probes that are most commonly used along with example targets that have been visualized using these probes. Additionally, I enumerate the methods of probe delivery, type of signal readout, as well as advantages and disadvantages of each probe type.

Table 1.1.3-1. ***Common nucleic acid-based probes***

Probe Type	Target type	Delivery Method	Signaling Method	Advantages and disadvantages

Linear antisense probes A dye-labeled recognition strand binds to its complementary target.	mRNA,[53] snRNA[54] rRNA,[54]	1.Microinjection[54] 2. Cell permeabilization[55] 3.Cationic lipids[53]	Fluorescence	**Advantages** 1.Simple probe design **Disadvantages** 1.High background 2. Unmodified probes prone to degradation 3.Nuclear sequestration possible 4. Requires method for transfection (e.g. Microinjection, Cell Permeabilization, etc.)
Linear FRET probes Hybridization of two different linear antisense probes to adjacent regions of a target sequence occurs, bringing a FRET pair into close proximity.	mRNA,[56]	1.Microinjection[56,57] 2.Microporation[58]	Fluorescence	**Advantages** 1.Better selectivity compared to linear antisense probes **Disadvantages** 1. Unmodified probes prone to degradation 2. Nuclear sequestration possible 3. Requires method for transfection 4. Requires binding to large stretch of RNA for hybridization-based approach

Molecular beacons (MBs)/aptamer beacons/aptamer switch probes Target binding induces opening of a hairpin ONT sequence, separating a fluorophore and quencher.	mRNA,[59] miRNA,[60] piRNA,[41] small molecules,[61] proteins,[62] temperature[43]	1. Microinjection[63–67] 2. Cationic lipids[41,60,68–72] 3. Microporation[64,73] 4. Aptamer cell recognition[74,75]	Fluorescence	**Advantages** 1. Better signal to noise ratio compared to linear antisense probes and linear FRET probes 2. Multiplexing commonly done **Disadvantages** 1. Prone to degradation 2. Nuclear sequestration possible 3. Requires method for transfection
Dual FRET beacons Two MBs bind to adjacent regions of a target sequence, whereby MB opening brings a FRET pair near one another resulting in turn-on of FRET signal.	mRNA[76]	1. Permeabilization[77] 2. Electroporation[76] 3. Microinjection[78]	Fluorescence	**Advantages** 1 Better signal to noise ratio compared to linear antisense probes, linear FRET probes and MBs 2. Better selectivity compared to MBs **Disadvantages** 1. Unmodified probes prone to degradation 2. Nuclear sequestration Possible 3. Requires method for transfection

				4. Requires binding to large stretch of RNA for hybridization-based approach
FIT probes A duplex sensitive dye of the thiazole orange family acts as a nucleobase surrogate in a recognition sequence such that target binding results in dye fluorescence turn-on.	mRNA[79]	1. Permeabilization[80–82] 2. Cationic polymer[79] 3. Microinjection[83]	Fluorescence	**Advantages** 1. Simple probe design (single modification) 2. Lack of false-positive signal due to degradation 3. Highly sensitive to single nucleotide mismatches 4. Multiplexing Possible **Disadvantages** 1. Nuclear sequestration Possible 2. Unmodified probes prone to degradation 3. Requires method for transfection 4. Less bright than conventional dyes like AlexaFluor488 5. Fluorescence enhancement strongly dependent on dye location in probe
ECHO probes	mRNA,[84] miRNA,[85]	1. Cationic lipids[85–88] 2. Microinjection[86]	Fluorescence	**Advantages** 1. Lower background signal than FIT probes

Generally, two thiazole orange fluorophores are covalently attached to one base of a recognition sequence, forming an H-aggregate. Target binding breaks the H-aggregate and turns-on fluorescence.	rRNA,[86] small nucleolar RNA[86]			2. Multiplexing possible **Disadvantages** 1. Nuclear sequestration Possible 2. Unmodified probes prone to degradation 3. Requires method for transfection 4. Fluorescence enhancement strongly dependent on sequence of target RNA
SNA-based structures SNAs consist of ONTs covalently functionalized around a spherical nanoparticle core, giving the ONTs a radial arrangement. Examples of nanoparticle cores used include gold,[44] upconverting nanoparticles,[89] micelles,[90] silica,[91] carbon-based,[92] and quantum dot[93]	mRNA,[44] miRNA,[89] proteins,[94] small molecules,[95] pH,[96] ions[97]	Active uptake[44,98]	Fluorescence SERS[99]	**Advantages** 1. Higher signal to noise ratio than molecular beacons 2. Uptake without transfection reagents 3. Resistant to degradation 4. Biocompatible 5. Multiplexing possible **Disadvantages** 1. Difficult to quantify endosomal escape 2. Fluorophore/quencher-

				based structures prone to false-positive signal if degraded
Structures based on ONTs adsorbed to nanoparticle surface ONT probes can be non-covalently associated with various nanoparticle cores for delivery into cells. Examples of nanoparticle cores used include gold,[100] polymer,[101] silica,[102] manganese dioxide,[103] carbon-based,[104] MOFs,[105] iron-oxide,[106] and quantum dot[107]	mRNA,[108] miRNA,[100] small molecules,[109,110] pH,[111]	Active Uptake[108]	Fluorescence	**Advantages** 1. Uptake without transfection reagents 2. Resistant to degradation 3. Biocompatible 4. Multiplexing possible **Disadvantages** 1. Difficult to quantify endosomal escape 2. Fluorophore/quencher-based structures prone to false-positive signal if degraded 3. Leaching of oligos from surface possible
Nanoparticles encapsulated with ONTs Nanoparticle cores capable of encapsulating ONTs can be used as a	miRNA,[40] mRNA,[112] small molecules[61]	Active Uptake[112]	Fluorescence	**Advantages** 1. Uptake without transfection reagents 2. Resistant to degradation 3. Biocompatible

means for carrying probes into cells. Examples of nanoparticle cores used include liposomes[40] and polymers.[112]				4. Multiplexing possible **Disadvantages** 1. Difficult to quantify endosomal escape 2. Fluorophore/quencher-based structures prone to false-positive signal if degraded 3. Strategy limited to use of nanoparticles that can be encapsulated with oligonucleotides
DNA nanomachine/ nanostructure-Based DNA can be assembled into 1D, 2D, and 3D nanomachines/nanostructures that act as sensing platforms.	mRNA,[113] miRNA,[114] pH,[115,116] ions,[117] radicals[118]	Active uptake[113,119]	Fluorescence, circular dichroism[120]	**Advantages** 1. Uptake without transfection reagents 2. Resistant to degradation 3. Multiplexing possible 4. Biocompatible **Disadvantages** 1. Difficult to quantify endosomal escape 2. Involved design requiring multiple ONT strands 3. Fluorophore/quencher

				based nanomachines prone to false-positive signal if degraded
Genetically-encoded aptamers RNA aptamers can be expressed in cells such that target binding allows the aptamer to bind a dye that results in a fluorescent signal	mRNA,[121] small molecules,[122] proteins[123]	Genetically encoded	Fluorescence	**Advantages** 1. Can be expressed in cells, so probe transfection is not necessary 2. Provides a facile way of visualizing small molecules and metabolites which are usually difficult to image 3. Dye has low background 4. Can monitor analytes dynamically *in situ* 5. Multiplexing possible, in principle **Disadvantages** 1. Poor folding *in vivo* 2. Typically requires long exposure times (10-100 ms) for imaging 3. Often requires a tRNA scaffold to promote *in cellulo* folding

				4. Requires genetic modification of cells for imaging

1.1.3 Common sensing strategies

Although numerous strategies relying on nucleic acids as probes have been developed for imaging intracellular analytes, most of the techniques employ one or more of the sensing strategies enumerated below:

Single fluorophore label

ONTs labeled with a single fluorophore can be used for detecting intracellular analytes of interest. Examples include probes labeled with commercially available fluorescein isothiocyanate or forced intercalation dyes of the thiazole orange family.[53,124]

Förster resonance energy transfer (FRET)

Nucleic acid probes based on FRET are designed such that the on/off state is dependent upon proximity between a donor and acceptor molecule due to energy transfer between the molecules. Examples include fluorophore/quencher MBs and FRET-based DNAzymes.[125,126]

Nanoparticle-based

Nanoparticles are commonly interfaced with nucleic acids for use in live cell imaging because they often confer advantageous properties over naked nucleic acids. These properties may be the ability to deliver payload into cells without the need of transfection reagents, protect cargo from nuclease degradation, act as a source of fluorescence or as a source of quenching (FRET), exhibit plasmonic

properties, and capability to absorb near infrared light for transition to a theranostic platform.[44,106,127–129] Examples of nanomaterials used include gold nanoparticles (e.g. SNAs), graphene oxide nanosheets, quantum dots, MOFs, etc.

Amplification

Incorporating an amplification element into sensing strategies is often used for detecting targets at low abundance. In live cells, target amplification methods like PCR are challenging, and as such, signal amplification methods are the most common route to lowering the limit of detection. Techniques for signal amplification include hybridization chain reaction (HCR), hairpin DNA cascade amplifier (HDCA), and DNA chain reaction (DCR).[72,108,130]

1.1.4 Design considerations for common application scenarios

Nucleic-acid based probes may be used in a variety of detection contexts, broadly classified as (a) detecting analytes and studying their spatiotemporal behavior, (b) comparing levels of analytes between different cells, (c) sorting rare cells in complex media, and (d) quantifying the amount of particular analytes present in a cell.

In the most simple case, a nucleic-acid based probe can be used to detect the presence of an analyte of interest in a cell, in certain contexts yielding important information about cellular state or the role of an analyte in disease.[131] Moreover, probes can be used to study the spatiotemporal evolution of key analytes, which can provide fundamental insight into the dynamics of these molecules and how these dynamics influence cellular functions.[132,133] For instance, Sticky-flares have been used to show for the first time that β-actin mRNA colocalizes with mitochondria in HeLa cells.[134] Furthermore, ChloropHore has been used for simultaneous tracking of pH and

chloride ion concentrations, providing fundamental insight into these analytes' association with Niemann-Pick disease.[117] Microscopy is the primary technique used in studying spatiotemporal behavior of analytes. However, for such an application, the signaling element of the probe (e.g. fluorescent element) must remain associated with the target in the complex celular environment for it to be possible to study spatiotemporal behavior.

It is also of interest to use nucleic-acid based probes for comparing the levels of analytes between different cell types.[68,135] This may yield fundamental information concerning the role of an analyte in diseased versus healthy cells, or allow one to distinguish different cell types based on their relative level of a known intracellular marker. When comparing distinct cell types, one must consider that differences in probe uptake must be accounted for, preferably through ratiometric analysis. Furthermore, if large numbers of cells are to be compared, flow cytometry will give relatively fast readouts and is thus preferable to microscopy.

Next, sorting and isolating rare cells in complex media based on molecular signatures is important both in fundamental and application-based situations.[136–138] For instance, the isolation of a rare cell may allow for further fundamental study of its genomic profile. On the other hand, knowing that a particular rare cell is present in a sample may allow one to diagnose a disease in a patient—an important application of such a strategy. As before, ratiometric probing is desirable in order to normaize probe uptake across the different cells that may be present in a sample. If the isolated cells are used for further studies and analysis, the probe used should be biocompatible and not impact cellular viability and function. For example, NanoFlares have been utilized to sort and isolate circulating tumor cells from blood based on their mRNA expession. Moreover, the isolated cells were subjected to mammosphere analysis to verify their retained viability and

functionality.[139] These types of sorting studies involving a large population of cells are best suited for fluorescence-activated cell sorting (FACS).

The last broad classification of detection scenarios concerns the ability to *quantify* targets intracellularly, in contrast to simply detecting or knowing relative amounts. FISH has widely been used for absolute quantification of transcript numbers in fixed cells.[9,140] Methods for quantitative probing in live cells usually incorporate a reference probe/dye as an internal control to which the signal from the targeting probe is normalized. For example, Tan et al. semi-quantitatively measured ATP in live cells using such an approach.[141] However, absolute quantification of intracellular targets in live cells remains a challenge in the field.

For all these detection scenarios, there are more considerations and challenges associated with probe design. These additional factors are discussed in section 6.

1.2. Hybridization-based probes

1.2.1. Linear antisense probes

Linear antisense ONTs labeled with a fluorophore can be introduced into live cells as a means of detecting their complementary mRNA transcript (Figure 1.2.1-1A). This method is akin to FISH done with fixed cells, but the washing step to remove unbound probes is not possible with live cells. As such, mRNA detection with linear ONT probes in live cells has an inherently high background signal as bound and unbound probes cannot be distinguished. In spite of its limitations, strategies exist in the literature for mRNA detection using linear ONT probes. One common strategy employed involves adding multiple probes that target the same mRNA sequence, such that binding of the probes results in large local fluorescence intensity that can be distinguished

from unhybridized probes.[54] Alternately, mRNA transcripts that are known to localize into specific domains would also result in large local fluorescence intensity from probes and can be visualized.[55] Early studies using linear ONT probes done by Politz et al. targeted the poly A tail to understand how mRNA is trafficked through the nucleus before its eventual release to the cytoplasm.[53] It was found that in large part, mRNA traffics randomly through the nucleus, and therefore, finds nuclear pores by chance before its release into the cytoplasm. In later studies, Molenaar et al. designed probes targeting U1 small nuclear RNA (snRNA), U3 snRNA, 28S ribosomal RNA (rRNA), and poly(A) RNA, and were able to detect these targets in the nucleus upon microinjection.[54] Note that although probes were microinjected into the cytoplasm, all probes were sequestered into the nucleus after approximately 60 seconds, showing the difficulty of the linear ONT approach for imaging targets in the cytoplasm.

Taken together, linear antisense probes have largely been limited in their use due to their inherently high background signal and are as such challenging to apply to targets at lower abundance or targets that are more diffuse in cells. Subsequent strategies have sought to create detection strategies with higher signal to noise ratio.

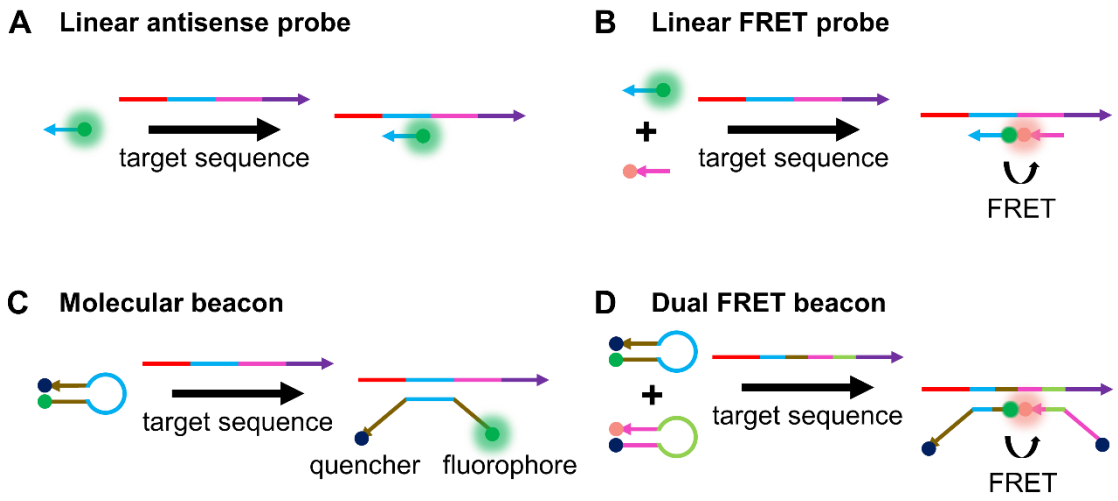

Figure 1.2.1-1. Working principles of common hybridization-based probes. (A) A schematic of linear antisense probes, whereby a dye-labeled recognition sequence binds to its complementary target illustrated in the same color.[9] (B) Linear FRET probes involve hybridization of two different linear antisense probes to adjacent regions of a target sequence, bringing a FRET pair into proximity that results in a fluorescence signal that can be monitored.[56] (C) In the off state, MBs have a duplexed stem region (illustrated in brown) that keeps a fluorophore and quencher in close proximity. Target binding to the loop region (illustrated in light blue) opens the stem region, separates fluorophore and quencher, and turns on fluorescence.[125] (D) Dual FRET beacons incorporate two MBs that can bind to adjacent regions of a target sequence. Similar to linear FRET probes, binding of the MBs to adjacent regions of a target sequence brings a FRET pair near one another, resulting in turn-on of FRET signal.[77]

1.3. FRET probes

1.3.1. Linear FRET probes

The use of linear FRET probes is commonly used to reduce the background from linear antisense probes. In this approach, two linear probes that are complementary to the same mRNA target and bind to adjacent regions on the mRNA are synthesized (Figure 1.2.1-1B). The 5' terminus of one probe and the 3' terminus of another probe are modified with donor and acceptor dyes, respectively, such that upon binding to mRNA, the FRET pair is brought close together. Proximity results in a decrease in donor fluorescence emission and increase in acceptor fluorescence

emission. The first studies done by Tsuji et al. used the FRET signal generated from probe binding to detect cytoplasmic c-fos mRNA in live COS-7 cells.[56] Similar to labeled antisense probes, linear FRET probes are also quickly trafficked to the nucleus after microinjection. As such, cytoplasmic detection required binding the linear FRET probes to a macromolecule (streptavidin) to prevent nuclear sequestration. Okabe et al. also studied c-fos mRNA in COS-7 cells, showing that inducing stress on cells results in the localization of c-fos mRNA in stress granules.[57] Linear FRET probes have also been used for detecting single nucleotide polymorphisms in mRNA. In one example, Dahan et al. designed FRET probes capable of detecting a single nucleotide mutation in the HRAS oncogene.[58]

While the linear FRET approach lowers background stemming from fluorescence from unbound probes, it also confers an additional benefit from the standpoint of selectivity. Because two probes must bind to adjacent regions of the mRNA sequence, it is highly unlikely that aberrant probe binding to mRNA will lead to false positive signal. However, because RNA is associated with proteins and often has complex secondary structure, inaccessibility of stretches of RNA target is a problem common to hybridization probes, especially so for linear FRET probes that often require ~40 bp for targeting.[56] Furthermore, non-judicious choice of donor/acceptor pairs may lead to a large amount of bleed-through of emission signal from the donor into the acceptor channel.[142]

1.3.2. Molecular beacons

One of the most common methods for visualizing mRNA in live cells is the use of hairpin ONT probes known as molecular beacons, which we refer to as MBs for simplicity. In the “fluorescence off” state of the probe, a stem region is hybridized such that a fluorophore and quencher are close to one another. Target binding to a loop region induces opening of the stem region, resulting in

separation of the fluorophore and quencher and introduction of the "fluorescence on" state (Figure 1.2.1-1C). Generally, signal to noise ratios are higher for MBs than for both linear antisense probes and linear FRET probes.[6,125] MBs were introduced by Tyagi et al. in 1996, and first used for live cell imaging in 1998.[125] For instance, Matsuo used MBs to study the distribution of basic fibroblast growth factor mRNA in trabecular cells.[59] In the same year, Sokol et al. leveraged MBs for studying β-actin mRNA and Vav mRNA in K-562 cells.[63]

Since then, numerous papers have been published that take advantage of the utility of MBs. MBs are commonly used for distinguishing different cell types based on mRNA level. In one example, a MB designed for a known oncogene, survivin, fluoresced in breast cancer cells (MDA-MB-435 and MDA-MB-231) but not in normal immortalized mammary epithelial cells (MCF-10A), showing that the beacons could successfully differentiate the cells based on survivin level.[68] Others, like Kang et al., have synthesized conventional MBs to visualize miR-26a and miR-206 simultaneously, two microRNA (miR) that are expressed heavily during myogenic differentiation, in C2C12 cells.[60] Targets need not be limited to miRNA or mRNA, as Park et al. have detected a class of non-coding small RNAs known as piwi-interacting RNAs (piR-36026 and piR-36743) in MCF-7 cells.[41] Others, like Zhao et al.[64] and Chen et al.[73], have claimed to be able to image transcripts at the single molecule level using MBs.

The fluorophore pairs in MBs need not be fluorophore/quencher pairs. Following the work of Zhang et al.,[143] Bohländer et al. described the use of two wavelength shifting MBs for multiplexed miRNA detection.[69] One MB, in the hairpin form, contained a green donor dye and a red acceptor dye in close proximity to one another. In this conformation, exciting the green dye led to emission from the red dye. Upon target binding and opening of the hairpin, exciting the green dye led to

emission from the green dye as the two fluorophores were no longer in close proximity. Another MB was designed in the same manner with a blue donor and a yellow emitter. In this way, four colors could be simultaneously monitored for detection of two different targets. The different targets chosen in this paper were miR-21 and miR-31, and they were studied in 293T, SW620, RKO, and WiDr cells.

Yet, one important advantage of fluorophore/quencher MBs is their relative ease of use for multiplexed detection. Namely, FRET is challenging to multiplex because of the difficulty in finding commercially available FRET pairs that fluoresce at distinct wavelengths.[144] Medley et al. showed that the microinjection of multiple fluorophore/quencher MBs containing dyes fluorescing at distinct wavelengths could be used to simultaneously detect mRNA associated with β-actin and manganese superoxide dismutase (MnSOD) mRNA in MDA-MB-231 cells.[65]

A problem with DNA MBs, similar to linear probes, is that they degrade in cells, sometimes within 30 minutes, leading to false positive signal.[66] To help alleviate this issue, modifications such as LNAs, 2'O-Me RNAs, morpholinos, PNAs, or serinol nucleic acids have been introduced into probes to increase biostability.[66,67,73,145–147] Moreover, base modifications can lead to enhanced hybridization kinetics, enhanced specificity, and enhanced target affinity.[148] For instance, Wu et al. introduced LNA into MBs to increase their stability and reduce their propensity for false positive signal due to degradation or protein binding.[66] LNA-enhanced MBs were functional even 24 hours after microinjection into cells, proving useful for long term imaging of MnSOD mRNA in MDA-MB-231 cells. Chen et al. synthesized morpholino molecular beacons (MOR-MBs) for use *in vivo*.[67] They hypothesized that the superior stability, biocompatibility, and affinity of morpholinos for RNA would lead to advantageous properties. MOR-MBs had no

increase in non-specific fluorescence signal in medaka fish embryos over the course of two hours. In contrast, DNA-MB signal increased gradually over the course of 45 minutes, likely due to degradation of the probe by nucleases. MOR-MBs were also able to distinguish between full complement or single base mismatch RNA targets *in vivo*. A new class of artificial nucleic acids based on a serinol backbone, called serinol nucleic acids, were incorporated into MBs by Murayama et al., and used for their enhanced biostability.[147] While imaging was done in fixed cells, signal to background ratios as high as 930 times were reported in solution, which was about 30 times higher for an equivalent MB synthesized with DNA.

Another issue, similar to other ONT probes already discussed, is that MBs may be sequestered to the nucleus following delivery, which is problematic for imaging targets in the cytoplasm. This sequestration has been prevented by linking MBs to a macromolecule, nanoparticle, or tRNA sequence.[149–151]

For detecting targets of low-abundance, it is sometimes necessary to employ strategies that amplify signal, in turn lowering the limit of detection. Strategies most often employed involve HCR or a slight variation thereof. HCR is an isothermal cascade reaction in which an initiator sequence triggers the hybridization of two complementary sequences trapped in metastable hairpin conformations.[152] Incorporating a donor or acceptor dye (FRET pair) into each of the hairpins is one common way to interface HCR with a readout event for target detection (Figure 1.3.2-1A). Strategies inspired by this approach include cascade hybridization reaction (CHR), developed by Cheglakov et al.[70] and branched HCR (b-HCR), developed by Liu et al.[71]

Inspired by the work of Yin et al.,[153] another amplification strategy was proposed by the Tan group in 2015, called hairpin DNA cascade amplification (HDCA, Figure 1.3.2-1B).[72] The probe

set consists of a total of four distinct strands. When no mRNA target is present, two DNA strands H1 and H2 are each in the form of a hairpin. Additionally, a fluorophore-labeled "reporter" strand is prehybridized to a quencher-labeled strand. When present, mRNA binds to the toehold region of H1, opening the hairpin and exposing bases which can bind to H2, which in turn displaces the mRNA due to stronger binding with H1. This strategy allows the mRNA to participate in more rounds of signal amplification. The H1-H2 complex formed has an overhang that is complementary to the "reporter" strand. The quencher strand is displaced providing a fluorescent readout. In proof-of-concept studies, MnSOD mRNA, associated with tumor proliferation, was detected in MDA-MB-231 cells after transfection of probes with Lipofectamine 3000. Notably, these probes were able to sense MnSOD mRNA even after the mRNA was knocked down using cordycepin, a scenario where a low abundance target could be detected.

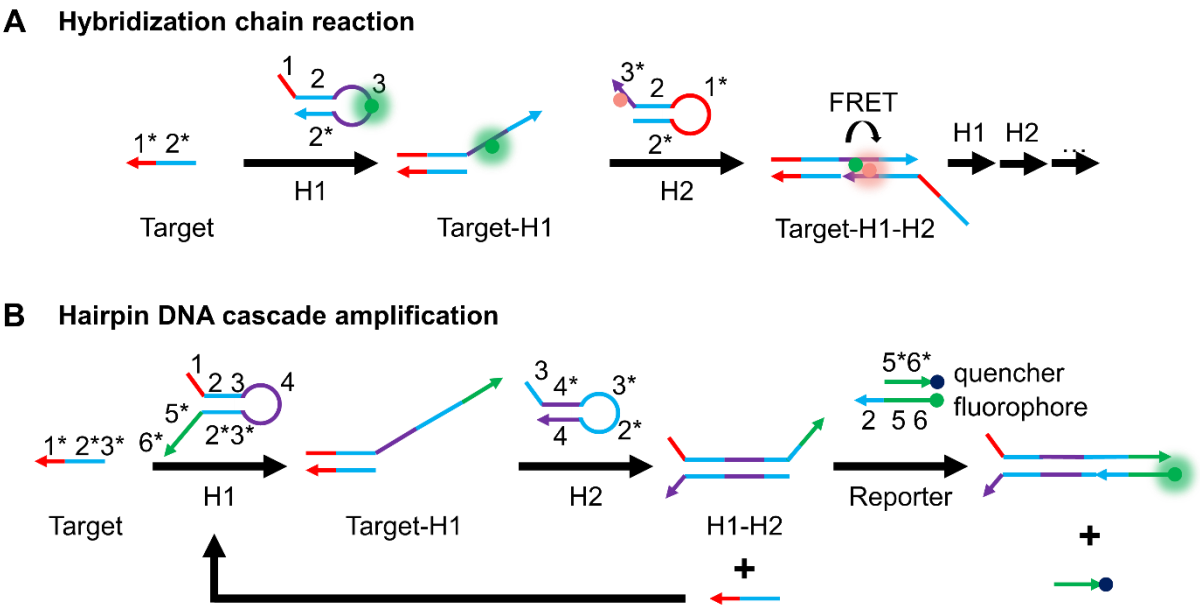

Figure 1.3.2-1. Two common oligonucleotide-based strategies for isothermal amplication of fluorescence signal. (A) Hybridization chain reaction[152] for enabling a FRET-based amplified fluorescence readout. The presence of a target sequence initiates a cascade hybridization reaction

between two metastable hairpins (H1 and H2) with extended regions of complementarity. Incorporation of a FRET-pair, one in the loop region of H1 and the other in the toehold region of H2 brings the FRET-pair into close proximity upon HCR. (B) Hairpin DNA cascade amplification.[72] Target binding to H1 exposes a region in H1 that can bind to H2. This releases the target and allows it to bind more H1 strands for amplified signal. The H1-H2 complex can bind to a fluorophore-labeled strand that is pre-hybridized to a quencher-labeled strand, displacing the latter and turning on fluorescence.

One problem with MBs (and linear probes) is that "naked" nucleic acids do not generally enter cells on their own, and thus require transfection strategies like cationic liposomes, conjugation to a cell penetrating peptide, microinjection, or electroporation.[6] Therefore, many recent approaches have sought to use aptamer-based or nanoparticle-based strategies to circumvent the need for these methodologies. While nanoparticle-based strategies will be the subject of a separate section (vide infra), we will briefly discuss strategies for aptamer-based entrance into cells in this section.

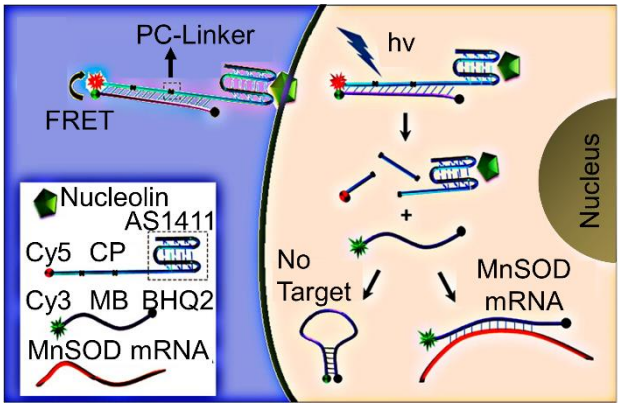

Figure 1.3.2-2. "On-demand" MBs incorporating an aptamer-targeting nucleolin (AS1411) for transfection reagent-free uptake into cells. Irradiation with UV-light activates the MB for use by cleaving the PC linkers and detaching the MB from the CP region. Adapted with permission.[74] Copyright (2013) American Chemical Society

The Tan group has designed MBs that start functioning "on demand" and enter cells without transfection reagents **(**Figure 1.3.2-2**)**.[74] Their carrier probe molecular beacons (CP/MBs) consist of two strands. One strand of the probe is the MB that is complementary to an mRNA transcript of interest. The other strand is an aptamer plus carrier probe (CP) sequence. The aptamer chosen

(AS1411) has been found to attach to nucleolin, which is a cell surface marker that is present on many cancer cells. The authors claimed that binding of the CP/MBs to nucleolin allowed for direct cytosolic entry of the probes. To make the probes "on demand," photocleavable (PC) linkers were incorporated into the CP region. Initially, the CP and MB region are hybridized, not allowing for the MB to bind to complementary mRNA in the cell. Upon UV irradiation, the PC linkers are cleaved and the MB is detached from the CP region, allowing the MB to bind to complementary mRNA. MnSOD was chosen as a model target and imaged in MCF-7 cells. Taken together, this construct allows for targeted delivery to cells, entrance into cells without transfection reagents, and "on demand" activation of the MB allowing for precise spatiotemporally controlled imaging in the cell.

Furthermore, Kim et al. developed RNA aptamer-based probes for detection of miRNA in live cells.[75] To allow for uptake into cells without the need of transfection reagents, mucin1 (overexpressed in malignant cancer cells)-binding aptamers were hybridized to the probe, resulting in probe endocytosis. As a proof-of-concept, miR-34a was imaged in MCF-7 cells and T47D cells.

1.3.3. Dual FRET beacons

One way to increase the signal to noise ratio of MBs is to employ a dual FRET approach (Figure 1.2.1-1D). In this design, two different MBs are designed that hybridize to adjacent locations on an mRNA transcript of interest. Each probe contains a fluorophore that can form a FRET pair with the fluorophore on the other probe. In the off state, fluorescence of both probes is quenched due to close proximity of a fluorophore and quencher. Upon binding of the MBs to the target, the fluorophores are unquenched and brought in close proximity to one another such that they can form a FRET pair. Importantly, with this strategy, one can differentiate signal due to non-specific

separation of fluorophore and quencher from actual signal due to binding by monitoring FRET signal. Santangelo et al. used dual FRET MBs to study the KRAS and survivin oncogenes in live human dermal fibroblasts and MIA PaCa-2 cells.[77] Indeed, they were able to show that signal due to non-specific separation of fluorophore and quencher could be distinguished from signal due to binding, thus reducing false-positive signal. King et al. have shown the utility of dual FRET MBs for detecting Oct4 mRNA and subsequently isolating Oct4 positive pluripotent human embryonic stem cells using flow cytometry.[76]

In spite of the fact that dual FRET beacons can improve signal to noise ratio, they suffer from the same limitations that linear FRET probes suffer. Namely, given the complex secondary structure of RNA and its association with proteins, finding large stretches of RNA that are accessible for probe binding is a challenge.

1.4. Quencher-free probes

1.4.1. FIT probes

Forced intercalation (FIT) probes were developed in 2005 by the Seitz group as a quencher-free method for nucleic acid detection (Figure 1.4.1-1A).[124] FIT probes consist of a sequence of nucleic acids and a single intercalator dye of the thiazole orange family, whereby the intercalator plays the role of a nucleobase surrogate. Dyes of the thiazole orange family fluoresce when rotation around their methine bridge is restricted. Thus, when a FIT probe binds to its complementary sequence, methine bridge rotation is hindered, which results in fluorescence being turned on. Notably, this strategy results in no false-positive signal as a result of probe degradation, overcoming a key limitation associated with MBs.[83] Furthermore, FIT probes offer fluorescence

enhancement, reported to be as high as 195 times upon addition of complementary target.[154] Much of the work in live cell imaging using FIT probes has relied upon the use of peptide nucleic acids (PNA) due to their biostability and both rapid and strong hybridization to complementary ONTs.[79–81,155,156] Kam et al., for example, used PNA FIT probes for detection of KRAS mRNA inside live cells.[79] They showed that FIT probes are sensitive to single nucleotide mismatches directly adjacent to the intercalator, such that single nucleotide polymorphisms (SNPs) in the KRAS gene could be discriminated. Importantly, a conventional fluorophore/quencher MB was unable to discriminate SNPs in the KRAS gene.

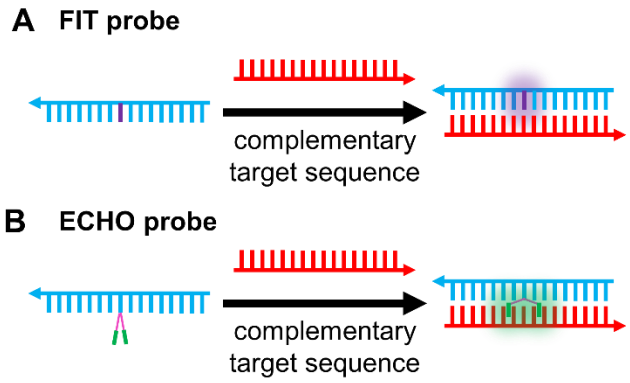

Figure 1.4.1-1. Quencher-free probes. (A) FIT Probes incorporate a viscosity sensitive dye, such that target binding results in turn-on of the dye[124] (B) ECHO probes contain two dyes (e.g. thiazole orange) that are covalently attached to the same base in a probe sequence. In the free probe, the dyes form an H-aggregate resulting in attenuated fluorescence emission. Target binding breaks the H-aggregation, and the dyes intercalate between the bases in the duplex with concomitant fluorescence turn on.[84]

More recent work in the area has looked into enhancing probe brightness, using more accessible nucleobase chemistry, and multiplexing of gene analysis. Imaging in cells and tissues with high sensitivity requires probes that are both responsive and sufficiently bright. Two different approaches have been used to enhance FIT probe brightness. In the first approach, a duplex responsive dye (thiazole orange) is paired to a highly emissive dye (oxazolopyridine analogue,

JO).[157] In the single strand, fluorescence is quenched due to dye twisting about the methine bridge and dye-dye contact. Upon binding of complementary target, quenching due to twisting and energy transfer are stopped, leading to fluorescence turn-on. TO is believed to play the role of a light collector that can transfer excitation energy to the highly emissive JO moiety.[157] As proof-of-concept, the TO/JO system was used to image oskar mRNA in the tissue of *Drosophila melanogaster* using wash-free FISH. Recently, mRNA associated with the mCherry protein was imaged using this system in live FIp-In™ 293 T-Rex cells expressing the gene.[82]

An alternative approach for enhancing the brightness of FIT probes involves the use of locked nucleic acids (LNAs).[83] Hövelmann et al. showed that the introduction of an LNA base directly adjacent to the duplex responsive dye introduces further rigidity in the local environment of the dye, resulting in more restricted rotation around the methine bridge and a concomitant increase in final brightness upon target hybridization. LNA-enhanced FIT probes were then used to track in real time oskar mRNA associated with ribonucleoproteins in *Drosophila melanogaster*.

Although PNAs impart increased nuclease resistance to the probes, they suffer from several limitations. The neutral backbone of PNAs renders them less soluble compared to conventional phosphate backbone-based ONTs and makes them susceptible to aggregation. Moreover, PNA synthesis is more costly than conventional nucleic acid synthesis and common protocols for nucleic acid transfection are not applicable to them. Therefore, recent work in FIT probes has focused on alternate strategies, for example, by modifying the sugar moieties in ONTs with phosphate backbones.[158] 2’-O-Me RNA and LNAs have been used in FIT probes due to their resistance to nuclease degradation and both rapid and high affinity binding to complementary nucleic acids.[83,154] FIT probes made of DNA have also been used for live cell imaging.[159]

Recently, the Seitz group reported the development of four new dyes for use in FIT probes.[154] Of these, three showed fluorescence enhancement upon addition of complementary target. Importantly, the new dyes fluoresce in distinct wavelength regimes, allowing later studies to do multiplexed live cell imaging of the poly A tail of mRNA and different regions of mCherry mRNA in Flp-In 293 T-REx cells. [159]

1.4.2. ECHO probes

A variant of FIT probes are exciton-controlled hybridization-sensitive fluorescent ONT (ECHO) probes (Figure 1.4.1-1B). When two thiazole orange fluorophores are covalently attached to the same base of a nucleic acid sequence and arranged parallel to one another (H-aggregation), fluorescence is largely attenuated due to excitonic interactions between the two fluorophores. Upon complementary nucleic acid binding, the H-aggregate is broken and each thiazole orange intercalates into the duplex such that fluorescence is turned on.[160] Early studies to assess the feasibility of ECHO probes in live cells consisted of designing probes targeting the poly A tail of RNA. Microinjecting these probes into HeLa cells resulted in fluorescence intensity observable in the cytoplasm and nucleus as a result of probe binding to target.[84]

To aid in multiplexed imaging, Ikeda et al. developed new fluorophores capable of use in ECHO probes.[85] While those fluorophores that were originally developed ranged in emission maxima from 455 nm to 677 nm, more recently near-IR dyes have also been developed for ECHO probes.[87] To show the capability of multiplexed live cell detection, ECHO probes with three different dyes were designed to target three different miRNA sequences. Microinjected probes proved useful for detecting the targeted miRNA in the nucleus of HeLa cells.[85]

Efforts have also been made to introduce base modifications to ECHO probes, as unmodified DNA probes are quickly degraded in cells, making long-term live cell imaging challenging. For instance, a 2'-O-Me-modified ECHO probe targeting the poly-A tail of RNA was used for imaging of HeLa cells.[88] Time-resolved imaging showed that fluorescence was much more intense at the mitotic phase than at the interphase, implying that relatively large quantities of mRNA are expressed as the cell divides. Later studies have shown the capability of ECHO probes to detect other intracellular RNA targets, including 28S rRNA and U3 small nucleolar RNA.[86]

1.4.3. Miscellaneous quencher-free probes

Min et al. took advantage of aggregation-induced emission for detection of miRNA.[161] DNA probes complementary to a target of interest were synthesized with aggregation-induced emission luminogens (AIEgens) on the 5' end. Upon binding of target, a duplex is formed. Addition of exonuclease III results in successive removal of mononucleotides from the probe sequence and subsequent release of both the RNA target and the AIEgens. The AIEgens are free to aggregate and turn on fluorescence, while the RNA target is free to bind to more probe, thus amplifying signal. The probe was efficacious in detecting miR-21 in HeLa and MCF-7 cells (high expression), and human lung fibroblast cells (HLF) (low expression).

Ro et al. leveraged the unique optical properties of pyrene-linked adenine (PyA) derivatives to detect miRNA in live cells.[162] The probe sequence was designed such that in the presence of the target miRNA, the PyA moieties were brought to close proximity that resulted in a wavelength shift in emission from 455 to 600 nm. A detection limit of 0.63 nM was found in solution, and the strategy was used to image miR-21 in HeLa, MCF-7, and NIH-3T3 cells successfully.

Østergaard et al. have developed quencher-free MBs.[163] 2′-N-(pyren-1-yl)carbonyl-2′-amino LNA monomers are incorporated into the loop region of a MB. Little fluorescence is seen for these LNA monomers when in a single stranded region, but significant fluorescence turn-on is observed when present in a duplexed strand. These so called "glowing LNAs" were used to image mRNA corresponding to component X of pyruvate dehydrogenase complex in 3T3-L1 cells.

1.5. Nanoparticle-based probes

1.5.1. Gold nanoparticle-based

1.5.1.1. Nanoflare

NanoFlares were invented and reported in 2007 by the Mirkin group as a new tool for studying mRNA (Figure 1.5.1-1A).[44] NanoFlares are SNA gold nanoparticle conjugates and consist of a dense shell of duplex DNA on a gold nanoparticle surface. One strand of the duplex, called the recognition strand, has a track (e.g. ~20 base pairs) complementary to an mRNA target of interest. The other strand of the duplex, called the flare strand, consists of a fluorophore and typically has ~8 base pairs of complementary to the recognition strand. When the recognition strand and flare strand are hybridized, the gold nanoparticle quenches fluorescence of the flare strand due to close proximity between the gold and the fluorophore. When the mRNA target of interest is present in the cell at sufficient concentrations, the mRNA binds to the recognition strand and the flare sequence is displaced, resulting in fluorescence turn-on.[164] Owing to the dense packing of DNA on the nanoparticle surface, NanoFlares exhibit high cellular uptake without the need for transfection reagents, display enhanced resistance to nuclease degradation in comparison to free nucleic acid probes, and exhibit little immunogenicity or toxicity.[165] In the first studies,

NanoFlares were used to differentiate between different cell lines based on expression of mRNA associated with the oncogenic marker survivin. Specifically, cells that do not express survivin (C166 cells) were differentiated from cells that express large amounts of survivin (SK-BR-3 cells).[44]

As NanoFlares bind to mRNA, studies in 2009 by Prigodich et al. showed that the platform can be used for the simultaneous detection and regulation of survivin in HeLa cells.[166] Consistent with previous studies, detection of survivin required relatively low concentrations and treatment times of NanoFlares with HeLa cells (0.5 nM and 6 h) while regulation required relatively high concentrations and treatment times (5 nM and 4 days) of NanoFlares with HeLa cells.

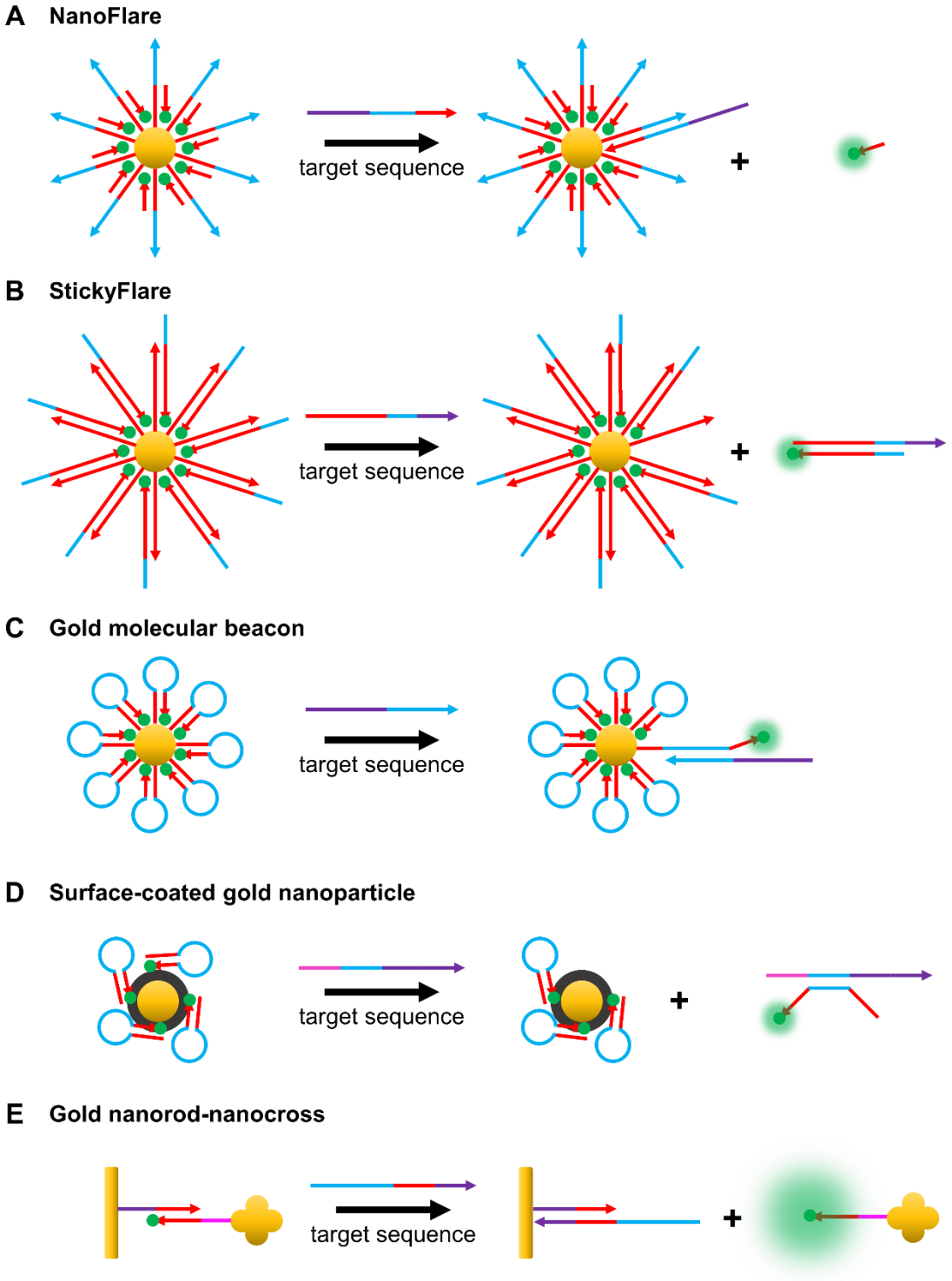

Figure 1.5.1-1. Common gold nanoparticle-based hybridization probes. (A) In the off state of a NanoFlare, a fluorophore-labeled flare strand is hybridized to a gold-bound recognition strand, allowing for gold to quench fluorescence. Target binding to the recognition strand displaces the

flare sequence, separates it from gold, and turns on fluorescence.[44] (B) In the StickyFlare construct, the fluorophore-labeled strand is designed to be complementary to the target. Therefore, upon probe-target binding, the target can be monitored, providing valuable spatiotemporal information about its dynamics.[134] (C) Gold MBs consist of fluorophore-labeled hairpin ONTs conjugated to the surface of gold nanoparticles. The principle of action is the same as that of MBs, except the central gold nanoparticle acts as a quencher.[98] (D) As opposed to chemical conjugation, fluorophore-labeled ONTs may also be adsorbed onto surface-coated gold nanoparticles. For example, as depicted in the figure, fluorophore-tagged hairpin ONTs can be adsorbed onto polydopamine (colored black)-coated gold nanoparticles.[167,168] Polydopamine acts as a further source of quenching and can be utilized in photothermal therapy due its ability to absorb NIR light. (E) Anisotropic gold nanoparticles have also been used as cores. For example, a gold nanorod (functionalized with the recognition strand) that acts as a quencher can be attached to a gold nanocross (functionalized with a complementary fluorophore-labeled strand). Upon target binding, the fluorophore-labeled strand attached to the nanocross is released, inducing fluorescence turn on. The presence of the nanocross further enhances the fluorescence due to surface enhanced resonance.[169]

Further work has leveraged the capability of NanoFlares to become the first example of a genetic based approach for simultaneous detection and isolation of *live* circulating tumor cells (CTCs) in and from human blood.[139] Vimentin and fibronectin, both known markers of the epithelial to mesenchymal transition (EMT), were targeted using Nanoflares. A known quantity of mCherry expressing MDA-MB-231 cells was added to samples of whole human blood, followed by incubation with either vimentin, fibronectin, or scramble control NanoFlares. mCherry positive and flare (Cy5) positive cells were isolated using flow cytometry. The NanoFlare was shown to detect as few as 100 CTCs in whole blood samples with an average recovery of cells of around 68%, on par with other techniques for CTC isolation.[170] In a different experiment, a GFP-expressing recurrent cell line known to form mammospheres was spiked into whole human blood. Cells isolated for GFP fluorescence and flare (Cy5) fluorescence were then subjected to a mammosphere analysis. As expected, isolated cells were capable of forming mammospheres indicating that these cells were indeed the GFP-expressing cells originally spiked into human blood and that NanoFlares had no detrimental impact on cell viability.

Recently, NanoFlares have been used for numerous applications *ex vivo* and *in vivo*. For instance, Yeo et al. utilized NanoFlares for abnormal scar detection.[135] The connective tissue growth factor (CTGF) mRNA is overexpressed in incidences of hypertrophic and keloidal scars, resulting in overproduction of collagen. *In vitro*, CTGF-targeting NanoFlares could be used to distinguish between keloidal scar fibroblasts (KSFs), hypertrophic scar fibroblasts (HSFs), and non-diseased dermal fibroblasts (NSFs). Mixing CTGF NanoFlares and HSFs together in matrigel and subsequent subcutaneous injection into mice showed that detection was possible *in vivo* as well. However, because human skin has more epithelial skin layers than mouse skin, it is in challenging to detect markers of aberrant scar formation in human skin. Using an *ex vivo* model of human skin, the study showed that NanoFlares infiltrate past the epidermis and distribute in the dermis. Importantly, the penetration depth of NanoFlares was sufficient to detect HSFs that had been injected into the dermal region of an *ex vivo* skin sample. Taken together, these findings are significant, since the NanoFlare has the potential to change paradigms in skin disease diagnosis from histopotalogy and biopsy to something non-invasive that is more amenable to earlier detection of aberrant scars.

Another example of NanoFlares used for investigating skin wound models comes from Vilela et al.[171] Wound healing involves an epithelial to mesenchymal transition, and as such monitoring of vimentin mRNA using NanoFlares can be used as a handle to monitor the progression of the process. Indeed, the study showed that light-sheet microscopy could be used to study the 3-dimensional distribution of vimentin mRNA in whole tissue samples obtained from mice.

Recently, Moros et al. used gold NanoFlares for detection of mRNA in live Hydra vulgaris organisms.[172] Their study targeted Hymyc1 mRNA, which is a member of the MYC family of

proto-oncogenes. After incubating Hydra polyps with NanoFlares targeting Hymyc1, the group found no toxicity to the organism due to the NanoFlares. Furthermore, animals treated with Hymyc 1 targeting NanoFlares showed fluorescence in their body column, but neither in their head nor tentacles, as expected. Scrambled NanoFlares with no target in the organism showed no fluorescence after incubation, while positive control NanoFlares targeting poly A RNA fluoresced throughout the organism, as expected. In another successful use of NanoFlares, Sozer et al. have recently used NanoFlares to detect single nucleotide mutations in Janus kinase 2 mRNA.[173]

Slight variations in the original NanoFlare design have led to NanoFlares with additional capabilities. For example, multiplexed NanoFlares were developed in 2012 to detect multiple mRNA transcripts with a single construct.[39] Recognition sequences targeting both β-actin and survivin were conjugated to the same nanoparticle. By hybridizing flare sequences containing either Cy3 (β-actin) or Cy5 (survivin), both targets could be simultaneously detected. Notably, simultaneous detection allowed for normalizing survivin flare signal to flare signal from a housekeeping gene, narrowing the normally broad distribution of fluorescence values seen due to differences in probe uptake and flare degradation amongst individual cells. The Tang group has also leveraged the strategy of multiplexed detection. In one example, mRNA associated with three different oncogenes was detected with a single construct.[174]

One improvement to the original NanoFlare was introduced by Yang et al. in 2015 in the form of FRET NanoFlares.[175] In this design, the flare strand contains an acceptor dye on the 3’ end and a donor dye on the 5’ end. When mRNA binds to the recognition sequence, the flare strand is displaced. With the proper flare sequence design, the strand folds into a hairpin upon displacement, bringing into close proximity the donor and acceptor dye and allowing for the

monitoring of FRET signal as the readout for mRNA binding. This new design holds a key advantage over the original NanoFlare design. Namely, no false-positive signal should be seen due to nuclease degradation or destruction of the gold-sulfur bond. However, this strategy does suffer from the need of having a dual fluorophore-labeled flare strand and necessitates more intricate flare sequence design.

A variant of the NanoFlare design was introduced in 2015 that allowed for simultaneous detection and tracking of mRNA transcripts, termed the Sticky-Flare (Figure 1.5.1-1B).[134] In the Sticky-Flare construct, the flare strand tagged with a fluorophore is complementary to the target mRNA, such that following binding, the mRNA can be tracked in real time. Sticky-Flares designed to target β-actin mRNA allowed for study of the mRNA's real time dynamics and final localization. β-actin mRNA in HeLa cells was observed to co-localize with the mitochondria, marking the first time this phenomenon has been observed in this cell line.

Other design variations have sought to add signal amplification to NanoFlares. Liang et al. recently developed an entropy driven amplifier in conjunction with conventional NanoFlares, reaching a detection limit of 8 pM in solution and imaging miR-21 in MCF-7, HeLa, HEK293, and MRC-5 cells.[176] Moreover, Li et al. recently interfaced FRET NanoFlares with an amplification element for sensitive miRNA detection.[177] This approach was able to detect miR-let-7a in cells with high expression (MCF-7) and cells with relatively low expression (A549).

Commercially available NanoFlares have also been used successfully by a number of groups for studying genetic content in live cells.[178–181]

1.5.1.2. Gold nanoparticle molecular beacon

Gold nanoparticle molecular beacons (NP-MBs), also variants of SNAs, offer a number of potential key advantages, including resistance to nuclease degradation and entrance into cells without the need of transfection reagents. Gold NP-MBs consist of a dye-labeled hairpin DNA sequence functionalized to a gold nanoparticle (Figure 1.5.1-1C). When the hairpin is closed, the dye is in close proximity to the gold, leading to the fluorescence off state due to gold quenching of fluorescence. When the target mRNA binds the DNA sequence, the hairpin is opened such that the dye is separated from the gold and fluorescence is turned on. Note that this strategy requires careful design of the MB sequence, as hairpin opening must result in sufficient distancing of the fluorophore and gold at risk of observing weak signal. Early work in this area was done by Harry et al., who were able to detect tyrosinase mRNA in melanoma cells.[182] Others, like Xue et al., have detected oncogenes like STAT5B in MCF-7 cells.[183] Uddin et al. have used NP-MB for detection of VCAM-1 mRNA, a marker of inflammation, in retinal microvascular endothelial cells.[184] Work by Qiao et al. has expanded on the original construct by conjugating two different MBs on the gold surface to do multiplexed analysis of survivin and cyclin D1 mRNA.[185] Jayagopal et al. simultaneously imaged GAPDH mRNA and respiratory syncytial virus (RSV) mRNA in Hep-2 cells.[98] In another example from the Tang group, four different oncogenes were detected simultaneously using a gold NP-MB.[186]

Examples of theranostic platforms also exist.[187,188] For example, in 2015, Bao et al. used an *in vivo* murine model of gastric cancer to show that gold NP-MBs were able to simultaneously detect, target, and knock-down the expression of the oncogenic KRAS gene.[187]

Moreover, Pan et al. have developed constructs capable of simultaneous detection of mRNA and matrix metalloproteipnases (MMPs).[94] MBs specific for TK1 mRNA and GalNAc-T mRNA

along with fluorophore-labeled peptides that are cleaved in the presence of MMP-2 and MMP-7 were functionalized to the surface. MB opening and peptide cleavage separated fluorophore from gold, yielding fluorescence. The probe proved useful for the simultaneous monitoring of these cancer associated biomarkers in MCF-7 and MCF-10a cells. Pan et al. have devised a slight variation of the original design to allow multiplexing using monitoring of a FRET signal.[189]

1.5.1.3. Surface-coated gold nanoparticles

Some have coated gold nanoparticles with polydopamine (PDA) as part of their platform. PDA is attractive becaucse it permits immobilization of probes onto the surface through π-π interaction rather than tedious chemical conjugation, acts as another source of fluorescence quenching, and can be used in photothermal therapy because it absorbs light in the near infrared region.[100,190–192]

Choi et al. coated gold nanoparticles with PDA and subsequently adsorbed fluorophore-labeled hairpin probes targeting miRNAs of interest (Figure 1.5.1-1D).[100,167] Duplexing with the miRNA causes release of the probes from the surface and subsequent fluorescence turn-on. The probe proved useful for long term imaging of miR-29b and miR-31, two osteogenic markers, in hMSCs and primary osteoblasts. In particular, a time-dependent fluorescence was seen in primary osteoblasts and hMSCs going through osteogenic differentiation. Importantly, fluorescence signal in these cells was visible for up to 5 days. On the other hand, fluorescence was neither seen in hMSCs that had not differentiated nor in 3T3 fibroblasts, as expected.

Furthermore, Zheng et al. developed a NanoFlare-like construct using PDA-coated gold nanoparticles.[168] Target binding to the recognition strand results in the fluorophore strand's displacement, leading to fluorescence turn-on. This probe was used to image miR-21 in HeLa cells.

Taking advantage of PDA's ability to absorb near-infrared light and potential as an agent for photothermal therapy, they showed that laser irradiation of HeLa cells treated with the probe resulted in a large decrease in cell viability.

Liu et al. have used PDA-coated gold nanoflowers for miRNA detection.[193] Nanoflowers were used for their high surface area providing access to higher loading densities of ONT probes. Two different hairpins are first adsorbed to the PDA-coated surface, whereby one of the hairpins is fluorophore-labeled. The target of interest opens the fluorophore-labeled hairpin, leading to fluorescence turn-on. Opening of the first hairpin also leads to exposure of a region that can bind to the second hairpin, whereby binding of the second hairpin leads to displacement of the bound target. In this way, the target is recycled to allow for binding to another fluorophore-labeled hairpin, leading to amplified signal. A low detection limit of 400 fM was found in solution. This amplification strategy was used for imaging miR-21 in HeLa cells.

Wu et al. developed the first example of HCR between hairpin probes for live cell mRNA detection.[108] Their construct consists of a gold nanoparticle coated with a layer of cationic peptides that are electrostatically complexed with hairpin DNA. Two different hairpin DNA are associated with the surface, each with a fluorophore that when near the other will form a FRET pair. While associated with the surface, the fluorescence of the dyes is quenched by the gold nanoparticle, leading to the probe "off state." The target mRNA triggers HCR between the hairpins leading to the "fluorescence on" state in which multiple FRET pairs are formed. The authors claimed a limit of detection of ~0.5 pM in beaker studies. Interestingly, the authors also noted that the constructs bypassed endosomes and entered the cytoplasm directly, enabling them to image survivin mRNA in HeLa cells.

1.5.1.4. Other gold-based approaches

Constructs with gold nanorod cores also have been studied. Interestingly, it has been reported that constructs based on gold nanorods exhibit nearly two fold higher signal to noise ratio than constructs based on gold nanospheres.[194] Furthermore, because gold nanorods absorb near infrared light, they have been widely used in the literature for photothermal therapy, making them candidates for use in theranostic platforms.[195–197]

In a strategy analogous to that used with spherical gold NP-MBs, Wang et al. used gold nanorod MBs for detection of Dll4 mRNA in HUVEC cells.[194] Importantly, they were able to track Dll4 mRNA and study its dynamics in individual cells. In another example, Riahi et al. used gold nanorod MBs for studying β-actin and HSP70 mRNA in human breast adenocarcinoma cells and mice tissues.[198]

Sun et al. developed a dual FRET/surface enhanced resonance nanosensor composed of both gold nanorods and gold nanocrosses (Figure 1.5.1-1E).[169] The recognition strand is conjugated to a gold nanorod, while a fluorophore-labeled complementary strand is conjugated to a gold nanocross. In the case where the two strands are hybridized, the fluorophore is in close proximity to the gold nanorod and fluorescence is quenched. When the target binds the recognition strand, the fluorophore-labeled strand conjugated to the gold nanocross is displaced, resulting in fluorescence turn-on. However, surface enhanced fluorescence is also observed due to the presence of the gold nanocross, resulting in further increase in fluorescence of the dye. The authors used the construct to study miR-21 in HepG2, H9C2, and BRL cells. Yan et al. electrostatically complexed probe sequences with polyethylenimine (PEI)-modified gold nanorods to achieve miRNA detection with amplified signal.[199] The first element of their system is a quencher

containing recognition strand prehybridized with a fluorophore containing strand. Target binding displaces the fluorophore-labeled strand, leading to fluorescence. Adding a fuel strand displaces the bound miRNA target, allowing the target to participate in more fluorophore strand displacement events to amplify signal. The nanosensor was used for detection of miR-21 in MCF-7 tumor bearing mice. Photothermal therapy was also done, as NIR irradiation of the constructs led to reductions in tumor volume.

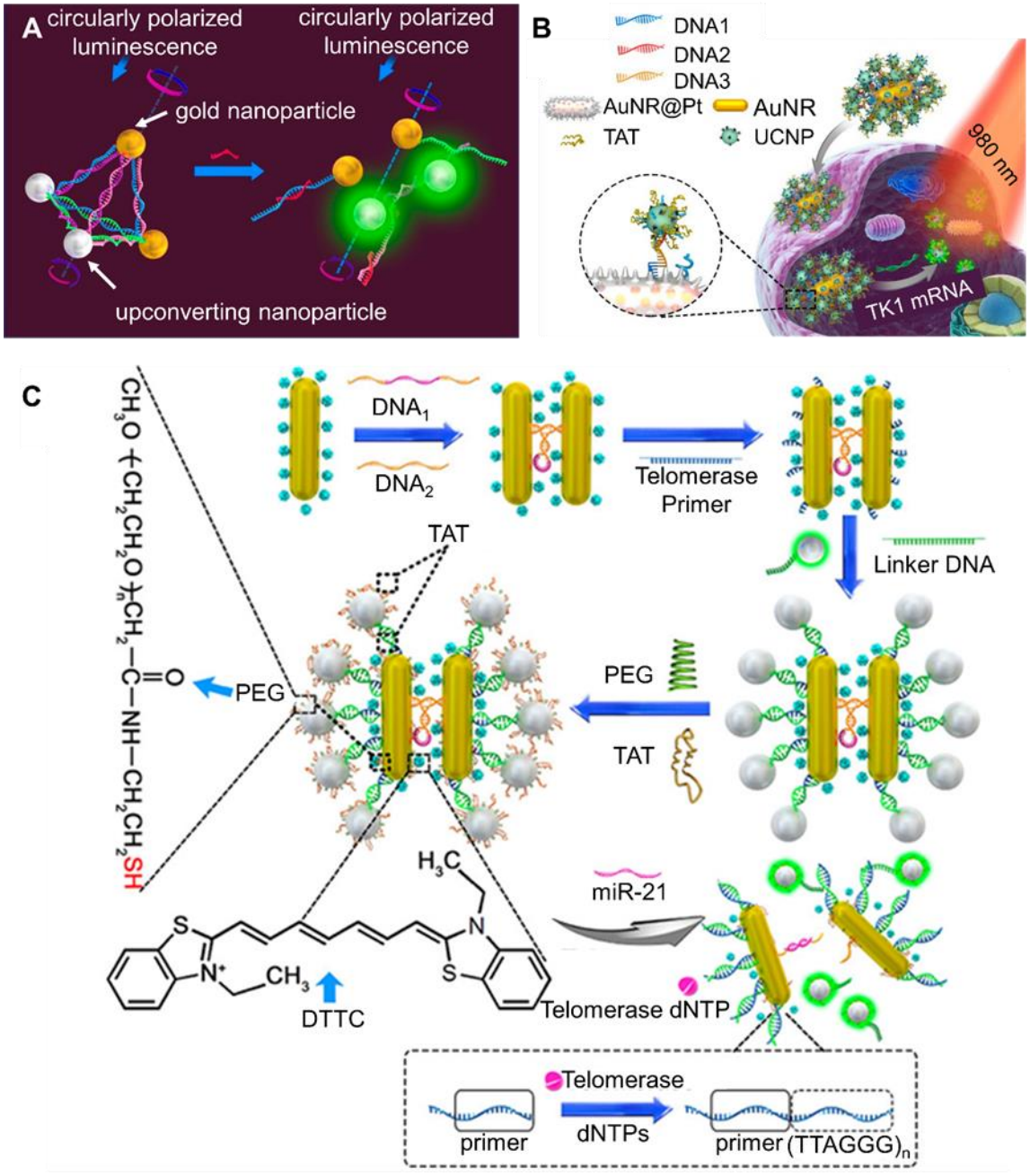

Figure 1.5.1-2. Selected upconverting nanoparticle-based hybridization probes. (A) A dual gold nanoparticle/upconversion system that allows for simultaneous monitoring of luminescent and circular dichroism (CD) signal change upon binding of miRNA. Target binding leads to structural disassembly, giving increased luminescence and decreased CD signal. Adapted with permission.[120] Copyright (2016) American Chemical Society. (B) AuNR/UCNP satellite assembly that is disassembled upon target binding, leading to increase in luminescence due to separation of UCNP and AuNR. A more detailed description of the platform is given in section 2.4.2. Adapted with permission.[89] Copyright (2018) American Chemical Society. (C) A

schematic of a AuNR@Pt-UCNPs satellite assembly that can detect both miR-21 and telomerase simultaneously. miRNA binding leads to separation of the nanorods and a change in Raman signal, while telomerase presence leads to separation of gold nanorods and UCNPs and a subsequent luminescence signal. Adapted with permission.[200] Copyright (2017) American Chemical Society.

1.5.2. Upconverting nanoparticle-based

Certain upconverting nanoparticles (UCNPs) have found use in live cell imaging due to their biocompatibility, high photostability, and unique optical properties.[89,120,201,202] These nanoparticles absorb two or more lower energy photons and emit a higher energy photon. In the context of live cell imaging, this property allows probes to be excited with near-IR light and observe emission in the visible range, thereby overcoming issues related to cellular autofluorescence. Li et al. have explored a nanoparticle strategy where a luminescent and circular dichroism (CD) signal can be simultaneously monitored using gold-upconverting nanoparticle (Au-UCNP) pyramids for detection of miRNA in live cells (

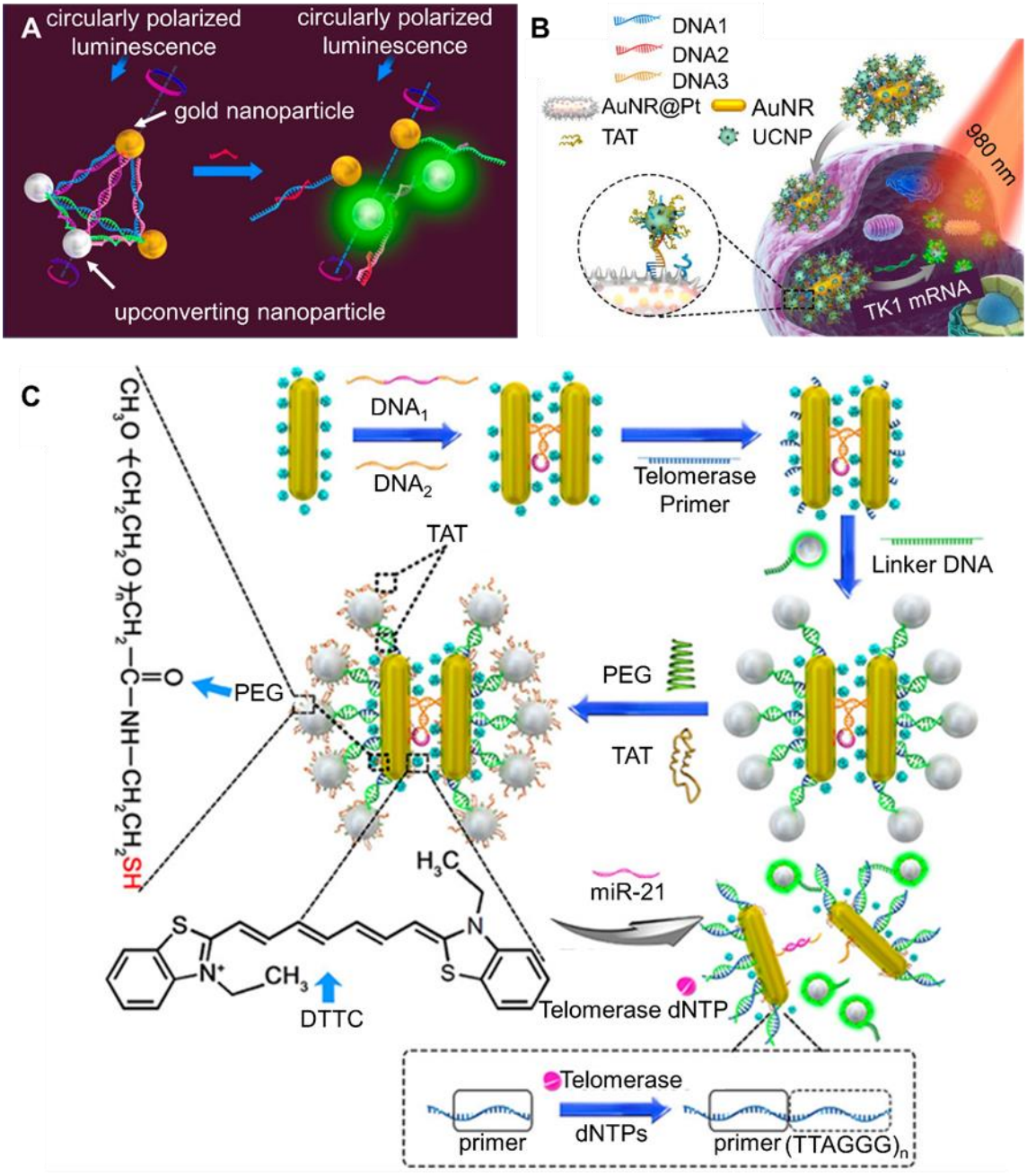

Figure 1.5.1-2A).[120] In the initial state, DNA linkages between nanoparticles result in the formation of a pyramidal structure. Binding of an miRNA sequence to a recognition region in the pyramid results in structure disassembly and subsequent separation of the gold nanoparticles and UCNPs. This separation is accompanied by an increase in luminescent signal (excitation = 980

nm, emission = 540 nm) from the UCNPs and a decrease in CD signal at 521 nm that can be monitored. To assess the feasibility of this strategy for miRNA detection in live cells, Au-UCNP pyramids were designed and synthesized for miR-21. HeLa cells were either transfected with miR-21 to increase its level or an miR-21 antisense sequence to decrease its level. Indeed, luminescent signal increased and CD signal decreased as the intracellular level of miR-21 increased. However, as the level of miR-21 was decreased in the cell, it was found that monitoring CD signal led to a 4-fold improvement in detection limit when compared to luminescence monitoring. This is important because it may potentially lead to the design of ultra-sensitive probes for intracellular detection based on monitoring CD signal, rather than solely monitoring luminescence signal.

Gao et al. have used upconverting nanoparticles for mRNA and miRNA detection in live cells (

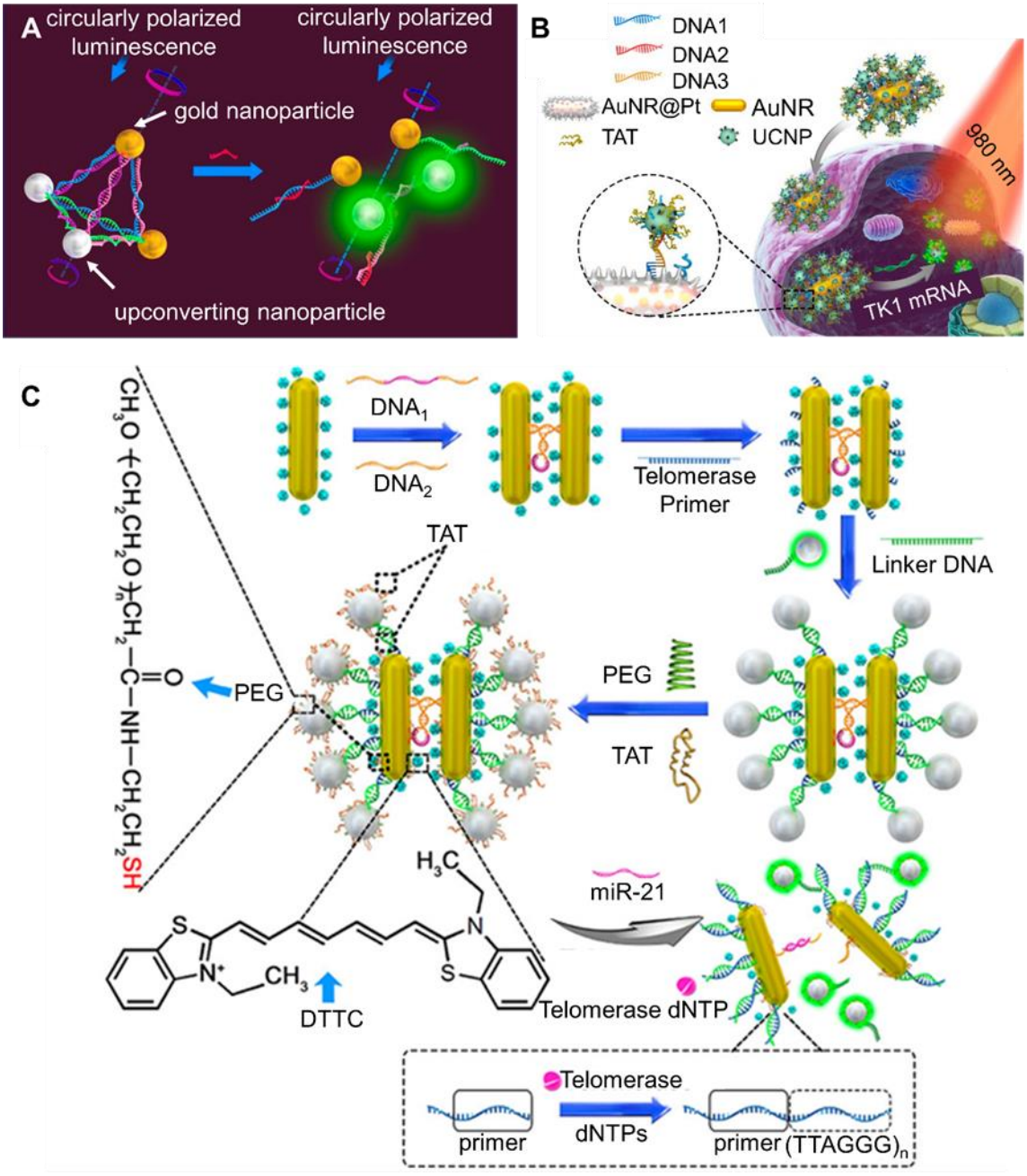

Figure 1.5.1-2B).[89] Gold nanorods are coated with a platinum shell and conjugated with DNA sequence #1, while upconverting nanoparticles are conjugated with DNA sequence #2. To create Au NR@Pt-UCNPs satellite assemblies, DNA sequence #1 and DNA sequence #2 are linked together using DNA sequence #3, which is a recognition sequence for an mRNA of interest. When

the mRNA is not present, the satellite assembly is intact and the luminescence of the upconverting nanoparticles is quenched. In the presence of the target mRNA, binding to the recognition sequence results in disassembly of the Au NR@Pt-UCNPs satellites, resulting in separation of the UCNPs from the Au NR@Pt and luminescence turn-on. In solution, the authors found that Au NR@Pt-UCNPs have a detection limit of 1.3 pM. Their efficacy in MCF-7, HeLa, and PCS-460-010 cells was confirmed by detecting TK1 transcripts, with relative luminescence intensities in the cell line corresponding to levels reported q-PCR. Finally, to show the versatility of the platform, miR-21 in HeLa cells was also imaged.

Ma et al. showed the utility of gold nanorod/UCNPs for simultaneous surface-enhanced Raman spectroscopy (SERS)/luminescence-based detection of miR-21 and telemorase in HeLa, MCF-7, and primary uterine fibroblast cells (

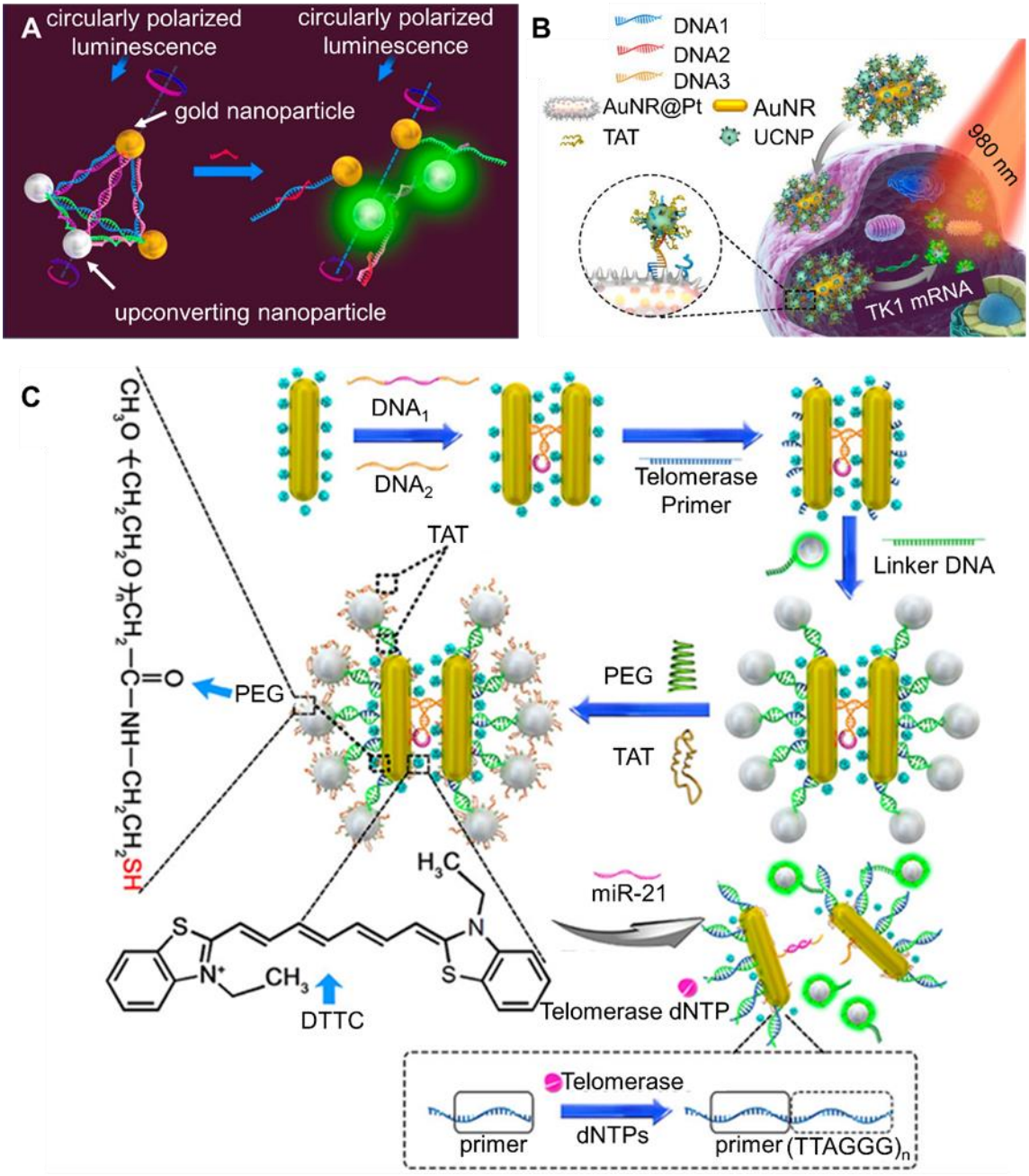

Figure 1.5.1-2C).[200] A recognition strand (DNA 1) on one nanorod is prehybridized to a different strand (DNA 2) on another nanorod. This hybridization brings the gold nanorods in close proximity. Target binding to the recognition strand dehybridizes the sequences, leading to separation of the nanorods. When the SERS tag 3,3′-diethylthiatricarbocyanine iodide (DTTC) is

loaded on the nanoparticle surface, this target binding induced separation leads to a decrease in Raman signal that can be monitored. To detect telomerase, the gold nanorods are further conjugated with a telomerase primer (TP) sequence while upconverting nanoparticles are conjugated with a mismatched sequence. The two components are "glued" using a linker strand, putting the upconverting nanoparticles near the gold nanorod and turning off fluorescence. Telomerase-induced extension of the TP strand results in release of the upconverting nanoparticles, leading to fluorescence turn-on.

1.5.3. Cationic liposome-based

Liposomes are attractive because of their biocompatibility, biodegradeability, ability to enter cells without transfection reagents, and ability to protect cargo from degradation through encapsulation.[40,203]

Kim et al. have used hyaluronic acid-coated liposomes for detection of miR-34a.[40] The hyaluronic acid coating allows for targeting CD44 for endocytic uptake into cells. Liposomes encapsulate within them duplexed strands composed of a fluorophore-labeled recognition strand and a short quencher-labeled strand. Disassembly of the liposome in acidic endosomes is believed to lead to endosomal membrane destabilization and subsequent release of probe into the cytoplasm. Target binding to the recognition strand displaces the quencher strand, recovering fluorescence. Beyond imaging miR-34a in cancerous cells *in vitro*, the study was also able to show the efficacy of the construct for imaging miR-34a in real time in a mouse breast cancer model.

Han et al. have made use of a similar liposome-based strategy.[204] Unlike Kim et al., no targeting moiety is used on the surface, and uptake is hypothesized to be due to both endocytosis and cell

membrane/liposome fusion. Indeed, they were able to show the utility of their sensor for monitoring miRNA associated with adipogenesis. In particular, constructs targeting miR-181a, miR-21, and miR-31 were incubated with bone marrow mesenchymal stromal cells during different differentiation days. As expected, miR-181a and miR-21 expression increased while miR-31 expression decreased as adipogenesis proceeded.

1.5.4. Polymer core-based

Wiraja et al. employed PLGA nanoparticles encapsulating MBs for mRNA detection,[112] using these constructs for studying the dependence of β-actin mRNA in MSCs on culture condition (2D vs. 3D culture).[112] Furthermore, chitosan has been used as a model for a positively charged polymer core for MB delivery.[101] Zhu et al. electrostatically complexed MBs with the chitosan nanoparticles, and used them for detection of MiR-155 in A549, SPC-A1 and PC-3 cells.

Linear FRET probes have been delivered using cationic shell-crosslinked knedel-like nanoparticles (cSCKs).[205] 2 PNA recognition probes labeled respectively with a donor and acceptor fluorophore are each hybridized to short DNA strands to allow for electrostatic complexation with cSCKs. Upon endocytosis, it is believed that cSCKs disrupt the endosomal membrane and release probes into the cytoplasm. Target binding displaces the short DNA complement on both strands. In turn, binding of the fluorophore-labeled recognition strands to adjacent regions in an mRNA of interest can be monitored through FRET signal. A gene associated with inflammation, inducible nitric oxide synthase (iNOS) mRNA, was studied in RAW 264.7 cells.

1.5.5. Micelle-based

Chen et al. have developed MB micelle flares (MBMFs).[90] MBs conjugated to diacyllipids self-assemble into micellular structures with a diacyllipid core and MB shell. Advantages of such a construct include ease of synthesis, biocompatibility, enhanced resistance to nuclease degradation, and uptake into cells without the need of transfection reagents. MBMFs designed to target a known oncogene c-Raf-1 were tested in A549 cells (lung cancer) and HBE135 cells (healthy lung cells). Indeed, MBMFs fluoresced much more strongly in A549 cells than in HBE135 cells. As a negative control, it was shown that non-targeting MBMFs do not fluoresce in A549 cells, indicating the probe was also specific.

Zhang et al. adopted the same structure for use as a theranostic platform.[206] This time doxorubicin, a known cancer drug, was incorporated into the MB stem and in the micelle's hydrophobic core. Indeed, the constructs proved useful for differentiating cells based on MDR1 mRNA expression, a gene associated with multidrug resistance. Furthermore, their constructs proved useful for knocking down MDR1 through an antisense mechanism. Lastly, release of doxorubicin from the core resulted in high chemotherapeutic efficiency of the theranostic agent in OVCAR8/ADR cells.

1.5.6. Silica core-based

Li et al. delivered probes targeting miR-21 into live MCF-7 cells using silica nanoparticles doped with $Ru(bpy)_3^{2+}$ for their strong photostability and biocompatbility.[91] The recognition strand, modified with 2'-O-methyl, contains a carboxyl group for functionalization to amines on the silica nanoparticle surface. The recognition strands also contains a disulfide group and a fluorophore (FAM). A short strand with a quencher is hybridized to the recognition strand, thereby turning off the fluorescence of FAM. An aptamer (AS1411) conjugated to the nanoparticle surface allows for

cell specific delivery, whereby the fluorescence of $Ru(bpy)_3^{2+}$ is used as a handle for cellular uptake. In the cell, it is claimed that glutathione and acidic conditions cleave the disulfide bond and release the duplexed strand. The target mRNA then binds the recognition strand, releasing the quencher strand and recovering the fluorescence.

Yang et al. have recently developed a novel transfection reagent-free silica@polydopamine-DNA-CeO_2 system for simultaneous detection of mi-RNA and H_2O_2.[102] First, Quasar 670-labeled recognition strands are quenched by PDA due to their adsorption on the silica@PDA surface. Duplex formation upon target hybridization releases the strand, leading to fluorescence recovery. Second, CeO_2 nanoparticles adsorbed with FAM-labeled DNA are also decorated around the silica@PDA surface. In a previous study, it has been shown that H_2O_2 can displace DNA from the CeO_2 surface, therefore leading to recovery of initially quenched fluorescence by the CeO_2.[207] Taken as a whole, this system could study the interplay between miR-21 and H_2O_2. For instance, it was found that elevating levels of H_2O_2 in H9C2 cells led to an increase in expression of miR-21.

Shen et al. reported the use of reverse-transcription helicase-dependent isothermal amplification in conjunction with mesoporous silica nanoparticles (MSNs) for mRNA imaging.[208] As opposed to most strategies which are based on signal amplification, this strategy was based on target amplification, with the authors claiming a detection limit of 4 amol in 40 uL of solution. Constructs were taken up through endocytosis, and the probe was effective in distinguishing A549 (cancerous) and CCC-HPF-1 (healthy) cells based on their relative expression of survivin.

Wang et al. used an HCR-based strategy with MSNs.[209] 2 hairpins able to participate in HCR are electrostatically associated with the MSN surface. One of the hairpins is synthesized with a

fluorophore/quencher, such that its opening leads to signal. The authors found a detection limit of 1 pM in solution. Substantiating its efficacy in cells, the probe targeting miR-21 in MCF-7, HeLa and HepG2 cells showed fluorescence bright spots, but showed negligible fluorescence in healthy L-02 cells as expected.

1.5.7. MnO_2 nanosheet-based

Probes using manganese dioxide (MnO_2) nanosheets have also been constructed. MnO_2 offers key advantages, including low cost and ease of preparation, quenching ability, biodegradability, biocompatibility, and efficient delivery of cargo into cells.[103,210,211]

Yang et al. physically adsorbed MBs to the surface of manganese dioxide nanosheets.[103] As mentioned above, manganese dioxide itself also quenches fluorescence, thereby lowering background fluorescence from the case of a free MB alone. Target binding opens the hairpin and releases the probe from the surface, resulting in fluorescence turn-on. Importantly, probes were taken up by cells without the need of transfection reagents. The authors used the system to successfully image miR-21 in HeLa cells.

Li et al. designed a MnO_2-based system that incorporated a signal amplification element.[212] Two different fluorophore-labeled hairpins are adsorbed to the MnO_2 surface such that they are released upon intracellular degradation of MnO_2 in the presence of glutathione. Target binding to one of the hairpins initiates HCR that brings together a FRET pair for signal readout. This strategy proved viable for detecting low abundance miR-21 in HeLa cells. Ou et al. recently used the same strategy, but incorporated two donor fluorophores into one of the DNA strands and an acceptor fluorophore in the other DNA strand.[213] In particular, the two donor/one acceptor (DD-A) system had higher

FRET efficiency than the one donor/one acceptor (D-A) system. miR-21 was studied in MCF-7, HepG2, and L02 cells.

1.5.8. Silver nanocluster-based

Silver nanoclusters have also recently found use in live cell RNA detection. Representing a new class of fluorophores, silver nanoclusters are of interest due to their good photostability and low cytotoxicity.[129,214–216] Strategies employing silver nanoclusters take advantage of the high sensitivity of their fluorescence to ONT surroundings. Yeh et al. have reported silver nanoclusters that transition from a dark state to a red emitting state when in close proximity to guanine bases.[129] In this strategy, silver nanoclusters are formed around a 12 bp nucleation strand. Extending off the nucleation strand is a 30 bp recognition sequence that targets a G-rich complement which upon binding turns on fluorescence. However, this original strategy was not applied to live cells.

More recently, Li et al. have extended silver nanoclusters to use in live cells.[214] Again, silver nanoclusters are formed around a nucleic acid nucleation site. However, in this case, hybridization of target to a recognition site close to the silver nanoclusters leads to both fluorescence turn-on and a shift in the silver nanocluster excitation/emission. This “spectrum switching” strategy was used to image TK1 mRNA in HeLa cells, whereby a mutated (scramble) probe was used as a negative control.

1.5.9. Carbon nanomaterial-based

Dong et al. have employed graphene nanoribbons, functionalized with the cationic polymer polyethylenimine (PEI), as a delivery vector for LNA-modified MBs.[217] In particular, a fluorophore/quencher-labeled MB is electrostatically loaded onto PEI-grafted graphene

nanoribbons, which is able to enter cells and detect miR-21 in HeLa cells. Because PEI is considered cytotoxic, subsequent strategies have aimed to achieve uptake without such agents.[104]

In this light, graphene oxide (GO) has found use in biosensors due to its ability to quench fluorescence, protect cargo against nuclease degradation, deliver cargo into cells without transfection reagents, and strong affinity for hydrophobic molecules and aromatic rings.[104,218]

For instance, Ryoo et al. have created a biosensor relying on the binding of a fluorophore-labeled peptide nucleic acid with nano-graphene oxide.[104] When bound, the fluorescence of the fluorophore is quenched by the GO. Binding to its complement results in the formation of a duplex and desorption of the probe from the surface, leading to fluorescence turn-on. In their work, Ryoo et al. claimed to reach a detection limit of 1 pM in buffer. The authors could detect miR-21 in live HeLa, MCF-7 cells, and MDA-MB-231 cells; they could also detect miR-29a in Hela cells. In MDA-MB-231 cells, they were able to achieve multiplexed detection of miR-21, miR-125b, and miR-96 using probes with three distinct fluorophores. Pan et al. have recently used a similar strategy for simultaneous detection of mRNA and miRNA.[219] Two different dye-labeled hairpins are adsorbed to the GO surface, complementary for miR-21 and PDCD4 mRNA. The probe was successfully used to image these targets in MCF-7 cells. Lastly, Li et al. have adsorbed hairpins on the GO surface that can participate in an HCR for amplified signal.[220] Two of the hairpins are specific for miR-21 and two other hairpins are specific for miR-let-7a, allowing for multiplexed detection in MCF-7 cells and MCF-10A cells.

A similar strategy based on GO sheets has been proposed by Lu et al.[127] MBs are adsorbed onto the surface of the sheets. The fluorophore on the MB is quenched by both a quencher moiety on the beacon and by the GO sheet. After target binding, the MB is opened and desorbed from the

surface, leading to fluorescence turn-on. This strategy was successfully employed to detect survivin mRNA in HeLa cells.

This "double quenching strategy" has also been employed by Yang et al. by using a MB labeled with Cy5 on both ends adsorbed to a GO surface.[221] Quenching from two sources is achieved—self-quenching of the Cy5 molecules and quenching from the GO surface. As such, a low background signal is achieved. Upon opening of the beacon, both Cy5 molecules are turned on, thus resulting in an enhanced signal. Compared to the same system with only one Cy5 molecule, this system had a reported detection limit one order of magnitude lower (30 pM). miR-21 was imaged successfully in MCF-7, HeLa, and HepG2 cells. Furthermore, the system was successfully used for *in vivo* imaging in three distinct mouse xenograft tumor models.

Li et al. have recently used dye-labeled circular DNA in conjunction with GO for mRNA detection.[222] Release of the circular DNA from the surface after target binding unquenches the dye, leading to signal readout for detection. This strategy was successful in multiplexed detection of c-raf and survivin mRNA in HeLa cells. Compared to ssDNA GO system, circular DNA GO had lower false positive signal, presumably due to the enhanced nuclease resistance of circular DNA compared to ssDNA.

As opposed to physical adsorption of probe sequences onto GO, Yu et al. have devised a different strategy for probe association with GO.[223] In particular, they propose a graft/base pairing strategy, whereby amino-labeled strands pre-duplexed with dye-labeled recognition sequences are covalently attached to the GO surface. In the fluorescence off state, dye-labeled strands are flexible and thus near the GO surface, leading to fluorescence quenching. The formation of a duplex in the recognition region due to target binding rigidifies the strand, leading to separation of

fluorophore and surface, giving turn-on of fluorescence. Compared to physical adsorption, which may be prone to probe displacement due to species in cell culture medium or in the cell, chemical conjugation is much more stable. The feasibility of the strategy was tested and confirmed in MCF-7 cells by simultaneous detection of three different miRNA targets— miR-21, miR-let-7a, and miR-125b.

Other carbon nanostructures with strong quenching capabilities have also been used in biosensing applications. For example, Liao et al. have taken advantage of the quenching ability of carbon nanospheres.[224] Initially, a dye-labeled strand is adsorbed on the carbon nanosphere surface. Desorption of the sequence after target binding results in recovery of fluorescence. miR-18a was detected in HepG2 cells using this strategy. In particular, the sensor was used to look at the levels of miR-18a at the S, G2/M, and G1 phases of the cell cycle. Ke et al. have designed a similar system based on polypyrrole nanoparticles.[225] In their system, hairpin DNA labeled with a fluorophore non-covalently associates with the polypyrrole surface, whereby fluorescence is quenched. Upon binding of mRNA target, the hairpin is opened and released, leading to fluorescence turn-on. This polypyrrole based system was used to differentiate cancer cells (MCF-7) from healthy cells (MCF-10A) based on detection of the oncogene c-Myc. Multiplexed detection was also shown by adding a second hairpin to the surface specific for the oncogene TK1, consequently detecting both c-Myc and TK1 simultaneously. One advantage of polypyrrole nanoparticles is their ability to absorb light in the near-IR regime. As such, this paper also showed the utility of polypyrrole nanoparticles to act as agents in photothermal therapy, paving the way for a potential theranostic platform.

Piao et al. have synthesized MBs that use graphite nanoparticles as the quenching moiety.[226] Compared to a conventional dabcyl quencher, using a graphite nanoparticle resulted in an ~11% improvement in quenching efficiency. They also entered cells without transfection reagents. These MBs were used to detect survivin mRNA in MCF-7 cells.

Wu et al. adsorbed MBs to the surface of single-walled carbon nanotubes.[227] The designed constructs were used to detect MnSOD mRNA in MDA-MB-231 cells. Importantly, the use of a carbon nanotube as the delivery vehicle yielded advantageous properties as compared to naked MB delivery, such as an enhanced resistance to enzymatic degradation and transfection reagent free uptake into cells. Moreover, the authors noted that association with the carbon nanotube allows the MB to remain in the cytoplasm, rather than being sequestered to the nucleus.

Noh et al. took advantage of the fluorescence of carbon nanodots to design a system for detecting miRNA.[92] In an SNA type strategy, carbon nanodots were functionalized with a recognition strand prehybridized to a short quencher-labeled strand. When hybridized, the quencher turned off the fluorescence of the carbon nanodot. Upon miRNA induced displacement of the quencher strand, fluorescence was recovered. The feasibility of this strategy in live P19 cells was confirmed by detecting miR-124a.

1.5.10. MOF-based

Metal organic framework (MOF) nanoparticles offer a number of interesting properties, including ease of synthesis, quenching ability, and tailorable chemistry.[228–231]

Wu et al. leveraged the properties of nano-MOFs for detection of miRNA in live cells.[105] A dye-labeled PNA is conjugated to a MOF, whereby metal centers in the MOF function to quench the

fluorescence of the dye. Target binding to the PNA results in its release from the MOF and subsequent recovery of fluorescence. In solution, this sensor could detect 10 pM miRNA. The probe was shown to be sensitive to changes in miR-21 level in live MCF-7 cells after addition of an inhibitor. Multiplexed analysis of miR-21, miR-96, and miR-125b was also possible in MDA-MB-231 using three different PNA-MOF complexes.

1.5.11. Plasmonic coupling-based

Although fluorescence-based strategies are most popular for intracellular analyte detection, strategies based on plasmonic coupling have also been developed. For example, Zhou et al used SERS to detect miRNAs of interest.[99] One sequence is conjugated to one gold nanoparticle, and another sequence is conjugated to a second gold nanoparticle. The miRNA of interest hybridizes partially to both sequences, thus bringing the two gold nanoparticles close together. The junctions between the gold nanoparticles form "hot spots," which can be monitored by SERS if Raman reporters are loaded on the gold nanoparticle surface. In this paper, an alkyne (C≡C) terminated Raman reporter was used for one target of interest, and a nitrile (C≡N) terminated Raman reporter was used for another target of interest. With this ability to multiplex, miR-21 and miR-155 were simultaneously monitored in MCF-7 cells. One advantage of a SERS-based strategy over fluorescence-based methods is potentially greater capability for multiplexing due to sharp spectrally distinct Raman bands.

In a similar strategy, Lee et al conjugated a gold nanoparticle with a sequence complementary to an mRNA of interest, while another gold nanoparticle was conjugated with a different sequence complementary to the same mRNA of interest.[128] The sequences are designed such that if the target mRNA is present, the two sequences will bind the mRNA in a manner that will bring the

gold nanoparticles in proximity for dimer formation. Due to plasmonic coupling, the formed dimer has a spectral shift that can be detected. In their work, Lee et al. used this system to detect multiple splice variants of BRCA1 mRNA at single-copy number resolution. Because different splice variants resulted in different scattering spectra, the group could effectively distinguish one splice variant from another.

1.5.12. Iron oxide core-based

Lin et al. have pioneered the use of Fe_3O_4@polydopamine core-shell nanocomposites (Fe_3O_4@PDA NCs) for use as a theranostic platform.[106] The PDA shell surrounding the Fe_3O_4 core can adsorb single-stranded nucleic acids that contain a dye and are designed to be complementary to an mRNA target of interest. After mRNA binding to the probe sequence, a duplex is formed that is desorbed from the PDA, resulting in turn on of fluorescence. Lin et al. showed the ability of this platform to differentiate healthy breast cells (MCF-10A) from cancerous breast cells (MCF-7) based on their relative expression of a known oncogene c-Myc. Displaying the versatility of the strategy, they were also able to adsorb multiple probe sequences on the surface with distinct dyes, allowing for simultaneous multiplexed detection of two oncogenes — c-Myc and TK1. These Fe_3O_4@PDA NCs were also efficacious for photothermal therapy due to PDA's ability to absorb near IR light and have also shown promise as an MRI contrast agent for imaging cancer cells.

1.5.13. DNA nanostructure-based

Probes based on nanostructures formed from DNA, like the DNA tetrahedron, are of interest in sensing applications because of their biocompatibility, uptake into cells without external agents, and ability to protect cargo from degradation.[113,232]

For instance, a design variation to linear FRET probes was introduced by the Tan group in 2017 with their advent of DNA tetrahedron Nanotweezers (DTNTs) for live cell mRNA detection (Figure 1.5.13-1).[113] DTNTs rely on the self-assembly of four different nucleic acid strands. In the off state, the self-assembly of the four nucleic acid strands keeps a donor and acceptor fluorophore separated from one another. mRNA binding to the DTNT induces a structural change that brings the donor and acceptor fluorophores close to one another, resulting in generation of a FRET signal. Beyond the fact that DTNTs were not prone to false positive signal, they also entered cells without the need of transfection reagents, unlike "naked" nucleic acids. In their initial study, a DTNT was designed targeting TK1 mRNA, which is known to be a marker for tumor growth. Indeed, DTNTs were able to distinguish cancer cells from healthy cells based on the level of TK1 mRNA.

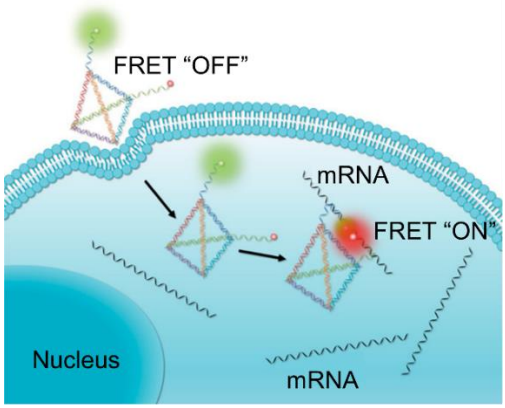

Figure 1.5.13-1. DNA nanotweezers for intracellular oncogenic mRNA detection. Target binding induces a structural change that brings a FRET pair together, resulting in a FRET signal. Adapted with permission.[113] Copyright (2017) American Chemical Society

Xie et al., on the other hand, described a DNA tetrahedron that incorporated a flurophore and quencher at the end of one of the strands making up the structure, thus putting the two moieties in close proximity when the tetrahedron is in the intact form.[233] Target binding induces a structural change that separates the fluorophore and quencher, turning on fluorescence. The nanosensor had the ability to detect TK1 mRNA in HepG2 cells.

Zhou et al. have expanded on these "tetrahedron" strategies for multiplexed detection of miRNA.[114] Hairpin DNA specific for two different miRNA are incorporated into two of the strands, while a fluorophore and quencher label the termini of two other strands. In the closed state, the intact structure causes the fluorophore and quencher to be near one another. Hairpin opening due to target binding then allows for recovery of fluorescence. Their strategy proved efficacious for imaging miR-155 and miR-21 simultaneously in MDA-MB-231 cells. Wang et al. expanded capabilities to simultaneous detection of three different mRNA targets.[234] c-Myc, TK1 and GalNAc-T mRNA were simultaneously studied in MCF-7 and MCF-10a cells.

Recently, the Tan group has introduced an amplification strategy, entropy-driven 3D DNA amplifier (EDTD), to boost signal from fluorophore/quencher DNA tetrahedron sensors.[235] All properties of tetrahedron probes are retained, including transfection-free cellular uptake and resistance to nuclease degradation. The EDTD probe was used to image TK1 mRNA in both normal and tamofixen (for TK1 knockdown)-treated cells. Conventional DNA tetrahedron molecular beacons (DTMBs) only produced negligible fluorescence in tamofixen treated cells, implying that EDTD tetrahedrons could be used to image mRNAs of low abundance but DTMBs could not.

Tay et al. took inspiration from nature and conventional DNA tetrahedron approaches to design a MB with enhanced resistance to nuclease degradation.[119] They termed their system the nano-snail-inspired nucleic acid locator (nano-SNEL). The first component of their system is a MB that acts as the sensing element. The second component of their system is a DNA tetrahedron. Conjugating the MB to the DNA tetrahedron conferred resistance to nuclease degradation, akin to a snail's shell affording it protection from environmental conditions. As opposed to naked MBs which do not enter cells, it was also shown that the presence of the DNA nanoshell results in these constructs being taken up by cells without the need of transfection reagents, allowing for detection of GAPDH in live DLD-1 and SW480 cells.

In another recently reported DNA nanostructure system, Ren et al. have developed an amplification strategy that overcomes limitations associated with HCR.[130] In particular, the rate of HCR is reliant on diffusion as each successive hybridizing DNA sequence must be found in a complex 3D milieu. Reactions have been reported to take as long as two hours to go to completion.[108] Ren et al. hypothesized that confining nucleic acids in close proximity to one another would accelerate the kinetics of such DNA chain reactions (DCR). In their design, two different hairpins are alternately hybridized in close proximity along a DNA nanowire. Akin to normal HCR, target binding opens the fluorophore/quencher-labeled hairpin, leading to fluorescence turn-on and a cascade of hybridization between the two hairpins to yield amplified signal. Compared to conventional HCR, the authors noted that this system had a limit of detection ~52 times lower in buffer experiments and required only 15 minutes of incubation time with complementary target. This system was ultimately used to image survivin mRNA in HeLa cells.

1.5.14. Quantum dot-based

Quantum dots (QDs) represent another class of nanoparticles used for live cell RNA detection. Advantages include good quantum yield, size dependent emissive properties, and high photostability.[236,237]

For instance, Dai et al. adsorbed MBs on the surface of molybdenum disulfide quantum dots (MDQDs).[107] MDQDs fluoresce in the blue regime, and can thus be used as a handle for cellular uptake. Transfection reagent-free uptake was achieved and used for imaging of miR-21 in HeLa and HaCaT cells.

Lee et al. employed a slightly different strategy.[93] QDs were covalently conjugated with a cell penetrating peptide for enhanced cellular uptake and a recognition strand prehybridized with a short quencher-labeled sequence. The quencher-labeled sequence, when hybridized, turns off the inherent fluorescence of the QDs. Target binding displaces the quencher sequence, recovering the fluorescence of the QD. Using this design, miR124-a was studied in P19 cells during differentiation.

Dong et al. used graphene QDs (GQDs) covalently conjugated with polyethylene glycol (PEG) and polylactic acid (PLA) as a nanosensor for miRNA detection.[238] PEG and PLA impart stability to the GQD in both aqueous and protein solution. As such, the bioluminescence properties of GQDs are stable over a wide range of pHs. MBs are associated with the GQD surface through π-π interactions. MB opening and release from the surface upon hybridization with target leads to fluorescence turn-on. Importantly, because GQD are photoluminescent themselves, their photoluminescence level in cells can be used as a measure of nanosensor uptake. Intracellularly, the probe was capable of imaging miR-21 in HeLa cells. The probe was also sensitive to downregulation of miR-21, resulting in less nanosensor fluorescence.

Wu et al. designed a two acceptor-one donor theranostic MB based on CdTe/CdS/ZnS QDs.[239] In the closed state, the QD acts as the donor and a BHQ moiety acts as the acceptor. Hairpin opening results in recovery of the QD fluorescence. However, opening of the hairpin also brings the donor QD into close proximity with an acceptor photosensitizer molecule that can produce singlet oxygen to promote cell death. Using MCF-7 cells, which express high level of cyclin D1 mRNA, the study was able to show that the theranostic was efficacious in both detecting the mRNA and inducing cell death.

Lastly, He et al. achieved miRNA detection using gold nanoparticle-QD nano-assemblies.[240] A nucleic acid strand modified with a CdTe QD is prehybridized to a recognition strand that in turn places the QD near the gold nanoparticle. Target binding displaces the QD modified strand, recovering fluorescence. An amplification element was also introduced by incorporating a fuel strand that displaces the target, therefore allowing the target to bind to multiple recognition strands. Shen et al. have used the same strategy, but have made their sensor start functioning "on demand" by pre-functionalizing the entire recognition strand with DNA so as to not allow target binding initially.[241] One of the strands functionalized to the recognition strand contains a photocleavable linker that is cleaved after UV radiation, thus partially exposing the recognition strand and yielding the same system as He et al.

1.6. Aptamer-based probes

1.6.1. DNA nanomachine-based

The Krishnan group provided an early demonstration of "DNA nanomachines" that are active in cells.[242] They developed the "I-switch" based on the pH-sensitive i-motif DNA (Figure 1.6.1-1A). The i-motif is a cytosine rich strand that adopts a folded tetraplex conformation at acidic pH held

together by C^+-H-C linkages and an extended single-stranded conformation at neutral pH. As such, the i-motif can be considered to be an aptamer for proton sensing. The pH ranges sensed by the i-motif can be shifted towards more acidic or basic pH through the incorporation of modified bases or different numbers of cytosine bases.[28,243,244] The I-switch consisted of two DNA duplexes that were linked together through a flexible tether and contained fluorophore-labeled i-motif forming overhangs at both ends (Figure 1.6.1-1A). Under acidic conditions, formation of the i-motif resulted in the "closed" state in which the fluorophores were brought to proximity resulting in a FRET signal. The I-switch could report pH changes in the range of 5.5-6.8. As two fluorophores were used, a ratiometric analysis of uptake and pH change could be performed. Utilizing the I-switch, the authors spatiotemporally mapped the pH changes associated with the endosomal pathway in live cells.

In a subsequent paper, Krishnan and co-authors demonstrated that pH changes within cellular compartments can be tracked in multicellular organisms.[52,245] In *Caenorhabditis elegans* worm models, these DNA nanomachines are recognized by scavenger receptors on the surface of scavenger cells called coelomocytes and taken up via receptor-mediated endocytosis. The I-switch has a half-life of ~8 h in cells and reports pH changes over the range 5.3-6.6 by resulting in a five-fold change in FRET signal as it transitions from an open to a closed state.

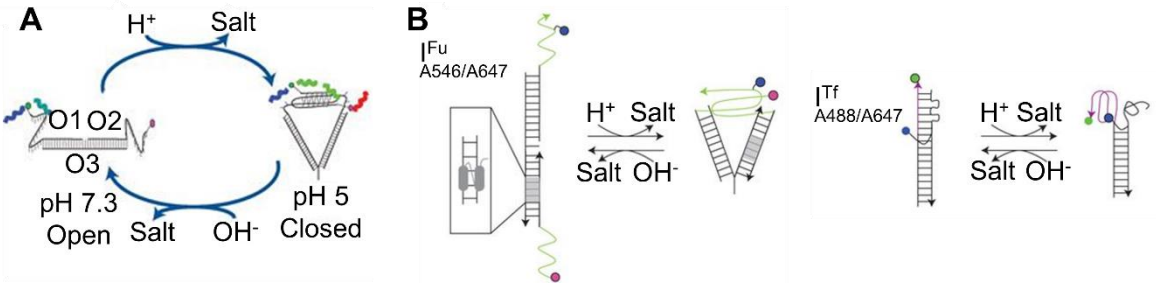

Figure 1.6.1-1. (A) The I –switch nanomachine for monitoring intracellular pH. A structural change from open (low FRET) to closed (high FRET) state occurs as pH is changed from basic to acidic condition. Adapted by permission from Springer Nature: Springer Nature, Nature Nanotechnology.[242] Copyright 2009. (B) By incorporating two sets of FRET pairs as well as two distinct targeting moieties (one on each I-switch), Modi et al. were able to use the I-switch for simultaneous monitoring of the furin retrograde endocytic pathway and the transferrin endocytic/recycling pathway. Adapted by permission from Springer Nature: Springer Nature, Nature Nanotechnology.[115] Copyright 2009.

Modi et al. developed a simultaneous pH mapping technology (SimpHony) using I-switches.[115] They demonstrated that pH changes along two different endocytic pathways (the furin retrograde endocytic pathway and the transferrin endocytic/recycling pathway) can be visualized using two I-switches labeled with two sets of FRET pairs (Figure 1.6.1-1B). A sequence-specific double-stranded DNA binding protein was expressed as a chimera with furin in HeLa cells to allow for monitoring the furin pathway. The I-switch targeting this pathway contained a double-stranded $(AT)_4$ region that could be recognized specifically by the DNA binding protein initiating uptake. The I-switch targeting the transferrin pathway was conjugated to transferrin to allow uptake upon recognition by the transferrin receptor. The use of such DNA nanomachines allowed the sensing of the same analyte in different cellular compartments. Moreover, the modular nature of the I-switch allows custom functionalization with proteins as well as with different FRET pairs. This strategy was later extended for the detection of pH changes associated with the trans-Golgi and cis-Golgi networks, and the endoplasmic reticulum.[243]

Bhatia et al. reported that synthetic DNA constructs can be utilized as hosts to deliver cargo within cells.[52] Fluorescein isothiocyanate-labeled dextran (FD) was encapsulated within a DNA icosahedron. Unlike free FD which cannot be targeted to specific endocytic pathways, encapsulated FD was taken up by the anionic ligand-binding receptor (ALBR) pathway in *Drosophila* hemocytes, demonstrating that the DNA host altered its targeting properties.

Similarly, encapsulated FD was taken up only by ALBR-expressing coelomocytes in *Caenorhabditis elegans*. The pH-sensitive property of fluorescein enabled monitoring of pH changes associated with endosomal maturation. In a subsequent study, photoresponsive polymers attached to small molecule payloads were loaded into DNA icosahedrons.[246] Light-activated release of the small molecule could be monitored with spatial and temporal precision. Single quantum dots could also be encapsulated within DNA icosahedrons.[247] By modifying the icosahedron with a single endocytic ligand (e.g. folic acid, galectin-3, and the Shiga toxin B-subunit), the endocytic pathway associated with the ligand can be imaged.

In addition to pH, nanomachines that are sensitive to intracellular chloride ion concentrations and that can be targeted to subcellular compartments have also been investigated. Unusual chloride ion concentrations in the lysosome can lead to lysosomal storage disorders. A DNA nanodevice called Clensor can report changes in chloride ion concentrations in a pH-independent manner.[248,249] Clensor consists of three parts: a sensing module containing a 12-base long PNA moiety labeled with a chloride-sensitive dye, 10,10′-bis[3-carboxypropyl]-9,9′-biacridinium dinitrate (BAC), a normalizing module containing a 38-base long Alexa 647-labeled DNA sequence, and a targeting module containing a 26-base long DNA. The probe could be taken up as is through the ALBR pathway due to its negative charge while modification of the targeting moiety with an RNA aptamer that binds to the transferrin receptor enables uptake through the transferrin pathway. Using this probe, chloride ion concentration in the lumen of acidic organelles in *Drosophila melanogaster* was monitored and it was revealed that the intracellular chloride transporter DmClC-b regulates lysosomal chloride ion concentration.

Recently, combining the advantages of I-switch and Clensor, a probe that can detect pH and

chloride ion concentration simultaneously was developed.[117] Using this probe termed as ChloropHore, subpopulations of lysosomes could be chemically resolved based on their chloride and proton content. Importantly, it was shown that lysosomes present in primary skin fibroblasts of healthy individuals could be categorized into two populations, whereas patients with Niemann–Pick disease only had one population. The absent second population could be recovered upon treatment of the disease. Similar strategies have been utilized to develop CalipHluor, a probe for pH-corrected measurement of calcium ions in subcellular compartments[116] and cHOClate, a probe for reporting pH and HOCl simultaneously in phagosomes of macrophages, neutrophils, and monocytes.[118]

One limitation of the early design of I-switch was the relatively long timescale for transforming into the folded state (few minutes). Yang et al. developed the t-switch as a solution to this problem.[250] The t-switch relies on a triplex formation mediated by C^+-G-C interactions. Similar to the I-switch, the t-switch reported changes in pH through a FRET-based mechanism, although the response time was only a few seconds. The t-switch was delivered to cells through complexation with the cationic polymer PEI. Compared to the naked t-switch whose dynamic range is pH 5.3 to 6.0, the PEI-t-switch has an extended dynamic range of 4.6 to 7.8. Intracellular pH in HepG2 cells was monitored using this probe.

Pei et al. demonstrated that DNA tetrahedra with dynamic sequences that are responsive to particular targets can be used to develop FRET-based sensors for the target molecules.[251] The authors utilized this construct for sensing ATP in live HeLa cells. Ohtsuka et al. utilized the thrombin binding aptamer (TBA) for detecting K^+ in live HeLa cells.[252] The TBA forms a G-quadruplex in the presence of K^+ ions. This structural transition was leveraged to create a FRET-

based probe. The TBA was biotinylated and conjugated to streptavidin which was further conjugated to biotinylated nuclear export signal peptide (B-NES). The formation of the ternary complex was important as without B-NES the probes were sequestered to the nucleus.

For more information on DNA nanomachine-based probes, the readers are directed to the review by Chakraborty et al.[253]

1.6.2. Gold nanoparticle-based

In 2009, the Mirkin group introduced aptamer NanoFlares for the detection of intracellular analytes in live cells.[95] Analogous to NanoFlares for mRNA detection, these probes are comprised of a gold nanoparticle core modified with ONT duplexes. One strand of the duplex is the aptamer sequence which is covalently attached to the gold nanoparticle through a gold-sulfur bond. The other strand is a shorter fluorophore-labeled strand whose fluorescence is quenched due to proximity to gold. Upon binding of the target molecule of interest, the aptameric strand folds, the fluorophore-labeled strand is displaced, and its fluorescence is turned on. Using this platform ATP was detected in live HeLa cells. One disadvantage of this strategy is that the binding affinity is reduced by two orders of magnitude compared to the free aptamer in solution, presumably due to partial blocking of the active site of the aptamer by the flare strand[254] and due to steric bulk arising from dense ONT functionalization.

Many groups have used NanoFlares for detecting and measuring other analytes in live cells. For example, by using i-motif forming ONTs (IFOs) labeled with a FRET-pair (rhodamine green and rhodamine red) at the two ends, NanoFlares that measure intracellular pH were developed by Huang et al.[96] Initially, the IFOs are duplexed to cDNA on the gold nanoparticle which results in

quenching of the acceptor dye. Lower pH induces a conformational switch such that a quadruplex structure is formed and the two ends of the ONT labeled with dyes are brought to proximity, turning on FRET signal. The presence of two dyes also allows ratiometric analysis of uptake and binding by monitoring the fluorescence ratio of the donor and acceptor. Using this probe, spatial mapping of intracellular pH in HeLa cells, HL-7702 cells, SMMS-7721 cells could be performed. The results revealed that the FRET signal increased with time, indicating that the probes were trafficked from neutral to more acidic environments. Later, using a similar strategy, the group developed aptamer NanoFlares for measuring the concentration of K^+ ions by employing ONTs that form a G-quadruplex in the presence of K^+ ions.[255]

Wang et al. developed a strategy[256] for plasmonic imaging of intracellular pH gradients in RAW 264.7 cells using two different sizes of gold nanoparticles assembled into core-satellite architectures.[257,258] The core nanoparticle is 50 nm in size and functionalized with G-rich ONT sequences. The satellite nanoparticles are 14 nm in diameter and functionalized with C-rich IFO forming sequences. At higher pH, the nanoparticles are assembled through Watson-Crick base pairing. Under acidic conditions, quadruplex structures are formed from the C-rich i-motifs and the structures are disassembled. The scattering spectra resulting from the assembly (yellow) and disassembly (green) of these structures are different and can be observed using a dark field microscope. As the pH drops along the endocytic pathway from early endosomes to late endosomes/lysosomes, a yellow to green transition in scattering spectra was observed, consistent with disassembly of the nanoparticles at lower pH.

Ma et al. developed a gold nanoparticle-based DNA nanomachine that detects low abundance microRNA through an ATP-fueled amplification strategy.[259] The probe was able to report differences in miR-21 levels between HeLa, HEK-293T, and MRC-5 cell lines.

1.6.3. Graphene oxide-based

Wang et al. demonstrated that aptamer/GO nanocomposites can be used as probes for monitoring ATP levels in real time in live cells.[109] In this study, a carboxyfluorescein-labeled ATP aptamer was adsorbed onto graphene oxide nanosheets (GO-nS) through π-π stacking interactions. The GO-nS quenched the fluorescence owing to FRET, acted as a transfection vector for the delivery of the ONTs into JB6 cells, and protected the ONT from nuclease degradation. Inside the cells, ATP binding released the aptamer from the GO-nS and turned on fluorescence. This platform was later extended for simultaneous detection of ATP and GTP in MCF-7 cells using two aptamers labeled with spectrally distinct fluorophores.[260] A detailed protocol for this process was later published by Wang et. al.[261] Using a similar strategy, Chen et al demonstrated the first visualization of translocation event of endogenous cytochrome c, a protein mediator of apoptosis, in HeLa cells.[262]

By incorporating a fluorophore-labeled single-stranded DNA (ssDNA) as an internal reference, Tan et al. showed semiquantitative detection of ATP in HeLa cells.[141] The ssDNA is released by non-specific interactions with intracellular proteins and by monitoring its ratio of fluorescence intensity to that of the aptamer MB, the amount of ATP can be determined semiquantitatively.

Intracellular pH has also been probed using DNA-GO-nS complexes. Li et al. engineered fluorophore-labeled ONT probes that transition from a duplex at pH 8 to a triplex at pH 5. The

duplex form consists of an ssDNA overhang labeled with rhodamine green. Due to stronger adsorption of ssDNA compared to triplex DNA, the fluorescence is quenched at higher pH. However, acidification induces a conformation shift and causes desorption of the triplex probe resulting in fluorescence turn on. This probe has been used to study apoptosis-induced acidification in Ramos cells.[263]

Shao et al. used IFOs as pH sensors.[111] The IFOs were immobilized on GO through interactions with amine-modified complementary DNA (cDNA). The cDNA was covalently attached to GO through NHS/EDC chemistry. A covalent attachment strategy was used as opposed to the more commonly used physisorption strategy to prevent non-specific release. However, in their study they observed that the interaction of DNA with GO under acidic conditions is too strong to distinguish between open and closed forms. To weaken the interactions, they treated GO with herring sperm DNA. This new probe was capable of detection of pH between the range of 5 and 7.3 and was used to demonstrate pH changes in live HeLa, MCF-7, MDA-MB-231, and A549c cells.

1.6.4. Upconverting nanoparticle (UCNP)-based

Ma et al. reported lanthanide-doped UCNPs for the detection of cytochrome c.[264] Fluorophore-labeled cytochrome c aptamers are hybridized to cDNA attached to polydopamine-coated UCNPs. The fluorescence is quenched by polydopamine in the absence of cytochrome c and activated when cytochrome c binds to the aptamer strand and displaces it from the surface of the UCNPs. The upconverted luminescence of the nanoparticles serves as an internal reference for probe uptake. The study claimed a detection limit of 20 nM and a dynamic range spanning 50 nM to 10 μM, which includes physiologically relevant concentrations (1–10 μM) of cytosolic cytochrome c found

in apoptotic cells. Etoposide induced apoptosis was studied in HepG2 cells using these probes. Low quantum efficiency of the UCNPs and poor DNA loading are two limitations of this strategy.

Zhao et al. developed an NIR-activated probe for imaging ATP in live cells.[265] Their construct was composed of lanthanide-doped UCNPs decorated with photo-cleavable aptamer-based DNA sensors. A fluorophore-labeled aptamer sequence was hybridized to cDNA containing a quencher and a photocleavable group. In the absence of NIR light, the fluorescence was quenched due to FRET and the cDNA prevented ATP-binding. Upon irradiation with 980 nm NIR light, the UCNPs luminesced in the UV and visible blue (peaks at 320, 365, 450, and 475 nm) regime, inducing photolysis of the cDNA into two short fragments. The reduced binding affinity of the generated fragments leads to strand displacement in the presence of ATP. Due to separation of fluorophore and quencher, a fluorescence signal is generated. Using this platform, the authors demonstrated ATP imaging in live HeLa cells as well as in mice bearing HeLa xenograft tumors. The advantage of such a system in which the sensor can be remotely activated by external stimulus is that it adds temporal control to imaging capabilities.

1.6.5. Polymer core nanoparticle-based

Özalp et al. developed an ATP aptamer that can detect intracellular ATP concentrations in the range between 0.5-8 mM.[61,266,267] The aptamer was converted into a fluorescent sensor using the "aptamer switch probe" strategy developed by Tang et al.[268] An aptamer switch probe consists of three parts: (i) the aptamer sequence, (ii) a short cDNA sequence, and a (iii) PEG linker connecting (i) and (ii). Moreover, the two ends contain a fluorophore and quencher, respectively. Analogous to a MB, in the absence of the target, the probe exists in a hairpin-like conformation that brings the fluorophore-quencher pair in proximity (Figure 1.6.5-1). ATP binding changes the

conformation of the probe such that the fluorophore and quencher are separated. The aptamer was encapsulated into polyacrylamide nanparticles for cellular delivery. The porous nanoparticles allow small molecules like ATP to diffuse inside, but prevents nuclease degradation. Real time variation in ATP levels in yeast cells could be monitored using these probes.

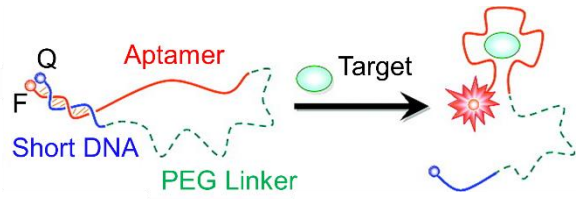

Figure 1.6.5-1. Target analyte detection based on an aptamer switch probe strategy. Target binding to the aptamer induces a structural change that separates a fluorophore and quencher, leading to fluorescence turn-on. Adapted with permission.[268] Copyright (2008) American Chemical Society.

Qiang et al. used polydopamine nanospheres as cores for delivery of ATP-sensing aptamers in cells.[269] Fluorescently-tagged ATP aptamers were adsorbed onto the nanoparticle surface such that the fluorescence was quenched by the core. In the intracellular environment, ATP binding desorbed the strand from the surface, leading to separation of fluorophore and quencher with concomitant increase in fluorescent signal. ATP was sensed in live HeLa cells using this probe.

1.6.6. Micelle-based

Wu et al. developed switchable aptamer micelle flares for the detection of ATP in live cells.[270] The probe consists of aptamer switch probe–diacyllipid chimeras that self-assemble to form micelles. Target binding causes the conformation of the aptamer to change, separating the fluorophore and the quencher, leading to fluorescence turn on. The fluorescence increases with

increasing concentration of ATP (between 0.1-3 mM) *in vitro* and saturates at ~4-fold enhancement. These probes could be internalized into cells without transfection reagents and colocalization experiments suggested that the majority of the probes are in the cytoplasm as opposed to being in the lysosome. Based on these results, the authors suggested that the probes enter cells mainly via membrane fusion.

1.6.7. MnO_2 nanosheet-based

Zhao developed a bimodal platform for detecting cancer cells based on aptamer-loaded MnO_2 nanosheets.[271] MnO_2 nanosheets served as a nanocarrier, quencher as well as an MRI contrast agent. The aptamer sgc8 which targets the protein tyrosine kinase 7 (PTK7) was fluorescently tagged and associated with MnO_2 nanosheets. Cells expressing PTK7 recognized the aptamer which then dissociated from the MnO_2 nanosheets, turning on fluorescence. Upon cellular entry of MnO_2 nanosheets, glutathione induced reduction led to the formation of large amounts of Mn^{2+} which could provide strong MRI contrast.

1.6.8. MOF-based

Deng et al. developed an upconverting nanoparticle core-MOF-shell based probe for targeted drug delivery and imaging in cancer cells.[272] The MOF surface was functionalized with the AS1411

aptamer that is known to target cancer cells. Following cellular entry, the MOF could release an encapsulated anti-cancer drug. The luminescent UCNP allowed for cellular imaging.

Liu et al. developed an aptamer conjugated MOF-based platform for cellular imaging and photodynamic therapy.[273] The PTK7-targeting aptamer sgc8 was fluorescently tagged and conjugated to the surface of a Zr-based porphyrinic MOF. The MOF acted both as a quencher as well as a photosensitizer for generating reactive oxygen species. Upon binding to PTK7-positive HeLa cells, the fluorescence from the aptamer was turned on allowing cellular imaging. Irradiation with 650 nm induced significant cell death. Thus, this platform acted as a theranostic for cancer.

1.6.9. Genetically-encoded aptamers

The Jaffrey lab pioneered the development of genetically-encoded aptamers for visualizing intracellular analytes in live cells.[121] Such aptamers are particularly advantageous for tracking of small molecules and metabolites in cells, imaging strategies for which are limited.

Paige et al. developed a 97-nt long aptamer that binds to 3,5-difluoro-4-hydroxybenzylidene imidazolinone (DFHBI), a dye resembling the fluorophore in green fluorescent protein (GFP).[122] The photophysical properties of this dye are similar to those of enhanced GFP. The free dye is non-fluorescent whereas upon aptamer binding the dye strongly fluoresces. Due to the

characteristic green florescence, the aptamer has been termed “Spinach”. As a first demonstration of the capability of Spinach aptamers in detecting mRNA in live mammalian cells, the authors fused Spinach to the 3′ end of the noncoding RNA 5*S*, transfected the entity into HEK293T cells, and incubated the cells with DFHBI. The fluorescence distribution from Spinach was similar to that of endogenous 5*S*, signifying that incorporation of Spinach did not significantly alter the dynamics of the target RNA. In addition to DFHBI, the Jaffrey lab developed a palette of dyes with fluorescence spanning the visible spectrum.[121,274]

Inspired by a strategy proposed by Stojanovic et al.,[275] Paige et al. created modular aptameric sensors for monitoring cellular metabolites (Figure 1.6.9-1). The probe consisted of three parts: (i) Spinach aptamer, (ii) a recognition module, and (iii) a transducer module.[122] When the target binds to the recognition module, the transducer region is duplexed which then leads to DFHBI binding to Spinach resulting in concomitant increase in fluorescence signal. Large fluorescence enhancements up to 32-fold were achieved in solution. Using this strategy, the authors imaged adenosine 5-diphosphate (ADP) and *S*-adenosylmethionine (SAM) in live *E. coli*.[122,276] In later studies, Song et al. demonstrated that such a method could be adapted for the imaging of proteins in live bacteria cells.[123] The authors visualized streptavidin as well as the synthesis of MS2 coat protein after infection with MS2 phages in *E. coli* cells.

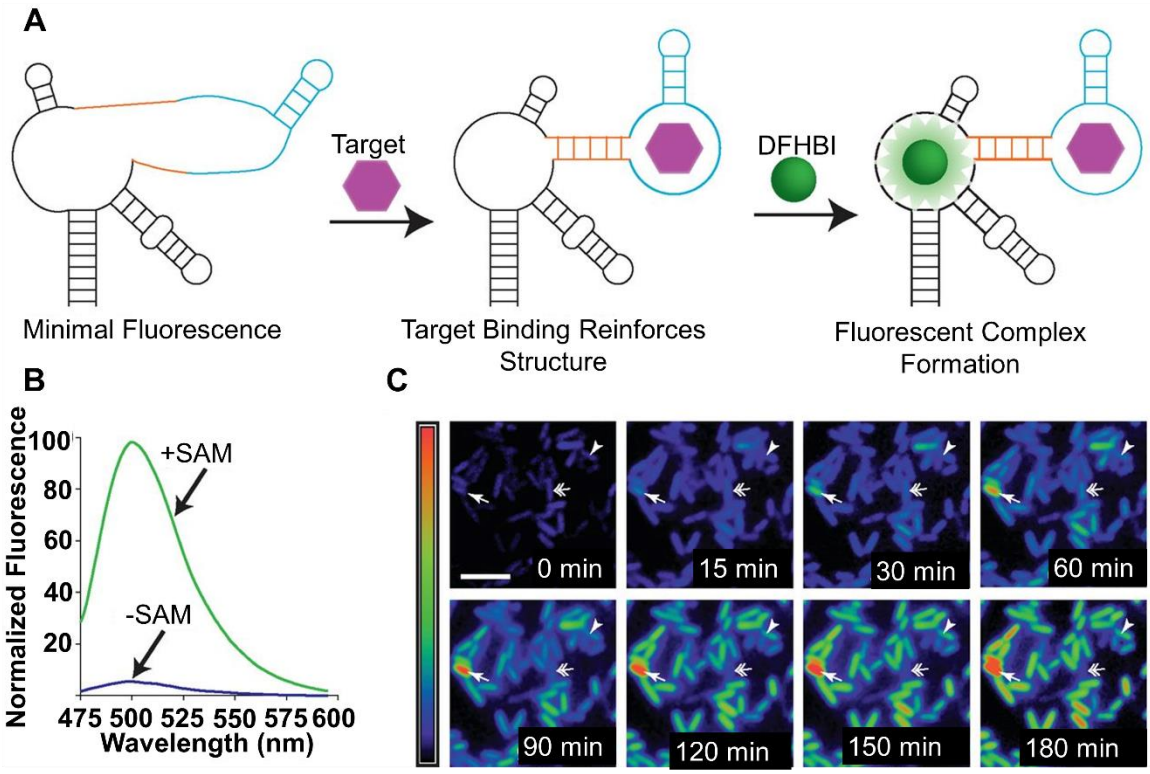

Figure 1.6.9-1. (A) Spinach aptamer composed of Spinach (black), transducer (orange), and aptamer (light blue) for detection of target analytes. Target binding to the aptamer induces a structural change that results in transducer duplexing and concomitant binding of DFHBI to Spinach to give fluorescence turn-on. (B) Fluorescence turn-on of Spinach aptamer in the presence of target SAM. (C) Monitoring of SAM in *E. coli* cells. Single arrows point to cells with relatively high SAM expression, arrowheads point to cells with increasing levels of SAM over time, while double-arrows point to cells whose SAM content first increases and then decreases over time.[122] Modified with permission from AAAS and authors.

Kellenberger et al. fused the Spinach aptamer to the naturally occurring GEMM-I riboswitch for intracellular detection of cyclic dinucleotides, c-Di-GMP and c-AMP-GMP.[277] Furthermore, enzymatic activity of DncV which catalyzes the synthesis of c-AMP-GMP was monitored. The Jaffrey lab further demonstrated that Spinach-based riboswitches can be utilized for visualizing several metabolites including 5′-pyrophosphate, S-adenosyl-methionine, adenine, and

guanine.[278,279] Pothoukalis et al. showed that Spinach aptamer can be used in conjunction with a fluorescent protein to simultaneously monitor both transcription and translation.[280] Ong et al. developed an unstable form of Spinach flanked with bases complementary to an mRNA sequence on either side such that the folded form of Spinach is formed upon binding to a target mRNA. This folded structure can then bind DFHBI and turn on fluorescence.[281]

Despite the strong brightness of Spinach *in vitro*, in cells, the brightness is significantly reduced due to improper folding of the aptamer. Therefore, ~1 s exposure time is necessary for imaging compared to 10-100 ms exposure times used in imaging GFP-labeled proteins under the same conditions. To address this limitation, Strack et al. developed Spinach2 through systematic mutagenesis of Spinach and demonstrated that it is 2-3-fold brighter than Spinach in both *E. coli* and HEK293T cells.[282] Using Spinach2, the dynamics and localization of CGG repeat-containing toxic RNAs were investigated.[282,283] Zhang et al. demonstrated by using multiple Spinach aptamers (8-64 repeats), mRNA molecules can be imaged with ~17-fold increased brightness in cells.[284] Importantly, such fusion did not adversely impact mRNA function. Structural minimization of Spinach led to the development of Baby Spinach which retains the functionality of Spinach but consists of 51 nt,[285] which was later utilized for imaging structured cellular RNAs.[286]

A limitation for generating "light up" aptamers like Spinach and Spinach2 is that aptamers are first selected based on their ability to bind fluorophores and then subsequently on their ability to turn on fluorescence. <1% of the aptamers that bind fluorophores lead to fluorescence enhancement.[287] Importantly, function of the isolated aptamers in cellular milieu is often compromised because these aptamers either need ions that are not present intracellularly or are misfolded due to the presence of adjacent sequences introduced for analyte sensing. Therefore, significant *in vitro* mutagenesis is required to render these probes useful in live cells. Filonov et al. developed an alternate strategy that allowed the selection of fluorescence-enhancing aptamers *in cellulo*, so that these problems could be mitigated.[287] This strategy led to the selection of the aptamer Broccoli, which binds the dye (*Z*)-4-(3,5-difluoro-4-hydroxybenzylidene)-2-methyl-1-(2,2,2-trifluoroethyl)-1*H*-imidazol-5(4*H*)-one) (DFHBI-1T). Compared to Spinach2, Broccoli has significantly reduced dependence on magnesium for proper folding, resulting in 2-fold increase in fluorescence signal *in vivo*. Moreover, Broccoli does not require tRNA scaffold which is incorporated into Spinach and Spinach2 to promote folding in cells. The 5S ncRNA was imaged in HEK293T cells using Broccoli. As an alternate strategy, Shu et al. incorporated the pRNA 3WJ motif of the phi29 DNA packaging motor into light up RNA fusions to enable predictable folding.[288] It was subsequently shown that Broccoli could be engineered to give a fluorescence readout in the presence of RNA-modifying enzymes.[289] For example, substitution of specific adenosine bases with N(6)-

methyladenosine rendered Broccoli non-fluorescent. Demethylation due to activity of RNA demethylases such as fat mass and obesity-associated protein (FTO) or ALKBH5 generated unmodified Broccoli and restored fluorescence in the presence of DFHBI-1T.

Dolgosheina et al. developed Mango, an aptamer that binds to thiazole orange derivatives and has significantly increased binding affinity and fluorescence efficiency compared to Spinach-type aptamers.[290] These properties could be leveraged to image RNA down to the single molecule level. Later, Autour et al. developed new Mango aptamers for imaging small non-coding RNA such as 5S, U6, and a box C/D scaRNA in fixed and live HEK293T cells.[291] The new aptamers were comparable in brightness to GFP and enhanced GFP. The Jaffrey lab developed Corn, a 28 nt aptamer, which binds to 3,5-difluoro-4-hydroxybenzylidene imidazolinone-2-oxime (DFHO), a mimic of the fluorophore in red fluorescent proteins. Compared to Spinach and Broccoli which lose >50% of fluorescence within 200 ms of constant irradiation, Corn is unaffected up to 10 s. Corn was utilized for quantitative measurement of Pol III transcription in HEK293T cells. DFHO could also bind to Broccoli derivatives yielding Red Broccoli and Orange Broccoli which have red shifted excitation and emission properties; however, these complexes were susceptible to rapid photobleaching.[292,293]

The Nilsen-Hamilton lab developed a FRET-based approach using Intracellular MultiAptamer GEnetic tags (IMAGEtags) for tracking gene expression *in vivo*. These probes gave higher

sensitivity compared to Spinach.[294,295] Jepsen et al. developed a genetically encoded FRET-based strategy for imaging intracellular analytes by incorporating Spinach and Mango aptamers in close proximity in single-stranded RNA origami scaffolds.[296] The validity of this system was demonstrated by imaging SAM in *E. Coli* cells.

The readers are directed to focused reviews by Ouellet, and You and Jaffrey for further information on genetically encoded-aptamers.[297,298]

1.6.10. Split aptamers

Split aptamers are comprised of aptameric sequences that have been divided into two parts. In the presence of a target, the two fragments form a ternary complex and this property can be used in designing proximity-dependent sensors. Split aptamers have been developed for detecting adenine, ATP, cocaine, thrombin, 17β-estradiol, D-vasopressin, and theophylline in solution.[299]

Zheng et al. developed a DNA nanoprism-based split-aptamer construct for the detection of ATP in live cells. The aptamer fragments were labeled with a FRET-pair such that in the presence of ATP a FRET signal was obtained.[300] The FRET signal increased linearly *in vitro* with increasing ATP concentrations between 0.03-2 mM and saturated at a 5-fold enhancement. The probe was also used for reporting changes in ATP concentrations in live HeLa cells.

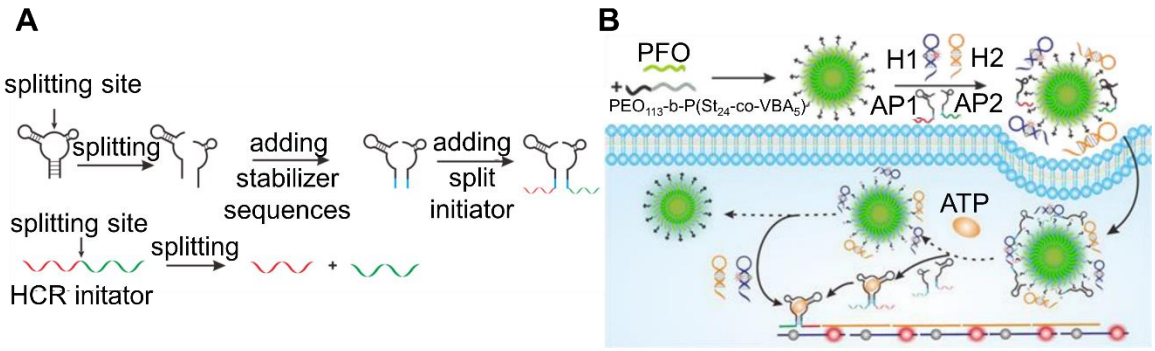

Figure 1.6.10-1. Split aptamers for ATP detection (A) Split aptamer design incorporating HCR for analyte detection. (B) A scheme of a nanoparticle/split aptamer detection strategy for sensing ATP in live cells. Binding of split aptamers AP1 and AP2 to ATP results in their tail regions coming into proximity, acting as an initiator for HCR with H1 and H2. The opening of H1 results in separation of a fluorophore and quencher, giving fluorescence. Adapted with permission.[110] Copyright (2018) American Chemical Society.

Recently, Zhang et al. reported the development of a nanoparticle-based split-aptamer sensor for detecting ATP in live cells through HCR (Figure 1.6.10-1).[110] In their work, Zhang et al. used four ONT sequences: (i) two sequences were the aptamer fragments (AP1 and AP2), each fragment consisting of a recognition element that binds to the target and a split initiator element for HCR (Figure 1.6.10-1). (ii) the remaining sequences were hairpin sequences H1 and H2. Upon binding to ATP, the tail regions of AP1 and AP2 were brought within close proximity, resulting in the formation of an active initiator sequence capable of activating HCR between H1 and H2. H1 was labeled with a fluorophore (TAMRA)-quencher (BHQ) pair such that the fluorescence was turned on by separation of TAMRA from BHQ upon opening of the hairpin due to ATP binding. Moreover, an amplified signal was attained as one ATP binding event results in a cascade of hybridizations. These ONTs were delivered to live cells using amino-functionalized fluorescent block copolymer nanoparticles (BCNs). The positively charged BCNs allowed electrostatic surface adsorption of the negatively charged ONTs as well as efficient transfection. Their inherent fluorescence also allowed the particles to be tracked independently of ATP. These constructs were

specific for ATP against CTP, GTP, UTP and TTP, were claimed to give a limit of detection of 30 nM in solution, and reported differences in the relative abundance of ATP inside cells with high signal-to-background ratios.

Wang et al. developed a "split-broccoli" system for imaging mRNA in live cells.[301] The Broccoli aptamer was split into two fragments and genetically encoded into live mammalian cells. Tandem binding of the aptamer fragments to the target mRNA created a binding pocket where the dye DFHBI could then bind and elicit a fluorescence signal. The authors termed this technique as aptamer-initiated fluorescence complementation (AiFC). The nomenclature was coined by drawing parallels to bimolecular fluorescence complementation (BiFC), a prevalent technique used in imaging protein-protein interactions using split-fluorescent proteins. Using this strategy, CFL1, β-actin, and GAPDH mRNA were imaged in HeLa and HuMSC cells. The authors further demonstrated the versatility of this system by engineering a new iSpinach RNA aptamer for monitoring β-actin. Similarly, Alam et al. also developed a split-broccoli system for monitoring RNA-RNA hybridization in live *E. coli* cells.[302]

1.6.11. Other strategies

Analogous to MBs, aptamer beacons were developed by Liang et al. for the imaging of HIV-1 reverse transcriptase in live HeLa and U1 cells.[62] This study addresses the challenge of visualizing endogenous proteins in genetically unmodified cells.

Ke et al. developed a noninvasive technique for the measurement of temperature in live cells using MBs synthesized from L-DNA, the enantiomer of naturally occurring D-DNA.[43] The fluorescence of the MBs is quenched below the melting temperature of the hairpin structure and increases gradually at higher temperatures. The use of L-DNA prevents non-specific binding to

cellular proteins and nucleic acids as well as nuclease degradation. Using palladium nanosheets that absorb NIR light (808 nm) to give rise to a photothermal effect, the authors showed that the fluorescence signal could be reversibly tuned over the range of 20-34 °C in live HeLa cells.

Strauss et al. developed slow off-rate modified aptamers (SOMAmers) for monitoring cell surface and intracellular targets using DNA points accumulation in nanoscale topography (DNA-PAINT).[303] DNA-PAINT is a single molecule imaging technique that allows ~ 5 nm spatial resolution.[304] The method involves the binding of dye-labeled DNA strands to their complements transiently. Unlike traditional aptamers, SOMAmers contain modified bases with hydrophobic residues allowing increased range of protein targets with high-affinity ligands. 7 different SOMAmers that can quantitatively image proteins in different cellular compartments such as the cell membrane, nucleus, lysosomal membrane, peroxisomes, and mitochondria, were identified. These proteins included EGFR, GFP-labeled Nup107, catalase proteins, ErbB2, HSP90, LIMP-2, and HSP60.

Several strategies aimed at identifying and isolating whole live cells based on aptamers or studying proteins on cell membranes have been published.[305–313] However, most of these aptamers target cell surface markers as opposed to intracellular markers and are, therefore, beyond the scope of this review.

1.7. DNAzyme-based probes

1.7.1. Gold nanoparticle-based

The Lu group pioneered the development of DNAzyme-based probes for imaging metal ions in live cells (Figure 1.7.1-1).[97] The 39E DNAzyme was chosen as a model as it detects its target

uranyl ions with excellent selectivity (>1 million-fold) and sensitivity (45 pM). A NanoFlare-like construct was used, consisting of a 13 nm gold core and a dense 39E DNAzyme shell. The enzyme strand of the DNAzyme was covalently attached to the gold core through a short thiolated poly A region at the 3' end. The substrate strand, labeled with Cy3 at the 5' end, was hybridized to the enzyme strand, resulting in quenched fluorescence due to proximity to the gold surface. The purpose of adding the poly A region was to ensure that steric bulk due to dense functionalization did not impede hybridization with the substrate strand. However, it was observed that this also led to decreased quenching efficiency. Therefore, the substrate strand was further modified with a quencher, BHQ, at the 3' end. In the presence of uranyl ions, the substrate strand was cleaved at the ribonucleotide site, resulting in a shorter strand with much lower melting temperature (21 °C) compared to the original intact strand (60 °C). Therefore, at physiological temperature (37 °C), the Cy3 containing short strand separated from the nanoparticle and fluorescence could be observed. Using this strategy, it was demonstrated that uranyl ions can be imaged in live HeLa cells pretreated with uranyl citrate. Moreover, using Lysotracker it was shown that the probes were mostly localized in the lysosomes. Li et al. later extended this strategy for the simultaneous imaging of Zn^{2+} and Cu^{2+} using two distinct fluorophores (FAM for Zn^{2+} and Cy5 for Cu^{2+}) in HepG2 cells.[314] In this context, we mention that a recent review by Zhou et al. provides a comprehensive overview of the state of metal sensing by DNA.[22]

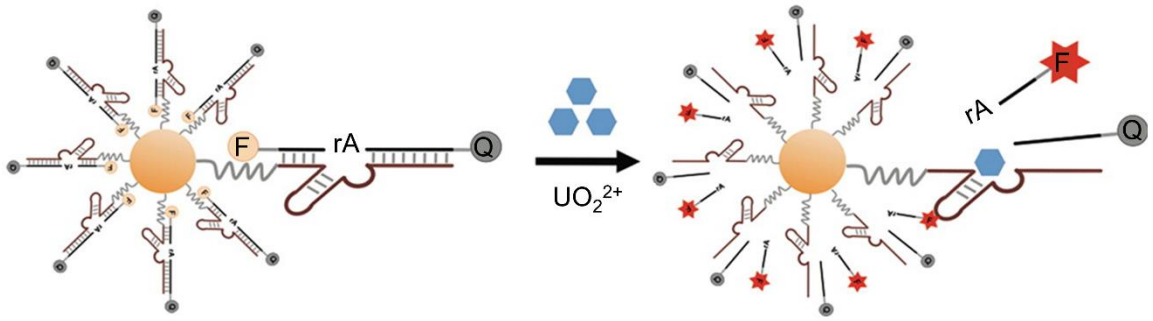

Figure 1.7.1-1. DNAzymes immobilized on the surface of gold nanoparticles for detection of uranyl ions. A fluorophore on the substrate strand is quenched by both gold and BHQ. Cleavage of the substrate strand in the presence of uranyl ions leads to separation of the fluorophore from both quenching elements and a subsequent fluorescence turn on. Adapted with permission.[97] Copyright (2013) American Chemical Society

The Wang group has developed several DNAzyme functionalized gold nanoparticle-based probes for live cell imaging. For example, Yang et al. reported the first aptazyme-based gold nanoparticle probe for the detection of ATP in live cells (Figure 1.7.1-2).[315] A 13 nm gold nanoparticle was densely functionalized with 3'-TAMRA-labeled substrate strands to which 5'-BHQ-2-labeled aptazymes specific for ATP were hybridized. The number of aptazyme strands were lower than the number of substrate strands. The aptazyme could not form a stable and active structure without ATP. However, in the presence of ATP and Mg^{2+} (a cofactor), a stable structure could be formed, leading to ATP-dependent cleavage of the substrate strand, separating the fluorophore from the quencher and eliciting a fluorescence signal. As one aptazyme can bind to several substrate strands in succession, a small number of ATP molecules could lead to a large fluorescence readout allowing a reported detection limit as low as 200 nM. The aptazyme-gold nanoparticle construct was used to image ATP in live HeLa cells. They later developed hairpin-locked DNAzyme probes[316] and split-DNAzyme-based probes for imaging microRNA in live cells.[317]

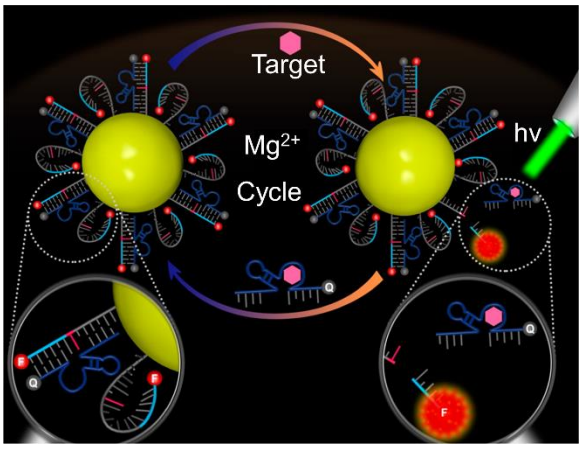

Figure 1.7.1-2. Workflow of aptazyme/gold nanoparticle-based method for detection of ATP molecules. Fluorophore-labeled substrate strands are conjugated to gold nanoparticles and prehybridized with a quencher-labeled aptazyme strand. The aptazyme is activated in the presence of ATP, leading to cleavage of the substrate strand and separation of fluorophore and quencher to yield fluorescence. Active aptazymes can bind to multiple substrate strands in succession, leading to amplified signal. Adapted with permission.[315] Copyright (2016) American Chemical Society

Using a slightly modified strategy employing two DNA hairpin strands (including a Zn^{2+}-specific DNAzyme), Liu et al. developed a probe for detecting microRNA.[318] Similarly, Peng et al. developed a "DNAzyme motor" probe, also for detecting microRNA.[50]

One limitation of DNAzymes is metal-dependent degradation prior to intracellular entry. As a potential solution to this problem, Wang et al. developed NIR activated DNAzymes.[319] Gold nanoshells were functionalized with a three-stranded DNAzyme precursor. Upon irradiation, local changes in temperature resulted in release of the DNAzyme from the gold surface, which could then form the active structure. In this study, Zn^{2+} was imaged in HeLa cells.

1.7.2. Graphene oxide-based

Kim et al. developed a theranostic platform for detection and regulation of mRNA based on DNAzyme-graphene oxide nanosheet (nGO) complexes.[320] nGO protected the DNAzyme against nuclease degradation and allowed its delivery into cells without the use of transfection reagents.

They demonstrated that using this construct, the Hepatitis C virus non-structural gene (NS3) can be detected and down-regulated in Huh-7-rep liver cells. The DNAzyme sequence used consisted of a catalytic domain flanked on both sides by bases complementary to the NS3 mRNA and a fluorophore label (FAM) at the 5' end. The fluorescence of FAM was quenched by 95% upon complexation of the DNAzyme with nGO and could be recovered upon separation of the DNAzyme from the nGO via binding to the target mRNA. Post mRNA binding, the DNAzyme elicited sequence specific mRNA cleavage resulting in changes in gene expression both at the mRNA and protein levels. The DNAzyme-nGO complex reduced mRNA and protein levels down to 32.6% and 26%, respectively, outperforming lipofectamine-transfected DNAzyme which led to reduction to 57.3% and 30.2%, respectively.

1.7.3. Polymer core nanoparticle-based

Zhang et al. developed dendritic polyethylene–cationic poly(p-phenylene ethynylene) nanoparticles for the delivery of DNAzymes into live cells.[321] The 8-17 DNAzyme that undergoes catalytic degradation in the presence of Pb^{2+} was used in this study. The DNAzyme was bound to the polymer core through electrostatic interactions. The 5' end of the substrate strand was labeled with Cy5.5 while the 3' end of the enzyme strand was labeled with BHQ-3, resulting in quenched fluorescence in the absence of Pb^{2+}. In buffer, addition of increasing concentrations of Pb^{2+} (up to 10 μM) led to increase in fluorescence signal (~10-fold) due to degradation of the substrate strand resulting in separation of the fluorophore and the quencher. The nanocomposite was internalized into HepG2 cells without transfection reagents. The cells were then treated with 0 to 725 mM Pb^{2+}. The blue-green fluorescence of the nanoparticle probe enabled monitoring uptake whereas the far-red fluorescence of the Cy5.5 allowed monitoring of Pb^{2+} concentration. Using confocal imaging

and flow cytometry, the authors demonstrated that the probe responded to changing concentrations of Pb^{2+} in live cells.

1.7.4. Dendrimer-based

The presence of inorganic cores used in delivering DNA-based probes has been shown to induce toxicity at high concentrations in some cases. To overcome this limitation, Meng et al. developed a nanocarrier composed entirely of DNA using a dendrimer-based strategy.[322] The sensing moiety of the dendrimer was based on a DNAzyme for detecting L-histidine and consisted of 4 strands as shown in Figure 1.7.4-1. The strand Y_{1b} was labeled with a quencher, BHQ-1, while the substrate strand X was labeled with the fluorophore FAM. In the presence of L-histidine, the substrate strand was cleaved, resulting in a shorter strand with a much lower melting temperature (12.7 °C) compared to the original full-length strand (44.3 °C). At physiological temperature, the strand dehybridized, resulting in separation of FAM and BHQ-1 leading to fluorescence enhancement. In buffer, the dynamic range was established to be 5 μM -10 mM, with a reported detection limit of 500 nM. Importantly, the dendrimer-based architecture imparted resistance to nuclease degradation as well as stability against degradation due to non-specific protein binding. In cell lysate, similar titration curves were obtained, with a dynamic range of 5-100 μM. To test whether these constructs function in live cells, MCF-7 (human breast cancer) cells were used as a model. Cells treated with the dendrimer nanocarrier, followed by 100 mM L-histidine and 150 mM K^+ (a cofactor in the catalytic reaction) showed significantly increased fluorescence compared to cells treated without one or more of the components. The authors also developed a sensor for detecting ATP using an ATP aptamer instead of the DNAzyme. Taken together, these results represent an advance towards developing more biocompatible nucleic acid-based probes.

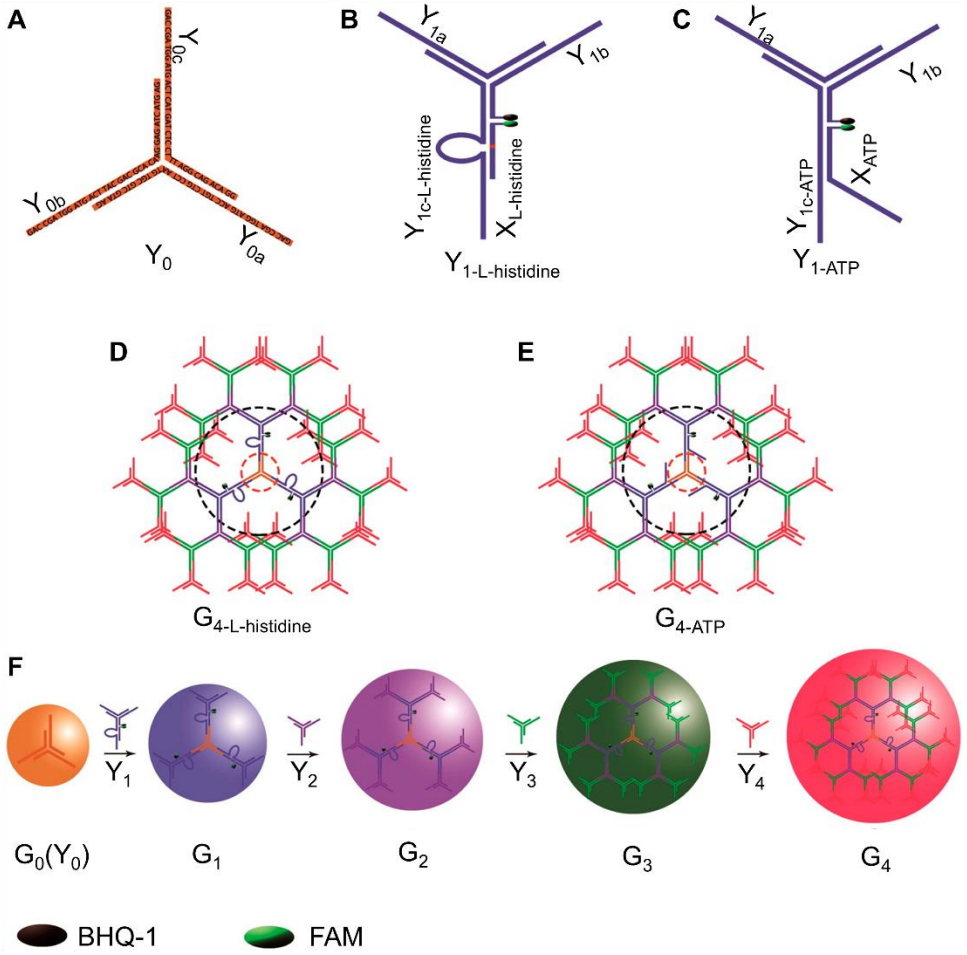

Figure 1.7.4-1. Design of dendrimer-based nanoparticles for detection of ATP and histidine. (A) The assembly of Y_0 containing a 3-way junction made from single-stranded components Y_{0a}, Y_{0b}, and Y_{0c}. (B) The assembly of $Y_{1\text{-L-histidine}}$ from single-stranded components Y_{1a}, BHQ1-Y_{1b}, $Y_{1c\text{-L-histidine}}$ and FAM-$X_{L\text{-histidine}}$. (C) The assembly of $Y_{1\text{-ATP}}$ from single-stranded components Y_{1a}, BHQ1-Y_{1b}, $Y_{1c\text{-ATP}}$ and FAM-X_{ATP}. (D) The assembly of $G_{4\text{-L-histidine}}$ from components Y_0, $Y_{1\text{-L-histidine}}$, Y_2, Y_3, and Y_4. (E) The assembly of $G_{4\text{-ATP}}$ from components Y_0, $Y_{1\text{-ATP}}$, Y_2, Y_3, and Y_4. (F) Layer-by-layer development of generations 1-4 of DNA dendrimers.[322] Adapted with permission. Copyright (2014) American Chemical Society.

1.7.5. MOF-based

Yi et al. developed a MOF-based probe for ratiometric detection of intracellular microRNA.[323] The 8-17 DNAzyme labeled with a FRET-pair was complexed with a zeolitic imidazolate framework-8 (ZIF-8). This nanostructure was taken up by cells. In the endosome, acidic digestion

of ZIF-8 released Zn^{2+}, which acts as a cofactor for the DNAzyme. In the presence of the target microRNA, a change in FRET signal is observed due to DNAzyme activity. This strategy was utilized in imaging miR-21 in MCF-7, HeLa, and L02 cells. Chen et al. developed MOF nanoparticles capped with DNAzymes and aptazymes as a therapeutic platform for treating cancer cells.[324] Doxorubicin was incorporated into the porous MOF structures and the DNAzymes/aptazymes acted as a cap. In the presence of a target metal ion (Mg^{2+} or Pb^{2+}) or target ligand for the aptamer (ATP), DNAzyme/aptazyme activity was observed, leading to drug release.

1.7.6. FRET-based

Hwang et al. developed photocaged DNAzymes for monitoring metal ions in live cells with spatial as well as temporal precision.[325] One challenge of using DNAzymes is premature cleavage of the substrate strand before the probes are completely internalized. As the 2' position of the ribonucleotide adenosine plays an important role in the catalytic activity of the DNAzyme, the authors modified the site with a photocleavable 2′-O-nitrobenzyl protection group. The 8-17 DNAzyme was chosen to image Zn^{2+} in live HeLa cells. The substrate strand was modified with fluorescein on the 5' end and BHQ-1 on the 3' end while the enzyme strand was modified with dabcyl on the 5' end. In the absence of the target, the two strands were hybridized, and the fluorescence was quenched. Notably, incubation of the probes with 50 µM Zn^{2+} in buffer and human serum for long periods (up to 7 days) did not result in significant increase in fluorescence indicating that cleavage was minimum in the absence of light. In contrast, the unprotected adenosine containing DNAzyme degraded within an hour. These probes were transfected into HeLa cells using Lipofectamine 2000, and upon irradiation with 365 nm light, the nitrobenzyl protection group was cleaved, thereby leading to Zn^{2+}-dependent cleavage of the substrate strand

with concomitant increase in fluorescence signal from fluorescein. Nuclear localization of the probes was observed, consistent with previous reports suggesting ONTs delivered using Lipofectamine are sequestered into the nucleus. One advantage of using this system is that it is highly modular i.e. by using the same substrate strand, but by replacing the catalytic core of the enzyme strand with a core sensitive to another metal ion, a new probe can be developed. The authors demonstrated this capability by using GR-5 as the catalytic core for detecting Pb^{2+}.

As an alternate strategy (but similar fluorescence reporting mechanism) to prevent false positive signal, Cui et al. developed L-DNAzymes to image Cu^{2+} in live HeLa cells.[326] Their rationale for choosing L-DNAzymes was to prevent false positive signal that may arise from digestion of probes by nucleases, non-specific protein or off-target binding of the probes. The L-DNAzyme probe, being an enantiomer of D-DNAzyme, retained its catalytic activity in the presence of the achiral metal ion, while imparting enhanced biostability to the probe. Compared to D-DNAzymes, these probes were resistant to nuclease degradation and resisted binding to single-stranded DNA protein. These probes were transfected into the cells using Lipofectamine and upon treatment of the cells with Cu^{2+}, fluorescence signal could be observed.

Torabi et al. developed the first Na^+-specific DNAzyme by *in vitro* selection and converted it into a fluorescent sensor for imaging Na^+ in live cells.[327] The DNAzyme was characterized by fast catalytic rate (observed rate constant ~0.1 min^{-1}), high selectivity (>10-000 fold) for Na^+ over competing ions (K^+, Li^+, etc.), and a dynamic range (0.135-50 mM) encompassing physiological concentrations of Na^+. By attaching a quencher (Iowa Black) to the 3' ends of the enzyme and substrate strands as well as a fluorophore (FAM) to the 5' end of the substrate strand, a fluorescent sensor for Na^+ was developed. The ribonucleotide adenosine site in the substrate strand was

protected by photocleavable 2′-O-nitrobenzyl protection group to enable controlled activation of the DNAzyme after probe internalization. Later, Wu et al. developed a catalytic hairpin assembly-based strategy for amplification of signal coming from Na^+-specific activity of the NaA43 DNAzyme.[328]

1.7.7. Other strategies

Zhang et al. developed a theranostic platform through which low-abundance microRNAs can be visualized using an *in situ* amplification strategy and drugs can be released in the presence of target microRNAs.[329] DNAzymes were attached to multifunctional nanoparticles. Two microRNAs, miR-21 and miR-145, which are up- and down- regulated in many types of tumor cells, respectively, were chosen as targets. Fluorophore-quencher-labeled multicomponent DNAzymes were attached to mesoporous silica-coated gold nanorods via azide-alkyne click chemistry. These constructs had a dynamic range between 2.5-250 pM and a reported detection limit of ~1 pM. They could be internalized into cells (HeLa, NIH 3T3, and HL-60) and in the presence of their targets, cleavage of the fluorophore-labeled substrate strands led to increased fluorescence. Using calibration curves, the authors quantified the number of transcripts per cell. Upon NIR irradiation, the gold nanorod could cause local increase in temperature, modulating cleavage activity. Moreover, doxorubicin could be incorporated within the mesoporous silica and the DNAzymes acted as a "gatekeeper," releasing the encapsulated drug only in the presence of the target microRNAs.

He et al. developed probes employing a dual amplification strategy for the detection of mRNA in live cells.[330] These probes consisted of a ZnO core onto which four hairpin DNA strands were adsorbed. This architecture allowed the probes to be taken up inside cells without the need for

transfection reagents and impeded nuclease degradation. In the endosome, it is believed that acid-triggered dissolution of the ZnO core resulted in cytosolic delivery of the nucleic acids. In the presence of the target mRNA, active DNAzymes were formed by self-assembly of the hairpin strands via HCR, which lead to a fluorescence readout. This strategy yielded a reported limit of detection as low as 0.1 fM. Using this method, the survivin mRNA, often overexpressed in cancer cells, was imaged in a variety of cells, including HeLa, L02, C166, MCF-10A, HepG2, SMCC-7721, and MCF-7 cells.

Some other recent developments in the area of DNAzyme-based detection involve the use of MnO_2 nanosheet carriers[331] and magnetic field-activated DNAzymes for imaging mRNA,[332] enzyme-initiated DNAzyme nanodevices,[333] as well as upconverting nanoparticles-based probes.[334]

1.8. Methods for Probe Delivery

The cell membrane is impervious to ONTs, making intracellular delivery of nucleic acid-based probes challenging. Moreover, for imaging, it is important to consider not only the probe uptake, but also the quantity of free probe available for binding to the desired targets. For example, a probe that targets a molecule in the cytoplasm must be able to reach the cytoplasm and should not be confined within cellular compartments. Some methods which have been widely utilized to deliver nucleic acid-based imaging probes include the use of microinjection, transfection reagents, and electroporation.[6] Recently, several nanoparticle-based platforms as well as aptamer-based strategies have been developed as transfection reagent-free strategies for intracellular delivery of probes via receptor-mediated internalization.[44,74]

Microinjection involves direct introduction of imaging probes into the cytoplasm of the cells. While structures of various sizes can be delivered effectively, the throughput is low. Moreover, microinjection can damage the cell and impede normal cell functions.

As an alternative strategy, various transfection reagents have emerged as popular vectors for introducing imaging probes inside cells. One class of transfection reagents involves toxin-based cell membrane permeabilization. For example, streptolysin O (SLO), is a bacterial protein that oligomerizes on the cell-surface in a cholesterol-dependent manner to form reversible pores with diameters of 25-30 nm. These pores facilitate the transfer of nucleic-acid based probes from extracellular space indirectly into the cytoplasm;[335] the cell membrane can be restored after SLO treatment by placing the cells in normal cell culture medium. Cell penetrating peptides (CPPs) (e.g. HIV-1 Tat peptide and its derivatives) are another class of transfection reagents. The positive charge associated with the cationic amino acids aids in cellular transfection.[336] Cationic liposome-based transfection reagents such as Lipofectamine have also been developed.[337] A major limitation of transfection reagents is induction of toxicity. Moreover, in some cases, transfection reagents can also alter gene expression. Some transfection reagents are susceptible to endosomal entrapment. Probes that enter through endosomal pathways are prone to rapid degradation by nucleases. Therefore, even when the probes do escape, only a small fraction of the probes remain functional.

To overcome challenges associated with endosomal entrapment, electroporation has been used to deliver imaging probes to cells with over 90% transfection efficiency.[150,338] Electroporation entails the application of strong electric fields to transiently destabilize cell membranes so that external reagents may be introduced within cells. Typically, low cell viability is often associated

with electroporation. Although recent advances such as microporation have minimized cell mortality (>85% cell viability[150]), optimization is necessary to determine the electrical parameters for efficient cellular delivery. The parameters depend on electrode design, cell type as well as identity of molecules to be introduced within cells.

Many nanomaterial-based nucleic acid imaging probes do not require transfection as they are taken up by cells through receptor-mediated endocytosis. For example, the spherical nucleic acid architecture which involves a dense DNA shell grafted to a nanoparticle core allows NanoFlares and structurally similar probes to be taken up by endocytosis.[139] Graphene-oxide based probes are also taken up spontaneously by cells.[261] A small fraction of probes being released from the endosome results in stoichiometrically meaningful quantities for detection. However, it is not known quantitatively what percentage of these probes escape from the endosome and remain functional. Inability to detect desired targets in the cytosol may arise from lack of careful optimization of incubation conditions, given that probe uptake and endosomal escape may be cell line dependent. It should be noted that in fluorophore-quencher based systems, separation of the fluorophore and the quencher due to nuclease degradation in the endosomes can be a significant contributor to the incidence of false positive signals.

Certain aptamer sequences can also enable probe internalization within cells without the need of transfection reagents. For example, the AS1411 aptamer that targets nucleolin, a protein often overexpressed on the surface of various cancer cell lines, has been used to deliver probes preferentially to cancer cells.[74] Similarly, the transferrin aptamer has been utilized to image the transport of chloride ions along the transferrin pathway using DNA nanomachines.[248]

Importantly, the use of aptamers allows probes to be delivered along different pathways so that chemical changes along these pathways can be individually imaged.[115,248]

1.9. Challenges

1.9.1. Target accessibility

Probes must be able to bind to their targets to elicit a detectable signal. However, not all targets are easily accessible for binding to the probes. For example, parts of an mRNA sequence might be bound to proteins or may have secondary structures, rendering it difficult for a complementary probe to bind. Therefore, while designing new probes, several sequences may have to be designed and tested to find the optimal probe. Studies have suggested that the starting and terminating codon regions of mRNAs fare as better targets.[339] Yet, probes must be carefully designed as a shift of only a few bases either towards the 3' or 5' can lead to an ineffective probe. Target analytes may also be localized within membrane-bound organelles and inability of probes to enter these organelles will impede detection.

1.9.2. Selection of fluorophores and quenchers

To establish quantitative imaging of intracellular analytes with high signal-to-background ratios, fluorophores and quenchers must be carefully chosen. For example, cellular autofluorescence in the green channel contributes to significant background. These effects can be mitigated by using dyes with red-shifted fluorsecence or by developing brighter dyes with greater quantum yields. Alternately, lanthanide-based dyes which have longer fluorescence lifetimes can be used for imaging to overcome interference from autofluorescence. A limitation of such an approach is the need for more complex instrumentation. Another important consideration is the photostability of

the dye. Long-term cellular imaging necessitates the use of dyes that are resistant to photobleaching. Designing fluorophores with desired brightness, photostability, and biocompatibility is still an active field of research. A major limitation of fluorescence-based approaches in general is that multiplexed imaging of more than 5 or 6 analytes is challenging due to the limited numbers of spectrally distinct fluorophores available. Moreover, the fluorescence intensity of fluorophores can also be impacted by local pH or interaction with other molecules, which can complicate the interpretation of results.

1.9.3. Sensitivity and selectivity of probes

The most challenging hurdle in developing fluorescent probes for imaging analytes in living cells is sensitivity of detection. Low-abundance molecules are particularly difficult to observe, although several amplification strategies such as HCR have been developed to enhance signal. Moreover, the binding affinity of the probes play an important role in determining the sensitivity with which targets can be detected. This is particularly important for aptamer-based probes which are typically evolved *in vitro* and therefore do not behave as expected inside cells and often show poor folding. Also important are the kinetics of probe-target binding. If the dynamics of the analyte of interest occur faster than the target binds, it will be impossible to follow the analyte with spatiotemporal precision. Importantly, probes should be carefully designed to be selective for their targets to avoid false positive signals.

1.9.4. Probe delivery and stability

As mentioned above, there are numerous challenges associated with the delivery of probes in live cells. Each technique has its own advantage and disadvantages. Probes must be able to reach their

targets to be able to detect them. Therefore, probe stability is of paramount importance. This is particularly important for monitoring long-term dynamics. Nucleic acid-based probes are inherently susceptible to enzymatic degradation. However, their stability can be increased via modification of the nucleic acid structure or association with nanoparticles. Also important for long-term monitoring of live cells is the impact of the probes themselves on the cells. For example, binding of antisense/DNAzyme probes to mRNA can induce down-regulation or degradation of mRNA over long treatment times.[166] Some of these challenges can be mitigated by using low concentrations of probes, while ensuring the concentration is high enough to elicit a signal, or shorter treatment times.

1.9.5. Motivation for a new class of live cell probes

The limitations of nucleic acid-based probes for live cell analysis summarized herein offer an opportunity to engineer a new class of structures that overcome these challenges. A class of probes that actively enter cells, are resistant to false-positive signal, have the ability to spatiotemporally track analytes, yield kinetically rapid response, and recognize a wide variety of analytes is highly sought after.

CHAPTER TWO

2. Forced Intercalation Aptamers (FIT-Aptamers)

Portions of this chapter reprinted (adapted) with permission from S.B. Ebrahimi, D. Samanta, H.F. Cheng, L.I. Nathan, C.A. Mirkin, *J. Am. Chem. Soc.* **2019**, *141*, 13744–13748.

2.1. Introduction

2.1.1. FIT-Aptamers as a New Paradigm for Sensitive Detection of Analytes

Aptamers, oligonucleotide sequences that can be evolved to bind to analytes with high sensitivity and specificity, have recently found widespread use as effective therapeutic and diagnostic tools.[25,340–342] To be used as a tool for detection, the binding of an aptamer to its target must result in a signaling event that can be monitored as a readout for target presence. Fluorescence-based techniques have emerged as popular readout platforms due to their simplicity, low-cost, high-throughput, and ability to multiplex.[121,122,254,268,292,293,343–347] For example, several strategies have been designed wherein target binding to an aptamer labeled with a fluorophore-quencher pair induces a structural change that separates the fluorophore and the quencher (e.g. structure-switching signaling aptamers,[254] aptamer beacons,[345] aptamer switch probes[268]). Alternatively, constructs that bring a pair of dyes into close proximity upon target binding to elicit a fluorescence signal by Förster resonance energy transfer (FRET) are also commonly employed.[346] More recently, Spinach aptamers and variants thereof have been developed that change structure after aptamer-target complexation, allowing a small molecule fluorophore to bind to the Spinach region in the sensing unit and yield fluorescence turn-on.[121,122,292,293]

While these methods constitute a powerful means to detect targets of interest, they also suffer from limitations. Strategies that rely on partial blocking of the aptamer site (i.e. structure-switching aptamers, aptamer beacons) retard aptamer-target binding kinetics, increasing the time required to obtain a readout.[348] Systems based on fluorophore/quencher pairs are prone to false-positive signals in complex media and cells due in part to nuclease degradation.[175] Moreover, strategies based on FRET are generally associated with low signal to noise ratios.[349] Platforms like Spinach

require long sequences to be appended to aptamers, making their folding and, therefore, efficacy difficult to predict in complex milieu.[287]

In this chapter, I present a fundamentally new design strategy for interfacing aptamers with a readout event via viscosity-sensitive fluorophores. The Seitz group has shown that dyes of the thiazole orange family can be covalently attached to mRNA recognition sequences to create "duplex-sensitive" fluorescence turn-on probes.[124,154,157,158] The fluorescence enhancement stems from the restricted rotation of the dye around its methine bridge upon forced intercalation (FIT) in the oligonucleotide duplex. Notably, these probes avoid false-positive signals because their turn-on does not rely on proximity between a fluorophore and a quencher. We hypothesized that by strategically placing the dye in an aptamer sequence such that structural changes of the aptamer upon ligand binding hinders the dye's internal rotation, a new class of false-positive resistant signaling aptamers can be designed (Figure 2.1.1-1). Additionally, we reasoned that these "FIT-aptamers" would respond faster compared to probes relying on partial blocking of the aptamer site and require only a single modification unlike Spinach-based platforms.[122]

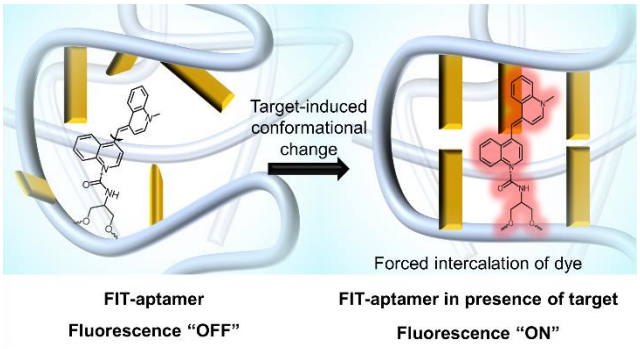

Figure 2.1.1-1. FIT-aptamers: Aptamers modified with a visco-sensitive dye (quinoline blue) fluoresce upon target binding due to target-induced conformational changes.

2.2. Materials and Methods

2.2.1. Oligonucleotide design, synthesis, purification, and characterization

2.2.1.1. Oligonucleotide design

Error! Reference source not found. lists all the oligonucleotide sequences used in this study. The dye quinoline blue, D, is represented by D.

Table 2.2.1-1. Oligonucleotide sequences used in this study

Abbreviation	Sequence (from 5' end to 3' end)	Purpose
HgA1	TCATG TTTGT TTG TTG GCC CCC CTT CTT TDT TA	Aptamer for Hg^{2+}
HgA1comp	CAA ACA AAC ATG A	Short complement to HgA1
HgA2	TTT D TTT TTT T TTT	Simpler/shorter aptamer for Hg^{2+}
HgA2-F	TTT T TTT TTT T TTT-fluorescein	Strands for FRET experiments with Hg^{2+}
HgA2-T	TAMRA dT-TTT T TTT TTT T TTT	
HgA2-FT	TAMRA dT-TTT T TTT TTT T TTT-fluorescein	
AgA	CCC D CCC AAAA CCC T CCC	Aptamer for Ag^{+}
I-mD	CCCC TAA CDCC TAA CCCC TAA CCCC	Aptamer for H^{+}
THR1D	GGT TGG TGT GGT TGG $(spacer18)_5$ CGC D TCT	Two aptamers that bind two distinct epitopes on thrombin
THR2	AGA T GCG $(spacer18)_5$ AGT CCG TGG TAG GGC AGG TTG GGG TGA CT	
THR1-F	GGT TGG TGT GGT TGG $(spacer18)_5$ CGC A TCT-fluorescein	Strands for FRET experiments for two epitope thrombin binding
THR2-T	TAMRA dT-AGA T GCG $(spacer18)_5$ AGT CCG TGG TAG GGC AGG TTG GGG TGA CT	
THR1-c	GGT TGG TGT GGT TGG $(spacer18)_5$ CGC A TCT	Control sequences for FRET experiments for two epitope thrombin binding
THR2-c	T AGA T GCG $(spacer18)_5$ AGT CCG TGG TAG GGC AGG TTG GGG TGA CT	
Split-THRa	TGG TTG G TTTTTT (sp18)5 C GCD TCT	Split aptamers for thrombin
Split-THRb	AGA TGC G (sp18)5 AAAAAA GGT TGG TG	
5'-TDT-3'	ATA TTC TGA A TDT CA TCC TGC	DNA sequences used to demonstrate that D can report the formation of T-Hg^{2+}-T base pairing within a preformed oligonucleotide duplex
5'-TDA-3'	ATA TTC TGA A TDA CA TCC TGC	
5'-ADA-3'	ATA TTC TGA A ADA CA TCC TGC	
3'-TGT-5'*	GCA GGA TG TGT T TCA GAA TAT	
3'-TGA-5'*	GCA GGA TG AGT T TCA GAA TAT	
3'-AGA-5'*	GCA GGA TG AGA T TCA GAA TAT	

*This sequence reads "…AGT…" from 5'-3'. However, it is named as 3'-TGA-5' as it reads "…TGA…" when written from 3'-5'.

2.2.1.1.1. Ligand-induced intramolecular conformational changes

We first selected a DNA sequence (5'-TCATG TTTGT TTG TTG GCC CCC CTT CTT TCT TA-3') that is known to bind to Hg^{2+} via intramolecular conformational changes. We replaced the underlined cytosine at the 4th position from the 3' end with D to obtain a FIT-aptamer (HgA1). We anticipated that in the presence of Hg^{2+}, T-Hg^{2+}-T base pairing would occur, turning on the fluorescence of D (Figure 2.3.1-1).

We note that the sequence used has been previously shown to detect Hg^{2+} as a structure-switching signaling aptamer that incorporates a fluorophore-quencher pair. This strategy necessitates that part of the aptamer be blocked by a short complementary strand. To study the impact of the short complement on the response time of the probe, we synthesized a 13-mer complement (HgA1comp).

We next synthesized the FIT-aptamer HgA2 consisting of a simple string of 14 thymine bases with the 4th base from the 5' end replaced with D (Figure 2.4.1-1A). To study how FIT-aptamers compare with FRET-based platforms, we synthesized three additional T_{14} sequences: the first sequence (HgA2-F) was labeled with fluorescein at the 3' end, the second sequence (HgA2-T) was labeled with TAMRA dT at the 5' end, and the third sequence (HgA2-FT) was labeled with both fluorescein and TAMRA at the 3' and 5' ends, respectively. Fluorescein and TAMRA are a well-known FRET pair. Hg^{2+}-mediated thymine coordination in HgA2-FT is expected to bring the FRET pair into close proximity, resulting in a FRET signal (Figure 2.3.1-3). HgA2-F and HgA2-

T were synthesized as control sequences, to study the influence of Hg^{2+} on the FRET signal in the absence of one of the dyes.

As a simple probe for Ag^{+}, a cytosine-rich strand was designed (AgA, Figure 2.3.1-4), while a modified sequence for the human telomeric i-motif was used to detect pH changes (I-mD, Figure 2.4.1-3A).

2.2.1.1.2. Aptamer-based sandwich assay

Thrombin was chosen as a model target for studying two epitope aptamer binding. Aptamers known to associate with thrombin at two distinct sites were used in this study. To generate FIT-aptamers, five spacer18 moieties and 7-base complementary sequences were appended to the 3' end of the first aptamer (THR1D) and 5' end of the second aptamer (THR2), respectively. The 4^{th} base from the 3' end of THR1D was replaced with D (Figure 2.4.1-4A).

2.2.1.1.3. Split-aptamers

Thrombin was chosen as a model target for studying the feasibility of designing FIT-based split-aptamers. A known aptamer for thrombin was fragmented into two parts. This aptamer is known to form a G-quadruplex and then bind to thrombin. To aid in G-quadruplex formation, complementary bases were appended to the 5' and 3' ends of the two aptamers, respectively. So that the designed FIT-aptamers reports target presence, a similar design strategy as used for two epitope binding was employed: five spacer18 moieties and 7-base complementary sequences were appended to the 3' end of the first aptamer (Split-THRa) and 5' end of the second aptamer (Split-THRb), respectively. The 4^{th} base from the 3' end of Split-THRa was replaced with D (Figure 2.3.3-1).

2.2.1.1.4. Intraduplex metallo-base pair formation

We synthesized three 21-base DNA sequences that differed only in terms of the bases at positions 11, 12, and 13 from the 5' end. The sequences consisted of TDT, TDA, and ADA regions and these sequences were correspondingly termed as 5'-TDT-3', 5'-TDA-3', and 5'-ADA-3', respectively. Three strands that are complementary to these sequences were also synthesized: 3'-AGA-5', 3'-AGT-5', and 3'-TGT-5'. The dye-labeled strands were added to the unlabeled strands in different combinations which resulted in the formation of duplexes with varying numbers of T-T mismatches adjacent to D (Table 2.2.1-2).

Table 2.2.1-2. Number of T-T mismatches in DNA duplexes

	5'-TDT-3'	**5'-TDA-3'**	**5'-ADA-3'**
3'-AGA-5'	0	0	0
3'-AGT-5'	1	0	0
3'-TGT-5'	2	1	0

2.2.1.2. Synthesis, purification, and characterization

DNA synthesis reagents were purchased from Glen Research. Oligonucleotides were synthesized either on a MerMade12 (MM12, BioAutomation Inc., Plano, Texas, USA) instrument using universal controlled pore glass (CPG) beads at a 5 μmol scale or an ABI 394 using CPG beads at a 1 μmol scale. After synthesis, the CPG-bound oligonucleotides were cleaved from the CPG beads and deprotected for 4 h at 55 ºC using 2 mL of 30% ammonium hydroxide. The ammonia was then evaporated off using an Organomation® Multivap® Nitrogen Evaporator. The volume of the remaining solution was adjusted to 2 mL using nanopure water. The solution was then filtered through a 0.2 μM syringe filter to remove the CPG beads. Subsequent purification was performed using reverse phase high pressure liquid chromatography (RP-HPLC, Varian ProStar 210, Agilent

Technologies Inc., Palo Alto, CA, USA) employing a C18 column and a gradient of 0 to 75% B over 45 min (A=triethylammonium acetate buffer, B=acetonitrile). Collected fractions were then lyophilized overnight and subsequently detritylated with 2 mL of 20% acetic acid for 1 h. The cleaved DMTr was extracted using ethyl acetate. The remaining acidic oligonucleotide solution was lyophilized overnight again, and resuspended in nanopore water. The fraction containing the product was identified using matrix-assisted laser desorption ionization time-of-flight mass spectrometry (MALDI-TOF MS). The concentration of product was determined via UV-VIS spectroscopy using the extinction coefficient at 260 nm obtained from the IDT Oligo Analyzer Tool.

2.2.2. Synthesis and characterization of quinoline blue (D)

2.2.2.1. General methods

All chemicals, reagents, and solvents were purchased as reagent grade from Sigma-Aldrich, Acros, or Alfa Aesar and used as received unless otherwise stated. When specified, solvents were degassed under a stream of argon before use. All glassware and stir bars were oven-dried at 180 °C. Flash chromatography was performed using SiO_2 60 (230–400 mesh ASTM, 0.040–0.063 mm; Fluka). Deuterated solvents were purchased from Cambridge Isotope Laboratories and used as received. ^{1}H and ^{13}C NMR spectra were recorded on a Bruker Avance 400 MHz NMR spectrometer at 298 K, and chemical shifts (δ) are given in parts per million. ^{1}H NMR spectra were referenced to residual proton resonances in the deuterated solvents (dimethylsulfoxide-d_6 = δ 2.50), while absolute referencing was applied for heteronuclear NMR spectra (Ξ_C = 25.145020). Electrospray ionization mass spectrometry (ESI-MS) was recorded on a Micromas Quatro II triple−quadrapole mass spectrometer in positive ion mode. N-methyl-4-chlorquinolinium iodide

and N-carboxylmethyl-4-methquinolinium bromide were synthesized following literature procedures.

2.2.2.2. Synthesis of quinoline blue derivative

D was synthesized as described previously with slight modifications. N-methyl-4-chlorquinolinium iodide (0.2636 g, 0.863 mmol, 1 equiv) and N-carboxylmethyl-4-methquinolinium bromide (0.292 g, 1.035 mmol, 1.2 equiv) were suspended in 2.2 mL of dichloromethane (CH_2Cl_2). To the brown suspension was added trimethylamine (0.4190 mL, 3.02 mmol, 3.5 equiv), and the resulting solution turned dark blue immediately. The mixture was stirred at room temperature in the dark overnight. The mixture was then dried and purified via flash chromatography (CH_2Cl_2:MeOH = 8:2). The product fractions were combined and dried *in vacuo* to obtain a bluish-purple powder (0.2083 g, 0.608 mmol, isolated yield = 71%). The product is stable when stored dried and shielded from light, but a solution of D would decolorize and degrade when exposed to light for an extensive period of time. ^{1}H NMR (400 MHz, DMSO-d_6) δ 8.71 – 8.62 (m, 2H), 8.24 (d, J = 7.1 Hz, 1H), 8.00 (d, J = 7.4 Hz, 1H), 7.90 – 7.82 (m, 2H), 7.82 – 7.78 (m, 1H), 7.78 – 7.70 (m, 2H), 7.67 – 7.54 (m, 2H), 7.51 (d, J = 7.5 Hz, 1H), 7.23 (s, 1H), 4.74 (s, 2H), 3.96 (s, 3H). ^{13}C NMR (101 MHz, DMSO-d_6) δ 165.89, 149.40, 147.26, 144.21, 142.43, 138.62, 138.58, 132.12, 132.09, 125.89, 125.54, 125.44, 125.35, 125.27, 124.62, 118.39, 117.15, 109.32, 106.83, 95.72, 59.35, 41.09. ESI-MS m/z Calcd for $[M+H]^+$: 343.14 *m/z*. Found: 343.14 *m/z*. Calcd for $[M+Na]^+$: 365.13 *m/z*. Found: 365.10 *m/z*.

2.2.2.3. NMR spectra

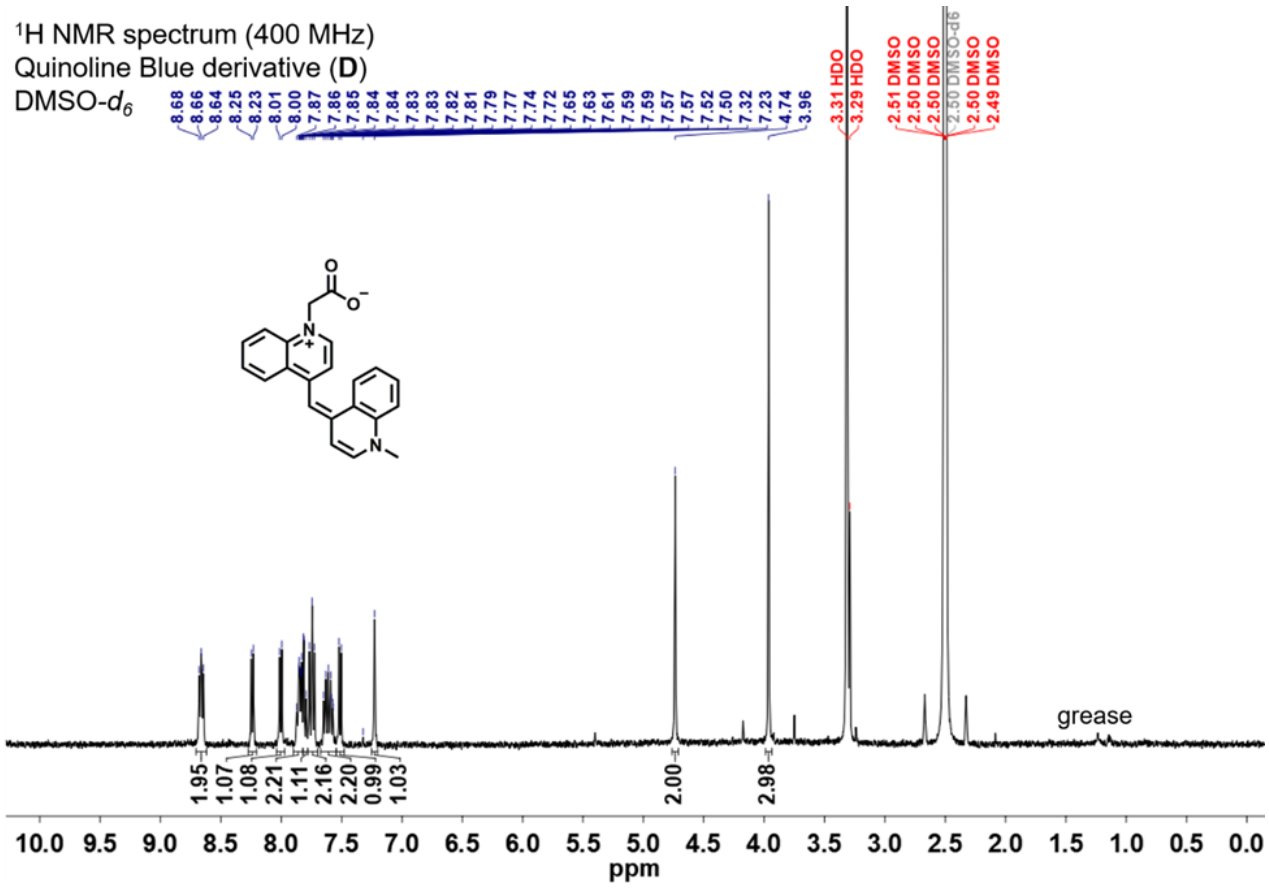

Figure 2.2.2-1. ^{1}H NMR (400 MHz, DMSO-d_6, 298 K) spectrum of D.

2.2.3. Coupling of D to oligonucleotide probes

D-carboxylate was coupled to oligonucleotide probes containing an amino-modifier (N-trifluoroacetyl serinol phosphoramidite) using a previously reported protocol with modifications (Figure 2.2.3-1). In a typical experiment, D-carboxylate (5 µmol) and pyridinium para-toluene sulfonate (5 µmol) were added to dimethylformamide (250 µL) and vortexed to dissolve the components. Thereafter, N-hydroxysuccinimide (25 µmol) and 1-Ethyl-3-(3-dimethylaminopropyl) carbodiimide (50 µmol) were added to the solution, and the mixture was incubated at 30 °C for 10 min. This activated dye solution was added to 100 nmol of oligonucleotides (dissolved in 250 µL of 0.1 M $NaHCO_3$) and allowed to incubate for 2 h.

The dye-oligonucleotide solution was added to water (15 mL) and filtered (3 kDa Amicon Ultra-15 centrifugal filter units, Millipore Sigma). The filtrate was discarded and the solution remaining in the filter was purified using a NAP™-10 (GE Healthcare) column to remove any unreacted dye. The dye-conjugated oligonucleotide was separated from unreacted oligonucleotides using RP-HPLC with a C18 column and a gradient of 0 to 75% B over 45 min (A=triethylammonium acetate buffer, B=acetonitrile). The product containing fraction was analyzed using MALDI-TOF and quantified using UV-Vis spectroscopy as before.

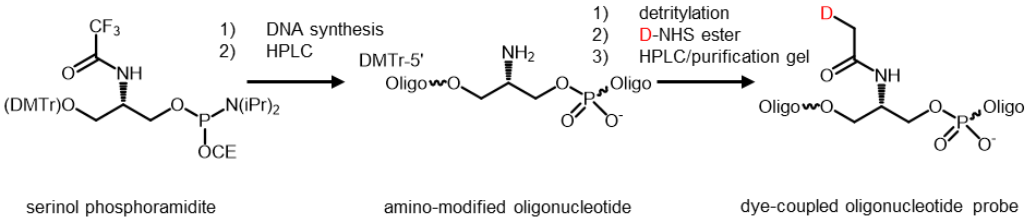

Figure 2.2.3-1. A scheme of the coupling of the serinol phophoramidite to an amino-modified oligonucleotide.

2.2.4. Fluorescence experiments

All measurements were performed in triplicate unless otherwise mentioned.

2.2.4.1. Aptamer-Hg^{2+} binding studies

2.2.4.1.1. Calibration curve

A calibration curve measuring the response of probe HgA1 to target in MOPS buffer (10 mM MOPS, 100 mM $NaNO_3$, pH 7.2) was constructed using a BioTek Synergy H4 Hybrid Reader. 50 nM HgA1 probe was challenged with different amounts (0, 25, 50, 75, 100, 150, 200, 250, and 300 nM) of $HgCl_2$ in different wells of a 96 well plate. The fluorescence reading was taken at 20 ºC.

2.2.4.1.2. Kinetics

50 nM HgA1 probe (with and without 100 nM of HgA1comp) was challenged with 250 nM $HgCl_2$ in MOPS buffer (10 mM MOPS, 100 mM $NaNO_3$, pH 7.2) at 20 ºC. The fluorescence was read using an ISS PC1. Fluorescence of just the probe was read before the addition of Hg^{2+}, and then monitored until the signal saturated after $HgCl_2$ addition.

2.2.4.1.3. Effect of pH on binding

250 nM HgA2 probe was challenged with 75 nM $HgCl_2$ in varying pH Britton-Robinson (BR) buffer (pH 6, 7, 8, 9, 10, and 11) and fluorescence was read using an ISS PC1 at 20 ºC. Fluorescence of the probe was read both before and after the addition of Hg^{2+}.

2.2.4.1.4. Effect of ionic strength

250 nM HgA2 probe was challenged with 75 nM $HgCl_2$ in pH 10 BR buffer at different ionic strengths (0, 100, and 500 mM NaCl) and fluorescence was read using an ISS PC1. Fluorescence of just the probe was read before the addition of $HgCl_2$. Fluorescence readings were taken at 20 ºC.

2.2.4.1.5. Calibration curve

All fluorescence readings were taken on an ISS PC1 at 20 ºC. In a representative experiment, a fluorescence reading was first taken of pH 10 BR buffer. Then, 50 nM HgA2 probe was added and another fluorescence reading was taken. Lastly, x nM $HgCl_2$ (where x is 10, 25, 50, 75, 100, 150, 200, or 250) was added and a fluorescence reading was taken. The cuvette was then washed, and this procedure was repeated for the next value of x. A corresponding spectrum was taken for each of these points by excitation at 560 nm and collection of emission from 590 nm to 750 nm.

2.2.4.1.6. Selectivity of Hg

50 nM HgA2 probe in pH 10 BR buffer was challenged with 500 nM of varying metals (Hg^{2+}, Ag^{+}, Pb^{2+}, NH_4^{+}, K^{+}, Fe^{3+}, Fe^{2+}, Mn^{2+}, Mg^{2+}, Cu^{2+}, Ca^{2+}, Co^{2+}, Ni^{2+}, Zn^{2+}, Cd^{2+}, and Ba^{2+}) and fluorescence was measured using a BioTek Synergy H4 Hybrid Reader. The fluorescence readings were taken at 20 ºC.

2.2.4.1.7. FRET experiments

All experiments were done in pH 10 BR buffer and fluorescence was collected using a BioTek Synergy H4 Hybrid Reader at 20 ºC. Excitation was performed at 480 nm and emission was collected at 520, 580, and 700 nm. 50 nM of HgA2-F, 50 nM of HgA2-T, or 50 nM of HgA2-FT probe were challenged with 500 nM $HgCl_2$.

2.2.4.2. Aptamer-Ag^+ binding studies

2.2.4.2.1. Calibration curve

All fluorescence readings were taken on an ISS PC1 at 20 ºC. In all experiments, 50 nM AgA probe was added to MOPS buffer (10 mM MOPS, 100 mM $NaNO_3$, pH 7.2). In a representative experiment, a fluorescence reading was first taken of the MOPS buffer. Then, 50 nM AgA probe was added and another fluorescence reading was taken. Lastly, x nM Ag^+ (where x is 10, 25, 50, 100, 250, 500, 750, or 1000) was added and a fluorescence reading was taken. The cuvette was then washed, and this procedure was repeated for the next value of x. A corresponding spectrum was taken for each of these points by excitation at 560 nm and collection of emission from 590 nm to 750 nm.

2.2.4.2.2. Selectivity

50 nM AgA probe in MOPS buffer (10 mM MOPS, 100 mM $NaNO_3$, pH 7.2) was challenged with 500 nM of varying metals (Ag^+, Hg^{2+}, Pb^{2+}, NH_4^+, K^+, Fe^{3+}, Fe^{2+}, Mn^{2+}, Mg^{2+}, Cu^{2+}, Ca^{2+}, Co^{2+}, Ni^{2+}, Zn^{2+}, Cd^{2+}, Ba^{2+}) and fluorescence was measured using a BioTek Synergy H4 Hybrid Reader. The fluorescence reading was taken at 20 ºC.

2.2.4.3. Studies with i-motif

All fluorescence readings were taken on an ISS PC1 at 25 ºC. 50 nM I-mD was added to pH x McIlvaine buffer (where x is 5.4, 5.6, 5.8, 6, 6.2, 6.4, 6.6, 6.8, 7.0, or 7.6). In a typical experiment, a fluorescence reading of pH x McIlvaine buffer was first taken. Then, 50 nM I-mD was added and a fluorescence reading was taken. The cuvette was washed, and this procedure was repeated for the remaining values of x. The procedure was repeated in full using the HgA2 probe as a

control. Corresponding spectra were collected for the I-mD probe at pH 5.4, 5.6, 5.8, 6.0, 6.2, 6.6, 7.0, and 7.6 by exciting at 560 nm and collecting emission from 590 nm to 750 nm.

2.2.4.4. Two-aptamer binding to thrombin

2.2.4.4.1. Effect of temperature on binding

All fluorescence readings were taken on an ISS PC1. In a typical experiment, a fluorescence reading was first taken of 1X Tris-buffered saline (20 mM Tris, 0.9% NaCl, pH 7.4). Then, 50 nM THR1D and 50 nM THR2 were added to 1X Tris-buffered saline and a fluorescence reading was taken after 3 min. 100 nM thrombin was then added, and a fluorescence reading was taken after 3 min. In this experiment, this procedure was done at 4 different temperatures (5, 10, 15, and 20 ºC) to determine the temperature of maximum fluorescence enhancement.

2.2.4.4.2. Calibration curve

All fluorescence readings were taken on an ISS PC1 at 10 ºC. In a typical experiment, a fluorescence reading was first taken of 1X Tris-buffered saline (20 mM Tris, 0.9% NaCl, pH 7.4). Then, 50 nM THR1D and 50 nM THR2 were added to 1X Tris-buffered saline and a fluorescence reading was taken after 3 min. x nM thrombin (where x is 2.5, 5, 10, 17.5, 25, 50, or 100) was then added, and a fluorescence reading was taken after 3 min. The cuvette was then washed, and the procedure was repeated for the remaining values of x. A corresponding spectrum was taken for each of these points by excitation at 560 nm and collection of emission from 590 nm to 750 nm.

2.2.4.4.3. Selectivity

All fluorescence readings were taken on an ISS PC1 at 10 ºC. In a typical experiment, a fluorescence reading was first taken of 1X Tris-buffered saline (20 mM Tris, 0.9% NaCl, pH 7.4). Then, 50 nM THR1D and 50 nM THR2 were added to 1X Tris-buffered saline and a fluorescence reading was taken after 3 min. 25 nM protein (where protein is thrombin, proteinase K, immunoglobulin G, hemoglobin, elastase, or single-strand DNA-binding protein) was then added, and a fluorescence reading was taken after 3 min. The cuvette was then washed, and the procedure was repeated for the remaining proteins.

2.2.4.4.4. FRET experiments

All fluorescence readings were taken on an ISS PC1 at 10 ºC in 1X Tris-buffered saline (20 mM Tris, 0.9% NaCl, pH 7.4). 6 different spectra were collected by exciting at 440 nm and collecting emission from 470 nm to 700 nm: (i) 1X Tris-buffered saline alone (ii) 50 nM THR1-F in 1X Tris-buffered saline, (iii) 50 nM probe THR1-F and 50 nM probe THR2-T in 1X Tris-buffered saline (after 3 min incubation), and (iv-vi) 50 nM THR1-F, 50 nM probe THR2-T, and x nM thrombin (where x was 5, 10, or 50) in 1X Tris-buffered saline (after 3 min incubation).

2.2.4.5. Split-aptamer

2.2.4.5.1. Calibration curve

All fluorescence readings were taken on an ISS PC1 at 10 ºC. In a typical experiment, a fluorescence reading was first taken of 1X Tris-buffered saline with 100 mM KCl (20 mM Tris, 0.9% NaCl, 100 mM KCl, pH 7.4). Then, 50 nM Split-THRa and 50 nM Split-THRb were added to the buffer and a fluorescence reading was taken after 3 min. x nM thrombin (where x is 25, 50, 100, 200, or 300 nM) was then added, and a fluorescence reading was taken after 3 min. The

cuvette was then washed, and the procedure was repeated for the remaining values of x. A corresponding spectrum was taken for each of these points by excitation at 560 nm and collection of emission from 590 nm to 750 nm.

2.2.4.5.2. Selectivity

All fluorescence readings were taken on an ISS PC1 at 10 ºC. In a typical experiment, a fluorescence reading was first taken of 1X Tris-buffered saline with 100 mM KCl (20 mM Tris, 0.9% NaCl, 100 mM KCl, pH 7.4). Then, 50 nM Split-THRa and 50 nM Split-THRb were added to buffer and a fluorescence reading was taken after 3 min. 25 nM protein (where protein is thrombin, proteinase K, immunoglobulin G, hemoglobin, elastase, or single-strand DNA-binding protein) was then added, and a fluorescence reading was taken after 3 min. The cuvette was then washed, and the procedure was repeated for the remaining proteins.

2.2.4.6. Intraduplex metallo-base pair

All experiments were done in 1X PBS (11.9 mM Phosphates, 137 mM NaCl, 2.7 mM KCl, pH 7.4) and fluorescence measurements were performed using a BioTek Synergy H4 Hybrid Reader at 20 ºC. In a typical experiment, 50 nM of a dye-labeled sequence was mixed with 50 nM of a complementary unlabeled sequence. The fluorescence was recorded in the absence and presence of $HgCl_2$. This procedure was carried out for all dye labeled sequence/complement combinations (i.e. TDT/TGT, TDT/TGA, TDT/AGA, TDA/TGT, TDA/TGA, TDA/AGA, ADA/TGT, ADA/TGA, and ADA/AGA). As a control, fluorescence readings were taken individually of just 50 nM of the dye-labeled sequences in the absence and presence of 500 nM Hg^{2+}.

2.2.4.7. Detection of thrombin in serum

All fluorescence readings were taken on an ISS PC1 at 20 ºC. One-part whole serum was diluted with 4-parts 1.25X Tris buffered saline (30 mM Tris, 1.13% NaCl, pH 7.4) to yield a 4:1 Tris buffered saline:serum buffer. This buffer was then filtered through a 0.2 um filter. In a typical experiment, 50 nM THR1D and 50 nM THR2 were added to the serum/buffer mixture and a fluorescence reading was taken after 3 min. x nM thrombin (where x is 2.5, 5, 10, or 50) was then added, and a fluorescence reading was taken after 2 min. The cuvette was then washed, and the procedure was repeated for the remaining values of x.

2.2.5. CD studies

Circular dichroism (CD) studies were performed using a Jasco J-1700 circular dichroism spectrometer. All samples were placed in a low-volume quartz cuvette with a 1 cm path length and the spectra were collected between 230-330 nm. HgA1, HgA2, and AgA were dissolved in 1X MOPS (pH 7.2, with 0.1 M $NaNO_3$), BR buffer (pH 10), and 1X MOPS (pH 7.2, 0.1 M $NaNO_3$), respectively, at a concentration of 2.5 µM. The spectra were recorded in the absence or presence of 10 equivalent target (Hg^{2+} or Ag^{+}). In the case of HgA1, additional spectra were recorded in the presence of 5 µM HgA1comp. Similarly, 1.25 µM of the i-motif was dissolved in McIlvaine buffer at different pH (7.0, 6.4, 6.2, 6.0, 5.8, 5.6, 5.4, or 5.2). The CD value at 290 nm, characteristic of i-motif formation, was monitored as a function of pH. In all cases, the spectra were corrected for the contribution from the buffers.

2.2.6. Data analysis

The values and error bars in all in graphs and charts represent the average and standard deviation, respectively, of 3 independent readings. The fluorescence enhancement was calculated according to **Equation 1**:

$$E.F. = \frac{I_f}{I_0} \qquad eq\ (1)$$

I_0 represents the initial fluorescence of the probe alone while I_f represents the fluorescence observed upon addition of analyte.

The calibration curves for HgA1, HgA2, and AgA were fit to a Hill-equation (**Equation 2**) to estimate the dissociation constant (K).

$$y = y_0 + \frac{y_m - y_0}{1 + \left(\frac{K}{x}\right)^n} \qquad eq\ (2)$$

x represents the concentration of the analytes added and y represents the corresponding fluorescence enhancement. y_0 and y_m represent the initial and maximum fluorescence enhancements and n represents the Hill-coefficient. n >1 is observed in all cases and is indicative of cooperative binding, consistent with previous reports.[1] It should be noted that in this study, K is reflective of the concentration of the analyte that causes half of the maximum fluorescence enhancement possible.

For I-mD, the data was fit to a sigmoidal curve (**Equation 3**):

$$y = y_0 + \frac{y_m - y_0}{1 + 10^{(a-x)*b}} \qquad eq\ (3)$$

Similar to **Equation 2**, x represents pH and y represents the corresponding fluorescence enhancement. y_0 and y_m represent the initial and maximum fluorescence enhancements. a represents the pH at which half of the maximum fluorescence enhancement possible is observed. b is a fitting parameter corresponding to the slope of the transition region.

For all analytes, the limit of detection (LOD) was determined by the $3\sigma/m$ method, where σ denotes the standard deviation of the response and m denotes the initial slope of the calibration curve.

2.3. Results

2.3.1. Intramolecular conformational changes

2.3.1.1. Studies with HgA1 and HgA1comp

As noted in section 1.1.1.1, we began by using a DNA sequence (5'-TCATG TTTGT TTG TTG GCC CCC CTT CTT TCT TA-3') that is known to bind to Hg^{2+} via intramolecular conformational changes. We replaced the underlined cytosine at the 4th position from the 3' end with D to obtain a FIT-aptamer (HgA1). By placing D between two thymines, we hypothesized that mercury induced coordination of thymines would result in the forced intercalation of D between the metallo-bps, therefore turning on fluorescence (Figure 2.3.1-1A).

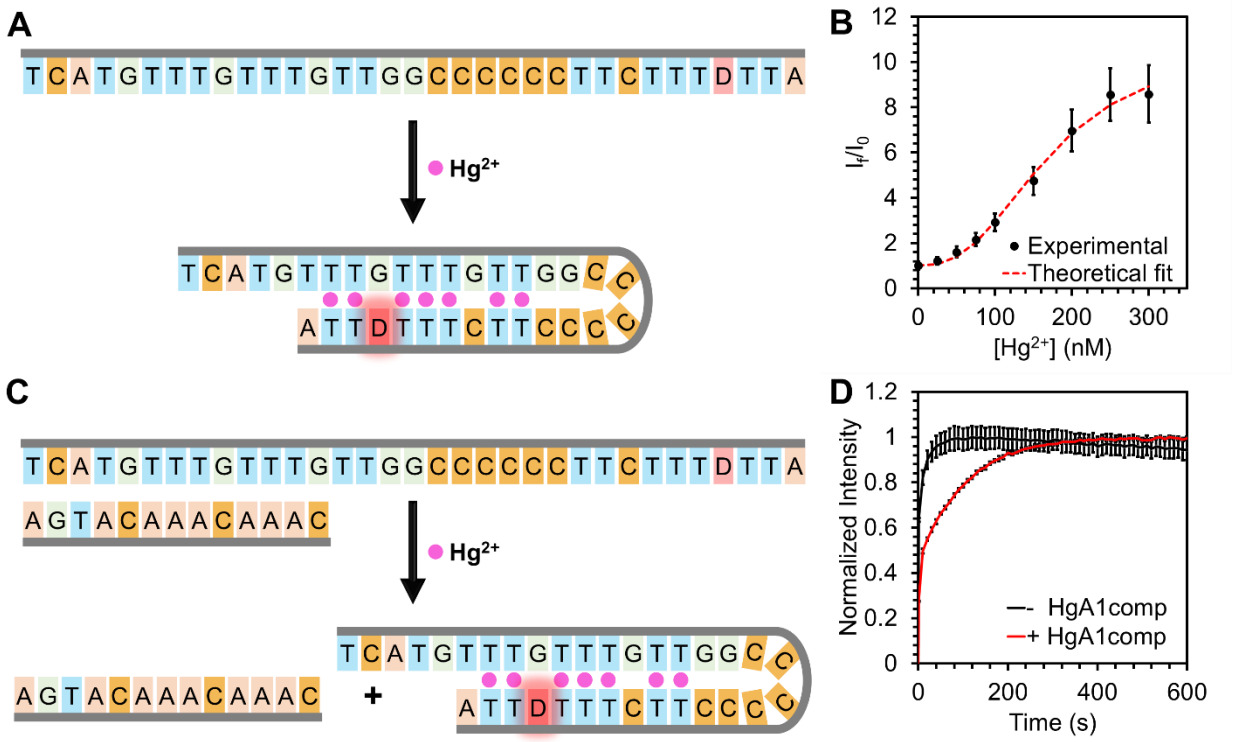

Figure 2.3.1-1. FIT-aptamer for Hg^{2+}. (A) Design scheme using HgA1. (B) Fluorescence enhancement vs [Hg^{2+}]. Red line denotes fit to a Hill-equation. (C) Scheme when a short complementary strand (HgA1comp) is used to partially block the Hg^{2+}-binding sites on HgA1. (D) Time taken for the fluorescence to change after Hg^{2+} addition to HgA1 in the absence and presence of HgA1comp.

To assess this hypothesis, we measured the fluorescence response of 50 nM HgA1 in the absence and presence of varying concentrations of mercury in MOPS buffer (10 mM MOPS, 100 mM $NaNO_3$, pH 7.2). A maximal 8-fold enhancement is observed at 250 nM and a LOD of 23 nM is found (Figure 2.3.1-1B).

In previous literature, HgA1 has been used as part of a structure-switching signaling aptamer for detecting mercury. In the previous system, the 5' end of 5'-TCATG TTTGT TTG TTG GCC CCC CTT CTT TCT TA-3' (i.e. HgA1 without the underlined cytosine being replaced by D) was labeled with a fluorophore and hybridized with a short 3' quencher labeled complement. In the fluorescence "off state" of the probe, the two sequences were hybridized, thus placing the

fluorophore and quencher in close proximity. Mercury induced coordination of thymines in the fluorophore-labeled strand resulted in its folding and subsequent displacement of the quencher-labeled strand, yielding fluorescence turn-on. However, partial blocking of the aptamer site has been shown to slow probe response.

To simulate a structure switching aptamer in order to study how a short complement partially blocking the aptamer impacts probe response time, we synthesized a 13-mer complement to HgA1 (HgA1comp, Figure 2.3.1-1C). We evaluated the change in fluorescence over time after addition of mercury to HgA1 only versus HgA1 partially blocked through prehybridization to HgA1comp. Our results indicate that partial blocking of the aptamer site slows probe response time by ~5-fold (Figure 2.3.1-1D). Because a FIT-based system does not require partial blocking of the aptamer site (in contrast to structure-switching signaling aptamers), its kinetic response is superior to structure-switching signaling systems.

2.3.1.2. Studies with HgA2

2.3.1.2.1. Effect of pH and ionic strength on fluorescence enhancement

We first determined the pH at which addition of Hg^{2+} results in maximum fluorescence enhancement. The fluorescence of 250 nM HgA2 dissolved in a buffered solution (pH 6-11) was monitored in the absence and presence of 75 nM Hg^{2+}. In order to keep the buffer composition the same across the different pH studied, we used BR buffer, considered to be a “universal buffer”, which was titrated to the desired pH using NaOH. Our results show that at pH 10, maximum fluorescence enhancement is observed (Figure 2.3.1-2A). We believe that this is because the pK_a

of thymine is 9.5.[7] Hg^{2+} competes with H^+, and therefore, at pH 10, the binding of Hg^{2+} is favored over H^+.

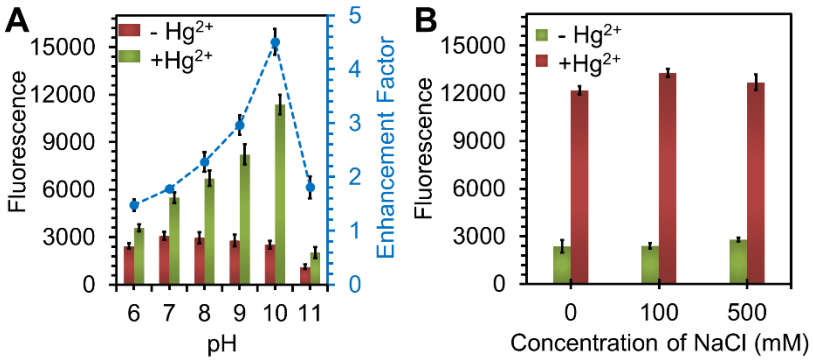

Figure 2.3.1-2. (A) Effect of pH and (B) ionic strength on fluorescence enhancement

We note that in a realistic sample, the ionic strength can vary significantly depending on the source of the sample (e.g. water from lakes, seas, ponds, etc.). Therefore, we next investigated the effect of ionic strength on fluorescence enhancement. As before, 75 nM Hg^{2+} was added to 250 nM HgA2 in BR buffer of pH 10. The ionic strength of the buffer was varied by adding different concentrations of NaCl. Our results (Figure 2.3.1-2B) show that the fluorescence enhancement changes negligibly over an ionic strength of 0-500 mM. Therefore, further experiments (Figure 2.4.1-1) were performed in BR buffer of pH 10 without any added NaCl.

2.3.1.2.2. FRET experiments

Using a T_{14} sequence (as used in HgA2) it is possible to imagine a probe that incorporates a FRET pair at its two ends such that Hg^{2+} binding brings them into close proximity resulting in a FRET signal (Figure 2.3.1-3A). To study how our FIT-aptamer compares with a traditional FRET-based probe, we synthesized a T_{14} strand labeled with fluorescein at the 3' end and TAMRA at the 5' end (HgA2-FT). As controls, two additional sequences were synthesized: HgA2-F which consisted

of a T_{14} sequence with only fluorescein at the 3' end and HgA2-T, comprised of a T_{14} sequence with only TAMRA at the 5' end.

500 nM Hg^{2+} was added to 50 nM of HgA2-FT, HgA2-F, and HgA2-T. The fluorescence of the donor (fluorescein) channel was monitored in the absence and presence of Hg^{2+} (Figure 2.3.1-3B) and used to calculate the FRET efficiency (E) via Equation 4:

$$E = \left(1 - \frac{F_{donor \rightarrow acceptor}}{F_{acceptor}}\right) * 100\% \qquad eq\ (4)$$

$F_{donor \rightarrow acceptor}$ is the fluorescence of the donor in the presence of the acceptor (i.e. donor channel fluorescence for HgA2-FT) and $F_{acceptor}$ is the fluorescence of the acceptor alone (i.e. donor channel fluorescence of HgA2-F). The signal to noise ratio was calculated by taking the ratio of the FRET efficiency in the presence of Hg^{2+} to the FRET efficiency in its absence.

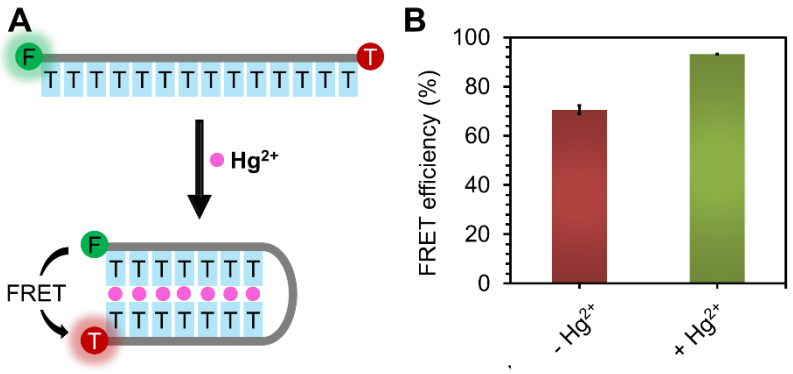

Figure 2.3.1-3. FRET-based Hg^{2+} probe. (A) Design scheme. (B) Donor channel fluorescence in the absence and presence of Hg^{2+}. The donor channel fluorescence of HgA2-T is indistinguishable from that of the buffer and is, therefore, omitted from the graph.

We observed a relatively high FRET efficiency (~71%) even in the absence of Hg^{2+}. This result is unsurprising given the short sequence length as well as the small persistence length of single-stranded DNA which results in the fluorophores being well within the Forster radius. Addition of

250 nM Hg^{2+} further decreases the distance between the fluorophores, increasing the FRET efficiency to ~93%. Therefore, the signal to background ratio is only 1.3, in sharp contrast to the 20-fold fluorescence enhancement observed using the FIT-aptamer (Figure 2.4.1-1B in main text). These results show that FIT-aptamers enable the use of shorter single-stranded probes with superior signal to background ratios compared to FRET.

2.3.1.3. Studies with AgA

To study whether our FIT-based strategy can detect Ag^{+}, we designed a DNA sequence that places D between two cytosines such that the coordination of cytosines by silver results in the forced intercalation of D between the metallo-bps (Figure 2.3.1-4A). The fluorescence of 50 nM AgA was measured in the absence and presence of varying amounts of Ag^{+} in MOPS buffer (10 mM MOPS, 100 mM $NaNO_3$, pH 7.2). We observe nearly a 5-fold maximal fluorescence enhancement in the presence of 500 nM Ag^{+} (Figure 2.3.1-4B) and find a limit of detection of 17 nM, below the level that the EPA deems as unsafe in drinking water. To ensure that AgA is also selective, we challenged 50 nM of the probe with 500 nM of varying metals (Figure 2.3.1-4C). These results indicate selective turn-on in the presence of silver.

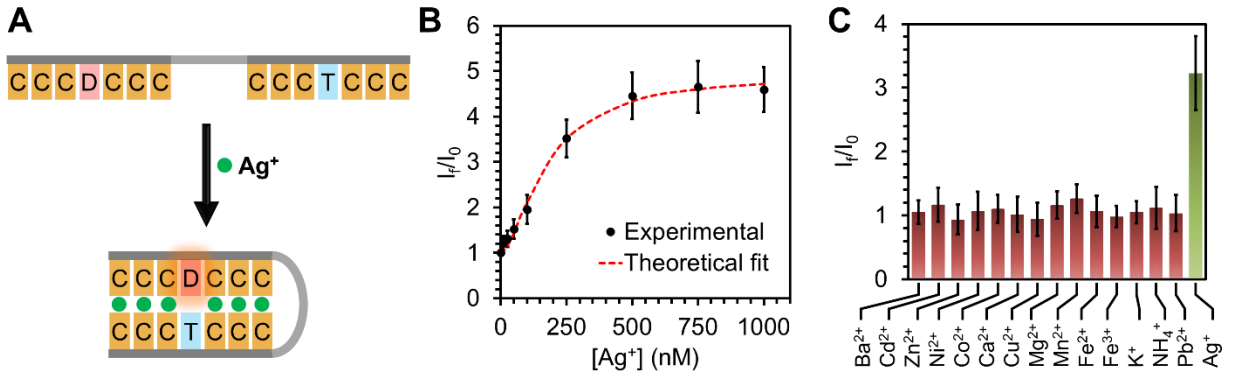

Figure 2.3.1-4. FIT-aptamer for Ag^+ (AgA). (A) Design scheme. Only bases involved in binding to Ag^+ are shown for clarity. (B) Fluorescence enhancement vs [Ag^+]. (C) Selectivity of the probe.

2.3.1.4. CD experiments

CD experiments were performed on 2.5 µM of the probes (HgA1, HgA1+ 2 eq. HgA1comp, HgA2, and AgA) in the presence and absence of 25 µM target (Hg^{2+} or Ag^+). We observe a dramatic change in the CD spectra of the aptamers in the presence of their targets, confirming that the probes undergo conformational changes upon target binding (Figure 2.3.1-5).

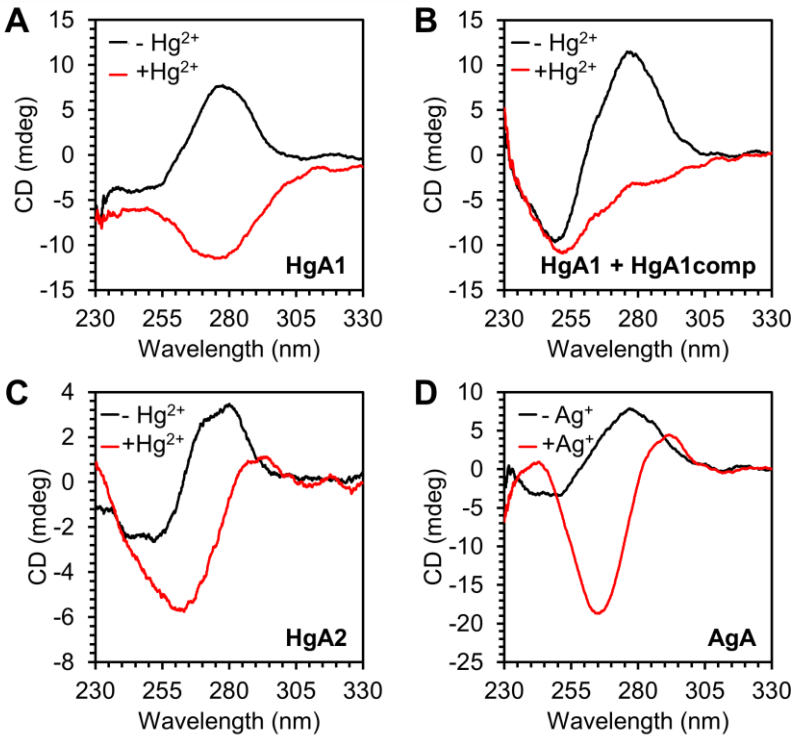

Figure 2.3.1-5. CD spectra of (A) HgA1, (B) HgA1 + HgA1comp, (C) HgA2, and (D) AgA in the presence and absence of Hg^{2+}.

2.3.2. Two epitope binding

2.3.2.1. Effect of temperature on fluorescence enhancement

We sought to expand the scope of detection contexts by studying FIT in the context of two epitope binding. Given that both DNA hybridization and aptamer-target binding are temperature dependent, we began by finding the temperature at which maximum fluorescence enhancement is observed upon addition of thrombin. The fluorescence of 50 nM THR1D and 50 nM THR2 in 1X Tris-buffered saline (20 mM Tris, 0.9% NaCl, pH 7.4) was measured in the absence and presence of 100 nM thrombin at 4 different temperatures (5 ºC, 10 ºC, 15 ºC, or 20 ºC). Maximal fluorescence enhancement was found to occur at 5 ºC and 10 ºC (Figure 2.3.2-1A). Subsequent experiments were performed at 10 ºC to facilitate binding kinetics. Figure 2.4.1-4 and Figure 2.3.2-1B show the fluorescence enhancements obtained upon addition of varying amounts of thrombin to the FIT-aptamers.

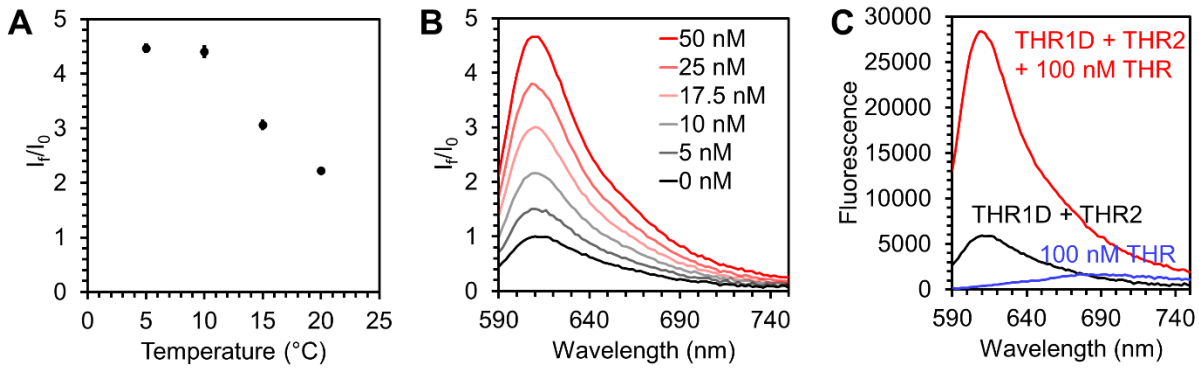

Figure 2.3.2-1. Two epitope aptamer binding to THR. (A) Effect of temperature on fluorescence enhancement. (B) Spectra showing fluorescence enhancement upon thrombin addition to the probes at 10 °C (ex. 560 nm). (C) Fluorescence spectrum of 100 nM thrombin (blue) in comparison to the spectra of the probes in the absence (black) and presence (red) of 100 nM thrombin (ex. 560 nm)

2.3.2.2. Fluorescence of thrombin

To ensure that thrombin itself does not contribute to fluorescence signal at the monitored wavelength (610 nm), the fluorescence of 1X Tris-buffered saline was monitored in the presence of 100 nM thrombin. Our results (Figure 2.3.2-1C) show that the fluorescence of thrombin has a negligible contribution to the fluorescence signal at 610 nm.

2.3.2.3. FRET experiments

To compare our FIT-based detection method with a conventional FRET methodology in the context of two epitope binding to thrombin, sequences THR1-F with a fluorescein at the 3' end and THR2-T with a TAMRA at the 5' end were synthesized. The binding of THR1-F and THR2-T to their respective epitopes allows for the complementary regions of the probes to hybridize, bringing the FRET pair into close proximity (Figure 2.3.2-2A). Excitation and emission spectra of 50 nM THR1-F and 50 nM THR2-T were first acquired to determine optimal excitation/emission wavelengths to use for future experiments (Figure 2.3.2-2B). Based on these results, the fluorescence of 50 nM THR1-F and 50 nM THR2-T was monitored in the absence and presence of different concentrations of thrombin (10 and 50 nM) using an excitation of 480 nm and collecting emission at 520 nm to calculate the FRET efficiencies (Figure 2.3.2-2C-D). Our results show a maximal ~1.4-fold increase in FRET efficiency at 50 nM thrombin. In comparison, a ~5-fold enhancement is observed when we employ our FIT strategy, adding 50 nM thrombin to 50 nM THR1D and 50 nM THR2 (Figure 2.3.2-2E).

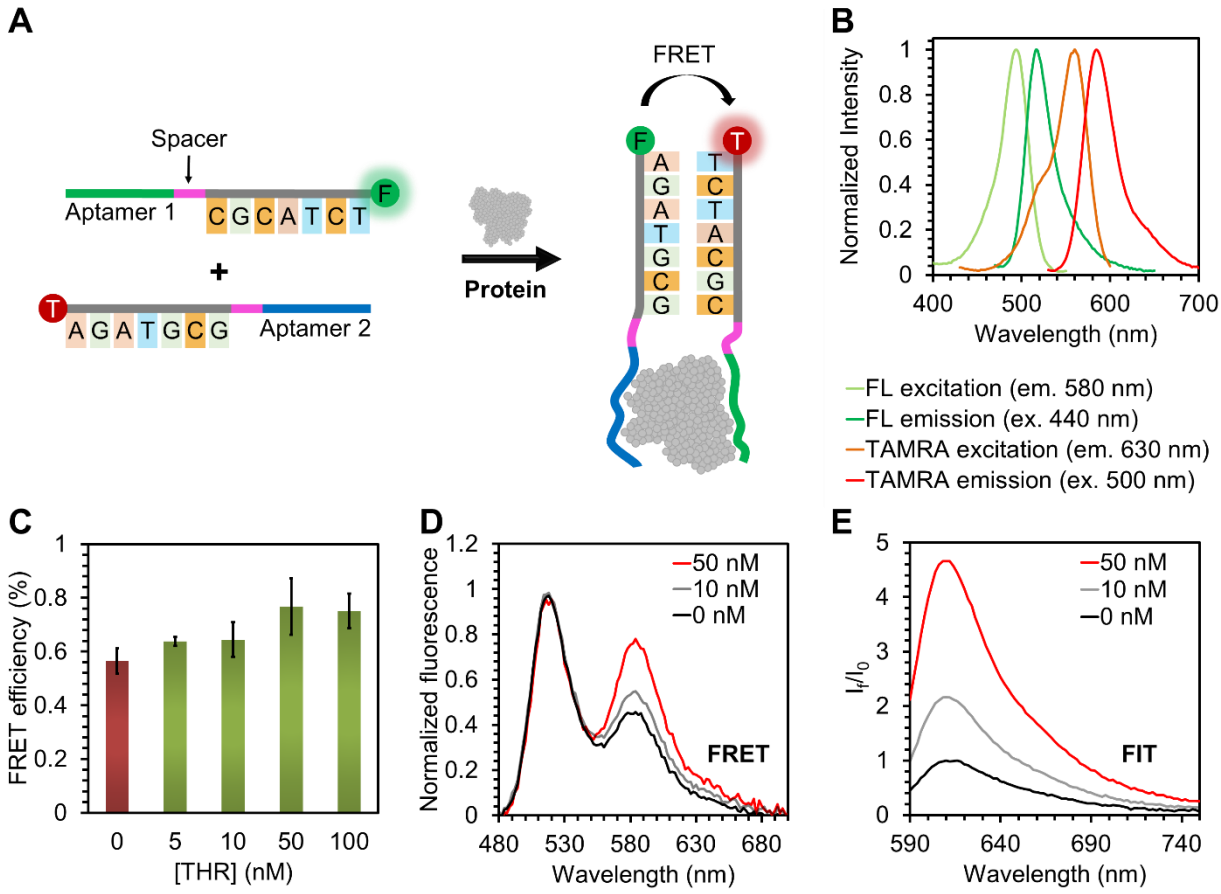

Figure 2.3.2-2. (A) A scheme of two epitope binding aptamers for thrombin that incorporate a FRET pair. (B) Excitation/emission spectra of THR1-F and THR2-T. (C) FRET efficiency of THR1-F and THR2-T as a function of thrombin concentration. (D) Fluorescence spectra of THR1-F and THR2-T for different concentrations of thrombin. (E) Fluorescence spectra of FIT-based strategy for different thrombin concentrations

As a control, strands THR1-F and THR2-T were also synthesized without fluorophores (THR1-c and THR2-c, respectively). The fluorescence of 50 nM of each fluorophore labeled probe was monitored in the absence and presence of 50 nM of its complementary control probe (i.e. THR1-F + THR2-c and THR2-T + THR1-c) to ensure that changes in fluorescence intensity were not due to duplexing alone.

2.3.2.4. Detection of thrombin in human serum

To simulate the detection of an analyte in a realistic scenario, we sought to detect thrombin in human serum. The fluorescence of 50 nM THR1D and 50 nM THR2 was measured in the absence and presence of varying amounts of thrombin in a buffered solution consisting of 4 parts 1.25X Tris-buffered saline and one-part whole serum. The fluorescence enhancement saturates at ~2-fold (Figure 2.3.2-3) and a limit of detection of 1.4 nM is found. Because the serum sample was diluted 5-fold, the limit of detection in whole serum is 6.8 nM, still below the 10 nM critical thrombin concentration in serum associated with blood clot formation.

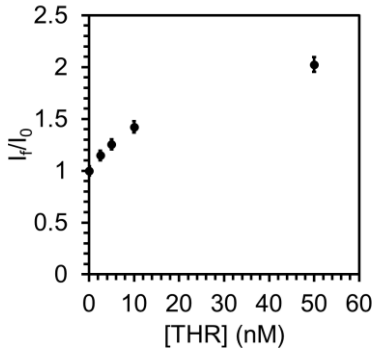

Figure 2.3.2-3. The fluorescence response of 50 nM THR1D and 50 nM THR2 to varying amounts of thrombin in a buffer/serum mixture.

2.3.3. Split-aptamer

2.3.3.1. Calibration curve

To study the response of the split aptamer system (described in section 1.1.1.3 and shown in Figure 2.3.3-1A) to thrombin, a calibration curve was constructed in 1X Tris-buffered saline. The fluorescence of 50 nM Split-THRa and 50 nM Split-THRb was measured in the presence and absence of varying amounts of thrombin. Our results show a maximal ~3 fold fluorescence enhancement at 200 nM thrombin and an LOD of 15 nM (Figure 2.3.3-1B).

2.3.3.2. Selectivity

The fluorescence of 50 nM Split-THRa and 50 nM Split-THRb in 1X Tris-buffered saline was measured in the absence and presence of 25 nM varying proteins [Proteinase K (PK), Immunoglobulin G (IgG), Hemoglobin (Hg), Elastase (Elt), or Single-strand DNA-binding protein (SSDBP), or Thrombin (THR)] to confirm that probe turn-on is selective. Probe turn-on is not observed in the presence of these other proteins (Figure 2.3.3-1C).

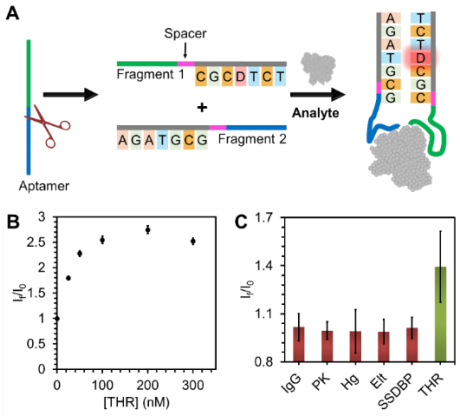

Figure 2.3.3-1. FIT-based split-aptamer. (A) Design scheme. (B) The fluorescence response of 50 nM Split-THRa and 50 nM Split-THRb to increasing concentrations of thrombin. (C) Selectivity of the probe.

2.3.4. Intraduplex metallo-base pairs

We next studied FIT in the context of local conformational changes. The strands 5'-TDT-3', 5'-TDA-3', and 5'-ADA-3' were added to complementary sequences 3'-AGA-5', 3'-TGA-5', and 3'-TGT-5' in all combinations. Fluorescence readings were taken in the absence and presence of 500 nM Hg^{2+}. Control experiments were also performed with the dye-labeled strands alone to ensure addition of Hg^{2+} itself did not increase fluorescence signal. Table 2.2.1-2 qualitatively summarizes the results obtained with explanations and Figure 2.3.4-1 shows the quantitative fluorescence enhancements (I_f/I_0, where I_0 refers to the initial fluorescence of each dye-labeled single strand). In Figure 2.4.1-2, I_0 refers to the initial fluorescence of a duplexed strand in the absence of Hg^{2+}.

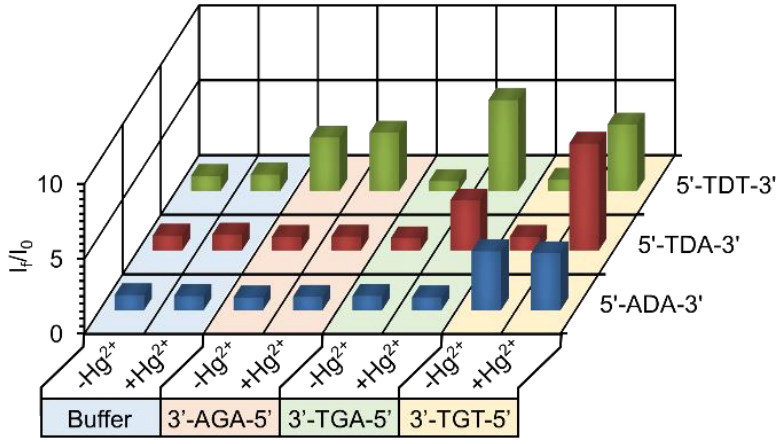

Figure 2.3.4-1. Fluorescence enhancement upon T-Hg^{2+}-T base pairing within a duplexed strand.

2.4. Discussion

2.4.1. Validating the FIT-based strategy

To evaluate the feasibility of realizing FIT-aptamers, we first chose a previously reported DNA sequence (Table 2.2.1-1), known to recognize Hg^{2+}, as an example of an aptamer that binds to its target through an intramolecular conformational change.[348] We used the aptamer sequence as a single-stranded probe and the FIT-dye quinoline blue (D) as a nucleobase surrogate. We considered that this aptamer adopts a hairpin-like structure in the presence of Hg^{2+} due to the Hg^{2+}-mediated bridging of thymine (T) bases (T-Hg^{2+}-T).[348,350] Therefore, we hypothesized that if a base sandwiched between two Ts in the aptamer sequence was replaced with D, forced intercalation of D between the metallo-base pairs (bps) would turn on its fluorescence. The FIT-aptamer (HgA1) was synthesized by substituting the fourth base from the 3' end of the sequence with an amino-modifier to which D-carboxylate was conjugated via carbodiimide crosslinking chemistry (Figure 2.2.3-1). HgA1 was then titrated with Hg^{2+} in a buffered solution. The fluorescence enhancement factor (I_f/I_0), defined as the ratio of the fluorescence in the presence of target (signal, I_f) to the initial fluorescence (background, I_0), increases with increasing concentrations of Hg^{2+} and reaches a maximum value of ~8. Significantly, when a short complementary sequence is used to partially block the aptamer akin to a structure-switching signaling aptamer,[348] the response time of the probe is 5 times slower, showing that single-stranded probes such as FIT-aptamers enable faster target detection.

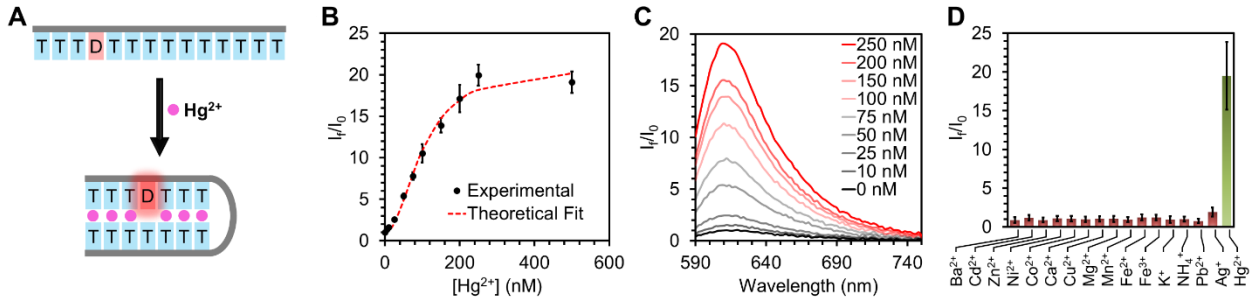

Figure 2.4.1-1. FIT-aptamer for Hg^{2+} (HgA2). A. Design scheme. B. Fluorescence enhancement (I_f/I_0) vs [Hg^{2+}] added. Black spheres denote experimentally observed values. Red dashed line indicates theoretical fit to a Hill-equation. C. Fluorescence spectra (ex. 560 nm) with increasing [Hg^{2+}]. D. Selectivity of the probe.

Based on these results, we speculated that this system would enable one to create a fast, highly sensitive, and extremely simple Hg^{2+} probe. Therefore, we proceeded to use a T_{14} sequence in which the fourth base from the 5' end was replaced with D (HgA2, Figure 2.4.1-1A). Remarkably, addition of aqueous Hg^{2+} (250 nM) to HgA2 results in a ~20-fold fluorescence enhancement (Figure 2.4.1-1B, C). In sharp contrast, a traditional FRET-based approach provides a signal-to-background ratio of 1.3 (Figure 2.3.1-3). Based on the calibration curve of HgA2, the limit of detection (LOD) of the FIT-aptamer assay is 1.8 nM, well below the 10 nM toxicity limit for Hg^{2+} in drinking water.[351] Importantly, challenging the probe with a panel of 15 different metal ions (Ba^{2+}, Cd^{2+}, Zn^{2+}, Ni^{2+}, Co^{2+}, Ca^{2+}, Cu^{2+}, Mg^{2+}, Mn^{2+}, Fe^{2+}, Fe^{3+}, K^{+}, Pb^{2+}, Ag^{+}, and Hg^{2+}) shows that HgA2 is highly selective for Hg^{2+} (Figure 2.4.1-1D). A small turn on (1.9±0.6) is detectable only in the case of Ag^{+} addition. Using a similar strategy, Ag^{+} ions can be detected via the formation of C-Ag^{+}-C bps using a cytosine-rich strand (Figure 2.3.1-4). To the best of our knowledge, this is the first use of forced intercalation to measure the formation of metal-mediated non-traditional bps.

While the above examples show that FIT-aptamers can report metallo-bp formation through global conformational changes, we hypothesized that the sensitivity of FIT-probes to single bp mismatches[124] can be utilized to sense metallo-bp formation in a preformed DNA duplex. Current methods for finding metallo-bps rely primarily on single crystal X-ray diffraction studies,[352] which necessitate challenging DNA crystallization, or NMR,[350] which requires a sufficiently large number of metal binding events to distinguish resonances of metal-bound nucleobases from the inherent signal of other bases in a strand.

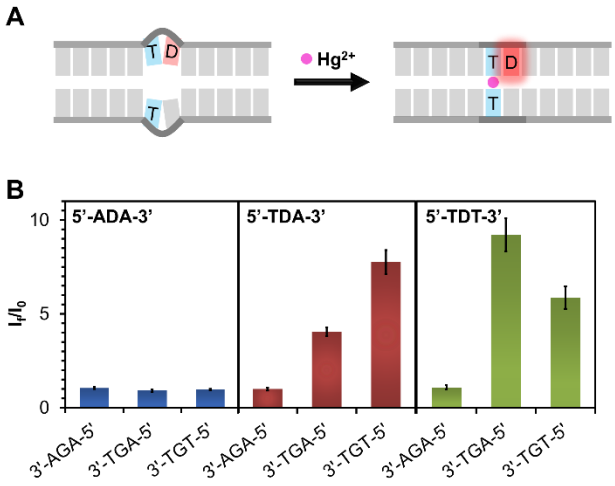

Figure 2.4.1-2. Detecting metallo-bps within a duplexed strand. A. Design scheme with T-Hg^{2+}-T as an example. B. Fluorescence enhancement when Hg^{2+} is added to DNA duplexes with 0, 1, and 2 T-T mismatches adjacent to the dye.

To assess whether FIT probes can be used as a simple alternative to allow rapid detection in solution, we synthesized six different 21-mer DNA sequences: three oligonucleotides containing TDT, TDA, and ADA regions, respectively, and their complements. The sequences containing D were added to the normal sequences in all combinations to form duplexes with zero T-T, one T-T, or two T-T mismatches directly adjacent to D. We observed that the addition of Hg^{2+} increased the

fluorescence only in the duplexes where T-Hg^{2+}-T bases could be formed adjacent to the dye, showing that D can report local conformational changes and, moreover, that this information can be used to determine the identity of the metallo-bp formed (Figure 2.4.1-2, Figure 2.3.4-1). This ability of "local probing" is not possible with FRET or fluorophore/quencher-based techniques and can be potentially useful for screening new metallo-bps, studying local structural changes in DNA and RNA during various biological processes,[353–355] or identifying drug binding sites on DNA and RNA.[356–359]

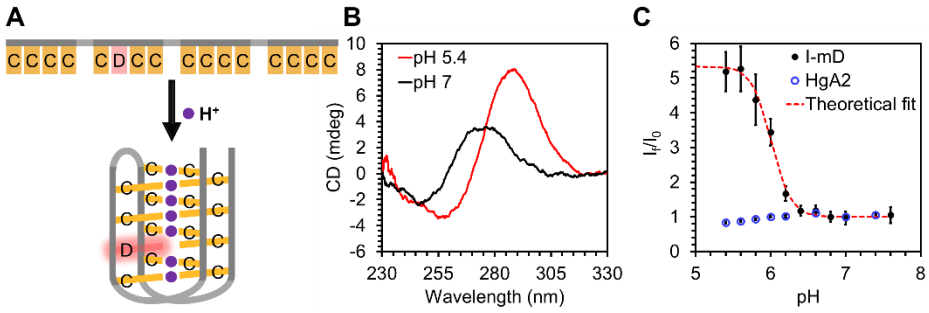

Figure 2.4.1-3. FIT-aptamer (I-mD) for pH sensing. A. Design scheme. Only bases involved in i-motif formation are shown for clarity. B. Circular dichroism spectra showing i-motif formation at lower pH. C. Fluorescence enhancement (I_f/I_0) vs pH. Red dashed line indicates theoretical fit to a sigmoidal curve.

We next investigated the possibility of designing FIT-aptamers that undergo more complex structural transitions upon target binding by studying the i-motif as an example. The i-motif is a cytosine-rich "proton aptamer" that adopts a quadruplex structure at acidic pH due to the formation of C-H^+-C bonds.[360,361] We replaced the ninth base of the i-motif with D (I-mD, Figure 2.4.1-3A). Circular dichroism spectra confirm that the presence of D does not impede i-motif formation (Figure 2.4.1-3B). Lowering the pH from 7.0 to 5.6 results in a 5-fold fluorescence enhancement (Figure 2.4.1-3C). Importantly, the fluorescence of HgA2 does not significantly change within this pH range, confirming that the enhancement is due to the forced intercalation of D in the i-motif

structure as opposed to the dye's inherent pH-sensitivity. Taken together, these results suggest that a FIT-based strategy could be adapted to detect various analytes that cause conformational changes in aptamers.

As a measure of versatility, we further explored how FIT-aptamers can be designed in other detection contexts. We considered that sandwich assays for detecting proteins based on antibodies are popular due to increased specificity.[362–364] Therefore, we examined systems that require the binding of two aptamers to generate a signal output.[365] As a model system, we used thrombin, since there are known aptamers that bind to two distinct sites.[366,367] Applying the FIT strategy, the two aptamer sequences were appended with spacer groups and short complementary sequences (Figure 2.4.1-4A), one of which (THR1D) was modified with D. The independent binding of these two aptamers (THR1D and THR2) to thrombin brings the complementary sequences into proximity, increasing their local concentration and allowing them to hybridize.

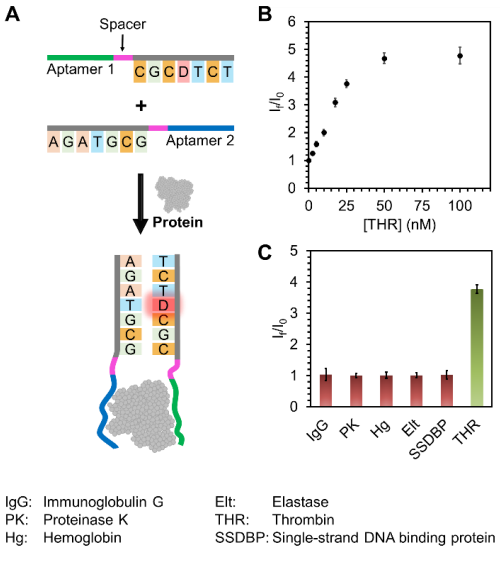

Figure 2.4.1-4. FIT-aptamers for two epitope binding. A. Design scheme. B. Fluorescence enhancement vs concentration of thrombin denoted as [THR]. C. Selectivity of the probe.

In buffer, we observed a 5-fold fluorescence enhancement upon target binding (Figure 2.4.1-4B). Negative controls involving proteins other than thrombin generated negligible signal (Figure 2.4.1-4C). The LOD was 1.4 nM. In comparison, a FRET-based method only yields a 1.4-fold enhancement (Figure 2.3.2-2). For FIT-aptamers to be useful, it is important to be able to use them in complex media at disease relevant target concentrations. As a clinically applicable model, we tested the potential for detecting thrombin in human serum using THR1D and THR2. Our results (Figure 2.3.2-3) show a limit of detection of 6.8 nM in whole serum. This value is below the 10 nM thrombin concentration in serum that is associated with blood clot formation,[368,369] demonstrating assay utility in medical diagnostic relevant media.

As a structurally similar but distinct detection mode, we also investigated how split-aptamers can be interfaced with a FIT-based strategy. In this case, the aptamer sequence is divided into two fragments such that the presence of the target templates their re-association.[299] Utilizing thrombin, we validated that FIT-based split-aptamers can be realized (Figure 2.3.3-1). This observation suggests that the FIT-aptamer approach can be used for detecting analytes that do not have well-characterized aptamer binding sites or do not support two epitope binding.

2.5. Conclusion

In summary, I have described a new class of signaling aptamers based on forced intercalation. I have shown that highly sensitive FIT-aptamers can be designed for the most common aptamer-target binding modes, exemplifying that FIT-aptamers constitute a new paradigm for simple, versatile, and reliable detection. FIT-aptamers provide key advantages over state-of-the-art fluorescence-based signaling aptamers. For example, they are kinetically superior to strategies that require partial blocking of the aptamer site and show higher signal-to-background ratios than

traditional FRET-based techniques. Furthermore, a FIT-based strategy enables the probing of local target-induced conformational changes, a powerful capability that is not possible with conventional fluorophore/quencher or FRET-based methodologies. The ability to detect thrombin in human serum bodes well for extending the FIT-aptamer strategy to a wide variety of biological detection scenarios.

CHAPTER THREE

3. Programming Fluorogenic DNA Probes for Rapid Detection of Steroids

3.1. Introduction

Fluorogenic probes that selectively turn on in the presence of their target analytes have revolutionized chemical and biological analysis.[18,44,95,122,125,346,370–373] As discussed in Chapter 2, probes based on aptamers, nucleic acid sequences capable of binding to targets of interest, have recently emerged as effective tools for probing complex media and cells.[25,340,342,374] By coupling aptamer-target binding to a fluorescence readout, several different classes of analytes ranging from simple ions to complex proteins can be detected and quantified.[122,375,376] Aptamers are attractive as they can be rapidly synthesized, exhibit high stability, are amenable to various chemical modifications, and can be used as recognition moieties in strategies that involve simple sample processing and the use of widely available instrumentation.[377] However, conventional aptamer-based strategies suffer from limitations such as kinetically slow responses, the presence of false-positive signals, and poor aptamer performance in complex milieu.[375]

Chapter 2 introduced the concept of forced intercalation (FIT)-aptamers by leveraging structures that switch from an unfolded to a folded state or by designing structures with appended bases such that hybridization is deliberately induced upon target binding.[378,379] FIT-aptamers contain a visco-sensitive dye as a base surrogate. Target binding leads to structural changes in the aptamer resulting in the forced intercalation of the dye between nucleic acid base pairs, turning on the dye's fluorescence. Chapter 2 showed that this enables target analyte detection with superior fluorescence enhancement and kinetics compared to state-of-the-art strategies.[378] In this chapter, steroid-binding aptamers are used as examples to show that a FIT-strategy allows one to transduce subtle binding induced structural changes to significant fluorescence turn-on. Such local structural changes are difficult to monitor by conventional techniques that rely on strand displacement.[95,376]

Importantly, the FIT strategy enabled us to develop the first fluorogenic aptamer capable of detecting dehydroepiandrosterone sulfate (DHEAS), a circulating adrenal androgen, in human serum and clinical samples.

We focus on steroids as these biomolecules play a central role in various physiological processes, including controlling gene transcription, regulating metabolism, and attenuating inflammatory response.[380,381] Therefore, their dysregulation can lead to many clinical indications. For example, elevated levels of DHEAS are found in patients with adrenal tumors, congenital adrenal hyperplasia, and polycystic ovary syndrome.[382] Steroids are typically detected using gas or liquid chromatography in tandem with mass spectrometry, immunoassays (e.g. Abbott Architect DHEAS test), or radioimmunoassays.[382] However, these methods require bulky, expensive, or specialized equipment, entail long turnaround times, necessitate highly trained personnel for sample preparation, instrument operation, and data analysis, or involve multistep reaction procedures.[383–387] Consequently, rapid, sensitive, and simple fluorescence tests for studying steroids in physiological media remain highly sought after.

3.2. Materials and Methods

3.2.1. Oligonucleotide design, synthesis, purification, and characterization

3.2.1.1. Design of FIT-aptamers based on computational modeling

While designing FIT-aptamers, we hypothesized that if the dye is placed in single stranded and double-stranded regions away from the binding site, DHEAS binding will not result in fluorescence enhancement. On the other hand, by placing the dye in double stranded regions close to the binding site, we hypothesized that fluorescence enhancement could be observed. We

reasoned that the dye would act as a base mismatch that destabilizes or partially destabilizes the double stranded regions in the absence of DHEAS and these regions would refold upon DHEAS binding. Finally, placing the dye directly in the binding pocket could either lead to fluorescence enhancement due to rigidification of the dye upon DHEAS binding or result in significant loss of binding affinity because of the base's importance to target recognition.

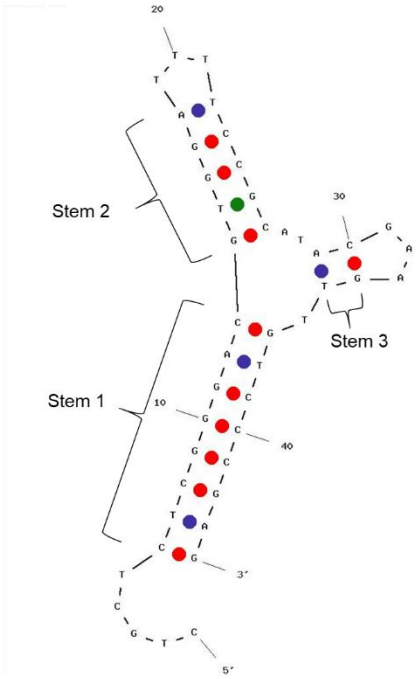

Figure 3.2.1-1. Mfold predicted structure of the native aptamer. Simulations performed using a solution condition of 0.1 μM DNA, 1 M NaCl, and 10 mM $MgCl_2$.

To determine which double-stranded regions could be classified as "close" or "far" from the binding site, we focused on the longest double-stranded region (Stem 1) and used Mfold to computationally model the expected DNA structure (Figure 3.2.1-1-Figure 3.2.1-3). The presence of the dye was simulated using a base mismatch. We note that when the base mismatch is placed within the first two bases from the binding site, the portion of the stem away from the binding site

is completely hybridized whereas that near the binding site is frayed. Therefore, it is reasonable to hypothesize that upon DHEAS binding, hybridization can be recovered. However, when the base mismatch is placed beyond the second base from the binding site, the stem is hybridized on both sides of the mismatch. Consequently, DHEAS binding would not result in additional base pairing. To test our hypothesis experimentally, we synthesized 20 different FIT-aptamer variants with single base mutations from the original aptamer as shown in Table 3.2.1-1 and Figure 3.2.1-4. The colors green, yellow, blue, and red correspond to (i) double-stranded regions close to the binding site, (ii) double stranded regions away from the binding site, (iii) bases in the binding site, and (iv) single stranded regions away from the binding site, respectively.

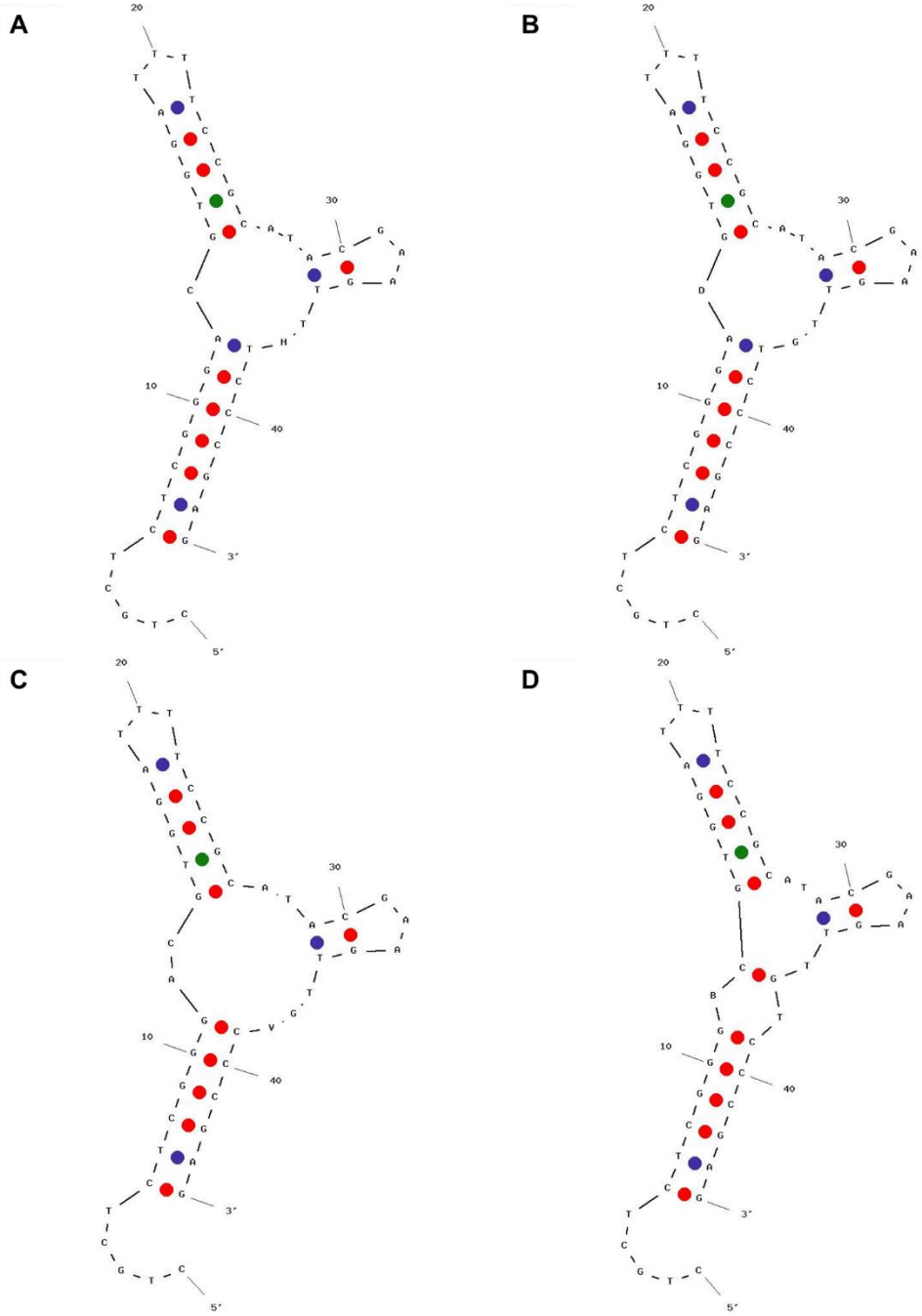

Figure 3.2.1-2. Mfold predicted structure of the aptamer with base mismatches at different locations along stem 1 within the first two bases from the binding site. Simulations performed using a solution condition of 0.1 μM DNA, 1 M NaCl, and 10 mM $MgCl_2$.

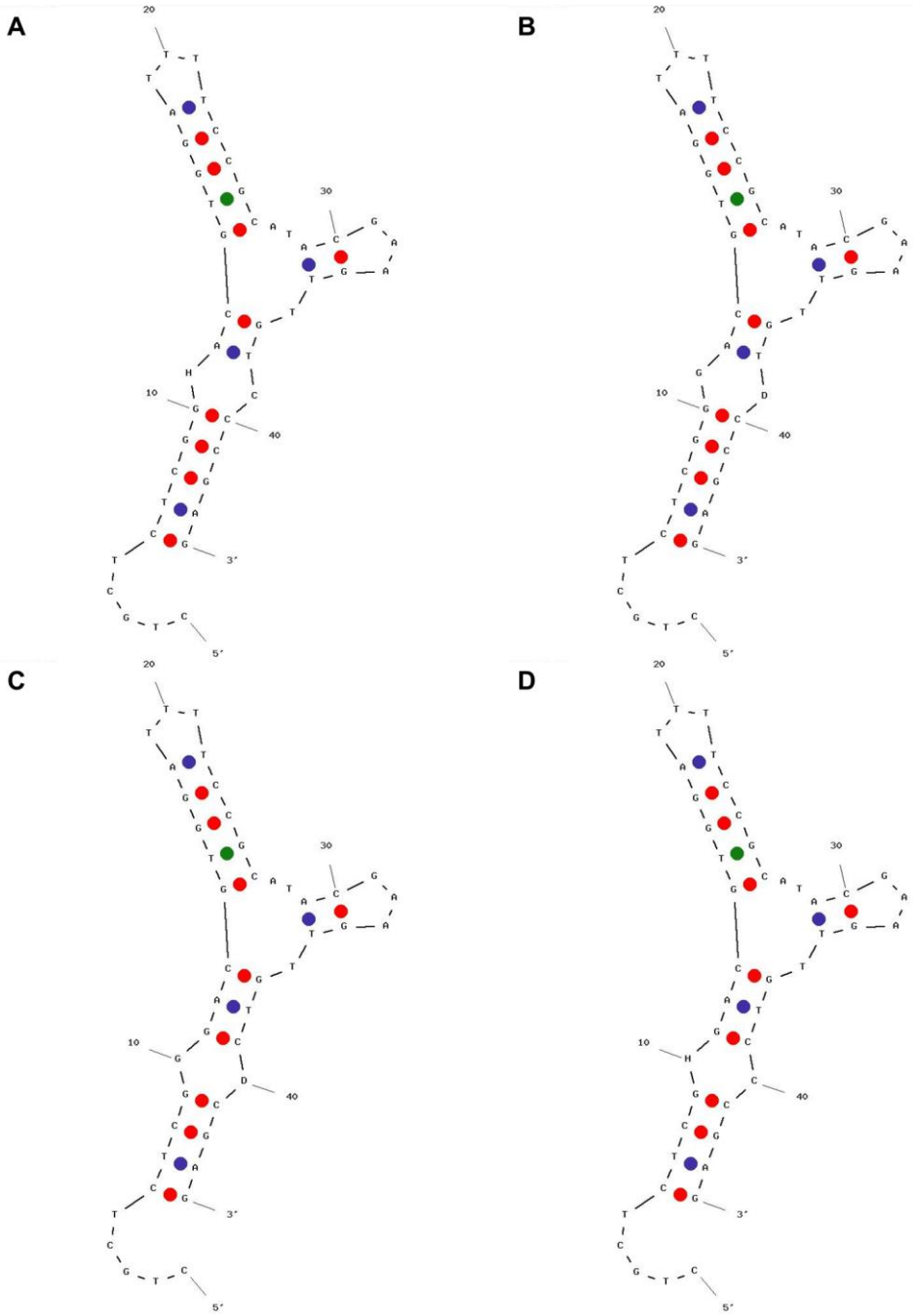

Figure 3.2.1-3. Mfold predicted structure of the aptamer with base mismatches at different locations along stem 1 beyond the first two bases from the binding site. Simulations performed using a solution condition of 0.1 μM DNA, 1 M NaCl, and 10 mM $MgCl_2$.

Table 3.2.1-1. Oligonucleotide sequences used in this study (DOG is deoxycorticosterone-21 glucoside, DCA is deoxycholic acid). D denotes the location of the forced intercalation dye thiazole orange (TO) in the sequence.

Identifier	Sequence (from 5′ end to 3′ end)
DHEAS	CTG CTC TCG GGA CGT GGA TTT TCC GCA TAC GAA GTT GTC CCG AG
a	CTG CTC TCG GGA CGD GGA TTT TCC GCA TAC GAA GTT GTC CCG AG
b	CTG CTC TCG GGA CGT GGA TTT TCC GCA TAC GAA GTT GDC CCG AG
c	CTG CTC TCG GDA CGT GGA TTT TCC GCA TAC GAA GTT GTC CCG AG
d	CTG CTC TCG GGA CGT GGD TTT TCC GCA TAC GAA GTT GTC CCG AG
e	CTG CTC TCG GGA CGT GGA TTT TCC GCA TAC GAA GTT GTC CCG DG
f	CTG CTC TCG GGA CGT GGA TTT TCC DCA TAC GAA GTT GTC CCG AG
g	CTG CTC TCG GGD CGT GGA TTT TCC GCA TAC GAA GTT GTC CCG AG
h	CTG CTC TCG GGA CGT DGA TTT TCC GCA TAC GAA GTT GTC CCG AG
i	CTG CTC TCG GGA CGT GDA TTT TCC GCA TAC GAA GTT GTC CCG AG
j	CTG CTC TCG GGA CGT GGA TTT TCC GCA TAC GAA GTT GTC CDG AG
k	CTG CTC TCG GGA CGT GGA TTT TCC GCA TAC GAA GTT DTC CCG AG
l	CTG CTC TCG GGA CDT GGA TTT TCC GCA TAC GAA GTT GTC CCG AG
m	CTG CTC TCG GGA CGT GGA TTT TCC GCD TAC GAA GTT GTC CCG AG
n	CTG CTC TCG GGA CGT GGA TTT TCC GCA TAC GAA GTD GTC CCG AG
o	CTG CTC TCG GGA CGT GGA TTT TCC GCA TDC GAA GTT GTC CCG AG
p	CTG CTC TCG GGA DGT GGA TTT TCC GCA TAC GAA GTT GTC CCG AG
q	CTG CTC TCG GGA CGT GGA TTT TCC GDA TAC GAA GTT GTC CCG AG
r	CTG CTC TCG GGA CGT GGA TTT TCC GCA TAC GAA GDT GTC CCG AG
s	CTG CTC TCG GGA CGT GGA TTT TCC GCA DAC GAA GTT GTC CCG AG
t	CTG DTC TCG GGA CGT GGA TTT TCC GCA TAC GAA GTT GTC CCG AG
DOG	CTG CTC TCG GGA CGT GGA TTT TCC ACA AAC CAG AAT GGT GTC CCG AGA
u	CTG CTC TCG GGA CGT GGA TTT TCC DCA AAC CAG AAT GGT GTC CCG AGA
v	CTG CTC TCG GGA CGT GGA TTT TCC ACA DAC CAG AAT GGT GTC CCG AGA
DCA	CTC TCT CGG GAC GCT GGG TTT TCC CAG GAC GAA GTC CGT CCC GA
w	CTC TCT CGG GAC GCD GGG TTT TCC CAG GAC GAA GTC CGT CCC GA

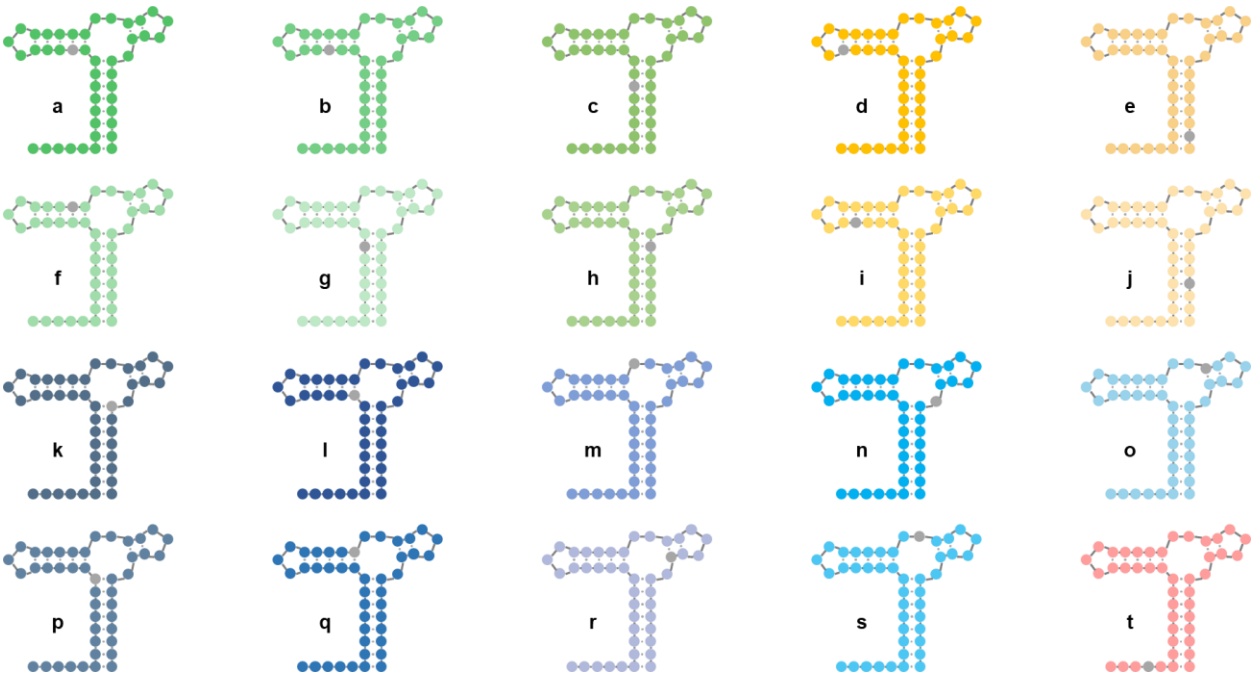

Figure 3.2.1-4. Cartoon structures of the 20 different FIT-aptamers (**a**-**t**) synthesized with single base mutations. The base replaced with thiazole orange is depicted in gray.

3.2.1.2. Synthesis, purification, and characterization

Materials for solid-phase DNA synthesis were acquired from Glen Research. DNA was synthesized on a MerMade12 (MM12, BioAutomation Inc., Plano, Texas, USA) synthesizer. After synthesis, DNA was cleaved off controlled pore glass beads by soaking them in 30% ammonium hydroxide solution for 16 h. After evaporating the ammonium hydroxide using an Organomation® Multivap® Nitrogen Evaporator, samples were run on a reverse phase high-performance liquid chromatography column (C18 column, Varian ProStar 210, Agilent Technologies Inc., Palo Alto, CA, USA) using a 0-75% ramp of acetonitrile over 45 min (A= triethylammonium acetate buffer). After lyophilizing the product fractions, the 4,4'-dimethoxytrityl protecting group was cleaved by adding 20% acetic acid and incubating for 1 h at room temperature. The 4,4'-dimethoxytrityl group was then removed using ethyl acetate extraction. After lyophilizing the acidic solution, samples were dissolved in water and characterized using Matrix-assisted laser desorption ionization time-of-flight mass spectrometry (MALDI-TOF MS) and quantified using UV-vis spectroscopy.

3.2.2. Coupling of TO to oligonucleotide probes

Carboxymethylated thiazole orange (TO) was synthesized and conjugated to DNA sequences using a previously reported protocol.

3.2.3. Fluorescence experiments

All experiments were performed in triplicate unless otherwise stated.

3.2.3.1. DNA library screening to determine impact of sodium ion and magnesium ion concentration on fluorescence enhancement

Each of the 20 probes in the DNA aptamer library was tested for its fluorescence enhancement in the presence of DHEAS (Cayman Chemical Item No. 15873) across different sodium ion and magnesium ion concentrations. For a given sequence, 100 nM probe was added to a well with 20 mM pH 8.0 Tris buffer that contained different amounts of sodium ions (0, 0.06, 0.12, 0.25, 0.50, or 1.0 M) and magnesium ions (0, 0.6, 1.2, 2.5, 5.0, or 10 mM) such that each possible combination of salt concentrations was tested (36 different combinations). A fluorescence reading of the probe was taken on a BioTek Cytation 5 fluorescence plate reader (excitation 485 nm, emission 528 nm). 100 µM DHEAS was then added to each of the wells, and another fluorescence reading was taken to determine the fluorescence enhancement (defined as the fluorescence of the probe in the presence of DHEAS divided by the fluorescence of the probe in the absence of DHEAS).

3.2.3.2. Calibration curve of best responding aptamers to DHEAS titration in buffer

The three probes (probes **o**, **s**, and **f**) with superior recognition properties and fluorescence turn-on in the presence of DHEAS from experiments were used to construct calibration curves. Different concentrations of DHEAS (in 20 mM pH 8.0 Tris buffer, 1 M NaCl, and 10 mM $MgCl_2$) were added to the wells of a 96 well plate, wherein the concentration of DHEAS was halved in each well through serial dilutions to give wells containing 200, 100, 50, 25, 12.5, 6.25, and 3.125 µM DHEAS. A separate set of wells contained 0 µM DHEAS. All wells contained 100 nM probe. A fluorescence reading was taken on a BioTek Cytation 5 fluorescence plate reader (excitation 485 nm, emission 528 nm).

3.2.3.3. Calibration curves of FIT-aptamers for deoxycorticosterone-21 glucoside and deoxycholic acid

Probes that were computationally designed to turn-on in the presence of deoxycorticosterone-21 glucoside and deoxycholic acid were used to construct calibration curves. Different concentrations of these steroids (in 20 mM pH 8.0 Tris buffer, 1 M NaCl, and 10 mM $MgCl_2$) were added to the wells of a 96 well plate, wherein the concentration of the steroids was halved in each well through serial dilutions to give wells containing 200, 100, 50, 25, 12.5, 6.25, and 3.125 μM deoxycorticosterone-21 glucoside or 800, 400, 200, 100, 50, and 25 μM deoxycholic acid. A separate set of wells contained 0 μM steroid. All wells contained 200 nM probe. A fluorescence reading was taken on a BioTek Cytation 5 fluorescence plate reader (excitation 485 nm, emission 528 nm).

3.2.3.4. Selectivity of best responding aptamers to off-target biomarkers in buffer

Selectivity of probes **o**, **s**, and **f** was assessed by challenging each probe with a panel of biomarkers (β-estradiol from Sigma E8875, neuropeptide y from Sigma N5017, deoxycholic acid from Sigma 264103, Deoxycorticosterone 21-glucoside from Santa Cruz Biotechnology sc-234526, DHEA from Cayman Chemical 15728, and DHEAS). For a given well of a 96 well plate, 100 nM probe was challenged with 25 μM of one of the biomarkers. A set of the wells contained 100 nM probe without any biomarkers to allow calculation of the enhancement factor. After a fluorescence reading was taken on a BioTek Cytation 5 fluorescence plate reader (excitation 485 nm, emission 528 nm), DHEAS was added to the wells that previously did not contain DHEAS to assess whether other biomarkers interfere with probe-DHEAS binding.

3.2.3.5. DHEAS detection in charcoal stripped fetal bovine serum

Probes **o**, **s**, and **f** were used to construct a calibration curve in steroid-free fetal bovine serum (Sigma F6765). Different concentrations of DHEAS (400, 200, 100, 50, 25, 12.5, 6.25, 3.125, and 0 μM) were spiked into a 50% serum solution (5 parts serum, 5 parts 40 mM Tris pH 8.0 with 2 M NaCl and 20 mM $MgCl_2$) containing 100 nM probe. The fluorescence reading was taken on a BioTek Cytation 5 fluorescence plate reader (excitation 485 nm, emission 528 nm.

3.2.3.6. DHEAS detection in charcoal dextran stripped human serum

Probe **f** was used to construct a calibration curve in charcoal dextran stripped human serum (Innovative Research catalog #ISERCDA100ML). Different concentrations of DHEAS (400, 200, 100, 50, 25, 12.5, 6.25, 3.125, and 0 μM) were spiked into a 40% serum solution (4 parts serum, 1 part water, 5 parts 40 mM Tris pH 8.0 with 2 M NaCl and 20 mM $MgCl_2$) containing 100 nM probe. The fluorescence reading was taken on a BioTek Cytation 5 fluorescence plate reader (excitation 485 nm, emission 528 nm. We observed a large loss in probe binding affinity for DHEAS in human serum, likely due to the strong binding affinity between DHEAS and serum proteins. Therefore, we developed a new procedure for the analysis of DHEAS in human serum.

In particular, a plasma crash method was used to remove interfering proteins from serum samples. For charcoal dextran stripped serum, DHEAS (final concentration 25 μM), EDTA (ethylenediaminetetraacetic acid, final concentration 2.5 mM) and SDS (1% final concentration) were added to the serum. Samples were vortexed, and then acetonitrile was added in a 3:1 ratio by volume to precipitate proteins. After centrifugation (15,000 rcf, 3 min), the supernatant was removed and dried using an Organomation® Multivap® Nitrogen Evaporator. The dried sample was resuspended in buffer (20 mM Tris pH 8.0 with 1 M NaCl and 10 mM $MgCl_2$), centrifuged (15,000 rcf, 3 min), and the supernatant was used for DHEAS analysis. 200 nM probe **f** was added

to the supernatant and a fluorescence reading was taken on a BioTek Cytation 5 fluorescence plate reader (excitation 485 nm, emission 528 nm). This fluorescence was compared to charcoal dextran stripped serum where no DHEAS was spiked in to calculate the enhancement factor. As a control, one set of samples had 25 µM DHEAS spiked into the supernatant *after* the plasma crash procedure in order to validate that fluorescence signal is the same as the case where DHEAS is spiked into the serum before the plasma crash procedure.

3.2.3.7. DHEAS detection in clinical samples after plasma crash

For clinical serum samples (Discovery Life Sciences), EDTA (final concentration 2.5 mM) and SDS (1% final concentration) were added to the serum. Samples were vortexed, and then acetonitrile was added in a 3:1 ratio by volume to precipitate proteins. After centrifugation (15,000 rcf, 3 min), the supernatant was removed and dried using an Organomation® Multivap® Nitrogen Evaporator. The dried sample was resuspended in buffer (20 mM Tris pH 8.0 with 1 M NaCl and 10 mM $MgCl_2$), centrifuged (15,000 rcf, 3 min), and the supernatant used for DHEAS analysis. 200 nM probe was added to the supernatant and a fluorescence reading was taken on a BioTek Cytation 5 fluorescence plate reader (excitation 485 nm, emission 528 nm). This fluorescence was compared to the same clinical sample where 200 nM control probe 21 (which does not turn-on in the presence of DHEAS) was spiked in to calculate the enhancement factor.

In the initial sets of experiments, 300 µL serum was treated with the plasma crash method, and 40 µL was analyzed in each well of a 96 well plate for its DHEAS concentration. We also repeated the plasma crash procedure using a lower initial volume of serum to simulate low-volume analysis. Specifically, 40 µL serum was treated with the plasma crash method and 10 µL was analyzed in each well of a 96 well plate.

3.2.4. Isothermal titration calorimetry experiments

Samples for isothermal titration calorimetry (ITC) experiments were prepared in 20 mM pH 8.0 Tris buffer, 125 mM NaCl, and 10 mM $MgCl_2$ at the following concentrations: 300 µM for DHEAS and 30 µM for the free aptamer and aptamer **f**. The ITC experiments were performed on a MicroCal ITC 200 instrument (Malvern Panalytical). Before each experiment, the reference cell was filled with deionized filtered water, and the sample solutions were degassed for 10 min; 40 µL of the DHEAS solution was loaded into the titrating syringe and 280 µL of the corresponding aptamer solution was placed in the ITC cell. After the instrument was equilibrated at 298 K and 1200 rpm syringe rotational speed, a first injection of 0.1 µL was performed followed by a series of 1.2 µL injections spaced at 120 s. The first injection was discarded from the analysis of the integrated data, in order to avoid artifacts due to the diffusion through the injection port during the equilibration period. To measure residual heat, a control experiment was performed. This consisted of 10 injections of DHEAS solution into buffer with the experimental settings described above. ITC data were processed with MicroCal Origin 7.0 software package as described previously.[388] Individual injection heats (q_i)—obtained by integrating the corresponding injection peaks—were normalized for ligand concentration and corrected for dilution heats. A non-linear regression fit to a single set of sites model provided the stoichiometry of binding N, equilibrium association constant K_a, and enthalpy change, ΔH, for each experiment.

3.2.5. Circular dichroism experiments

Circular dichroism (CD) experiments were performed using a Jasco J-1700 circular dichroism spectrometer. Samples were placed in a quartz cuvette with a 1 cm path length and the spectra were collected from 230-320 nm. The native aptamer and FIT-aptamer **f** were dissolved in 1X PBS

containing 1 M NaCl and 10 mM $MgCl_2$ at a concentration of 2 µM. The spectra were recorded in the absence and presence of 100 µM DHEAS. A control experiment was performed by recording the spectra of DHEAS alone. All spectra were corrected for contributions arising from the buffer.

3.2.6. Differential scanning calorimetry experiments

Differential scanning calorimetry (DSC) experiments were performed on a TA Instruments NanoDSC calorimeter running DSCRun (TA Instruments, v4.7.1) data acquisition software. All solutions were prepared in buffer (20 mM Tris pH 8.0 with 1 M NaCl and 10 mM $MgCl_2$) and degassed using a TA Degassing Station for 10 min at 600 mmHg. The sample cell and reference cell (cell volume: 300 µL) were loaded, respectively, with the solution for analysis and the buffer. The sample and reference were subjected to a five-step thermal treatment: (1) cooling from 30 to 10 °C; (2) heating from 10 to 110 °C; (3) cooling from 110 to 10 °C; (4) heating from 10 to 110 °C; (5) cooling from 110 to 10 °C. All heating and cooling ramps were 1 °C/min. This sequence erases the thermal history of the sample (steps 1 and 2), allows the sample to fold under controlled conditions (step 3), and measures the melting of those structures (step 4). A buffer-to-buffer run was performed under identical conditions with buffer in both sample and reference cells.

Data analysis was performed with NanoAnalyze (TA Instruments, v3.11.0) software. Data from the second heating (step 4) were used for analysis. Data from the buffer-to-buffer run were subtracted from the data of the sample under analysis to give buffer-corrected data. Due to inherent changes in heat capacity not associated with folding or unfolding events, the buffer-corrected data did not present a zero baseline, and thus a sigmoidal baseline correction was applied. This baseline was determined using a 1^{st} order pre-transition baseline (fixed at 25 and 35 °C) and a 2^{nd} order post-transition baseline (fixed at 95 and 105 °C). The resulting baseline-corrected data were fit

with a mathematical model comprising the sum of two Gaussian functions. Statistical analysis using NanoAnalyze generated 95% confidence intervals for the fitting parameters, using 100 trials.

3.3. Results

3.3.1. High-throughput screening of FIT-aptamers that turn on in the presence of DHEAS

We first studied the fluorescence enhancement of the different aptamer sequences synthesized as a function of salt concentrations (varying $MgCl_2$ and NaCl concentration). In all experiments, 100 nM probe and 100 μM DHEAS were used. The fluorescence enhancement was calculated as the fluorescence of the probe in the presence of DHEAS divided by the fluorescence of the probe in the absence of DHEAS. The observed fluorescence enhancement is first plotted as a heatmap for the ease of visualization and rapid identification of desirable probes (Figure 3.3.1-1). From this heatmap, we observe that 5 probes turn on, namely, sequences **b**, **f**, **o**, **r**, and **s**, of which sequences **f**, **o**, and **s** show more than a 50% increase in fluorescence.

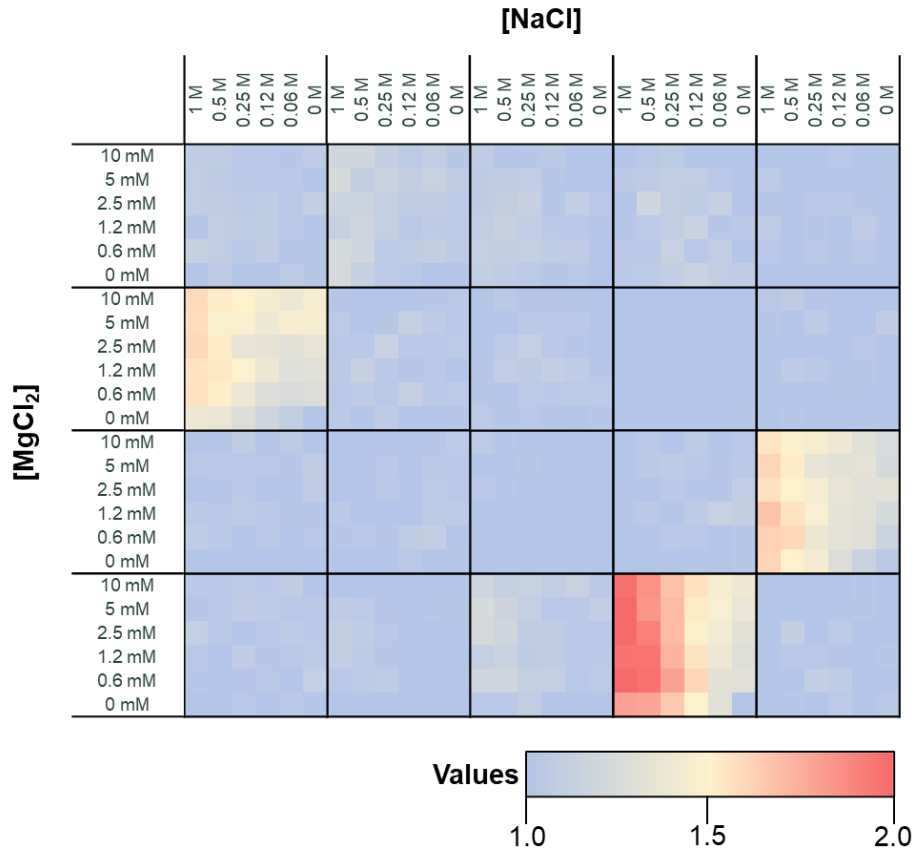

Figure 3.3.1-1. Heatmaps showing the fluorescence enhancement at different NaCl and $MgCl_2$ concentrations. Row one: sequences **a**, **b**, **c**, **d**, **e**; row two: sequences **f**, **g**, **h**, **i**, **j**; row three: sequences **k**, **l**, **m**, **n**, **o**; row four: sequences **p**, **q**, **r**, **s**, **t**.

We next plotted the fluorescence enhancements as bar graphs (**Figure 3.3.1-2**) to capture the variation observed from sample to sample. We note that while the trends clearly show that while NaCl concentrations strongly impact fluorescence enhancements, $MgCl_2$ concentrations have a relatively modest effect.

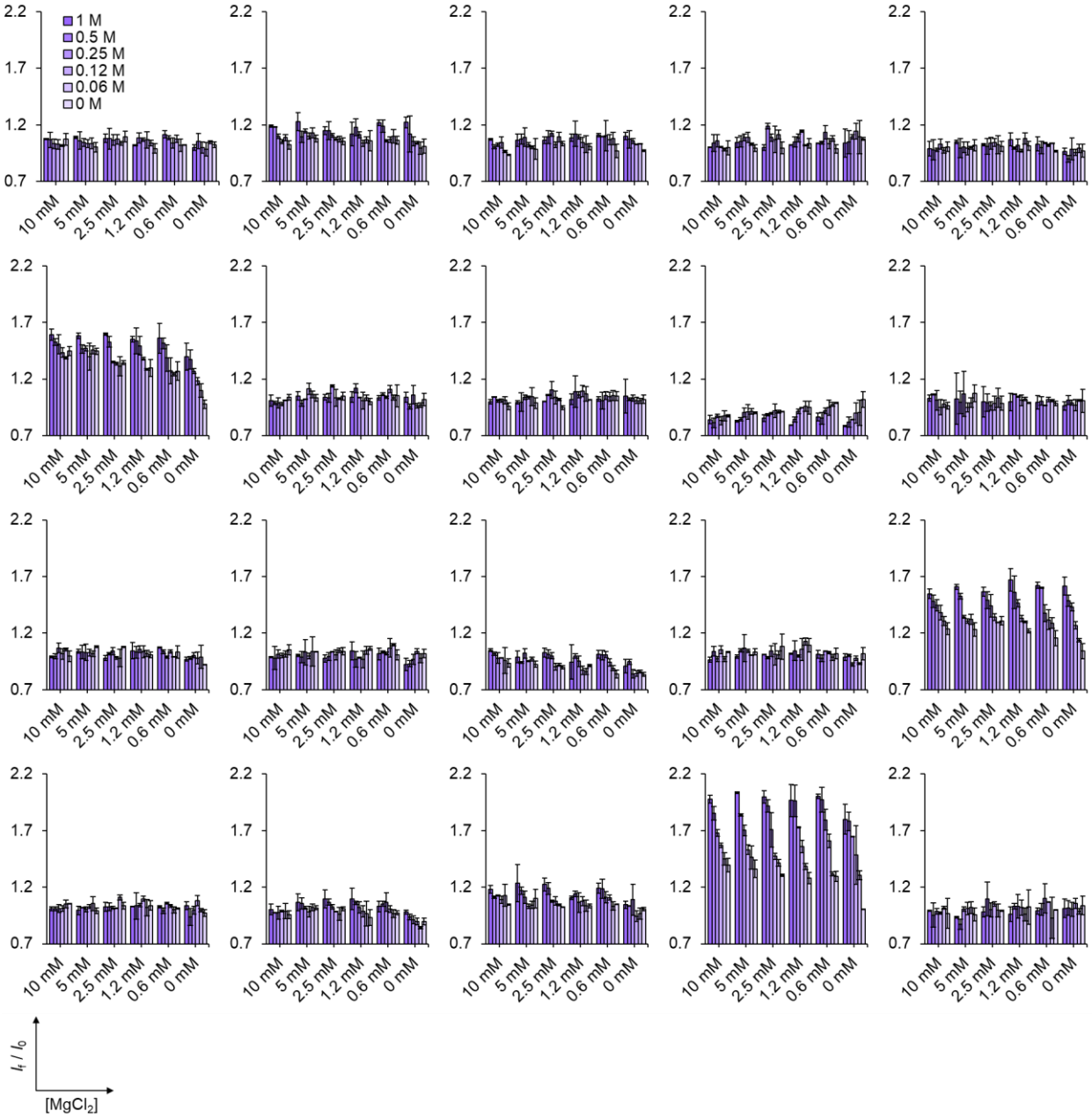

Figure 3.3.1-2. Dependence of the fluorescence enhancement (I_f / I_0) on NaCl and $MgCl_2$ concentrations. Row one: sequences **a**, **b**, **c**, **d**, **e**; row two: sequences **f**, **g**, **h**, **i**, **j**; row three: sequences **k**, **l**, **m**, **n**, **o**; row four: sequences **p**, **q**, **r**, **s**, **t**

3.3.2. Rationalization of experimentally observed results based on computationally predicted structures of the FIT-aptamers

Our initial screen (Figure 3.3.2-1) shows that five FIT-aptamers turn on in the presence of 100 μM DHEAS by more than 15%, namely, sequences **b**, **f**, **o**, **r**, and **s**, of which sequences **f**, **o**, and **s** show more than a 50% increase in fluorescence. We note that both **b** and **f** have TO placed within 2 bases from the binding site whereas **o**, **r**, and **s** have TO directly in the binding site. These results agree with our initial hypothesis. However, we note that sequence **a** and **g** do not turn on despite the TO being within the first two bases. To understand this, we studied the computationally predicted structures of all the FIT-aptamers synthesized. These results are shown in Figure 3.3.2-2-Figure 3.3.2-21. We further note that the fluorescence enhancement increases at increased salt concentrations, suggesting that in conditions where the secondary structure of the aptamer is preserved to a greater extent (Figure 3.3.2-22), the aptamer binds more strongly to the target.

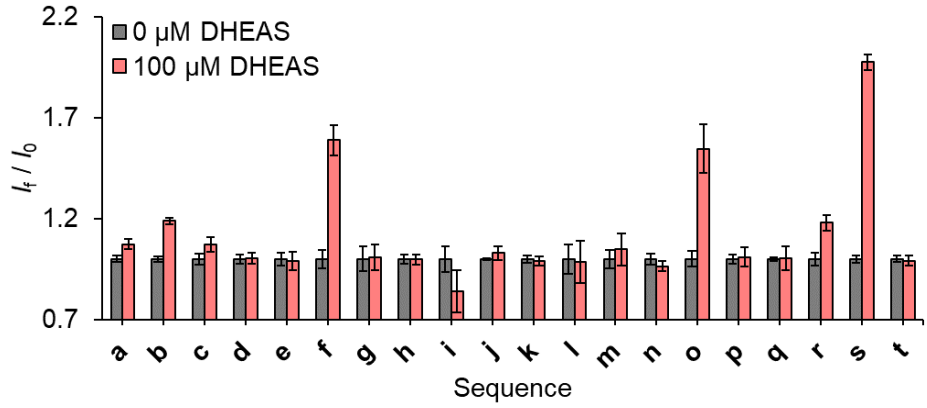

Figure 3.3.2-1. Fluorescence enhancement of the different FIT-aptamers synthesized at 1 M NaCl and 10 mM $MgCl_2$.

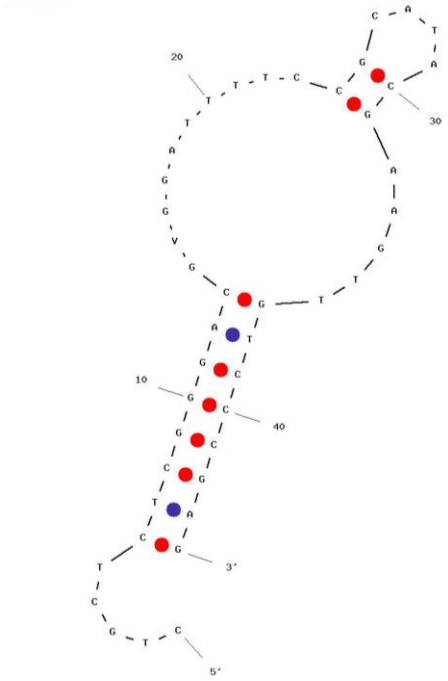

Figure 3.3.2-2. Mfold predicted structure of the FIT-aptamer **a**. Simulations performed using a solution condition of 0.1 μM DNA, 1 M NaCl, and 10 mM $MgCl_2$. A base mismatch completely changes the structure of the binding site compared to the original aptamer, thus a significant structural reorganization is necessary for DHEAS binding. This reason is potentially why no fluorescence turn on is observed.

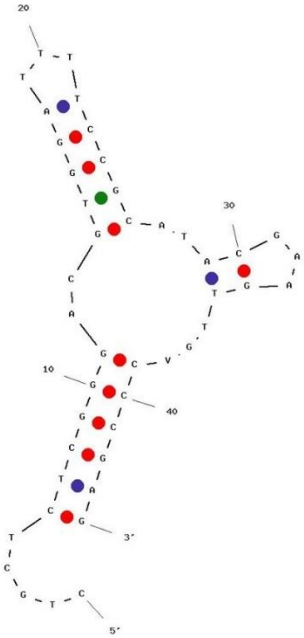

Figure 3.3.2-3. Mfold predicted structure of the FIT-aptamer **b**. Simulations performed using a solution condition of 0.1 μM DNA, 1 M NaCl, and 10 mM $MgCl_2$. DHEAS binding potentially causes refolding of the frayed region of stem 1, resulting in a fluorescence enhancement.

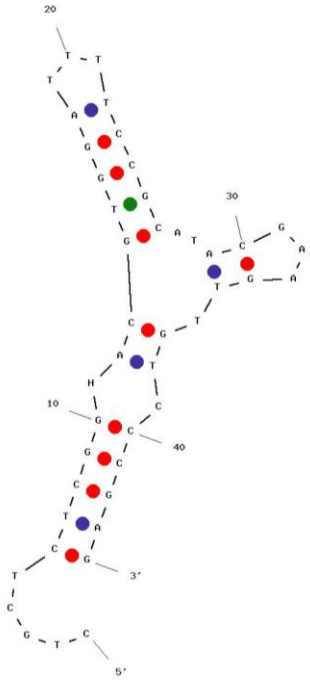

Figure 3.3.2-4. Mfold predicted structure of the FIT-aptamer **c**. Simulations performed using a solution condition of 0.1 μM DNA, 1 M NaCl, and 10 mM $MgCl_2$. As the binding site is intact, DHEAS binding does not lead to a fluorescence enhancement.

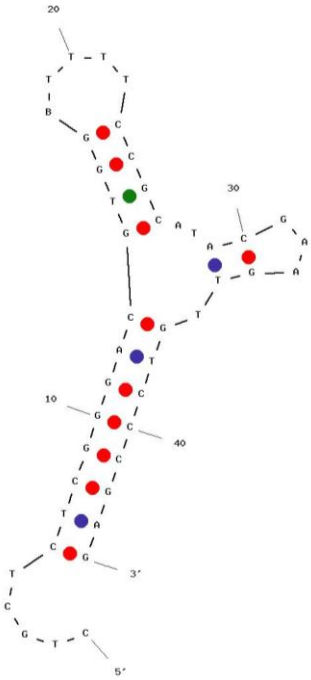

Figure 3.3.2-5. Mfold predicted structure of the FIT-aptamer **d**. Simulations performed using a solution condition of 0.1 μM DNA, 1 M NaCl, and 10 mM $MgCl_2$. As the binding site is intact, DHEAS binding does not lead to a fluorescence enhancement.

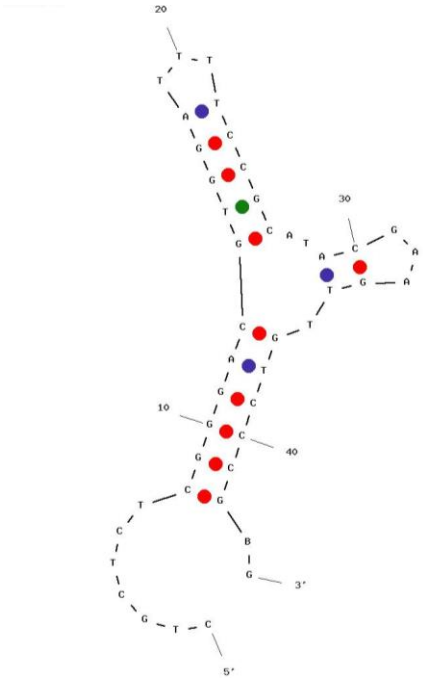

Figure 3.3.2-6. Mfold predicted structure of the FIT-aptamer **e**. Simulations performed using a solution condition of 0.1 μM DNA, 1 M NaCl, and 10 mM $MgCl_2$. As the binding site is intact, DHEAS binding does not lead to a fluorescence enhancement.

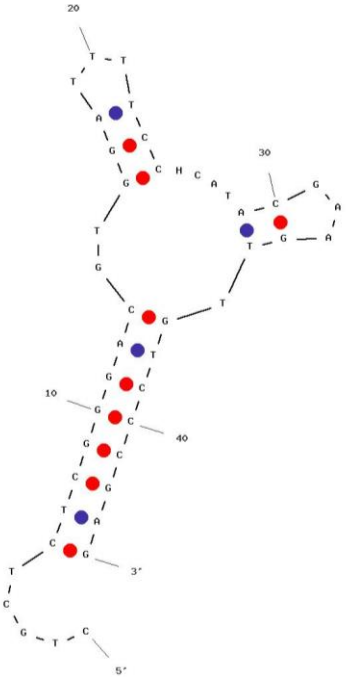

Figure 3.3.2-7. Mfold predicted structure of the FIT-aptamer **f**. Simulations performed using a solution condition of 0.1 μM DNA, 1 M NaCl, and 10 mM $MgCl_2$. DHEAS binding potentially causes refolding of the frayed region of stem 2, resulting in a fluorescence enhancement.

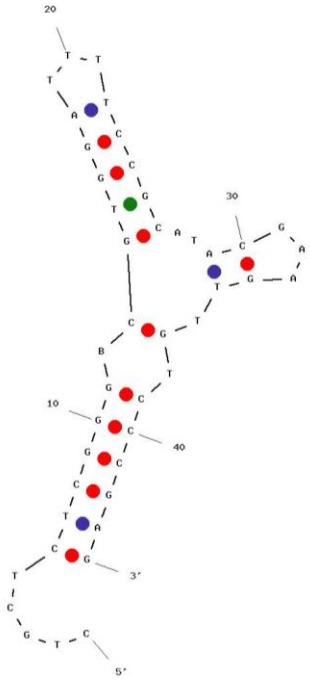

Figure 3.3.2-8. Mfold predicted structure of the FIT-aptamer **g**. Simulations performed using a solution condition of 0.1 μM DNA, 1 M NaCl, and 10 mM $MgCl_2$. DHEAS binding is not expected to result in additional base pairing, thus no fluorescence enhancement is observed.

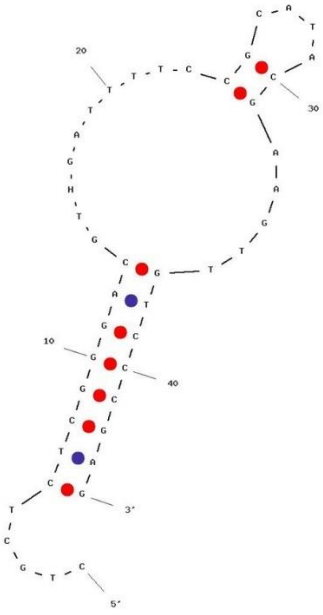

Figure 3.3.2-9. Mfold predicted structure of the FIT-aptamer **h**. Simulations performed using a solution condition of 0.1 μM DNA, 1 M NaCl, and 10 mM $MgCl_2$. A base mismatch completely changes the structure of the binding site compared to the original aptamer and thus a significant structural reorganization is necessary for DHEAS binding. This reason is potentially why no fluorescence turn on is observed.

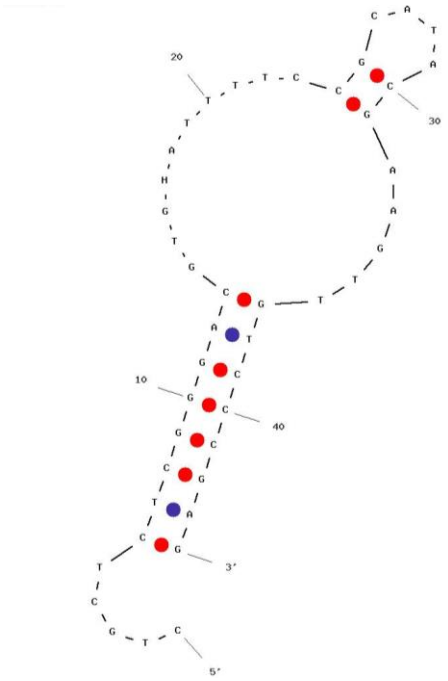

Figure 3.3.2-10. Mfold predicted structure of the FIT-aptamer **i**. Simulations performed using a solution condition of 0.1 μM DNA, 1 M NaCl, and 10 mM $MgCl_2$. A base mismatch completely changes the structure of the binding site compared to the original aptamer and thus a significant structural reorganization is necessary for DHEAS binding. This reason is potentially why no fluorescence turn on is observed.

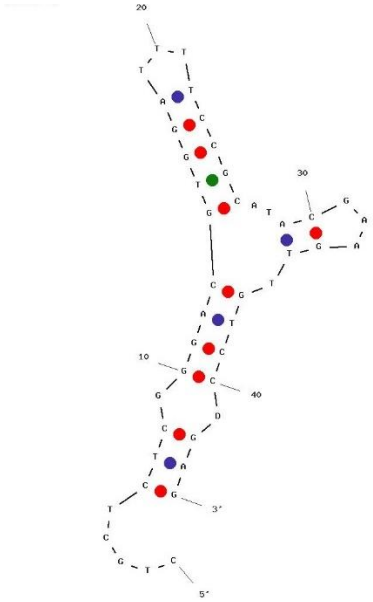

Figure 3.3.2-11. Mfold predicted structure of the FIT-aptamer **j**. Simulations performed using a solution condition of 0.1 μM DNA, 1 M NaCl, and 10 mM $MgCl_2$. As the binding site is intact, DHEAS binding does not lead to a fluorescence enhancement.

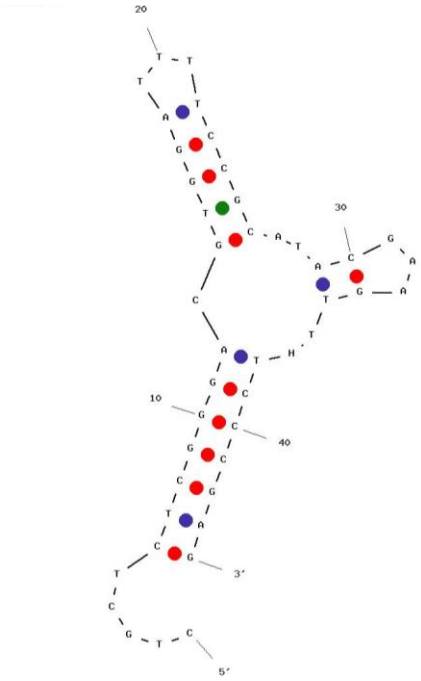

Figure 3.3.2-12. Mfold predicted structure of the FIT-aptamer **k**. Simulations performed using a solution condition of 0.1 μM DNA, 1 M NaCl, and 10 mM $MgCl_2$. No fluorescence enhancement was observed upon DHEAS binding even though the dye is placed in the binding site.

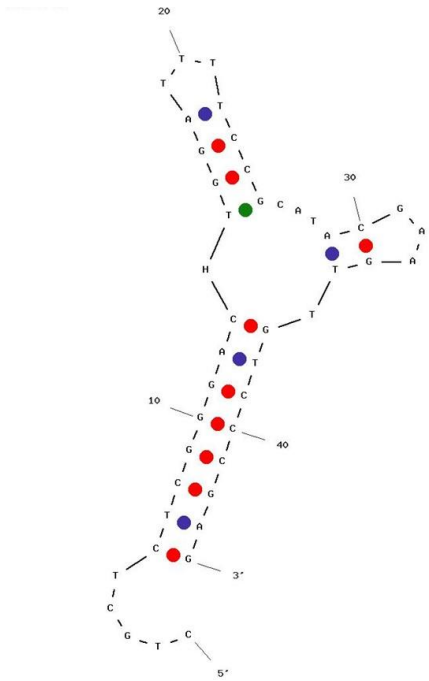

Figure 3.3.2-13. Mfold predicted structure of the FIT-aptamer **l**. Simulations performed using a solution condition of 0.1 μM DNA, 1 M NaCl, and 10 mM $MgCl_2$. No fluorescence enhancement was observed upon DHEAS binding even though the dye is placed in the binding site.

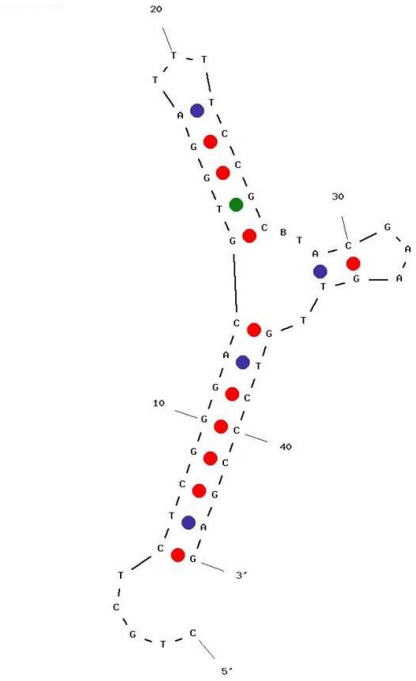

Figure 3.3.2-14. Mfold predicted structure of the FIT-aptamer **m**. Simulations performed using a solution condition of 0.1 μM DNA, 1 M NaCl, and 10 mM $MgCl_2$. No fluorescence enhancement was observed upon DHEAS binding even though the dye is placed in the binding site.

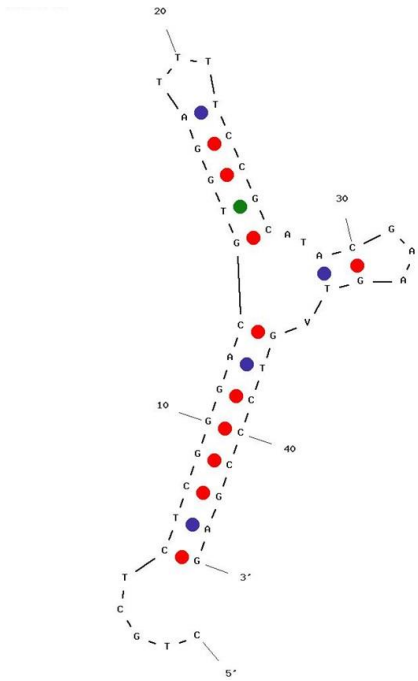

Figure 3.3.2-15. Mfold predicted structure of the FIT-aptamer **n**. Simulations performed using a solution condition of 0.1 μM DNA, 1 M NaCl, and 10 mM $MgCl_2$. No fluorescence enhancement was observed upon DHEAS binding even though the dye is placed in the binding site.

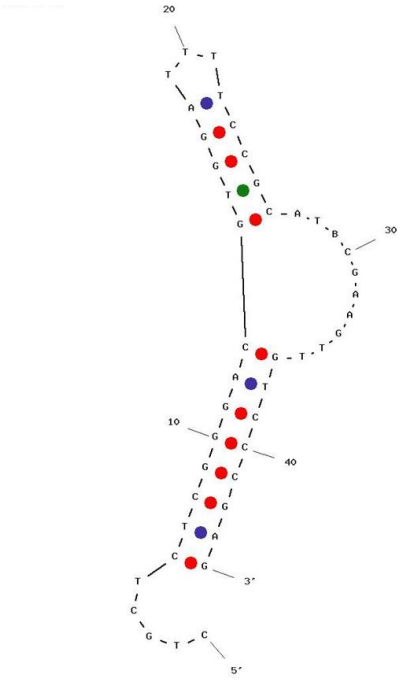

Figure 3.3.2-16. Mfold predicted structure of the FIT-aptamer **o**. Simulations performed using a solution condition of 0.1 μM DNA, 1 M NaCl, and 10 mM $MgCl_2$. DHEAS binding potentially causes refolding of stem 3, resulting in a fluorescence enhancement.

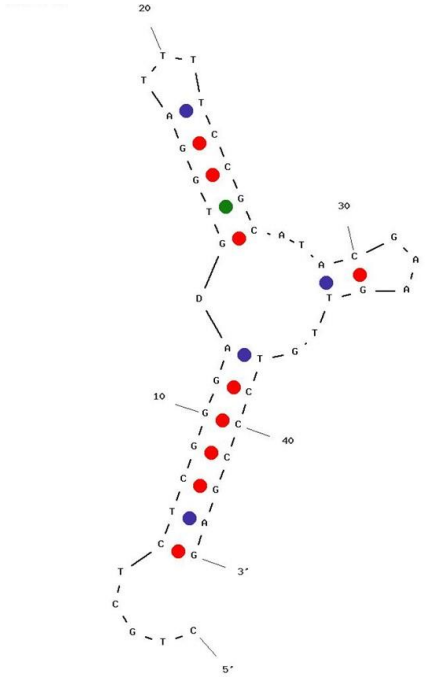

Figure 3.3.2-17. Mfold predicted structure of the FIT-aptamer **p**. Simulations performed using a solution condition of 0.1 μM DNA, 1 M NaCl, and 10 mM $MgCl_2$. No fluorescence enhancement was observed upon DHEAS binding even though the dye is placed in the binding site.

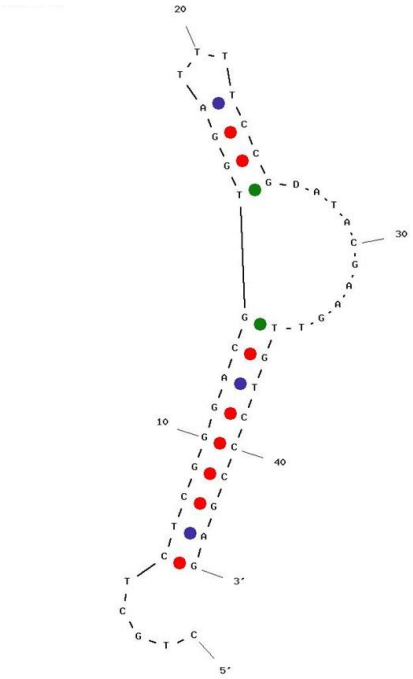

Figure 3.3.2-18. Mfold predicted structure of the FIT-aptamer **q**. Simulations performed using a solution condition of 0.1 μM DNA, 1 M NaCl, and 10 mM $MgCl_2$. No fluorescence enhancement was observed upon DHEAS binding even though the dye is placed in the binding site.

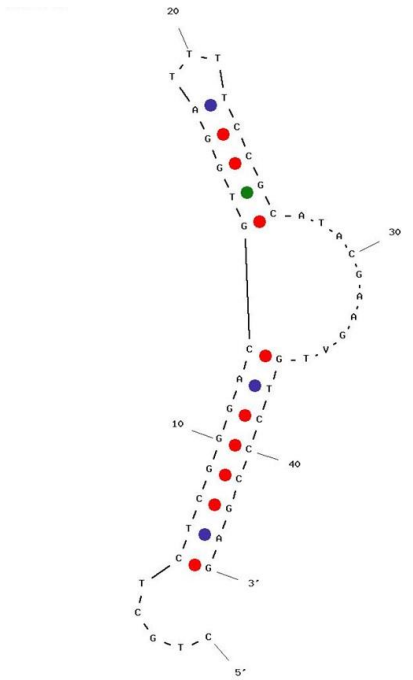

Figure 3.3.2-19. Mfold predicted structure of the FIT-aptamer **r**. Simulations performed using a solution condition of 0.1 μM DNA, 1 M NaCl, and 10 mM $MgCl_2$. DHEAS binding potentially causes refolding of stem 3, resulting in a modest fluorescence enhancement.

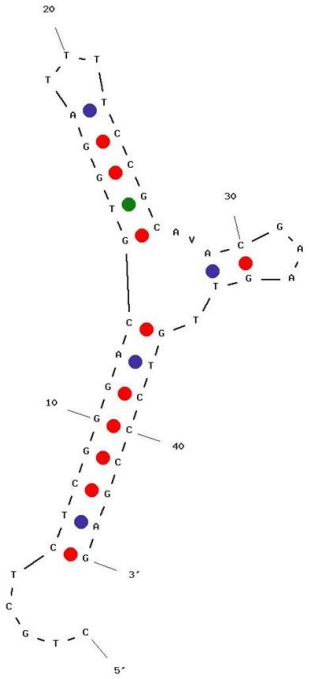

Figure 3.3.2-20. Mfold predicted structure of the FIT-aptamer **s**. Simulations performed using a solution condition of 0.1 μM DNA, 1 M NaCl, and 10 mM $MgCl_2$. Given that the dye is placed directly in the binding site, DHEAS binding results in a fluorescence enhancement but also reduces the binding affinity of the aptamer.

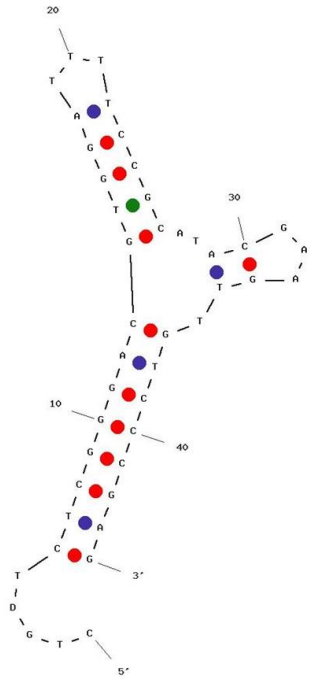

Figure 3.3.2-21. Mfold predicted structure of the FIT-aptamer **t**. Simulations performed using a solution condition of 0.1 μM DNA, 1 M NaCl, and 10 mM $MgCl_2$. As the binding site is intact, DHEAS binding does not lead to a fluorescence enhancement.

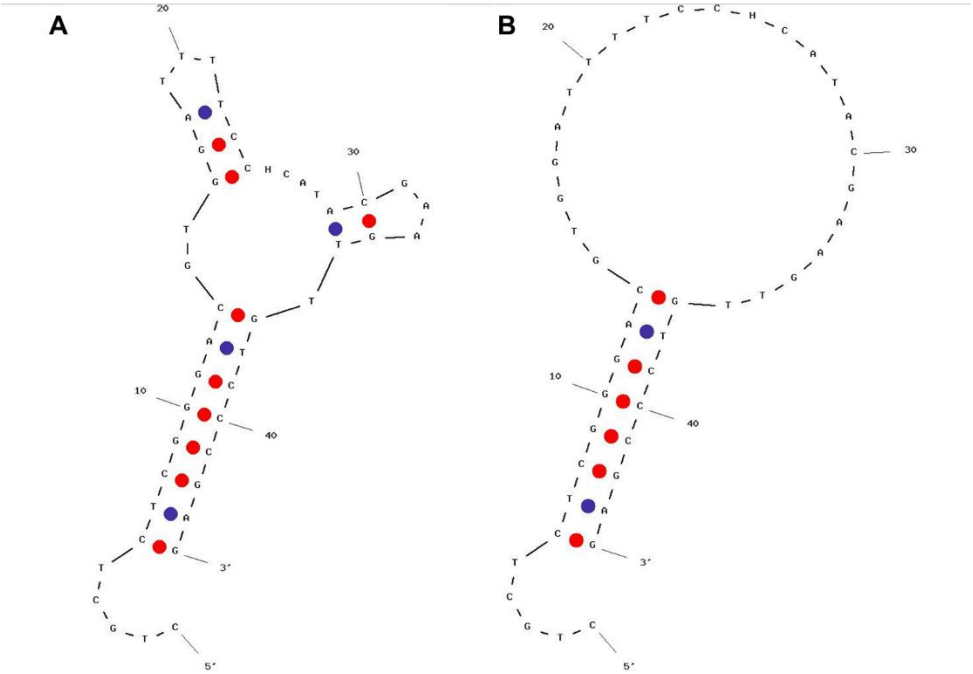

Figure 3.3.2-22. Structure of FIT-aptamer **f** at (A) 1 M NaCl and 10 mM $MgCl_2$ and (B) 6.25 mM NaCl and 0 mM $MgCl_2$. We note that the fluorescence enhancement under condition (A) is 1.6 while that under condition (B) is 1.1, suggesting that conditions that preserve the secondary structure of the aptamer increase target binding.

3.3.3. DHEAS detection experiments

3.3.3.1. Detection of DHEAS in fetal bovine serum

We selected the three FIT-aptamers with the highest fluorescence enhancements and tested whether these sequences allow for the detection of DHEAS in steroid-free fetal bovine serum with different concentrations of DHEAS spiked in. We note from Figure 3.3.3-1 that the trends in dissociation constants observed mirror those observed in the selection buffer (Figure 3.4.1-3). However, the absolute values of the dissociation constants are significantly increased in fetal bovine serum.

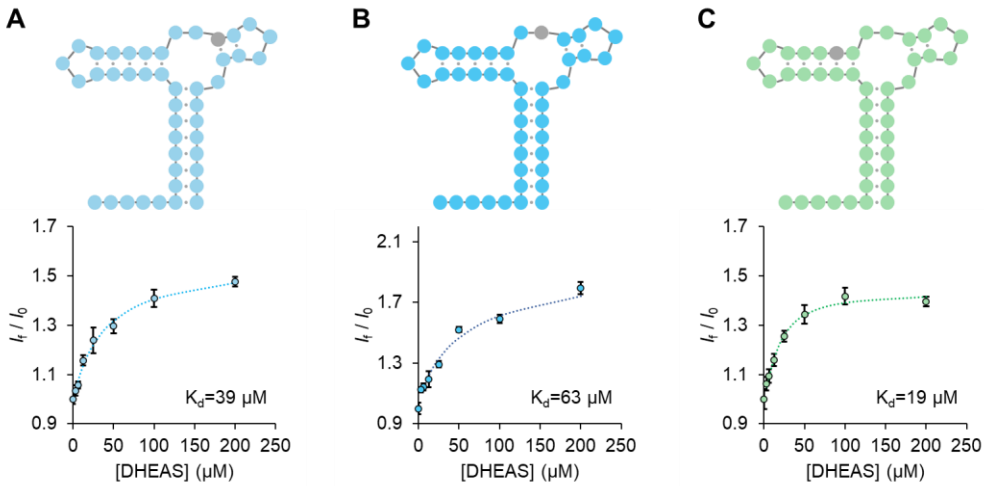

Figure 3.3.3-1. Calibration curve of DHEAS spiked into steroid-free fetal bovine serum for sequences (A) **o**, (B) **s**, and (C) **f**.

3.3.3.2. Direct detection of DHEAS in human serum

We selected FIT-aptamer **f** which has the lowest dissociation constants in both buffer and fetal bovine serum for subsequent experiments with human serum. We tested whether sequence **f** allows for the detection of DHEAS in steroid-free human serum with different concentrations of DHEAS spiked in. We could not detect DHEAS in 100% serum and therefore we performed experiments with 40% human serum (diluted with the selection buffer). We note from Figure 3.3.3-2 that the dissociation constant increases by over 25-fold relative to the selection buffer. Consequently, the limit of detection in the original sample is raised to ~27 µM. These experiments indicate that we cannot detect clinically relevant amounts of DHEAS in human serum without further processing of the serum.

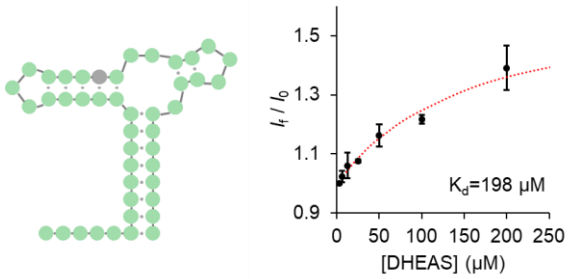

Figure 3.3.3-2. Calibration curve of DHEAS spiked into steroid-free human serum for sequence **f**.

3.3.3.3. Images of the plasma crash procedure

We hypothesized that the apparent dissociation constant of the aptamer significantly decreases in human serum due to the competing interaction of the DHEAS with serum proteins. Therefore, we developed a plasma crash method to precipitate the serum proteins and extract the DHEAS into the aptamer selection buffer. Figure 3.3.3-3 shows images corresponding to the various stages of the serum processing during the plasma crash method. It should be noted that the addition of a 3:1 ratio of acetonitrile (ACN) to serum causes the serum proteins to precipitate. The resulting DHEAS-containing supernatant is clear.

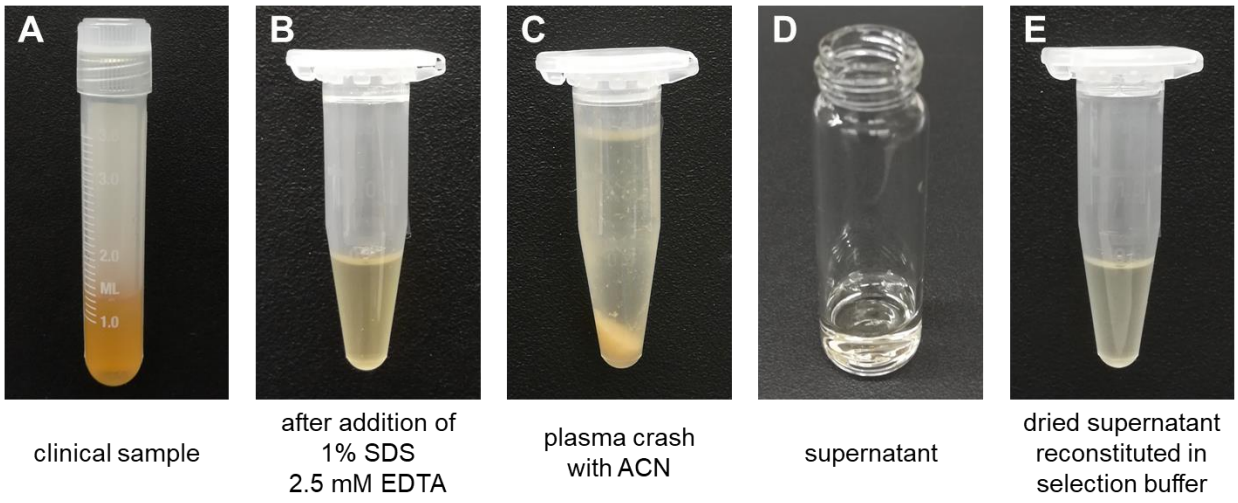

Figure 3.3.3-3. Images of (A) a clinical sample, (B) an aliquot of the clinical sample after addition of SDS and EDTA, (C) the sample after plasma crash with ACN, (D) the supernatant containing DHEAS, and (E) the evaporated supernatant reconstituted in the aptamer selection buffer.

3.3.3.4. Detection of DHEAS in human serum using the plasma crash method

Different concentrations of DHEAS were spiked into charcoal dextran stripped (i.e. steroid-free) human serum. A calibration curve was constructed, and the data points were fit to the Hill equation. The Hill-parameters obtained closely match those obtained when the calibration curve is performed in pure buffer, showing that the plasma crash approach is successful in extracting DHEAS from human serum. Moreover, when no DHEAS is added, we observed that the fluorescence enhancement obtained using the target probe is similar to that obtained using a control probe (that does not turn on in the presence of DHEAS). Therefore, the fluorescence of the control probe can be utilized as I_0 in calculating the fluorescence enhancement in samples with unknown DHEAS concentrations.

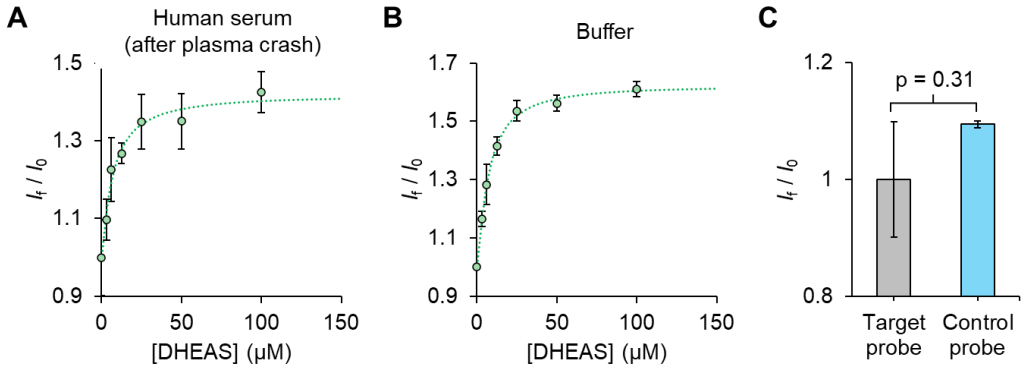

Parameter	Value	Error
y_0	1.00	0.03
y_m	1.42	0.05
K_d	6.90	2.10
n	1.14	0.39

Parameter	Value	Error
y_0	1.00	0.01
y_m	1.63	0.02
K_d	7.17	0.56
n	1.27	0.12

Figure 3.3.3-4. Detection of DHEAS spiked into steroid-free human serum using the plasma crash method. (A) Calibration curve obtained using the plasma crash method. (B) Calibration curve obtained in buffer. The data are fit to the Hill-equation and the parameters are tabulated below the respective graphs. There is a slight reduction in y_m; however, both graphs show similar values for y_0, K_d, and n, indicating that the plasma crash approach yields similar results compared to buffer. (C) Comparison of signal obtained from the target probe and a control probe when no DHEAS is added to the serum. The differences in the signals obtained are statistically insignificant (*i.e.*, $p > 0.05$), indicating that the signal from the control probe can be utilized as I_0 in calculating fluorescence enhancement in samples with unknown DHEAS concentrations.

3.3.3.5. DHEAS detection in low volume clinical sample

To investigate whether low sample volumes can be used to detect DHEAS, we used three clinical samples with DHEAS concentrations of 20.5, 2.9, and 0.2 μM, respectively. After plasma crash, we treated 10 μL of these samples with the scramble and target probe in succession. The relative fluorescence enhancements with the lowest value normalized to 1 are shown in Figure 3.3.3-5. From this figure, we see that the relative fluorescence enhancements correlate with the DHEAS concentrations even when low sample volumes (10 μL) are used.

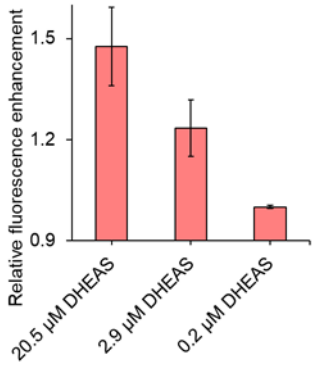

Figure 3.3.3-5. Detection of DHEAS in low volume clinical samples. Volume of the clinical sample used per well is 10 µL.

3.3.4. Isothermal titration calorimetry experiments

We next investigated whether replacing a base with TO results in a significant loss of binding affinity compared to the native aptamer. Therefore, we performed ITC on the native aptamer and the best performing FIT-aptamer, sequence **f**. Our results indicate that the dissociation constants of both sequences are the same within error.

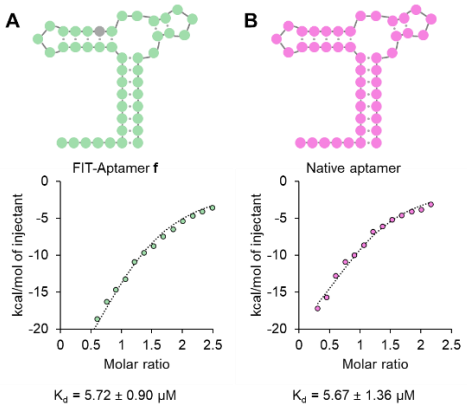

Figure 3.3.4-1. Dissociation constants of (A) FIT-aptamer **f** and (B) the native aptamer as determined by isothermal titration calorimetry. The results indicate that replacement of a base with TO at the position shown by a gray dot in (A) does not significantly alter the binding affinity of the aptamer.

3.3.5. Circular dichroism experiments

We performed CD experiments to study the change in aptamer structure upon DHEAS binding. Our results indicate that there are no large changes in structure for either the native aptamer or the FIT-aptamer **f**.

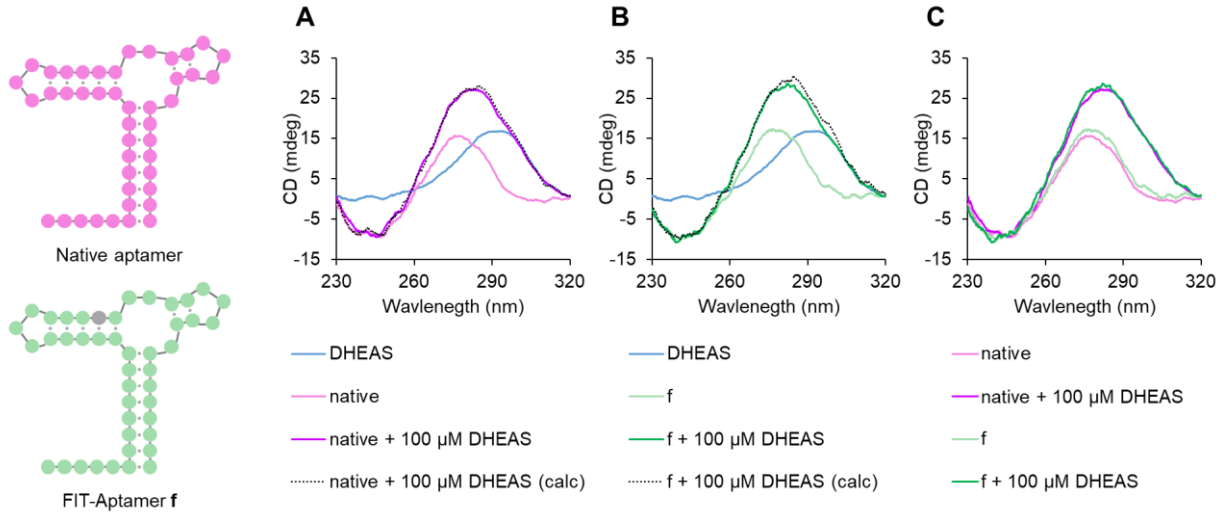

Figure 3.3.5-1. CD spectra of 2 µM native aptamer and FIT-aptamer **f** in the presence and absence of 100 µM DHEAS. The CD spectra look nearly identical for both the native aptamer and **f** in the absence of DHEAS. Although the signal increases for both in the presence of DHEAS, the calculated CD spectra of the aptamers in the presence of DHEAS can be expressed as a sum of the CD of DHEAS and that of the aptamers by themselves. Therefore, we conclude that there is no additional contribution from the aptamer-DHEAS binding. These results further confirm that a significant structural change in the aptamer does not accompany DHEAS binding.

3.3.6. Design of FIT-aptamers for deoxycorticosterone-21 glucoside and deoxycholic acid

To test the generality of our system, we designed two FIT-aptamers for deoxycorticosterone-21 glucoside based on simulation-guided design. We note from Figure 3.3.6-1 that **u** contains TO in one of the stems whereas **v** contains TO in the binding pocket. While both sequences result in a florescence turn on (Figure 3.3.6-2), the binding affinity is significantly reduced for **v**, consistent with prior observations in the case of the DHEAS FIT-aptamers. Therefore, we designed a FIT-aptamer, **w**, for deoxycholic acid by replacing a base in one of the stems with TO (Figure 3.3.6-3). This sequence was successful in detecting its target (Figure 3.3.6-4).

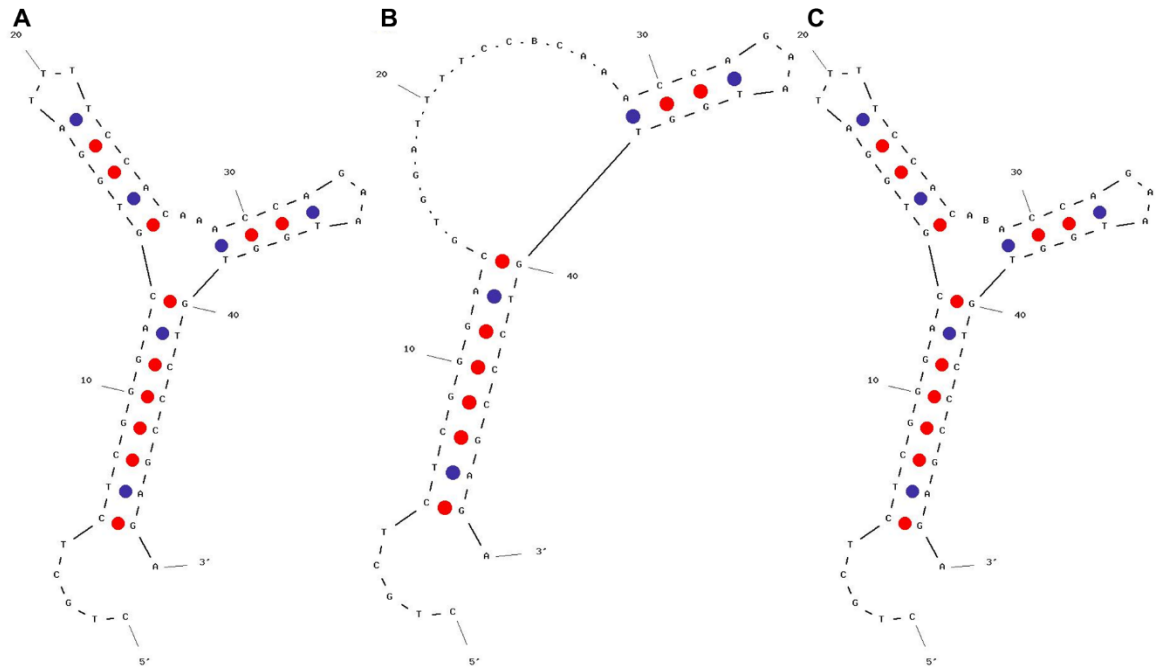

Figure 3.3.6-1. Mfold predicted structure of (A) DOG, (B) the FIT-aptamer **u**, and (C) the FIT-aptamer **v**. Simulations performed using a solution condition of 0.2 μM DNA, 1 M NaCl, and 10 mM $MgCl_2$. Binding of deoxycorticosterone-21 glucoside potentially causes refolding of the destabilized stem in (B) resulting in a fluorescence enhancement. In case of (C), given that the dye is placed directly in the binding site, target binding results in a fluorescence enhancement but also reduces the binding affinity of the aptamer.

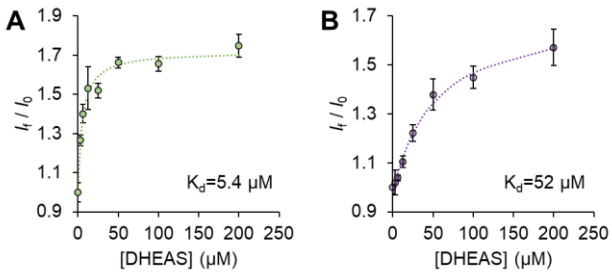

Figure 3.3.6-2. Calibration curves of deoxycorticosterone-21 glucoside in buffer for FIT-aptamers (A) **u** and (B) **v**. We note that the binding affinity is significantly reduced when a base in the binding pocket is replaced by the dye.

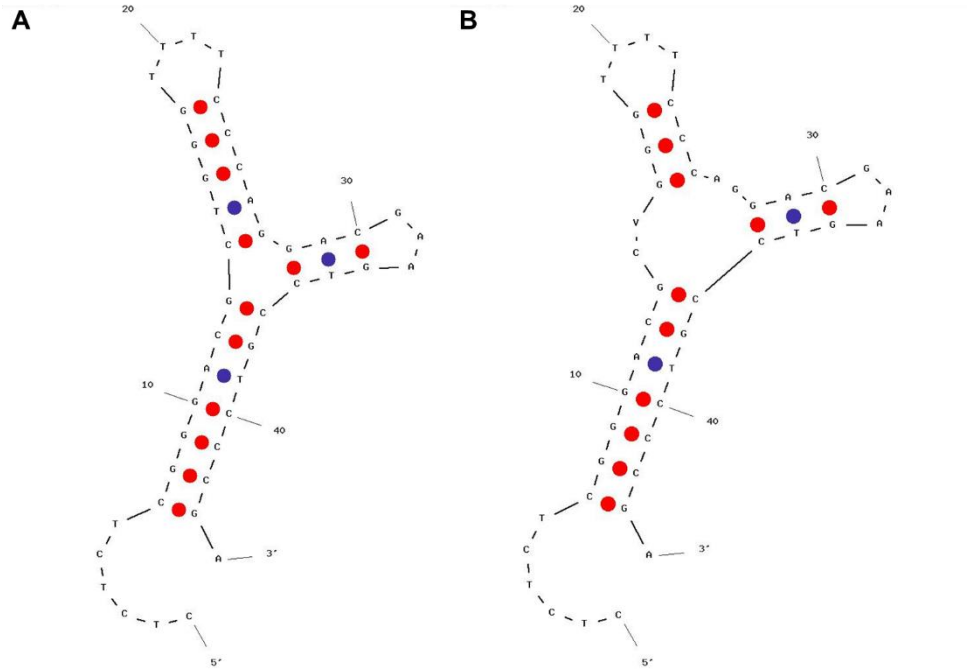

Figure 3.3.6-3. Mfold predicted structure of (A) DCA and (B) the FIT-aptamer **w**. Simulations performed using a solution condition of 0.2 µM DNA, 1 M NaCl, and 10 mM $MgCl_2$. Binding of deoxycholic acid potentially causes refolding of the destabilized stem in (B) resulting in a fluorescence enhancement.

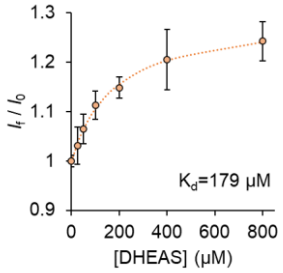

Figure 3.3.6-4. Calibration curve of deoxycholic acid in buffer for FIT-aptamer **w**.

3.3.7. Differential scanning calorimetry experiments and detailed Mfold modeling

DSC data collected upon heating for both the native aptamer and FIT-aptamer **f** can be modeled by a sum of two Gaussian peaks (Figure 3.3.7-1), suggesting that the melting of the aptamers occurs in two distinct stages. The peak temperatures of these Gaussian peaks are consistent with the melting temperatures predicted for stem 1 (major peak) and stems 2+3 (minor peak) by Mfold simulations (Figure 3.3.7-2). We note that the expected area ratio of the minor:major peak (which corresponds to the ratios of the enthalpies associated with the melting transitions) is 0.66 for the native aptamer in the absence of DHEAS. The experimentally observed value is 0.39, suggesting that stems 2+3 are not fully folded. Moreover, the ratio increases to 0.70 in the presence of 100 µM DHEAS indicating that stems 2+3 are considerably stabilized upon DHEAS binding.

We further note that the area ratio of the minor:major peak in FIT-aptamer **f**, which contains a base mismatch in stem 2, is significantly decreased to 0.12, indicating that the base mismatch substantially destabilizes the stem. The ratio increases to 0.15 upon DHEAS addition indicating that the stability is partially recovered upon target binding.

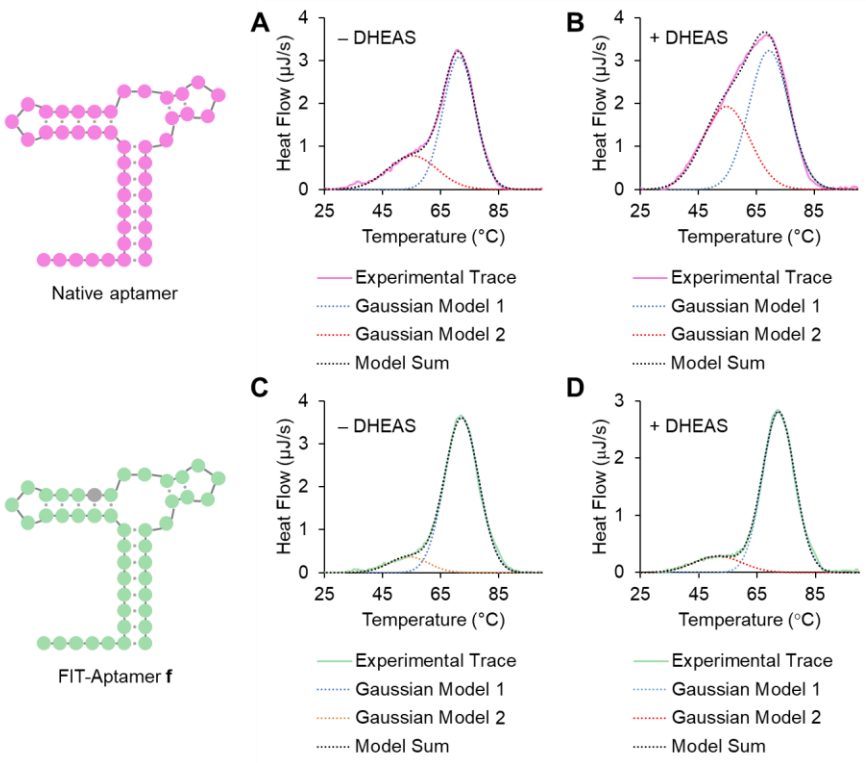

Figure 3.3.7-1. DSC traces of 50 µM of the (A, B) native aptamer and the (C, D) FIT-aptamer **f** in the absence (-) and presence (+) of 100 µM DHEAS, respectively.

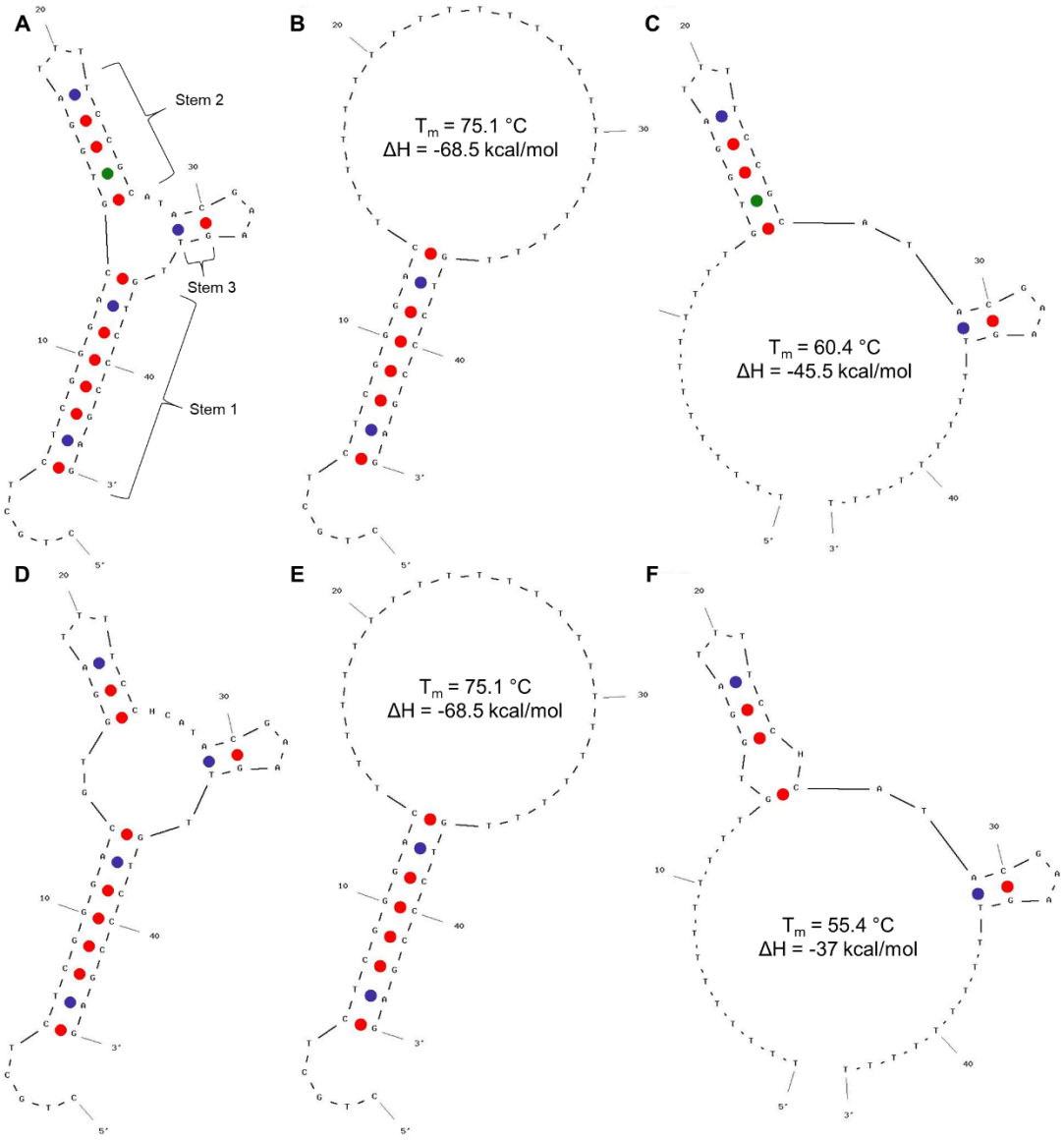

Figure 3.3.7-2. Structures of (A) the native aptamer, (B) a sequence of the same length as the native aptamer that contains only stem 1, (C) a sequence of the same length as the native aptamer containing only stems 2 and 3, (D) FIT-aptamer **f**, (E) a sequence of the same length as **f** that contains only stem 1, and (F) a sequence of the same length as **f** containing only stems 2 and 3.

Table 3.3.7-1. Melting temperatures (T_m) of the stems of the native aptamer and FIT-aptamer **f** as determined using DSC experiments and Mfold simulations

Aptamer	without DHEAS						100 µM DHEAS		
	T_m (°C) (major)		T_m (°C) (minor)		Area Ratio (minor/major)		T_m (°C) (major)	T_m (°C) (minor)	Area Ratio
	DSC	Mfold	DSC	Mfold	DSC	Mfold	DSC	DSC	DSC
native	71.4	75.1	55.3	60.4	0.39	0.66	69.4	54.7	0.70
f	72.3	75.1	54.0	55.4	0.12	0.54	72.4	51.5	0.15

3.4. Discussion

3.4.1. Validating a FIT-based approach for rapid detection of steroids

In the results section, we developed steroid-binding FIT-aptamers using thiazole orange (TO) as the visco-sensitive dye whose fluorescence is turned on when rotation about its methine bridge is restricted.[124,154] We began by selecting a previously evolved aptamer for DHEAS.[389] The minimum energy structure predicted by Mfold[390] indicates that the free aptamer exists in a folded conformation at room temperature, containing three double-stranded regions (Figure 3.4.1-1**,** Figure 3.2.1-1). These results are consistent with experimentally observed differential scanning calorimetry (DSC) traces (Figure 3.3.7-1). The junction of the double-stranded regions forms the binding pocket. Therefore, we needed to develop a strategy that could detect the subtle structural changes that would accompany DHEAS binding (Figure 3.3.5-1).

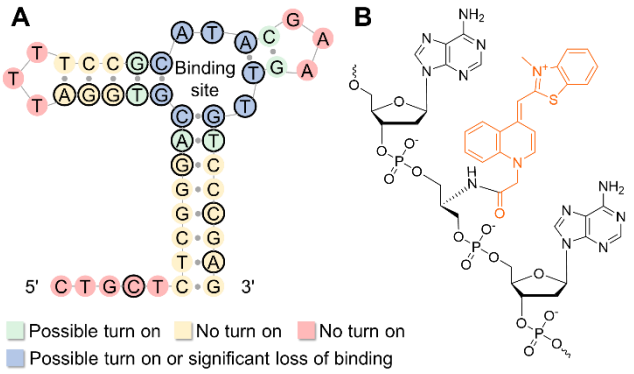

Figure 3.4.1-1. (A) Secondary structure of the aptamer for DHEAS showing predicted fluorescence turn on when FIT-aptamers are designed by substituting TO at different locations on the sequence. The FIT-aptamer library was generated by synthesizing 20 different sequences such that in each sequence one of the bases circled in black was substituted with TO. (B) Chemical structure of an oligonucleotide with TO as a base surrogate.

By analyzing the structure of the DHEAS aptamer, we noted that there are four types of sites (Figure 3.4.1-1): (i) single-stranded regions away from the binding site, (ii) double-stranded

regions away from the binding site, (iii) double-stranded regions close to the binding site, and (iv) bases in the binding site. We reasoned that if TO is placed in regions (i) and (ii), no fluorescence turn-on will be observed because the local environment of the dye should not change significantly upon DHEAS binding. On the other hand, placing TO in regions (iii) and (iv) may result in a fluorescence turn on due to restricted internal rotation of the dye upon target binding. We predicted the aptamer structure after TO substitution by computational modeling using Mfold, where we used a base mismatch to simulate the incorporation of TO. From our initial set of simulations, we anticipated that regions within 2 base pairs of the binding site may undergo local conformational changes upon DHEAS binding sufficient for fluorescence turn-on.

To test our hypothesis, we synthesized a library of 20 variants of the DHEAS aptamer, each with a single point mutation (Figure 3.4.1-1, Table 3.2.1-1) where TO is used as a nucleobase surrogate. We screened ~1500 points in high throughput corresponding to selection buffers with different NaCl and $MgCl_2$ concentrations (Figure 3.3.1-1-Figure 3.3.1-2). At each condition, we added 100 μM DHEAS and calculated the fluorescence enhancement, defined as the fluorescence of the aptamer in the presence of the target, I_f, relative to the fluorescence of the aptamer alone, I_0 (Figure 3.4.1-2**,** Figure 3.3.1-1-Figure 3.3.1-2). Our initial screen resulted in the selection of 5 sequences that turn-on (sequences **b**, **f**, **o**, **r**, and **s**), which can be rationalized based on Mfold simulations (Figure 3.3.2-1-Figure 3.3.2-21). The fluorescence enhancement increases with increasing salt concentrations, reaching up to 2-fold. These results suggest that conditions in which the secondary structure of the aptamer is preserved to a greater extent facilitate DHEAS binding (Figure 3.3.2-22). We further validated the generality of this approach by using simulation guided design

to program fluorescence into FIT-aptamers for other steroids such as deoxycorticosterone-21 glucoside and deoxycholic acid (Figure 3.3.6-1-Figure 3.3.6-4).

We next measured the fluorescence response of the 3 FIT-aptamers with >50% fluorescence increase (sequences **f**, **o**, and **s**) as a function of DHEAS concentration (Figure 3.4.1-3). By fitting the data to the Hill equation, we calculated the apparent dissociation constants, K_d, to be 7, 23, and 21 μM, respectively. We note that DSC experiments suggest that in probe **f**, the TO-containing region is destabilized relative to the unmodified aptamer. The stability is partially recovered in the presence of DHEAS (Figure 3.3.7-1). However, the K_d of probe **f** is not significantly changed compared to the unmodified aptamer, as ascertained by isothermal titration calorimetry. In contrast, probes **o** and **s**, both of which have TO in the binding pocket, have higher dissociation constants, suggesting that modifications outside of the binding pocket are more desirable for creating probes with higher sensitivity. Notably, the apparent K_d of probe **f** designed using a FIT-strategy is significantly smaller than that observed when a fluorophore-quencher-based strategy that requires strand displacement is used.[389]

We next investigated the specificity of aptamers **f**, **o**, and **s** for DHEAS (Figure 3.4.1-3). Due to the structural similarity of DHEA and DHEAS and the evolutionary promiscuity of these aptamers towards deoxycorticosterone-21 glucoside,[389] we observe fluorescence turn-on in the presence of these two steroids. However, physiological concentrations of DHEAS are 1-2 orders of magnitude higher than that of deoxycorticosterone-21 glucoside and DHEA, alleviating challenges with cross-reactivity in biologically relevant media.[391–393] Moreover, other off-target biomarkers like deoxycholic acid, neuropeptide Y, and β-estradiol cause negligible turn-on, and the presence of off-target biomarkers in a mixture of the aptamer and DHEAS does not inhibit binding.

Importantly, these results show that for the structures studied, the selectivities of FIT-aptamers are the same as that of the original aptamers.[389] Given that all three show comparable selectivity, we identified probe **f** to be the best FIT-aptamer in the library since it has the lowest K_d (and consequently, a limit of detection of 1.3 μM). Therefore, we next evaluated its ability to sense DHEAS in serum.

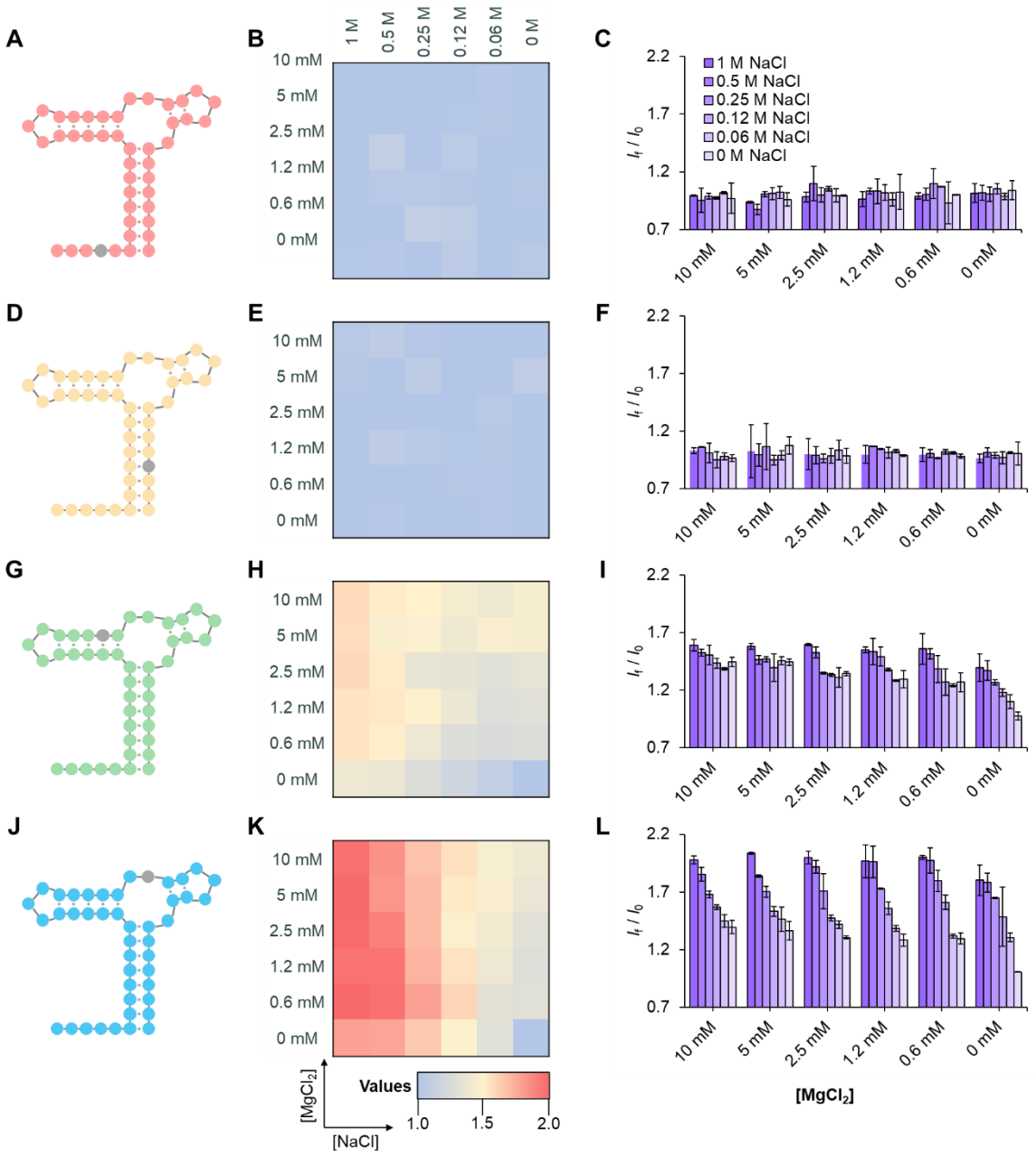

Figure 3.4.1-2. Fluorescence enhancement (I_f/I_0) screening data for 4 representative FIT-aptamers with TO substitution at different locations along the sequence. In all cases, 0.1 µM probe and 100 µM DHEAS were used. (A, D, G, J) Schemes for sequence **t**, **j**, **f**, and **s**, respectively. TO substitution is denoted by a grey circle. (B, E, H, K) Corresponding fluorescence enhancement heatmaps. (C, F, I, L) Fluorescence enhancement shown as bar graphs.

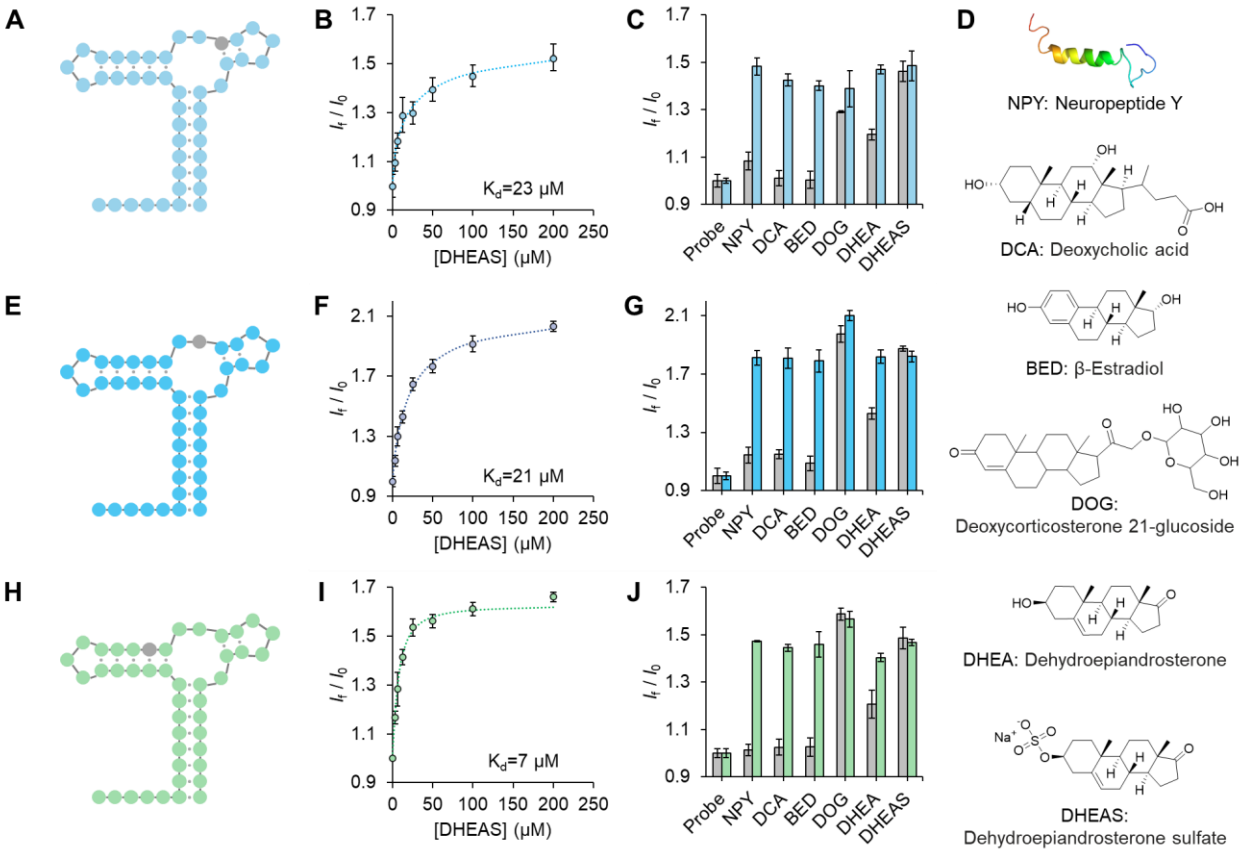

Figure 3.4.1-3. Sensitivity and selectivity of the best FIT-aptamers from the initial library screen. (A, E, H) Schemes of sequence **o**, **s**, and **f**, respectively with the dye denoted by a grey circle. (B, F, I). Fluorescence enhancements of 0.1 μM of FIT-aptamers **o**, **s**, and **f**, respectively with varying DHEAS concentration. (C, G, J) Selectivity of FIT-aptamers **o**, **s**, and **f**, respectively. Gray bars denote fluorescence enhancement after addition of 25 μM of different analytes to 0.1 μM probe. Colored bars represent fluorescence enhancement after DHEAS is added to this mixture. "Probe" denotes FIT-aptamers with no added analyte. (D) Structures of the biomarkers used for selectivity studies.

Studies where DHEAS was spiked into steroid-free human serum showed a significant loss in binding affinity (K_d = 198 μM) of the aptamer (Figure 3.3.3-2), likely due to interaction of DHEAS with serum proteins.[394] We therefore developed a plasma crash procedure to break these interactions and remove proteins from serum (Figure 3.4.1-4A**,** Figure 3.3.3-3). Briefly, the

proteins were denatured with ethylenediaminetetraacetic acid (EDTA) and Sodium dodecyl sulfate (SDS) and precipitated with acetonitrile (ACN). The supernatant containing DHEAS was dried and resuspended in buffer. Thereafter, the FIT-aptamer was added for taking fluorescence readings. Serum samples with DHEAS-spiked in before and after the treatment showed that this procedure yields fluorescence turn-ons comparable to that observed in buffer (Figure 3.3.3-4), indicating that the treatment is effective in extracting DHEAS (Figure 3.4.1-4B).

We next assessed the ability of the FIT-aptamer to make measurements of DHEAS in clinical serum samples. Specimens from 13 different individuals with known DHEAS levels, measured using the Abbott Architect chemiluminescent assay, were acquired and tested blind using probe **f**. A control probe (sequence **n**) that does not result in fluorescence turn-on upon binding DHEAS was used as a baseline to enable comparisons between the different samples. The observed fluorescence values were sorted based on the known DHEAS concentrations (Figure 3.4.1-4C). The target probe yields a Spearman's rank correlation coefficient of 0.90 ($p < 2.2E-16$) between the average fluorescence and the concentration, whereas the control probe yields a coefficient of 0.42 ($p = 0.16$). These results show that the signal from probe **f** increases monotonically with increasing concentrations of DHEAS whereas that from the control probe does not. Moreover, we verified using a $\chi 2$ goodness-of-fit test that the fluorescence enhancement relative to the control probe observed as a function of concentration is well-described by the Hill-equation (Figure 3.4.1-4D). Taken together, these results show that FIT-aptamers can be utilized for the measurement of clinically relevant concentrations of steroids in serum. Importantly, the FIT strategy enabled us to use a plate reader-based format to make high throughput measurements with sample volumes as low as 10 µL in 30 min (Figure 3.3.3-5). This reduces the volume of serum

required by up to 20-fold compared to routinely used electrochemiluminescence immunoassays and yields immediate results.[395]

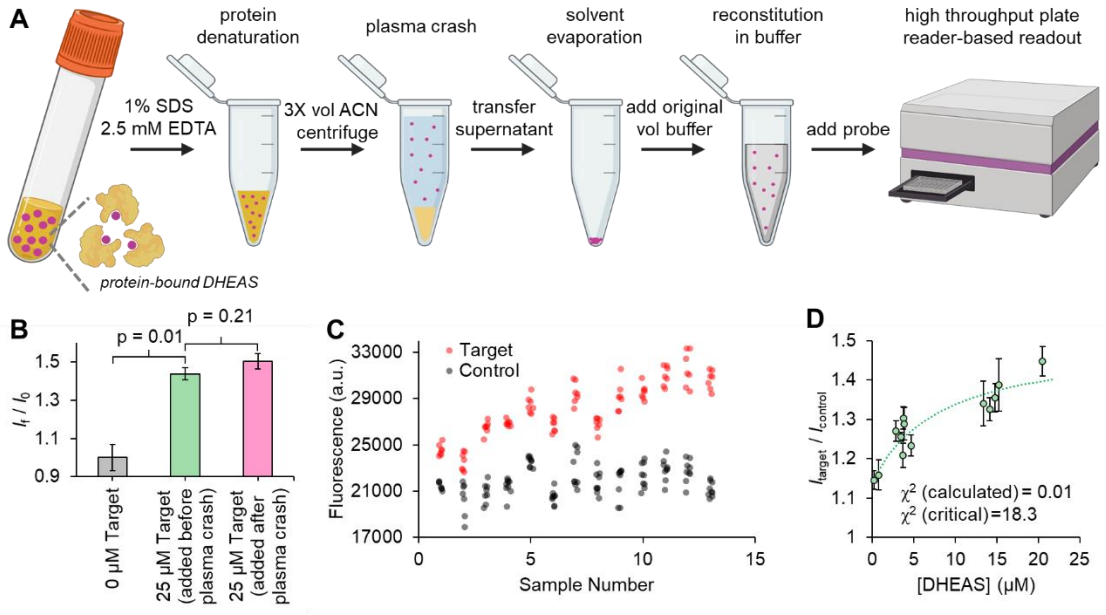

Figure 3.4.1-4. DHEAS measurement in serum. (A) Plasma crash procedure. Created using biorender.com. (B) Fluorescence enhancement of FIT-aptamer **f** after spiking in DHEAS in steroid-free serum. (C) Measured raw fluorescence of target and control probes in clinical serum samples. (D) Fluorescence enhancement in clinical samples plotted against concentration reported by the Abbott Architect assay.

In summary, we have shown that fluorogenic aptamers for steroids can be programmed using a FIT strategy with the aid of simulation guided design. Importantly, our results show that global structural transitions from an unfolded to a folded state are not necessary for the design of FIT-aptamers. If designed correctly, these structures can retain the binding affinity of the original aptamers and enable target detection in complex biological media. Specifically, for steroids, this strategy allows rapid (<30 min), high throughput detection using low sample volumes (10 µL), without the use of complex instrumentation. These results bode well for the use of FIT-aptamers as a new and general strategy for sensing other important biological markers whose binding may lead to subtle changes in aptamer structure.

CHAPTER FOUR

4. Protein Spherical Nucleic Acids for Live-Cell Chemical Analysis

Portions of this chapter reprinted (adapted) with permission from D. Samanta, S. B. Ebrahimi, C. D. Kusmierz, H. F. Cheng, C. A. Mirkin, *J. Am. Chem. Soc.* **2020**, *142*, 13350–13355.

4.1. Introduction

The chemical analysis of live cells at the molecular level provides fundamental insight into dynamic cellular processes, informs about the role of intracellular analytes in disease progression, and has guided the development of new medical diagnostic tools.[117,375,396–398] Although fluorescent probes based on both molecular recognition (binding-based sensing)[375,399] and molecular reactivity (activity-based sensing)[400] have led to significant new capabilities, the majority of techniques either necessitate the fixing or lysis of the cells, the use of cytotoxic transfection reagents, or the genetic encoding of the cells. Specifically, protein- and nucleic acid-based approaches, such as enzyme-linked immunosorbent assays,[401] genetically encoded-fluorescent proteins[402] and RNA sensors,[122] polymerase chain reaction,[403] and fluorescence *in situ* hybridization,[404] are routinely used to detect a wide variety of biological analytes. However, exogenous proteins and nucleic acids are not efficiently internalized by cells; thus, their development into live-cell intracellular probes is challenging.

To overcome these limitations, in this chapter I introduce a powerful new class of intracellular probes based on protein spherical nucleic acids (ProSNAs).[405,406] This design allows analyte detection via a quencher-free approach using either the nucleic acid or the protein component. Additionally, this platform allows the detection of intracellular analytes through binding-based or activity-based sensing. ProSNAs are based on the SNA architecture and consist of a protein core functionalized with a dense shell of radially oriented oligonucleotides. The SNA architecture is ideally suited for making intracellular measurements as it is non-toxic to cells, elicits minimal immune response, can be taken up by cells without the need for transfection reagents, and is more resistant to nuclease degradation compared to traditionally used linear oligonucleotide probes.[165]

Additionally, it allows the intracellular delivery of functional proteins and confers stability against protease degradation.[405,406]

The first examples of SNA-based intracellular probes were NanoFlares (NFs).[44,164] As discussed in Chapter 1, the NF construct consists of a gold nanoparticle core that acts as a quencher. Oligonucleotide duplexes comprising a recognition strand and a shorter fluorophore-labeled reporter strand are immobilized onto the gold nanoparticle through a gold-thiol linkage. Inside the cell, the target of interest displaces the reporter strand as it binds to the recognition sequence, and results in a fluorescence turn on due to separation of the fluorophore and the quencher. By designing the recognition strand to be complementary to nucleic acids in cells, genetic content can be measured.[44,90,98,164,171,174] On the other hand, using aptamer and DNAzyme sequences, ions, small molecules, and proteins can be detected.[95,97,407] NFs allow live-cell genetic and metabolic analyses,[44,95] the sorting and isolation of circulating tumor cells based on variations in genetic profiles,[139] and the identification of diseased tissue *in vivo*.[135,408,409] However, NFs suffer from several limitations. Since their fluorescence is solely dependent on the fluorophore's distance from the gold core, NFs are susceptible to false-positive signals arising from nuclease degradation of the oligonucleotides, dehybridization of the reporter strands, or cleavage at the gold-thiol linkage.[175] In addition, NFs rely on a displacement event for signal generation which retards probe-target binding kinetics.[410] Finally, NFs can only be designed for targets with known nucleic acid-based recognition sequences.[375]

4.2. Materials and Methods

4.2.1. Oligonucleotide design, synthesis, purification, and characterization

4.2.1.1. Design

We have used 3 types of spherical nucleic acid (SNA)-based constructs in this study. There are

(i) Gold NanoFlares (NFs)
   a. With a pH-sensitive i-motif sequence as the recognition strand
   b. With a pH-insensitive control sequence as the recognition strand

(ii) β-galactosidase (β-gal) SNAs
   a. With a pH-sensitive i-motif sequence as the "FIT-aptamer". This construct is referred to as ProTOn
   b. With a pH-insensitive control sequence

(iii) Glucose oxidase SNAs (GOx-SNAs)

The DNA sequences used in designing the SNAs are provided in Table 4.2.1-1. D denotes the location of the forced intercalation dye thiazole orange in the sequence. Note that the 7th T from the 5' end in the design of GOx-SNAs is modified with an amino group (amino-modifier C2 dT).

Table 4.2.1-1. Oligonucleotide sequences used in this study

Abbreviation	**Sequence (from 5' end to 3' end)**
Gold NF i-motif recognition	CCC TAA CCC TAA CCC TAA CCC Cy5 T_{15}-SH
Gold NF control recognition	TTT CTA TCG CGT ACA ATC TGC Cy5 T_{15}-SH
Gold NF i-motif flare	Cy3-A_6 AGG GTT AGG GTT A
Gold NF control flare	Cy3-A_6 AGC AGA TTG TAC G
ProSNA i-motif	5'-DBCO TEG- T_{15} C_4 TAA CDCC TAA C_4 TAA CTCC-3'
ProSNA control	5'-DBCO TEG- T_{15} T_4 TTT TDTT TTT T_4 TTT TTTT-3'
GOx DNA*	DBCO TEG- T_{13}

Cy3 denote cyanine-3. Cy5 denotes cyanine-5. DBCO-TEG denotes 10-(6-oxo-6-(dibenzo[b,f]azacyclooct-4-yn-1-yl)-capramido-N-ethyl)-O-triethyleneglycol-1-[(2-cyanoethyl)-(N,N-diisopropyl)]-phosphoramidite

4.2.1.2. Synthesis, purification, and characterization

All reagents for DNA synthesis were purchased from Glen Research. Oligonucleotides were synthesized using solid-phase phosphoramidite coupling chemistry. Universal or thiolated controlled pore glass (CPG) beads were used as the solid support. Synthesis was performed either using a MerMade12 (MM12, BioAutomation Inc., Plano, Texas, USA) or an ABI 394 instrument at 5 or 10 µmol scales. The oligonucleotides were then cleaved from the CPG beads using standard deprotection techniques (4 h at 55 ºC or 16 h at room temperature using 2 mL of 30% ammonium hydroxide). An Organomation® Multivap® Nitrogen Evaporator was then used to evaporate off the ammonia. The remaining solution was adjusted to 2 mL in volume using nanopure water and filtered through a 0.2 µM syringe filter to remove the CPG beads. The filtrate was subjected to reverse phase high-performance liquid chromatography (RP-HPLC, Varian ProStar 210, Agilent Technologies Inc., Palo Alto, CA, USA) to isolate the product. A C4 or C18 column and a gradient of 0 to 75% B over 45 min (A = triethylammonium acetate buffer, B = acetonitrile) were used. The collected fractions for sequences terminating in a 4,4'-dimethoxytrityl (DMTr) group were lyophilized and re-dissolved in 20% acetic acid for 1 h for detritylation. The cleaved DMTr group was removed by ethyl acetate extraction (3 times). The remaining acidic solution was lyophilized and re-dissolved in water. Sequences not terminating in a DMTr group did not require treatment with acetic acid. Matrix-assisted laser desorption ionization time-of-flight mass spectrometry (MALDI-TOF MS) was used to identify the product. The concentration (c) of the final product was determined using UV-VIS spectroscopy. Specifically, $c = A/\varepsilon$ where A is the absorbance

measured and ε is the extinction coefficient of the oligonucleotide at 260 nm obtained from the IDT Oligo Analyzer Tool.

4.2.2. Synthesis and characterization of thiazole orange (D)

4.2.2.1. General methods

All of the chemicals, reagents, and solvents were purchased as reagent grade from Sigma-Aldrich and used as received unless otherwise stated. Glassware and stir bars were oven-dried at 180 °C prior to use. Flash chromatography was performed with SiO_2 (230–400 mesh ASTM, 0.040–0.063 mm; Fluka). Deuterated solvents were purchased from Cambridge Isotope Laboratories and used as received. ^{1}H and ^{13}C NMR spectra were recorded on a Bruker Avance 400 MHz NMR spectrometer at 298 K, and chemical shifts (δ) are given in parts per million. ^{1}H NMR spectra were referenced to residual proton resonances in the deuterated solvents (methanol-d_4 = δ 3.31), while absolute referencing was applied for heteronuclear NMR spectra (Ξ_C = 25.145020). N-carboxylmethyl-4-methquinolinium bromide was synthesized following literature procedures.[411]

4.2.2.2. Synthesis of thiazole orange derivative

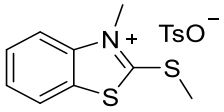

3-Methyl-2-(methylthio)-benzothiazolium tosylate was synthesized as described previously with slight modifications.[411] Solid 2-methylthiobenzothiazole (4.12 g, 22.7 mmol, 1 equiv) was added to neat methyl p-toluenesulfonate (4.66 g, 25 mmol, 1.1 equiv) in an oven-dried round bottom flask and heated to reflux at 130 °C for 1 h. Reaction mixture was cooled to 70 °C, and acetone was added till creamy precipitates formed. Reaction was then refluxed at 70 °C. After 30 min, the mixture was cooled to room temperature, filtered and washed with acetone. The creamy precipitates collected were dried vacuo to yield the product (8.11 g, 22.1 mmol, isolated yield =

97 %). ^{1}H NMR (400 MHz, methanol-d_4) δ 8.20 (ddd, J = 8.2, 1.3, 0.7 Hz, 1H), 8.05 (dt, J = 8.6, 0.8 Hz, 1H), 7.82 (ddd, J = 8.5, 7.3, 1.2 Hz, 1H), 7.71 (ddd, J = 8.3, 7.3, 1.0 Hz, 1H), 7.69 – 7.61 (m, 2H), 7.22 – 7.14 (m, 2H), 4.12 (s, 3H), 3.10 (s, 3H), 2.33 (s, 3H). ^{13}C NMR (101 MHz, MeOD) δ 181.12, 141.97, 141.63, 139.45, 128.62, 127.78, 127.65, 126.41, 124.80, 122.53, 114.37, 34.77, 19.20, 16.42.

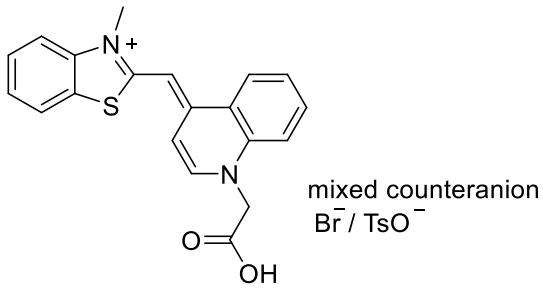

Carboxymethylated thiazole orange was synthesized as described previously with slight modifications.[411] N-carboxylmethyl-4-methquinolinium bromide (1.52 g, 5.39 mmol, 1.25 equiv) and 3-methyl-2-(methylthio)-benzothiazolium tosylate (1.58 g, 4.31 mmol, 1 equiv) were dissolved in dichloromethane. Triethylamine (1.5 mL, 10.8 mmol, 2.5 equiv) was then added. The reaction mixture, which turned dark red immediately, was stirred in dark at room temperature for 16 h. The reaction mixture was dried on a rotary evaporator to give a red residue, which was dissolved in 325 mL of boiling methanol. 815 mL of water was then added to the red solution, which was stored at 4 °C over 3 days for crystallization. The red precipitate formed was collected by filtration, washed with a small amount of cold water, and dried in vacuo to give a red powder (1.64 g, 3.83 mmol, 89 % isolated yield). Note that the product gradually decomposes in solution if it is exposed to light. ^{1}H NMR (400 MHz, methanol-d_4) δ 8.66 – 8.60 (m, 1H), 8.34 (d, J = 7.2

Hz, 1H), 7.96 – 7.86 (m, 2H), 7.75 – 7.56 (m, 4H), 7.49 (dd, J = 7.2, 2.3 Hz, 1H), 7.46 – 7.37 (m, 1H), 6.93 (s, 1H), 5.17 (s, 2H), 4.00 (s, 3H).

4.2.2.3. NMR spectra

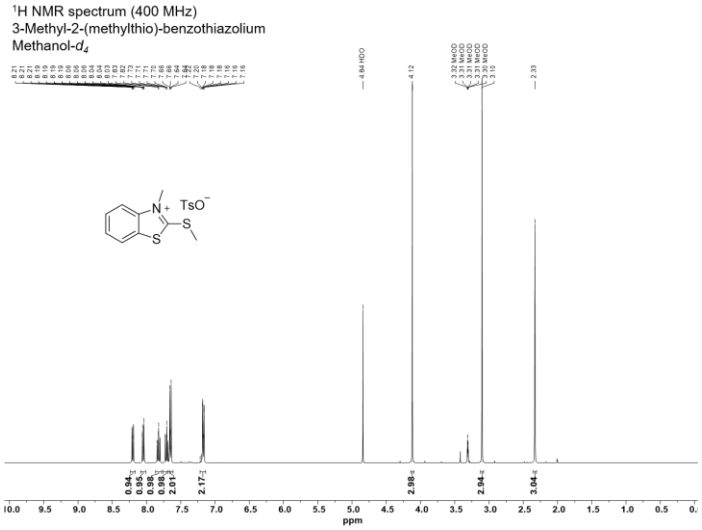

Figure 4.2.2-1. ^{1}H NMR (400 MHz, methanol-d_4, 298 K) spectrum of 3-methyl-2-(methylthio)-benzothiazolium tosylate.

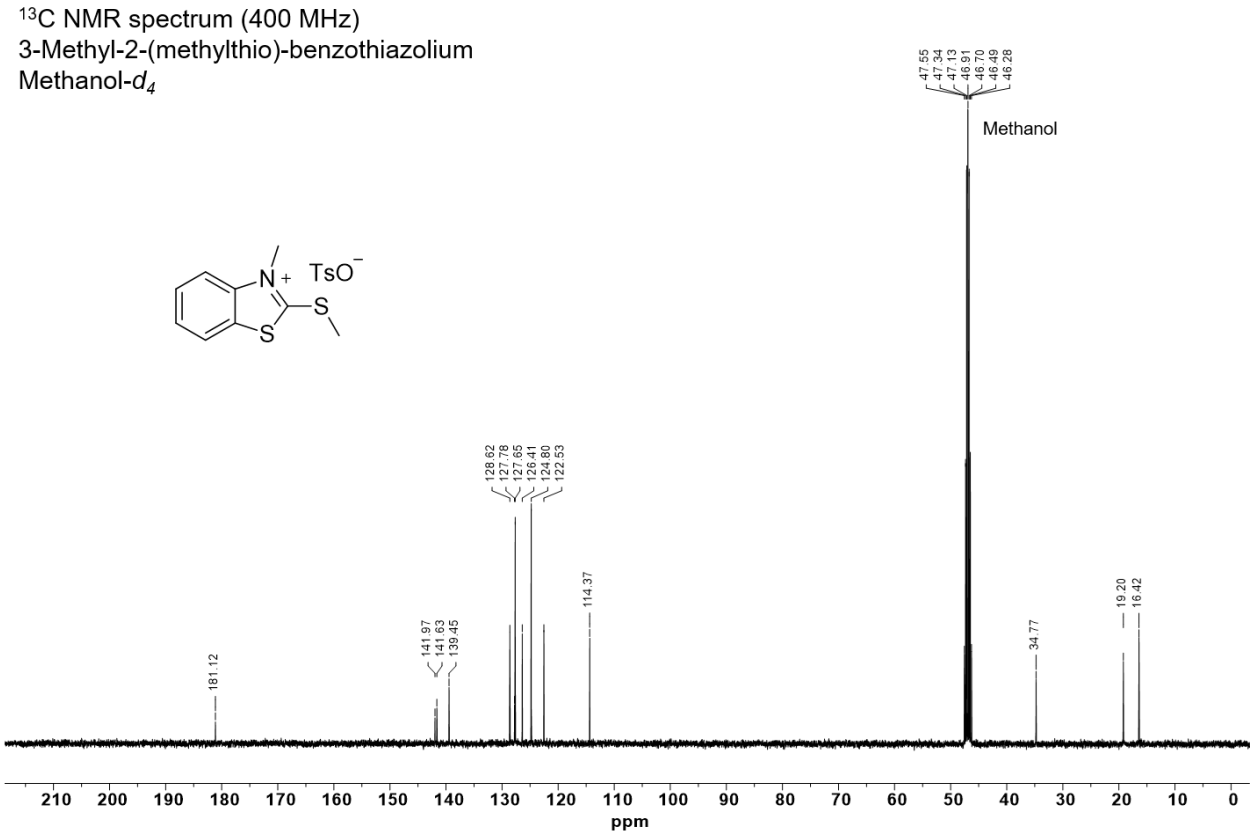

Figure 4.2.2-2. ^{13}C NMR (101 MHz, methanol-d_4, 298 K) spectrum of 3-methyl-2-(methylthio)-benzothiazolium tosylate.

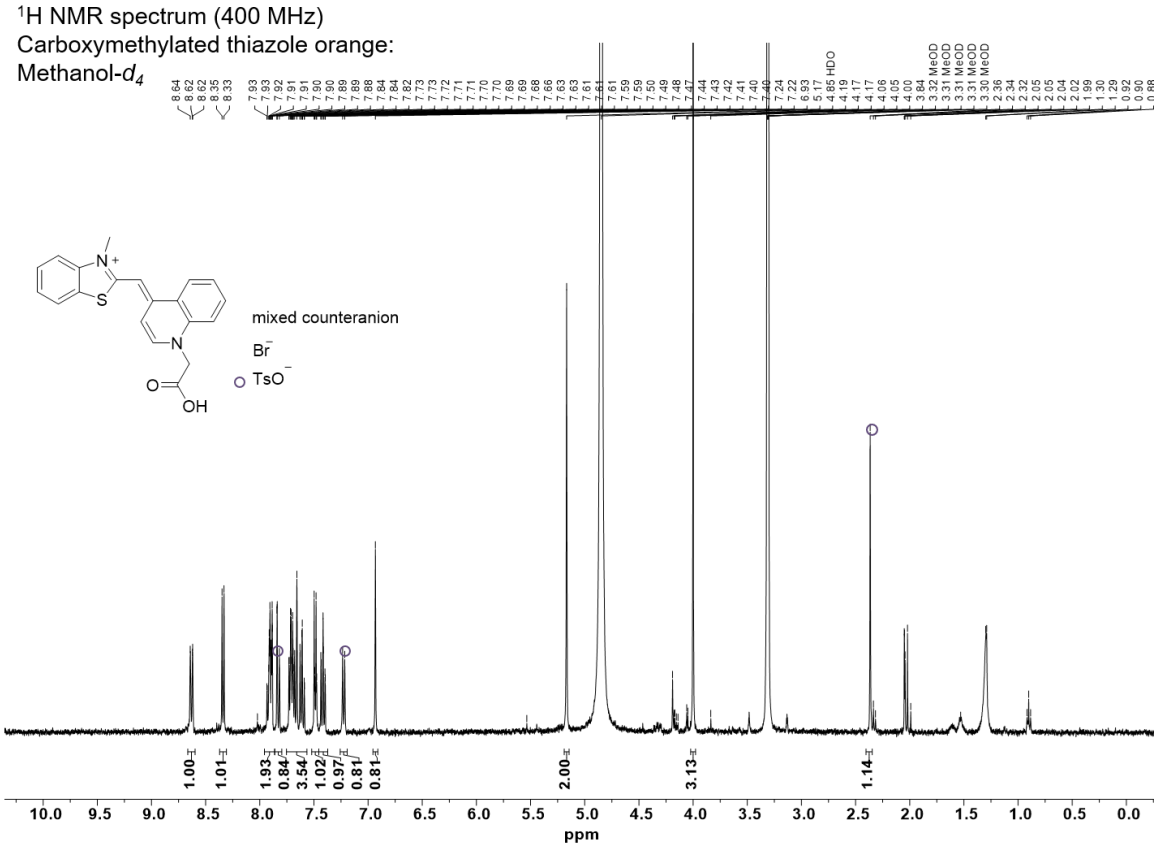

Figure 4.2.2-3. ^{1}H NMR (400 MHz, methanol-d_4, 298 K) spectrum of carboxymethylated thiazole orange.

4.2.3. Coupling of D to oligonucleotide probes

Thiazole orange was conjugated to DNA sequences composed of an amino-modifier (Ntrifluoroacetyl serinol phosphoramidite) according to a previously reported protocol.[378] In a typical reaction, thiazole orange (5 µmol), pyridinium para-toluene sulfonate (5 µmol), N-hydroxysuccinimide (25 µmol), and 1-Ethyl-3-(3- dimethylaminopropyl) carbodiimide (50 µmol) were dissolved in 250 µL dimethylformamide and shaken for 10 min at 30°C. After 10 min, 100 nmol of amino-modified DNA in 250 µL of 0.1 M NaHCO3 was added to the solution and shaken at room temperature for 2h. After 2 h, the reaction mixture was run through a NAP™-10 (GE Healthcare) column to separate away any free dye. To separate DNA sequences with and without the dye modification, RP-HPLC was then run on a C18 column (0 to 75% B, 45 min, A = triethylammonium acetate buffer, B = acetonitrile).

4.2.4. Synthesis, purification, and characterization of i-motif and control gold NFs

In a typical reaction, 2 mL of 13 nm gold NPs were added to a 15 mL falcon tube and supplemented with Tween to a final concentration of 0.2%. 10X PBS was added to the falcon tube such that its final concentration became 1X. The mixture was vortexed for 30 seconds and then sonicated for 30 seconds.

In a separate tube, recognition strand and flare strand were mixed in a 1:1 molar ratio and adjusted to 50 µM concentration in 1X duplexing buffer (30 mM HEPES, 100 mM KOAc, 2 mM MgOAc). This mixture was heated at 95 °C for 5 min and then allowed to cool to room temperature. The duplex was then added to the AuNP mixture at 300 equiv. duplex per AuNP. The subsequent mixture was allowed to incubate for 2 h, at which point 5 M NaCl was added to make the NaCl

concentration 350 mM. After 1 h of further incubation, more 5 M NaCl was added to make the final NaCl concentration 500 mM. The mixture was then shaken for 48 h. After 48 h, the gold NFs were purified using 5 rounds of centrifugation (15000 rcf, 10 min) through successive pelleting and resuspension steps in 1X PBS.

The concentration of the gold NFs was determined via UV-VIS spectroscopy using an extinction coefficient of 2.7 x 10^8 $M^{-1}cm^{-1}$ for 13 nm gold nanoparticles. Next, the number of DNA strands per particle was determined. 40 μL of 50 nM gold NFs were added to 140 uL 8 M urea. 180 μL of 40 mM KCN were added to this mixture. Over the next 5-10 min, the gold nanoparticles were etched completely by KCN and this process could be followed visually as the wine-red color of the nanoparticles disappeared. The solution was heated to 60 ºC for 10 min. The fluorescence of the resultant solution was measured using a plate reader both in the Cy3 (excitation: 488 nm, emission 525 nm) and Cy5 (excitation: 647 nm, emission: 700 nm) channels. The concentration of DNA could be calculated from a calibration curve of the Cy3- and Cy5-labeled recognition and flare strands in the same solvent mixture. All fluorescence measurements were performed in triplicate. The ratio of the concentration of DNA to that of the nanoparticles yielded the number of strands per particle. On average, each gold nanoparticle had ~40 duplexes (one flare strand for every recognition strand).

4.2.5. Synthesis, purification, and characterization of i-motif and control ProSNAs

β-gal ProSNAs were synthesized and characterized following previously reported procedures.[405,406] Lyophilized β-galactosidase (β-Gal) from an E. coli overproducer (Roche) was centrifuged and resuspended in 1X PBS three times using a 100 kDa MWCO Amicon® filter to remove storage salts. Next, a thiol-reactive Alexa Fluor™ 647 C2 Maleimide (ThermoFisher) was

introduced at a ten-fold excess, and the reaction was allowed to proceed overnight at 4 °C in 1X PBS with shaking. Multiple washing cycles were conducted in a 100 kDa MWCO Amicon® filter to remove the unreacted dye, resuspending β-Gal-AF647 in 1X PBS after each centrifuge. Wash cycles were stopped once the filtrate did not have a detectable absorbance signal at ~653 nm, as monitored by a Cary-500 UV-vis spectrophotometer. A 350-fold excess of NHS-PEG_4-Azide (ThermoFisher) was added to β-Gal-AF647 and incubated overnight at 4 °C in 1X PBS with shaking. Unreacted linker was removed by ten wash cycles using a 100 kDa MWCO Amicon® filter, resuspending the β-Gal-AF647-azide in 1X PBS after each centrifugation. The number of Alexa Fluor 647 modifications made to the protein were calculated based on absorbance spectra collected on a Cary-500 UV-vis spectrophotometer and their respective extinction coefficients ($\varepsilon_{\beta\text{-gal}}$ = 1,142,000 $M^{-1}cm^{-1}$ at 280 nm and 596,268 $M^{-1}cm^{-1}$ at 260 nm; $\varepsilon_{AF\text{-}647}$ = 270,000 at 650 nm). The number of PEG_4-azide linker modifications was assessed by MALDI-TOF MS using sinapinic acid (ThermoFisher) as a matrix in a Bruker AutoFlex-III. Each linker addition leads to an increase in 275 m/z. In a typical reaction, 60 molar equivalents (DNA:protein) of DBCO-modified DNA was added to a 1.5 mL Eppendorf tube and dried on a Centrivap. Protein (1X PBS, concentration ~6 μM β-galactosidase) was then added to this DNA and shaken for 3 days (60 eq DNA:protein). After 3 days, the ProSNAs were purified through ~15-20 washes (1X PBS) using a 100 kDa Amicon filter. The number of DNA strands per protein was calculated based on UV-vis spectroscopy ($\varepsilon_{\text{i-motif DNA}}$ = 337,600 $M^{-1}cm^{-1}$ at 260 nm and $\varepsilon_{\text{control DNA}}$ = 315,400 $M^{-1}cm^{-1}$ at 260 nm). Because the DNA's max absorbance (260 nm) overlaps with the protein's max absorbance (280 nm), the AF-647 UV-vis trace was used to back-calculate the protein's concentration. There

were ~6.8 AF-647 dyes per protein. ~30 DNA strands were attached per i-motif ProSNA (ProTOn) and ~40 DNA strands per control ProSNA.

4.2.6. Design, synthesis, purification, and characterization of GOx-SNAs

Due to the absence of chemically accessible cysteine residues on the surface of GOx, both AF-647 and DNA were conjugated to the surface through lysine residues. The relative ratios of the two modifications were controlled by controlling the molar equivalents and the conjugation reaction time. On average, each protein contained ~2 AF-647 dyes and ~28 DNA strands. A simple DBCO-labeled T_{13} sequence was used as the DNA shell to allow probe uptake and as in the case of β-gal, the AF-647 dyes allow the monitoring of probe uptake.

Glucose oxidase protein (Millipore-Sigma G7141) was first dissolved in 0.1 M $NaHCO_3$ at 10 mg/mL. Alexa Fluor 647 NHS Ester (Thermo-Fisher A37573) was dissolved at a concentration 10 mg/mL in DMF. This dye solution was added dropwise to the protein solution while vortexing in 13-fold molar excess. After shaking the mixture for 1 h at 1400 rpm, the unfunctionalized Alexa dye was separated from the protein using a 30 kDa Amicon filter (13,000 rcf at 4 ºC) and washing 10 times using 0.1 M $NaHCO_3$.

The protein was then labeled with PEG-azide to allow subsequent functionalization to DBCO-modified DNA. 300 µL of 50 µM protein in PBS was reacted with 18 µL NHS-PEG_4-Azide for 1.75 h. The mixture was then purified using a 30 kDa Amicon filter by washing with 1X PBS (10 washes, 13,000 rcf at 4 °C).

In a typical DNA functionalization reaction, 300 molar equivalents (DNA:protein) of DBCO-modified DNA was added to a 1.5 mL Eppendorf tube and dried on a Centrivap. Protein (1X PBS,

concentration ~10 μM) was then added to this DNA and shaken for 3 days (300 eq DNA:protein). After 3 days, GOx-SNAss were purified through ~15-20 washes (1X PBS) using a 100 kDa Amicon filter.

The number of dye and DNA per protein was calculated via UV-VIS spectroscopy using the extinction coefficient of the DNA (ε_{DNA} = 113,900 $M^{-1}cm^{-1}$), protein (ε_{GOx} = 267,200 $M^{-1}cm^{-1}$), and the dye ($\varepsilon_{AF\text{-}647}$ = 270,000 $M^{-1}cm^{-1}$).

4.2.7. Fluorescence experiments

All experiments were done in triplicate unless otherwise stated.

4.2.7.1. Experiments with i-motif and control gold NFs

4.2.7.1.1. Fluorescence melt to determine duplex melting temperature

The melting temperature of the flare/recognition strand duplex was determined by fluorescence melt experiments. This was done to ensure that the i-motif recognition/flare and control recognition/flare have comparable melting temperatures. ~3 nM by gold i-motif or control NFs were added to pH 7.5 clamping buffer (Thermo-Fisher P35379). The temperature of a BioTek Cytation 5 fluorescence plate reader was set to *x* °C (where *x* = 28, 29, 31, 33, 35, 37, 39, 41, 43, 45, 47, 49, 51, 53, 55, 57, 59, 61, 63, 65) and samples were shaken for 5 min. After 5 min, a fluorescence reading was taken, acquiring a fluorescence reading at each temperature (excitation: 554 nm, emission: 600 nm for the Cy3 dye; excitation: 647 nm, emission: 700 nm for the Cy5 dye).

4.2.7.1.2. pH sensitivity of i-motif gold NFs in buffer

i-motif or control NFs were incubated in clamping buffer of varying pH to assess the response of the constructs to pH. The pH of buffer was adjusted using NaOH. 1.7 nM by gold i-motif or control NF was added to buffer of pH 4.5 5.0, 5.5, 6.0, 6.5, 7.0, 7.5 and incubated for 30 min at 37 °C. A BioTek Cytation 5 fluorescence plate reader (excitation 554 nm, emission 600 nm for the Cy3 dye, excitation 647 nm, emission 690 nm for the Cy5 dye) was used to measure the fluorescence at each pH.

4.2.7.1.3. Fluorescence response of gold NFs in presence of nuclease in buffer

In triplicate, 2 nM (by gold) was added to 100 µL 1X DNAse buffer and allowed to incubate at 37 °C for 30 min. After 30 min, 10 µL of 0.2 U/µL DNAse I (Themo-Fisher AM2224) was added to each well (10 µL of water was added to wells not treated with DNAse as a DNAse free control). Fluorescence was monitored on a BioTek Cytation 5 plate reader (excitation 554 nm, emission 600 nm for the Cy3 dye, excitation 647 nm, emission 690 nm for the Cy5 dye) every 1 min over the course of 15 min.

4.2.7.1.4. Change of fluorescence signal over time of gold NFs *in cellulo*

MDA-MB-231 cells were treated in a 24 well plate with 1 nM (by gold) i-motif or control NFs in Opti-MEM (Thermo-Fisher 31985062). All cells were pulsed for 1 h and chased for either 0, 2, or 4 h in triplicate. Cells were washed with 400 µL Opti-MEM before the pulsing step and 400 µL Opti-MEM before the chasing step. After the chasing step, cells were detached from the plate using 1X TrypLE (Thermo-Fisher 12604021) with added DAPI and then analyzed using flow cytometry (BD LSRFortessa and BD Symphony A3).

4.2.7.2. Experiments with i-motif and control ProSNAs

4.2.7.2.1. pH sensitivity of ProTOn in buffer

i-motif or control ProSNAs were incubated in clamping buffer of varying pH to assess the response of the constructs to pH. 500 nM (by DNA) of ProTOn or control ProSNA were added to buffer of pH 5.0, 5.5, 6.0, 6.5, 7.0, and 7.5 in triplicate at room temperature. A BioTek Cytation 5 fluorescence plate reader (excitation 485 nm, emission 527 nm for the thiazole orange dye, excitation 647 nm, emission 690 nm for the Alexa Fluor 647 dye) was used to measure the fluorescence at each pH.

4.2.7.2.2. Fluorescence response of ProSNAs in presence of nuclease in buffer

In triplicate 500 nM (by DNA) of i-motif or control ProSNA was added to 100 µL 1X DNAse buffer and incubated at 37 °C for 15 min. 10 µL of 0.2 U/µL DNAse I was added to induce nuclease degradation. 10 µL of water was added to the wells not treated with DNAse I as a control. The fluorescence was monitored on a BioTek Cytation 5 plate reader (excitation 485nm, emission 528 nm for the thiazole orange dye) every 1 min over the course of 15 min.

4.2.7.2.3. Response of ProSNAs to proteases in buffer

For this specific study, the ProSNA used was comprised of β-Galactosidase densely functionalized with a $(sp18)_2T_{30}$ sequence (~34 DNA per protein). The native protein and the ProSNA were incubated with a 250 mg L^{-1} Trypsin (Gibco) in 1X PBS at 37°C with shaking. As the degradation reaction proceeded, aliquots were removed every ten minutes for a total of 70 min and loaded onto a 7.5% Mini-PROTEAN TGX precast gel (BioRad). The protein bands were visualized by staining using a SimplyBlue SafeStain (Thermo Fisher).

4.2.7.2.4. Change of fluorescence signal over time of ProSNAs *in cellulo*

MDA-MB-231 cells were treated in a 24 well plate with 500 nM (by DNA) of ProTOn or control ProSNAs. All cells were pulsed for 1 h and chased for either 0, 2, or 4 h in triplicate. Cells were washed with 400 µL Opti-MEM before the pulsing step and 400 µL Opti-MEM before the chasing step. After the chasing step, cells were detached from the plate using 1X TrypLE containing DAPI and then analyzed using flow cytometry.

4.2.7.2.5. Fluorescence response of i-motif ProSNA after clamping cellular pH

MDA-MB-231 cells were treated in a 24 well plate with 500 nM (by DNA) of ProTOn or control ProSNA. Cells were treated for 3 h, after which they were washed once with 400 µL Opti-MEM and subsequently detached using 1X TrypLE. Each well of the plate was then pipetted into separate Eppendorf tubes, after which tubes were centrifuged to pellet the cells. The supernatant was aspirated off, and cells were suspended in pH 5.5 or pH 7.5 clamping buffer for 10 min before being analyzed by flow cytometry. Control cells not treated with SNAs were also analyzed to ensure that different pH's do not alter the autofluorescence of the cells. As a control, commercially available pHrodo™ Red AM Intracellular pH Indicator (Thermo Fisher P35372) was also used to measure the fluorescence difference between cells clamped at pH 5.5 and pH 7.5. Cells were treated according to manufacturer protocol with no modification.

4.2.7.3. Experiments with GOx-SNAs

4.2.7.3.1. Fluorescence response of GOx-SNAs to glucose in buffer

Varying concentrations of glucose (in 1X PBS) were added to the wells of a 96 well plate, whereby the concentration of glucose was halved in each well through a half serial dilution (a separate set of wells were prepared that had 0 mM glucose). All wells contained 5 µM FBBBE (Cayman

Chemical 14606). The plate was then allowed to incubate for 15 min at 37 °C. After 15 min, an automatic dispensing unit on a BioTek Cytation 5 fluorescence plate reader was used to add GOx-SNAs to each well at a final concentration of 20 nM by protein (a buffer only set of wells was also prepared). After addition, the BioTek Cytation 5 plate reader was used to shake the sample for 15 s, and subsequently a fluorescence reading was taken every 3 min over 2 h (excitation 460 nm, emission 530 nm for FBBBE, excitation 640 nm, emission 700 nm for the Alexa Fluor 647 dye).

A separate control experiment was done to ensure that the dye fluorescence in the absence of GOx-SNAs does not change with increasing glucose concentration. Varying concentrations of glucose (in 1X PBS) were added to the wells of a 96 well plate, whereby the concentration of glucose was halved in each well through a half serial dilution (a separate set of wells were prepared that had 0 mM glucose). All wells contained 5 μM FBBBE. The sample was incubated at 37°C for 30 min, after which a fluorescence reading was taken every 3 min over 2 h (excitation 460 nm, emission 530 nm for FBBBE).

4.2.7.3.2. GOx-SNAs fluorescence response to “off-target” sugars in buffer

In triplicate, 20 nM (by protein) GOx-SNAs was co-incubated with 5 μM FBBBE and one different sugar (either 5 mM glucose, sucrose, xylose, mannose, glucose 6-phosphate, fructose, maltose, lactose, or galactose) in 1X PBS. Controls for GOx-SNAs+FBBBE, FBBBE only, GOx-SNAs only, and 1X PBS only were also done. Samples were incubated at 37 °C for 30 min after which a fluorescence reading was taken on a BioTek Cytation 5 plate reader (excitation 460 nm, emission 530 nm for the FBBBE dye).

In another experiment, 10 nM (by protein) GOx-SNAs were incubated with 5 μM FBBBE and all the sugars (5 mM glucose, sucrose, xylose, mannose, glucose 6-phosphate, fructose, maltose, lactose, and galactose) in 1X PBS. Controls for GOx-SNAs+FBBBE+5 mM glucose, GOx-SNAs+FBBBE, FBBBE only, GOx-SNAs only, and 1X PBS only were also done. Samples were incubated at 37 °C for 30 min after which a fluorescence reading was taken on a BioTek Cytation 5 plate reader (excitation 485 nm, emission 528 nm for the FBBBE dye).

4.2.7.3.3. GOx-SNAs activity versus native protein

20 nM native glucose oxidase protein or 20 nM GOx-SNAs were added to 1X PBS in the presence of 1 mM glucose and 5 μM FBBBE at 37 °C in triplicate. A reading of fluorescence was taken every 3 min over 2 h on a BioTek Cytation 5 (excitation 485 nm, emission 527 nm for the FBBBE dye, excitation 647 nm, emission 690 nm for the Alexa Fluor 647 dye).

4.2.7.3.4. Fluorescence response of GOx-SNAs in different cell lines

Adherent cells were detached from culture dish using 1X TrypLE and subsequently pelleted by centrifugation. The supernatant was removed and the cells were washed twice with 6 mL glucose free DMEM (Thermo-Fisher 11966025) through successive pelleting and resuspension steps. After the second wash, the cell suspension was split into 3 different treatment groups each run in triplicate. In two of the treatment groups, cells were suspended in glucose free media only and in the third treatment group the cells were suspended in glucose free media containing 40 nM GOx-SNAs (by protein). After 30 min, cells were pelleted by centrifugation, the supernatant was removed, and all cells were washed twice with 1 mL glucose free media through successive pelleting and resuspension steps. In the first treatment group, previously untreated cells were

resuspended in DMEM supplemented with 25 mM glucose (untreated group). In the second treatment group, previously untreated cells were resuspended in DMEM supplemented with 25 mM and 50 μM FBBBE (dye only group). In the third treatment group, previously SNA treated cells were resuspended in DMEM supplemented with 25 mM and 50 μM FBBBE (dye+SNA group). After 30 min, cells were pelleted by centrifugation, resuspended in 1X TrypLE containing DAPI, and analyzed using flow cytometry. This procedure was the same for all adherent cell lines.

Suspension cells were pelleted by centrifugation and washed twice with 6 mL glucose free DMEM through successive pelleting and resuspension steps. After the second wash, the cell suspension was split into 3 different treatment groups each run in triplicate. In two of the treatment groups, cells were suspended in glucose free media only and in the third treatment group the cells were suspended in glucose free media containing 40 nM GOx-ProSNA (by protein). After 30 min, cells were pelleted by centrifugation, the supernatant was removed, and all cells were washed twice with 1 mL glucose free media through successive pelleting and resuspension steps. In the first treatment group, previously untreated cells were resuspended in DMEM supplemented with 25 mM glucose (untreated group). In the second treatment group, previously untreated cells were resuspended in DMEM supplemented with 25 mM and 50 μM FBBBE (dye only group). In the third treatment group, previously SNA treated cells were resuspended in DMEM supplemented with 25 mM and 50 μM FBBBE (dye+SNA group). After 30 min, cells were pelleted by centrifugation, resuspended in 1X TrypLE containing DAPI, and analyzed using flow cytometry. This procedure was the same for all suspension cell lines.

4.2.7.3.5. *In cellulo* fluorescence response of GOx-SNAs to varying glucose concentrations

EL4 suspension cells were pelleted by centrifugation and washed twice with 6 mL glucose free DMEM through successive pelleting and resuspension steps. After the second wash, the cell suspension was split into different treatment groups each run in triplicate. The cells were suspended in glucose free media containing 40 nM GOx-SNAs (by protein). After 30 min, cells were pelleted by centrifugation, the supernatant was removed, and all cells were washed twice with 1 mL glucose free media through successive pelleting and resuspension steps. The cells were then resuspended in DMEM containing 50 μM FBBBE with 0 mM or 25 mM glucose. After 30 min, cells were pelleted by centrifugation, resuspended in TrypLE containing DAPI, and analyzed using flow cytometry. Relative glucose levels in cells measured by flow cytometry were compared with glucose levels measured in cell lysates using a commercially available glucose assay kit (**Section 4.2.7.3.8**).

4.2.7.3.6. In cellulo fluorescence response of GOx-SNAs to increase in glucose uptake

The insulin-sensitive MC38 cell line was used in this study. MC38 cells were detached from culture dish using 1X TrypLE and subsequently pelleted by centrifugation. The supernatant was removed and the cells were washed twice with 6 mL glucose free DMEM (Thermo-Fisher #11966025) through successive pelleting and resuspension steps. After the second wash, the cell suspension was split into different treatment groups, each run in triplicate. The cells were suspended in glucose-free media containing 40 nM GOx-SNAs (by protein). After 30 min, cells were pelleted by centrifugation, the supernatant was removed, and all cells were washed twice with 1 mL glucose-free media through successive pelleting and resuspension steps. The cells were resuspended in DMEM containing 5 mM glucose and 50 μM FBBBE with 0 nM or 100 nM insulin

from Thermo Fisher catalog #12585014. After 30 min, cells were pelleted by centrifugation, resuspended in TrypLE containing DAPI, and analyzed using flow cytometry.

4.2.7.3.7. *In cellulo* fluorescence response of GOx-SNAs to inhibition of glucose uptake

EL4 suspension cells were pelleted by centrifugation and washed twice with 6 mL glucose free DMEM through successive pelleting and resuspension steps. After the second wash, the cell suspension was split into different treatment groups, each run in triplicate. The cells were suspended in glucose-free media containing 40 nM GOx-SNAs (by protein). After 30 min, cells were pelleted by centrifugation, the supernatant was removed, and all cells were washed twice with 1 mL glucose-free media through successive pelleting and resuspension steps. The cells were resuspended in DMEM containing 25 mM glucose and 50 µM FBBBE with 0 µM or 10 µM cytochalasin B from Millipore Sigma catalog #C6762. After 30 min, cells were pelleted by centrifugation, resuspended in TrypLE containing DAPI, and analyzed using flow cytometry. Relative glucose levels in cells measured by flow cytometry were compared with glucose levels measured in cell lysates using a commercially available glucose assay kit (**Section 4.2.7.3.8**).

4.2.7.3.8. Measurement of glucose in cell lysate

EL4 cells were pelleted by centrifugation and washed twice with 6 mL glucose free DMEM through successive pelleting and resuspension steps. After the second wash, the cell suspension was split into 3 different treatment groups each run in triplicate. In all of the treatment groups, cells were first suspended in glucose free media. After 30 min, cells were pelleted by centrifugation, the supernatant was removed, and then cells were treated in 3 groups. In the first treatment group, cells were resuspended in DMEM containing no glucose (0 mM glucose

treatment group). In the second treatment group, cells were resuspended in DMEM supplemented with 25 mM glucose and 10 μM cytochalasin B (glucose inhibitor group). In the third treatment group, cells were resuspended in DMEM supplemented with 25 mM glucose (25 mM glucose treatment group). After 30 min, cells were combined and pelleted by centrifugation, the supernatant was removed, and cells were washed twice with 6 mL DPBS through successive pelleting and resuspension steps. After the 2nd wash, cells were resuspended in 1 mL of glucose assay buffer (Abcam 169559). Cells were then lysed through 5 freeze-thaw cycles.

After lysis, cells were centrifuged to remove any cellular debris and the supernatant was collected for further analysis. A glucose assay kit (Abcam 169559) was used to measure relative glucose concentrations between the 3 different conditions (150,000 cells analyzed in each well). Lysate was first filtered through a 10 kDa Amicon filter to remove any interfering proteins, and then assayed according to the manufacturer protocol using a BioTek Cytation 5 fluorescence plate reader.

4.2.8. Data analysis and statistics

All figures provided show the mean of three independent readings unless otherwise mentioned. Error bars correspond to one standard deviation. For Figure 4.4.1-2, the p-value was determined via a t-test using a one-tailed hypothesis (this is because fluorescence at pH 5.5 should be higher than fluorescence at pH 7.5).

4.3. Results

4.3.1. i-motif and control gold NFs

4.3.1.1. Fluorescence melt to determine the melting temperature of flare strands

For a fair comparison of the false-positive signal obtained from gold NFs, it is important to ascertain that the flares strands bind to the recognition sequences with similar affinity. As a proxy for the binding affinity, we investigated the melting behavior of the duplexes. When the flare strand is hybridized to the recognition sequence, its proximity to the gold nanoparticle quenches its fluorescence. However, as the temperature of the sample is gradually increased, DNA dehybridization occurs. Therefore, the fluorescence of the flare sequence gradually increases as it is separated from the gold nanoparticle. From the figure below, we observe that the melting temperatures of the flare strands are nearly identical for both the i-motif and the control gold NFs.

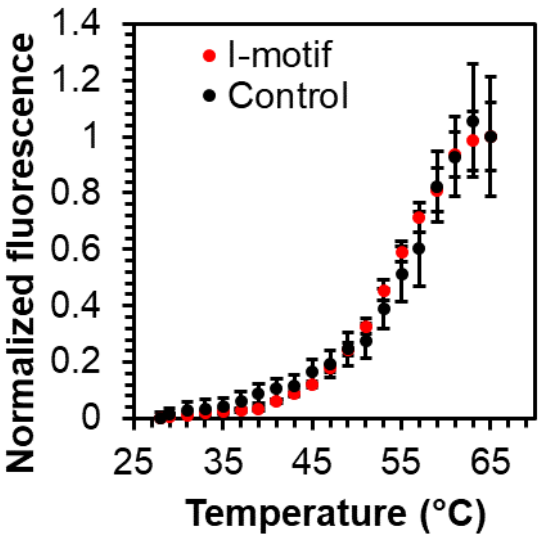

Figure 4.3.1-1. Fluorescence melt experiment to determine melting temperature of pH-sensitive i-motif and pH-insensitive control NFs recognition/flare duplex. It can be seen from the plot that the melting temperatures are nearly identical. Data points and error bars represent the mean and standard deviation of 3 replicates, respectively.

4.3.1.2. pH-sensitivity of i-motif gold NFs in buffer

~1.7 nM of i-motif and control gold NFs were subjected to different pH between 7.5 and 4.5 at 37 °C and their fluorescence was monitored. The fluorescence of I-motif gold NFs increases by up to ~3.5-fold as the pH decreases due to the formation of i-motif structures and displacement of the flare sequence. In contrast, the fluorescence of the pH-insensitive control NF does not change significantly in this pH range.

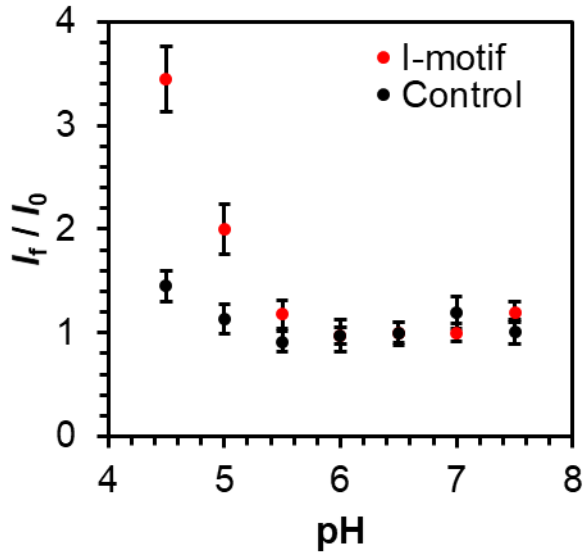

Figure 4.3.1-2. Fluorescence enhancement (I_f / I_0) versus pH for gold NF constructs in buffer. Fluorescence enhancement is defined as the fluorescence intensity of the solution at a given pH (I_f) relative to the least fluorescence intensity of the solution across all the pH tested (I_0). All fluorescence intensities are corrected for the fluorescence intensity of the buffer. Data points and error bars represent the mean and standard deviation of three replicates, respectively.

4.3.1.3. Fluorescence response of gold NFs in the presence of nucleases in buffer

To investigate the effect of nuclease degradation on gold NFs, 2 nM gold NFs were incubated with 2 U DNAse I for at 37 °C. In the presence of DNAse I, the fluorescence increases over time for both the i-motif and the control sequence. In contrast, in the absence of DNAse I, the fluorescence remains unchanged. These results show that nuclease degradation leads to over 15-fold fluorescence enhancement in the absence of a recognition event, giving rise to false-positive signals.

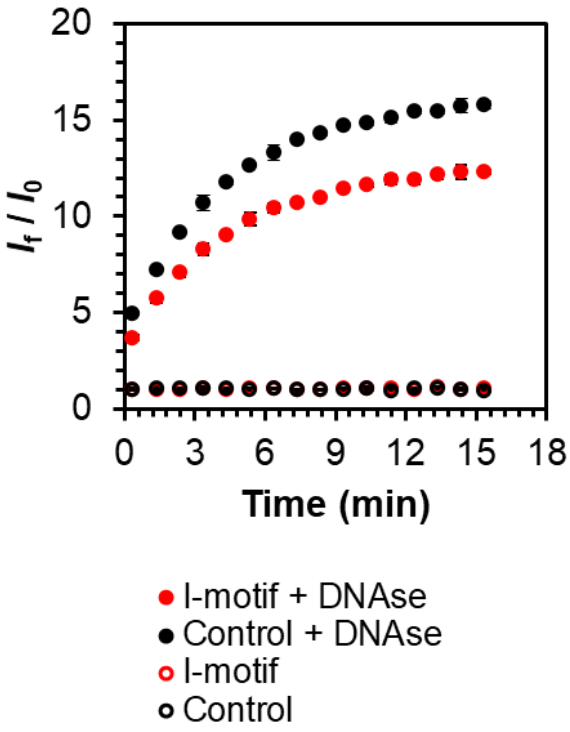

Figure 4.3.1-3. Fluorescence enhancement over time of 100 µL of 2 nM i-motif or control gold NF in the presence of 10 µL of 0.2 U/µL DNAse I. Fluorescence enhancement is defined as the fluorescence intensity of the solution at a given time (I_f) relative to the initial fluorescence intensity of the same solution (I_0). All fluorescence intensities are corrected for the fluorescence intensity of the buffer. In the presence of DNAse I, the fluorescence increases by over 15-fold while in the absence of DNAse I, the fluorescence remains unchanged. Data points and error bars represent the mean and standard deviation of three replicates, respectively.

4.3.1.4. Change of fluorescence signal over time of control gold NFs *in cellulo*

To determine the extent of false-positive signal obtained from NFs in cells, pulse-chase experiments were performed with the control gold NFs. 1 nM of the control NFs were incubated with MDA-MB-231 cells for 1 h in serum-free media. The cells were then washed thoroughly and after additional 0, 2, and 4 hours, they were analyzed by flow cytometry. The fluorescence from the flare strand was monitored and it was found to increase over time. These results show a time-dependent false-positive fluorescence signal is observed from gold NFs in cells.

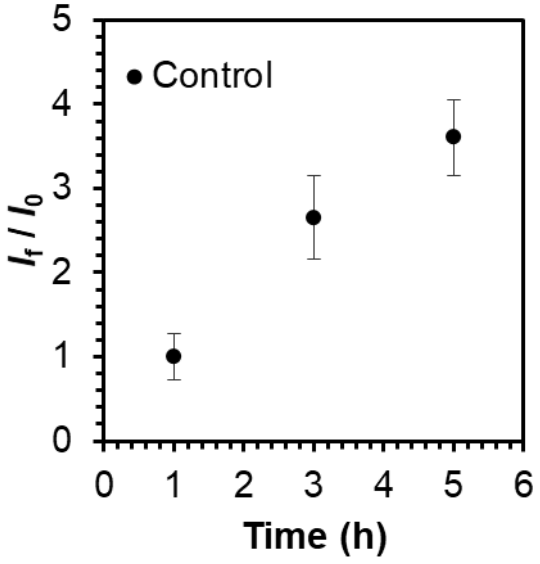

Figure 4.3.1-4. Fluorescence enhancement over time of MDA-MB-231 cells treated with control gold NFs. Fluorescence enhancement is defined as the mean fluorescence intensity of the cells at a given time (I_f) relative to the mean fluorescence intensity (I_0) at the initial timepoint. All fluorescence intensities are corrected for the mean fluorescence intensity of untreated cells. Time 1 h corresponds to a 1 h pulse, 0 h chase. Time 3 h corresponds to a 1 h pulse, 2 h chase. Time 5 h corresponds to 1 h pulse, 4 h chase. The fluorescence increases by ~3.5 fold over time. Data points and error bars represent the mean and standard deviation of three replicates, respectively.

4.3.2. ProTOn and control ProSNAs

4.3.2.1. Fluorescence response of ProSNAs in presence of nuclease in buffer

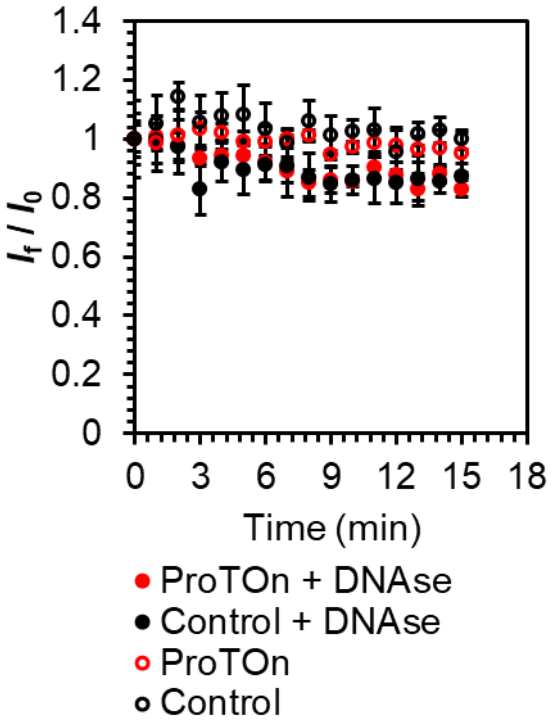

Figure 4.3.2-1. Fluorescence enhancement over time of 100 µL of 500 nM (by DNA) of ProTOn or control ProSNA in the presence of 10 µL of 0.2 U/µL DNAse I. The fluorescence of samples without DNAse I was monitored over time as a control. Fluorescence enhancement is defined as the fluorescence intensity at a given time (I_f) relative to the fluorescence intensity (I_0) at the initial timepoint. All fluorescence intensities are corrected for the fluorescence intensity of the buffer. Data points and error bars represent the mean and standard deviation of three replicates, respectively.

4.3.2.2. Change of fluorescence signal over time of control ProSNAs *in cellulo*

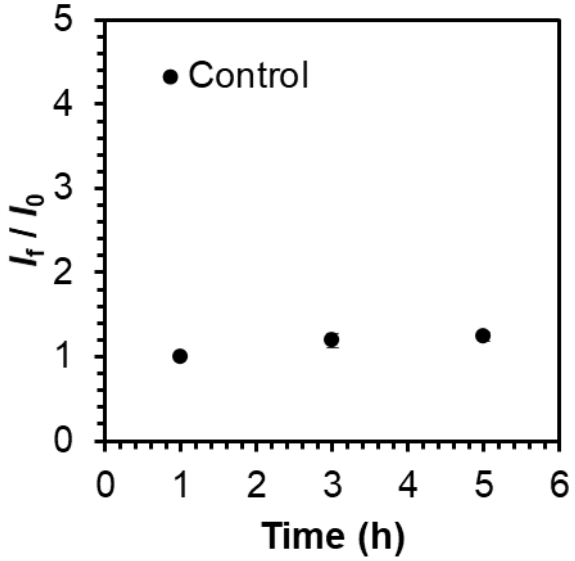

Figure 4.3.2-2. Fluorescence enhancement over time of MDA-MB-231 cells treated with control ProSNAs. Fluorescence enhancement is defined as the mean fluorescence intensity of the cells at a given time (I_f) relative to the mean fluorescence intensity (I_0) at the initial timepoint. All fluorescence intensities are corrected for the mean fluorescence intensity of untreated cells. Time 1 h corresponds to a 1 h pulse, 0 h chase. Time 3 h corresponds to a 1 h pulse, 2 h chase. Time 5 h corresponds to a 1 h pulse, 4 h chase. Unlike the case of gold NFs (Figure 4.3.1-4), the fluorescence does not significantly change over time. Data points and error bars represent the mean and standard deviation of three replicates, respectively.

4.3.2.3. Fluorescence response of pHrodo™ Red AM Intracellular pH Indicator

To benchmark ProTOn against a commercially available intracellular pH indicator, we studied the pH response of pHrodo™ Red AM. This hydrophobic pH-sensitive dye is cell permeable. In the cell, non-specific esterases cleave the AM ester groups and, consequently, the dye is retained intracellularly. We studied the pH response of pHrodo™ Red AM both in buffered solutions as well as in cells clamped to specific pH.

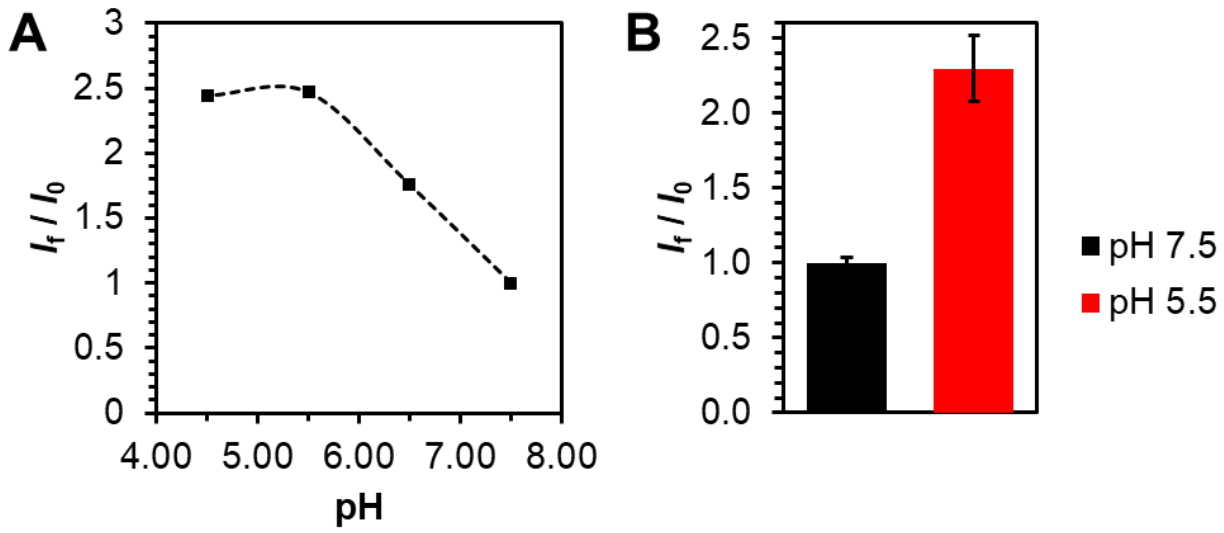

Figure 4.3.2-3. Fluorescence enhancement of pHrodo™ Red in (A) buffer at different pH and (B) cells clamped at different pH. Fluorescence enhancement is defined as the fluorescence intensity of the pHrodo™ Red solution/cells at a given pH (I_f) relative to the fluorescence intensity (I_0) at pH 7.5. All fluorescence intensities are corrected for the fluorescence intensity of the buffer/untreated cells. Intracellularly, pHrodo results in approximately ~2-fold fluorescence enhancement when clamped at pH 5.5 relative to pH 7.5. Data points and error bars represent the mean and standard deviation of three replicates, respectively.

4.3.2.4. The ProSNA architecture protects the protein against protease degradation

To demonstrate the effectiveness of the SNA architecture in protecting a protein from protease degradation, both the native protein and the ProSNA were incubated with a protease (trypsin) and aliquots of this degradation reaction were loaded on an SDS-PAGE gel. We observed that the native protein incubated with trypsin produced several lower molecular weights corresponding to degradation products after 10 minutes. Furthermore, the intensity of these degradation products increased with time. However, with the ProSNA these degradation bands were not observed suggesting that the DNA shell is able to partially protect the protein from substantial degradation by trypsin.

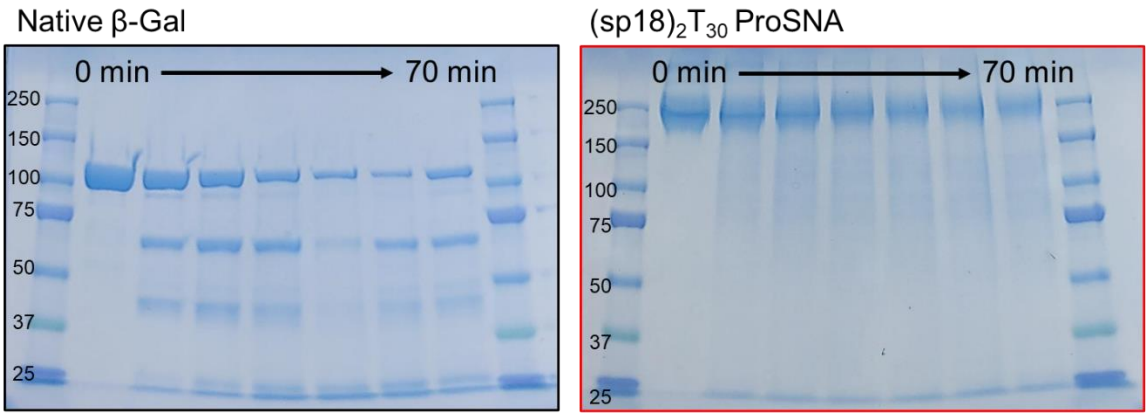

Figure 4.3.2-4. SDS-PAGE gel of β-gal and β-gal ProSNA treated with trypsin (protease) shows that while β-gal degrades over a time course of 70 min (as evidenced by the appearance of multiple bands at lower molecular weights), β-gal ProSNA does not. The β-gal ProSNA used in this specific study consists of the DNA sequence 5'-DBCO-$(sp18)_2T_{30}$-3'.

4.3.3. GOx-SNAs

4.3.3.1. GOx-characterization

Since this is the first report of GOx-SNAs, we provide UV-Vis characterization data below. We note that native GOx has an absorbance peak at 280 nm. Upon modifying the GOx with AF-647 and PEG azides (i.e. for GOx-AP), an additional absorbance peak is observed at 650 nm corresponding to AF-647. Upon further functionalization with DNA (i.e. for GOx-SNAs), an additional peak is observed at 260 nm corresponding to the DNA. Based on the extinction coefficients of the GOx, AF-647, and DNA, the number of AF-647 per GOx-SNA calculated to be ~2 while the number of DNA strands were calculated to be ~28.

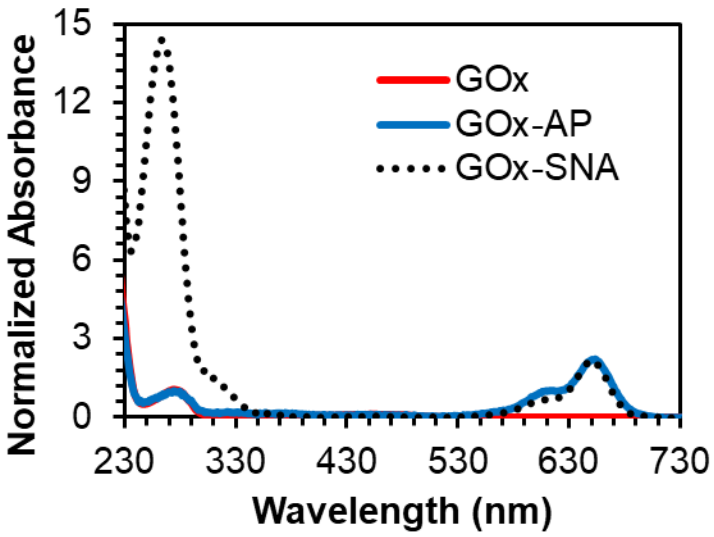

Figure 4.3.3-1. UV-Vis characterization of GOx-SNAs.

4.3.3.2. Activity of GOx-SNAs compared to native GOx

To determine the effect of conjugation of DNA to GOx on its catalytic activity, we incubated identical concentrations (20 nM) of GOx and GOx-SNAs with and without 1 mM glucose in 1X PBS containing 5 µM FBBBE at 37 °C. GOx catalyzes the conversion of glucose to gluconic acid with concomitant production of hydrogen peroxide. The hydrogen peroxide formed reacts with FBBBE and cleaves the boronate ester groups, yielding highly fluorescent fluorescein. We observe from the figure below that the fluorescence increases significantly over time in the presence of glucose. Importantly, the increase in fluorescence for both GOx and GOx-SNAs is nearly identical showing that the activity of GOx is retained in SNA.

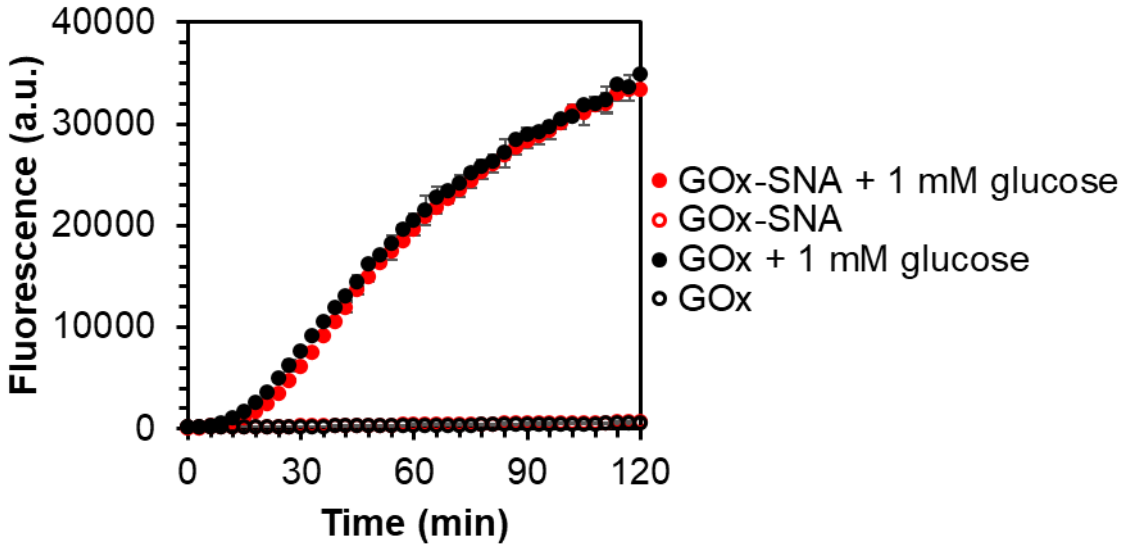

Figure 4.3.3-2. Comparison of catalytic activity of GOx and GOx-SNAs at 37 °C. 20 nM GOx-SNA or 20 nM native GOx are treated with 0 mM and 1 mM glucose in 1X PBS containing 5 µM FBBBE. The fluorescence at each time point is corrected for the fluorescence of the dye alone in buffer. The fluorescence is monitored by exciting FBBBE at 485 nm and collecting the emission at 528 nm. The results show that the protein's native activity is retained in the SNA form. Data points and error bars represent the mean and standard deviation of three replicates, respectively.

4.3.3.3. Response of GOx-SNAs to increasing glucose concentrations in buffer

To determine the response of GOx-SNAs to increasing glucose concentrations in buffer, we incubated 20 nM GOx-SNAs with 5 µM FBBBE in 1X PBS at 37 °C and added varying amounts of glucose between 0-5 mM. The fluorescence from FBBBE was monitored over a period of 2 h. A calibration curve was constructed at the 30-min time point and the 2 h time point. The limit of detection (LOD) was determined at each time point by the $3\sigma/m$ method, where σ denotes the standard deviation of the response and m denotes the initial slope of the calibration curve. The LODs were to be ~17 µM and ~5 µM at 30 min and 2 h, respectively. Both LODs are well below the typical concentration of glucose in cells (0.1-2 mM).[412,413]

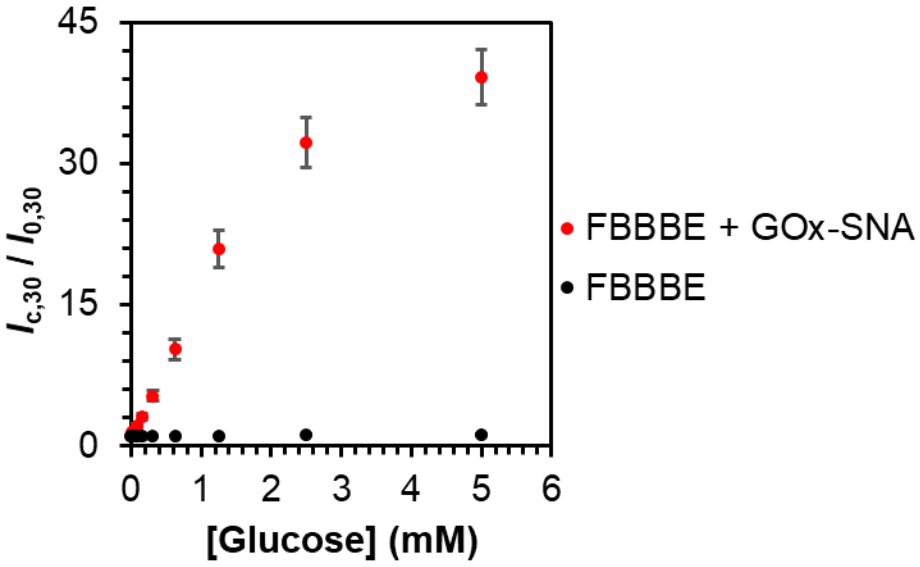

Figure 4.3.3-3. Fluorescence enhancement of 20 nM GOx-SNAs + 5 µM FBBBE in the presence of varying amounts of glucose at 37 °C. The fluorescence enhancement is calculated as the ratio of $I_{c,30}$ / $I_{0,30}$. $I_{c,30}$ represents the fluorescence of the solution at the 30-min time point when a concentration c of glucose is added. $I_{0,30}$ represents the fluorescence of the solution at the 30-minute time point when a concentration 0 mM of glucose is added. The fluorescence is corrected for the fluorescence of the buffer. The fluorescence is monitored by exciting FBBBE at 460 nm and collecting the emission at 530 nm. Data points and error bars represent the mean and standard deviation of three replicates, respectively.

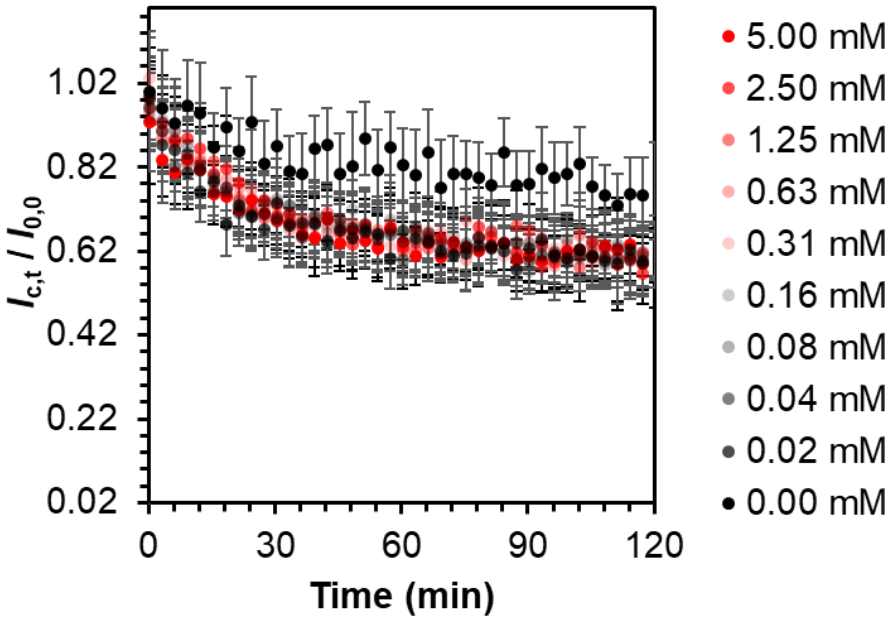

Figure 4.3.3-4. Fluorescence enhancement over time of AF-647 conjugated to GOx-SNAs in the presence of varying amounts of glucose and 5 µM FBBBE 1X PBS at 37 °C. The fluorescence enhancement is calculated as the ratio of $I_{c,t}$ / $I_{0,0}$. $I_{c,t}$ represents the fluorescence of the solution at the time t when a concentration c of glucose is added. $I_{0,0}$ represents the fluorescence of the solution at the initial time point when a concentration 0 mM of glucose is added. These results show that the AF-647 signal from GOx-SNAs is not affected by the formation of FBBBE. The slight decrease in fluorescence over time is attributed to photobleaching. The fluorescence is monitored by exciting GOx-SNAs at 640 nm and collecting the emission at 700 nm. Data points and error bars represent the mean and standard deviation of three replicates, respectively.

4.3.3.4. Selectivity of GOx-SNAs for glucose over other sugars in a complex mixture

We studied whether GOx-SNAs can selectively detect glucose in the presence of other sugars (sucrose, xylose, mannose, fructose, maltose, lactose, galactose, and glucose-6-phosphate). We note that the fluorescence observed in the presence of glucose is nearly identical to the fluorescence observed when glucose is present in a mixture of other sugars. Importantly, the fluorescence observed in the absence of glucose is negligible.

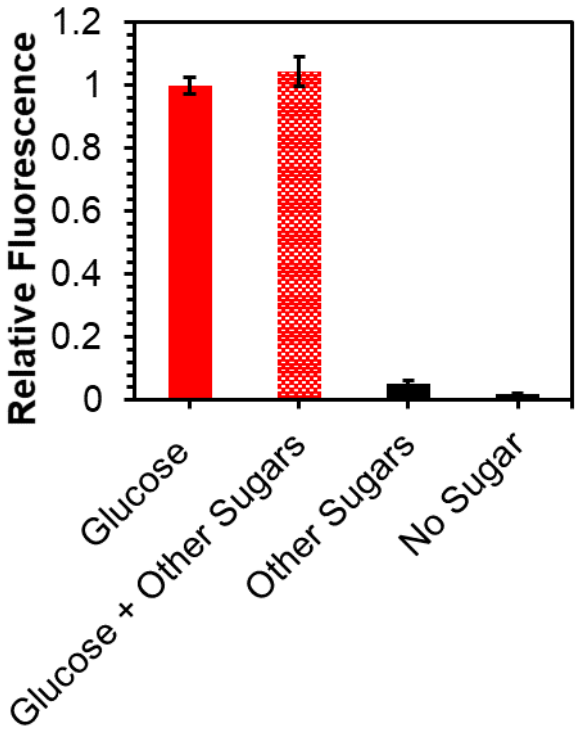

Figure 4.3.3-5. Selectivity of GOx-SNAs for glucose over other sugars in a complex mixture. 10 nM GOx-SNAs were incubated with 5 μM FBBBE at 37 °C for 30 min in the presence or absence of 5 mM of sugars. The fluorescence observed when 5 mM glucose is added to the GOx-SNA/FBBBE solution is normalized to a value of one. The other values are plotted relative to this value. The fluorescence of all three data points was corrected for the fluorescence of a solution of containing only FBBBE. The fluorescence was monitored by exciting FBBBE at 485 nm and collecting the emission at 528 nm. Data points and error bars represent the mean and standard deviation of three replicates, respectively.

4.3.3.5. Response of GOx-SNAs in different cell lines

Several different cell lines were tested for their fluorescence after treatment with the ProSNA probe set. Flow cytometry experiments are shown in this section.

4.3.3.5.1. Example flow cytometry gating strategy

We show here an example of our gating strategy for flow cytometry experiments validating the ProSNA probes.

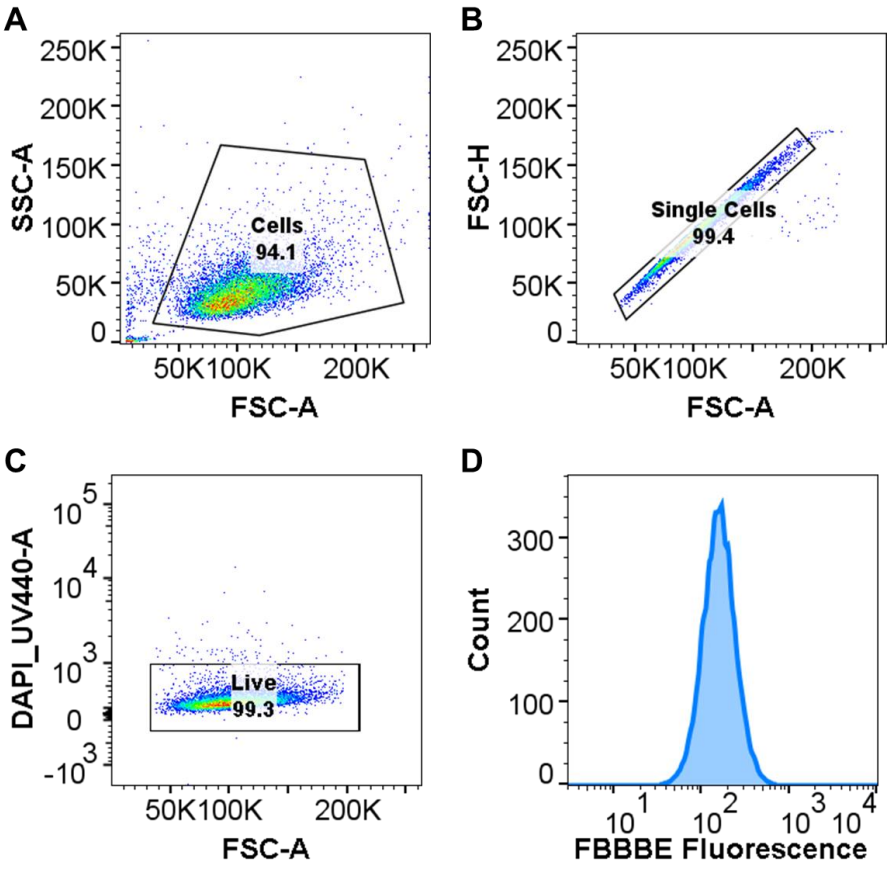

Figure 4.3.3-6. Example flow cytometry gating strategy. (A) Cells are first distinguished from debris based on forward and side scatter. (B) Single cells are distinguished from clusters of cells. (C) Live cells are selected based on the fluorescence of the dye DAPI which preferentially stains dead cells. (D) The fluorescence histogram of live cells in the FBBBE channel is plotted. In this example, EG7-OVA cells treated with FBBBE have been analyzed.

4.3.3.5.2. MDA-MB-231

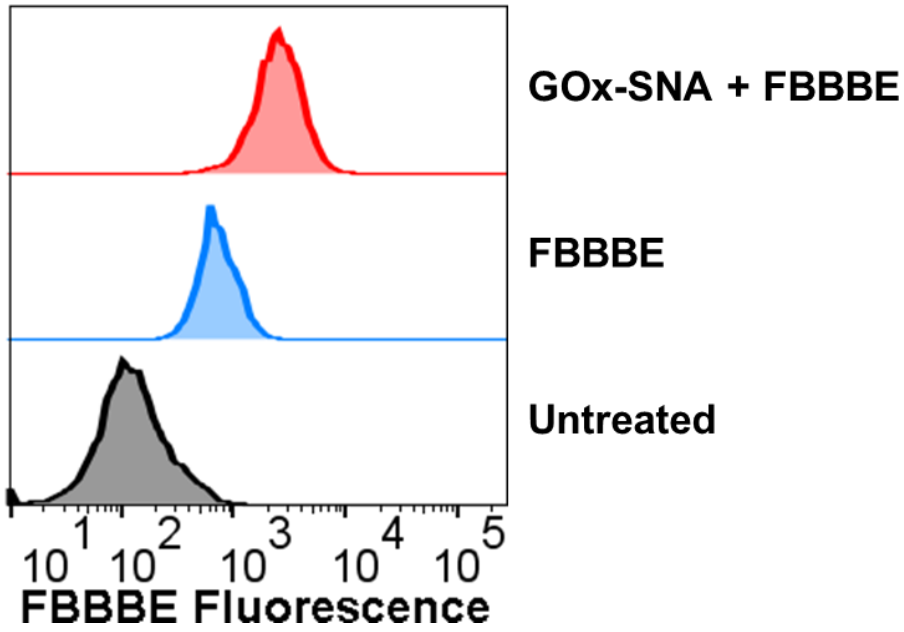

Figure 4.3.3-7. Representative fluorescence histograms of untreated cells, cells treated with 50 µM FBBBE and cells treated with 40 nM GOx-SNA and 50 µM FBBBE.

4.3.3.5.3. U87

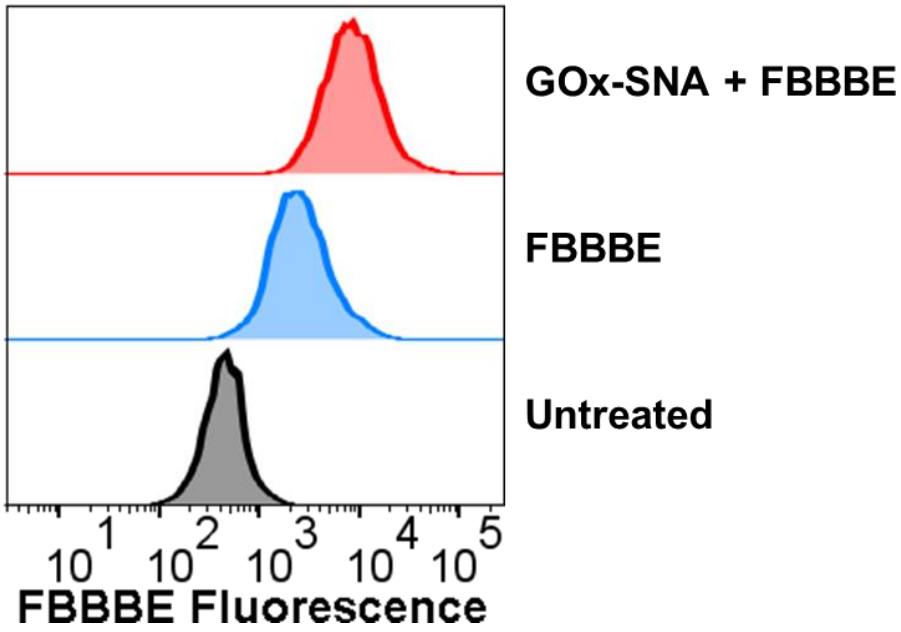

Figure 4.3.3-8. Representative fluorescence histograms of untreated cells, cells treated with 50 µM FBBBE and cells treated with 40 nM GOx-SNA and 50 µM FBBBE.

4.3.3.5.4. SKOV-3

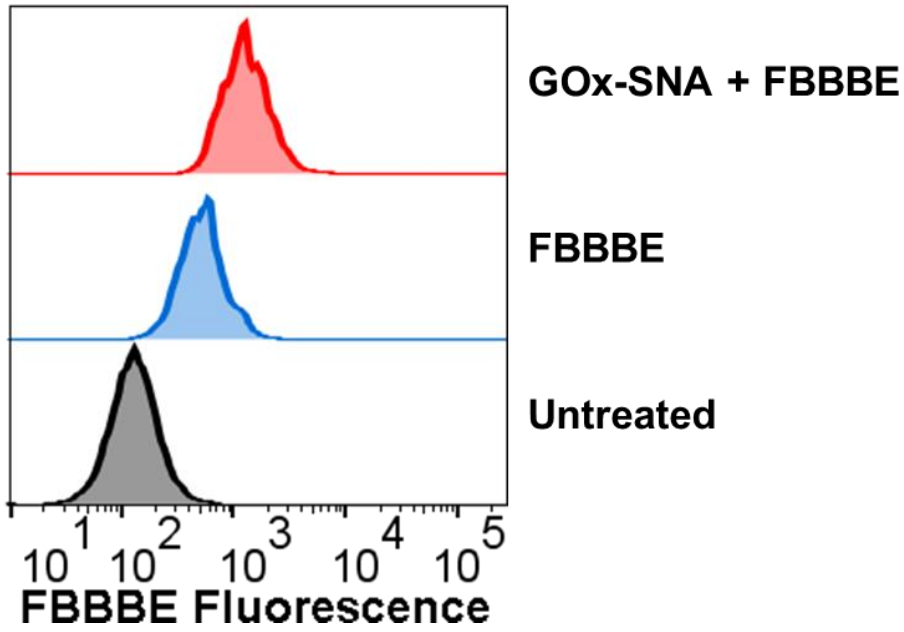

Figure 4.3.3-9. Representative fluorescence histograms of untreated cells, cells treated with 50 µM FBBBE and cells treated with 40 nM GOx-SNA and 50 µM FBBBE.

4.3.3.5.5. EL4

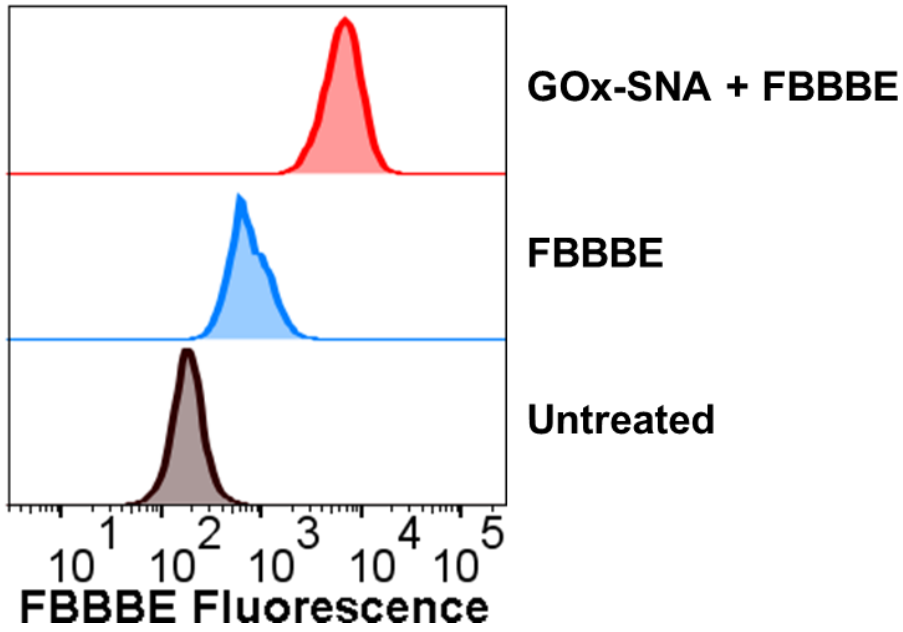

Figure 4.3.3-10. Representative fluorescence histograms of untreated cells, cells treated with 50 µM FBBBE and cells treated with 40 nM GOx-SNA and 50 µM FBBBE.

4.3.3.5.6. Human Dermal Fibroblasts (HDF)

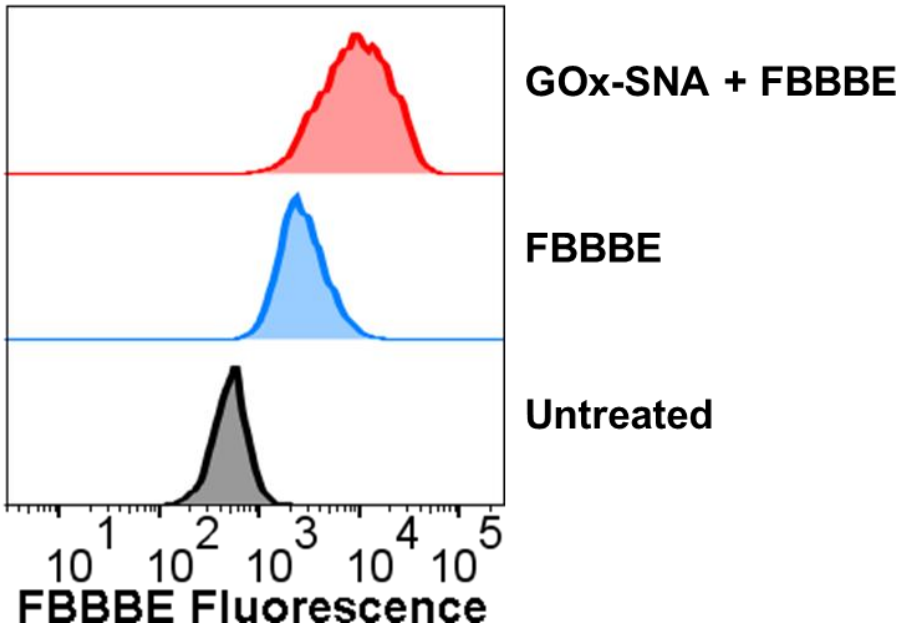

Figure 4.3.3-11. Representative fluorescence histograms of untreated cells, cells treated with 50 µM FBBBE and cells treated with 40 nM GOx-SNA and 50 µM FBBBE.

4.3.3.5.7. MC38

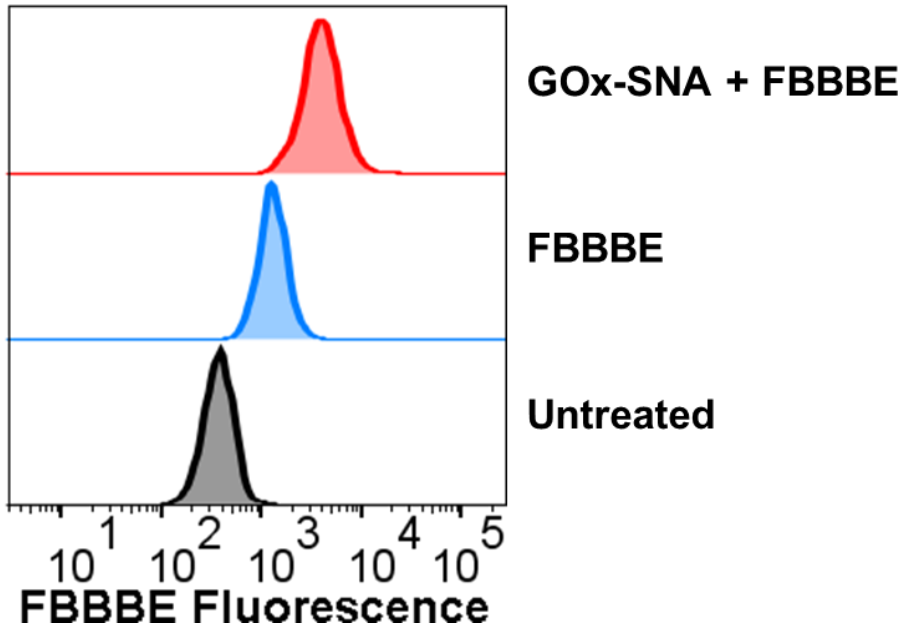

Figure 4.3.3-12. Representative fluorescence histograms of untreated cells, cells treated with 50 µM FBBBE and cells treated with 40 nM GOx-SNA and 50 µM FBBBE.

4.3.3.5.8. NIH-3T3

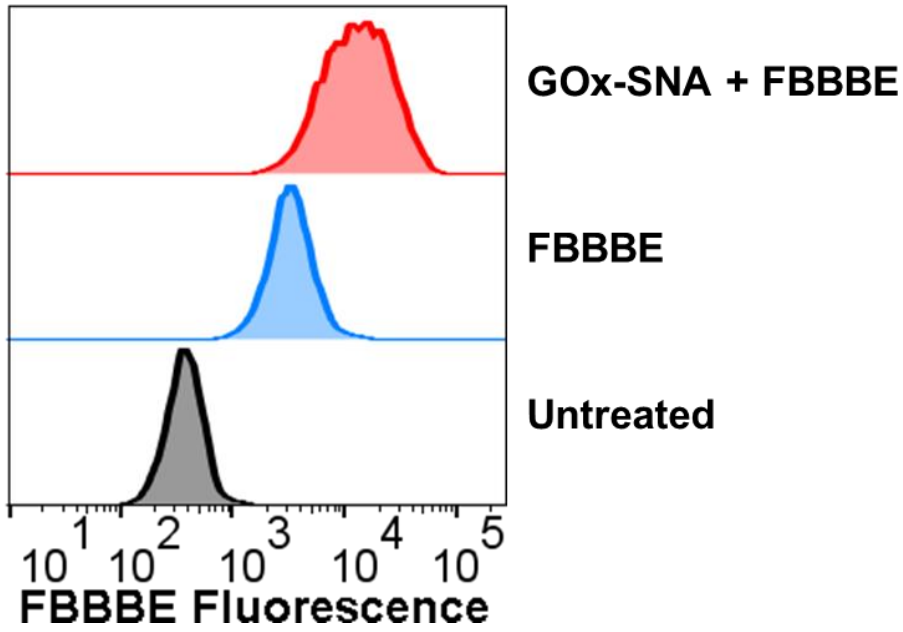

Figure 4.3.3-13. Representative fluorescence histograms of untreated cells, cells treated with 50 µM FBBBE and cells treated with 40 nM GOx-SNA and 50 µM FBBBE.

4.3.3.5.9. 4T1

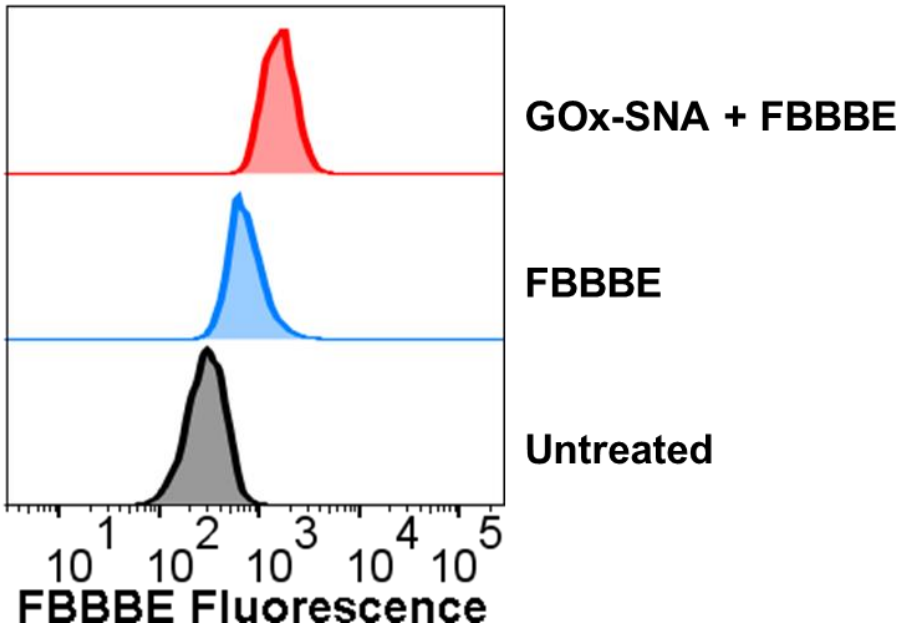

Figure 4.3.3-14. Representative fluorescence histograms of untreated cells, cells treated with 50 µM FBBBE and cells treated with 40 nM GOx-SNA and 50 µM FBBBE.

4.3.3.5.10. EG7-OVA

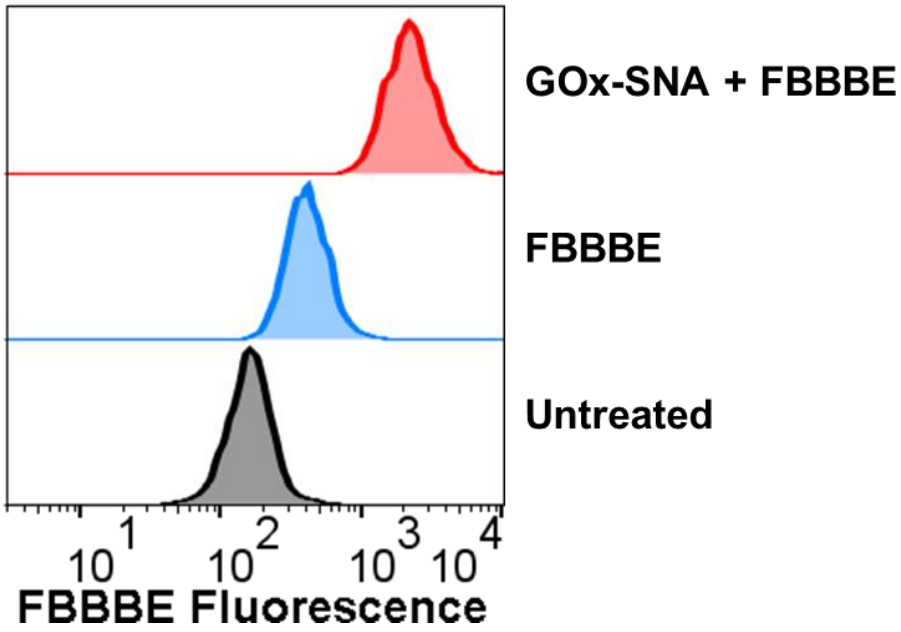

Figure 4.3.3-15. Representative fluorescence histograms of untreated cells, cells treated with 50 μM FBBBE and cells treated with 40 nM GOx-SNA and 50 μM FBBBE.

4.3.3.6. Intracellular response of GOx-SNAs to varying glucose concentrations in cell culture media

To study the effect of glucose add to cell culture media on the fluorescence reported by GOx-SNAs, EL4 cells were first treated with 40 nM GOx-SNAs in glucose-free media. After washing the cells thoroughly, 50μM FBBBE in 0 mM or 25 mM glucose-containing media was added to the cells. The cells were incubated at 37 °C for 30 min and then analyzed by flow cytometry. We note that the fluorescence of cells subjected to 25 mM glucose-containing media is ~50% higher than cells incubated in 0 mM glucose. Importantly, these results agree with the fluorescence observed from cell lysates when a commercially available glucose assay kit is used.

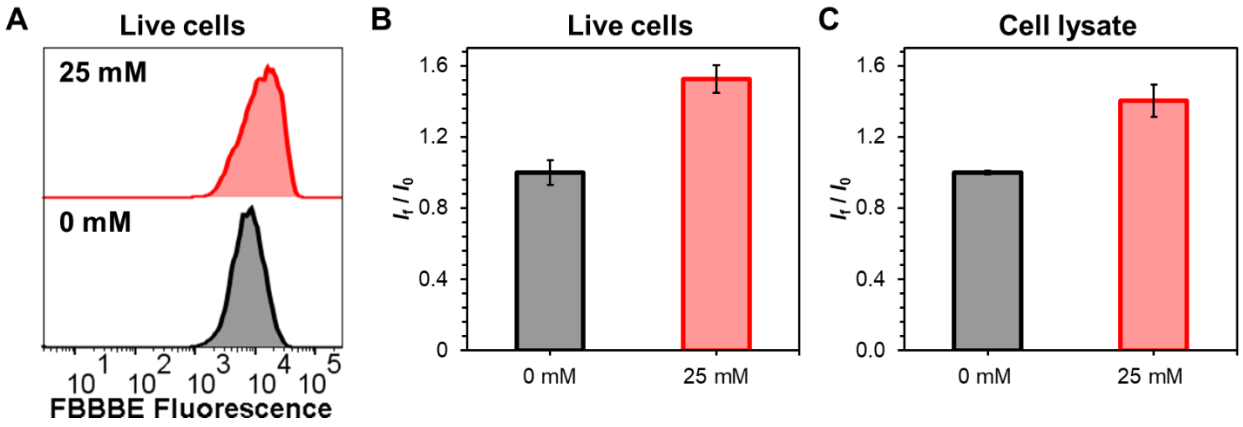

Figure 4.3.3-16. Intracellular response of GOx-SNAs to varying glucose concentrations in cell culture media. (A) Representative fluorescence histograms of GOx-SNA-treated cells incubated in cell culture media containing 0 mM and 25 mM glucose. (B) Mean fluorescence of GOx-SNA-treated cells incubated in cell culture media containing different glucose concentrations (I_f) relative to the mean fluorescence of cells incubated in 0 mM glucose-containing media (I_0). Data points and error bars represent the mean and standard deviation of three replicates, respectively. (C) Relative fluorescence values of cells incubated in cell culture media containing 0 mM and 25 mM glucose as measured using cell lysates through a commercially available glucose assay kit. Data points and error bars represent the mean and standard deviation of three replicates, respectively.

4.3.3.7. Intracellular response of GOx-SNAs to increased glucose uptake

To study the effect of increased glucose uptake on the fluorescence reported by GOx-SNAs, MC38 cells were first treated with 40 nM GOx-SNAs in glucose-free media. After washing the cells thoroughly, 50μM FBBBE in 5 mM glucose-containing media was added to the cells. Additionally, either 0 nM or 100 nM insulin, well-known to increase glucose uptake was added.[414,415] The cells were incubated at 37 °C for 30 min and then analyzed by flow cytometry. We note that the fluorescence of cells subjected to 100 nM insulin is increased by ~90% compared to cells not treated with the insulin. Importantly, these results agree with previous reports of the effect of insulin on glucose uptake in MC38 cells measured using radiolabeled glucose.[414]

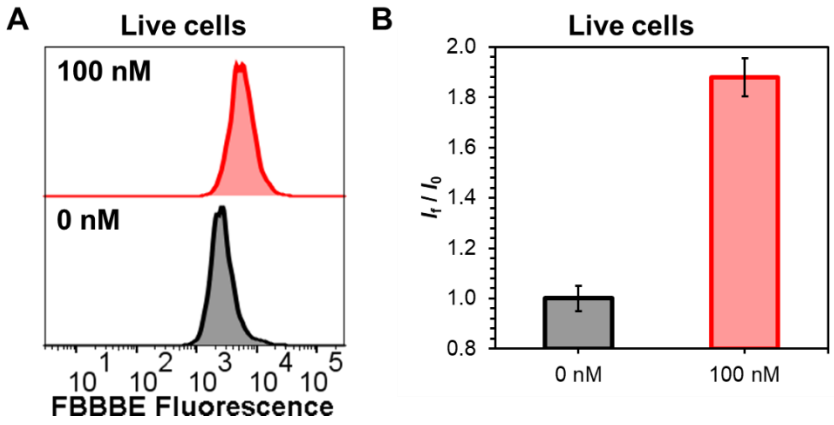

Figure 4.3.3-17. Intracellular response of GOx-SNAs to increase of glucose uptake. (A) Representative fluorescence histograms of GOx-SNA-treated cells incubated in cell culture media containing 0 nM and 100 nM insulin. (B) Mean fluorescence of GOx-SNA-treated cells incubated in cell culture media containing different insulin concentrations (I_f) relative to the mean fluorescence of cells incubated in 0 nM insulin-containing media (I_0). Data points and error bars represent the mean and standard deviation of two replicates, respectively.

4.3.3.8. Intracellular response of GOx-SNAs to inhibition of glucose uptake

To study the effect of blocking glucose receptors on the fluorescence reported by GOx-SNAs, EL4 cells were first treated with 40 nM GOx-SNAs in glucose-free media. After washing the cells thoroughly, 50μM FBBBE in 25 mM glucose-containing media was added to the cells. Additionally, either 0 μM or 10 μM cytochalasin B, a well-known glucose transport inhibitor was added.[416] The cells were incubated at 37 °C for 30 min and then analyzed by flow cytometry. We note that the fluorescence of cells subjected to 10 μM cytochalasin B is reduced by ~25% compared to cells not treated with the inhibitor. Importantly, these results agree with the fluorescence observed from cell lysates when a commercially available glucose assay kit is used.

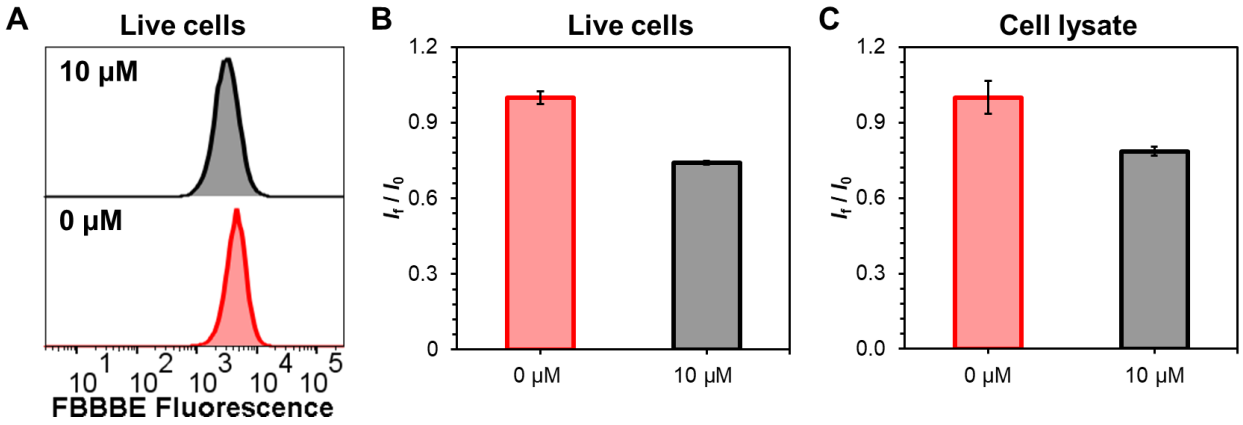

Figure 4.3.3-18. Intracellular response of GOx-SNAs to inhibition of glucose uptake. (A) Representative fluorescence histograms of GOx-SNA-treated cells incubated in cell culture media containing 0 μM and 10 μM cytochalasin B. (B) Mean fluorescence of GOx-SNA-treated cells incubated in cell culture media containing different cytochalasin B concentrations (I_f) relative to the mean fluorescence of cells incubated in 0 μM cytochalasin B-containing media (I_0). Data points and error bars represent the mean and standard deviation of three replicates, respectively. (C) Relative fluorescence values of cells incubated in cell culture media containing 0 μM and 10 μM cytochalasin B as measured using cell lysates through a commercially available glucose assay kit. Data points and error bars represent the mean and standard deviation of three replicates, respectively.

4.4. Discussion

4.4.1. Validating the ProSNA approach

We hypothesized that the use of a quencher-free strategy coupled to an SNA architecture could overcome many of the challenges associated with NanoFlares discussed in section 4.1. To test this hypothesis, we first designed SNAs in which the nucleic acid sequences act as the recognition element. We used a duplex-sensitive dye, thiazole orange (TO), as a base-surrogate in an oligonucleotide recognition sequence that is designed to bind to the target analyte (Figure 4.4.1-1, Figure 4.2.2-3). This class of dyes, derived from intercalators, have low fluorescence in a single-stranded oligonucleotide due to unrestricted rotation about the methine bridge in the molecules.[124] In contrast, upon binding to the target analyte, the dye undergoes forced intercalation (FIT) (Chapter 2) between the oligonucleotide base pairs, thereby restricting its motion, leading to enhanced fluorescence.[124,154,378] The use of a duplex-sensitive dye no longer necessitates the presence of a "chemically inert" gold core and allows us to expand the core selection. Here, we use a protein core as a model system due to its well established biocompatibility, biodegradability, and site-specific attachment points.[417,418]

For proof-of-concept, we chose an i-motif sequence as the recognition strand that undergoes pH-dependent structural changes between an unfolded and a tetraplex form.[253,419] The i-motif is an aptamer for protons, and we converted the i-motif into a FIT-aptamer using a strategy previously reported by our group.[378] β-galactosidase (β-gal) was chosen as the protein core. A fluorescent dye AlexaFluor 647 (AF-647) was covalently conjugated to the cysteine residues of the protein through maleimide-thiol coupling to enable the monitoring of the cellular uptake of the probe. DBCO-TEG terminated DNA was attached orthogonally to the lysine residues modified with

PEG-azides. These modifications gave rise to a TO containing i-motif-β-gal ProSNA termed as ProTOn (Figure 4.4.1-1).

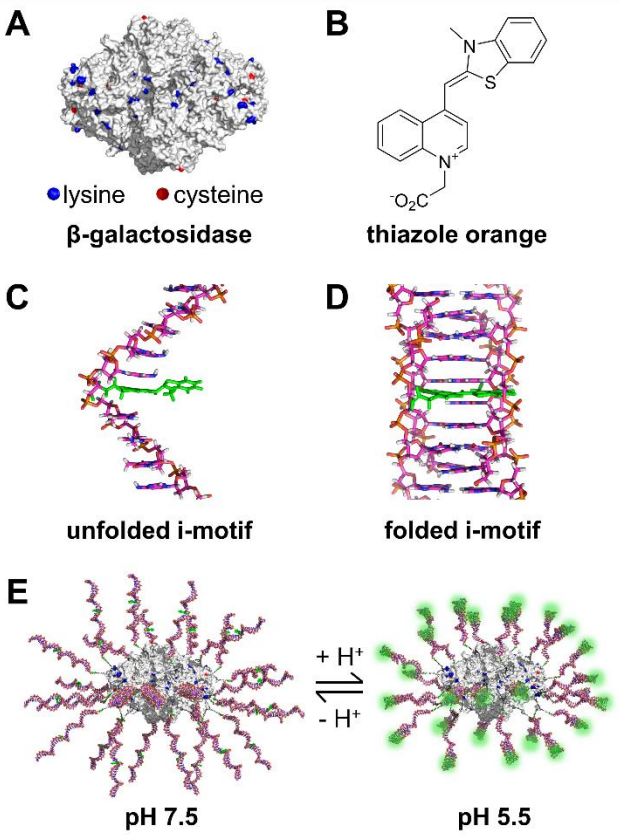

Figure 4.4.1-1. (A) Structure of β-galactosidase with lysine and cysteine residues highlighted. (B) Structure of the forced intercalation dye thiazole orange (TO). (C) Unfolded i-motif sequence with a single base replaced with TO. (D) Folded i-motif with TO intercalated between base pairs. (E) Structure of ProTOn at pH 7.5 and pH 5.5. The formation of the i-motif structure leads to fluorescence turn on of TO.

We first established that ProTOn is capable of detecting pH changes *in vitro* (Figure 4.4.1-2) by subjecting it to buffered solutions at different pH. Our results show a gradual increase in the fluorescence enhancement of TO, saturating at 9-fold, when the pH of the solution changes from 7.5 to 5.0. No change in fluorescence signal is observed from AF-647 in this pH range. Similarly,

ProSNAs containing a control sequence that does not form the i-motif structure results in no fluorescence enhancement either in the TO channel or the AF-647 channel in this pH range.

Next, we determined the ability of ProTOn to report changes in intracellular pH (Figure 4.4.1-2). The MDA-MB-231 cell line, a human epithelial breast cancer cell line, was chosen as a model. These cells were incubated with 40 nM ProTOn in serum-free media for 4 h. The cells were then clamped at pH 5.5 and pH 7.5 and analyzed by flow cytometry. The mean fluorescence of cells at pH 5.5 is almost double that of cells at pH 7.5, consistent with the results obtained when pHrodo™ Red AM, a commercially available intracellular pH probe, is used as a benchmark (Figure 4.3.2-3). As before, control ProSNAs do not elicit a significant fluorescence change, demonstrating the specificity of ProTOn.

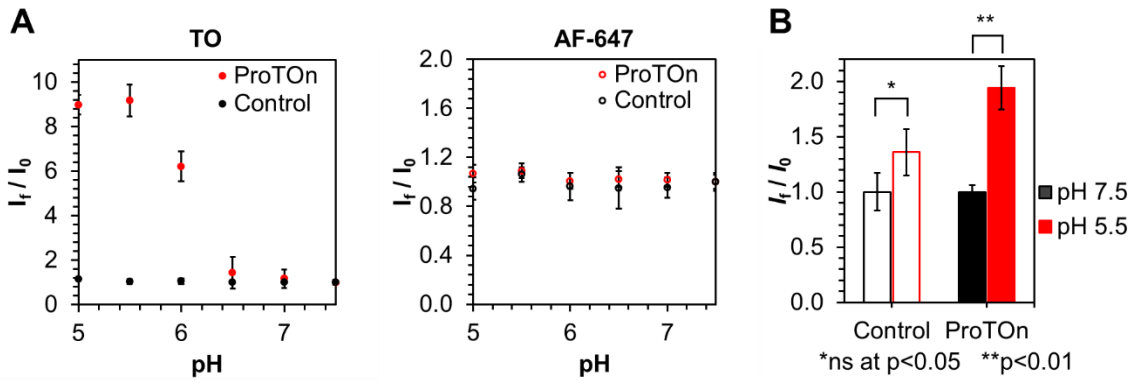

Figure 4.4.1-2. (A) *In vitro* fluorescence response of ProTOn and a control probe to different pH. The fluorescence in the TO increases as pH decreases due to the formation of i-motifs in ProTOn. The control probe does not form an i-motif and, therefore, shows no change in fluorescence. The fluorescence of AF-647 remains unchanged for both ProTOn and the control probe. (B) TO channel fluorescence response of MDA-MB-231 cells treated with ProTOn and a control probe. ProTOn-treated cells clamped at pH 5.5 are almost twice as fluorescent as those clamped at pH 7.5. Cells treated with the control probe show no significant difference in fluorescence.

Importantly, this new quencher-free ProSNA-based design is not prone to false-positive signals, as evidenced by *in vitro* nuclease degradation experiments (Figure 4.3.1-3, Figure 4.3.2-1) and

pulse-chase experiments in MDA-MB-231 cells (Figure 4.3.1-4, Figure 4.3.2-2). Moreover, the use of a FIT-strategy does not require strand displacement, overcoming limitations associated with non-specific dehybridization of the reporter strand and allowing faster binding to the target analyte.[378] Taken together, these results show that ProSNA-based quencher-free probes constitute a next-generation platform for monitoring intracellular analytes in live cells compared to gold-NFs.

Moreover, the use of a ProSNA allows one to not only detect analytes through the nucleic acid shell but also vastly expands the range of analytes that can be detected by taking advantage of the functional protein core. We hypothesized that using an enzyme, we can detect analytes for which nucleic acid-based recognition sequences are not known. To test this hypothesis, we designed a ProSNA for intracellular glucose detection using glucose oxidase (GOx) as the core (Figure 4.4.1-3). We chose glucose as a model analyte because of its fundamental importance to maintaining cellular functions, its high intracellular abundance (~0.1 mM-2 mM),[412,413] and the lack of a glucose aptamer with a biologically relevant binding affinity.[420] Remarkably, the activity of GOx-SNAs remains unchanged compared to the native protein (Figure 4.3.3-2).

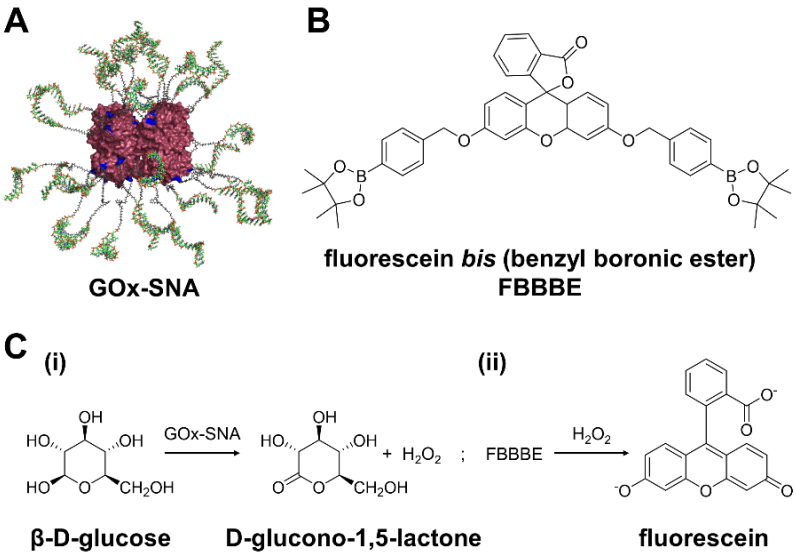

Figure 4.4.1-3. (A) Structure of glucose oxidase SNAs (GOx-SNAs). (B) Structure of fluorescein bis (benzyl boronic ester), FBBBE. (C) A two-step assay developed for glucose detection. (i) First, GOx-SNA catalyzes the conversion of β-D-glucose to D-glucono-1,5-lactone with the formation of H_2O_2. (ii) The H_2O_2 formed reacts with non-fluorescent FBBBE and yields highly fluorescent fluorescein.

To detect glucose intracellularly, we developed a new two-step assay. In the first step, cells are treated with GOx-SNAs in glucose-free media. Upon entering the cells, GOx-SNAs catalyze the conversion of glucose to D-glucono-1,5-lactone and produce hydrogen peroxide. In the second step, the cells are washed thoroughly and treated with fluorescein *bis* (benzyl boronic ester), FBBBE, a cell-permeable, non-fluorescent fluorescein derivative.[421] In the presence of hydrogen peroxide, the boronate groups are cleaved and highly fluorescent fluorescein is formed and retained intracellularly. Therefore, the fluorescence is directly proportional to the amount of glucose in the cell. This assay results in a 120-fold fluorescence enhancement in the presence of glucose (Figure 4.4.1-4A) *in vitro*. Due to the high specificity of GOx, the probe is selective against other sugars including sucrose, xylose, mannose, fructose, maltose, lactose, galactose, as well as

glucose-6-phosphate which results from rapid phosphorylation of glucose upon cellular entry (Figure 4.4.1-4B, Figure 4.3.3-5).[422]

To ensure the validity of this new assay in cells, we tested nine different cells lines (MDA-MB-231, MC38, U87, SKOV3, HDF, EL4, EG7-OVA, 4T1, and NIH/3T3), representing a mix of cancer and normal cells, adherent and suspension cells, and human and murine-derived cells (Figure 4.3.3-7-Figure 4.3.3-15). Flow cytometry experiments show that cells treated with FBBBE alone have increased fluorescence compared to untreated cells. These results are expected because some fluorescein is formed due to the basal level of H_2O_2 produced in the cells. Cells pre-treated with GOx-SNAs show up to ~12-fold increase in fluorescence due to the elevated levels of H_2O_2 produced (Figure 4.4.1-4C).

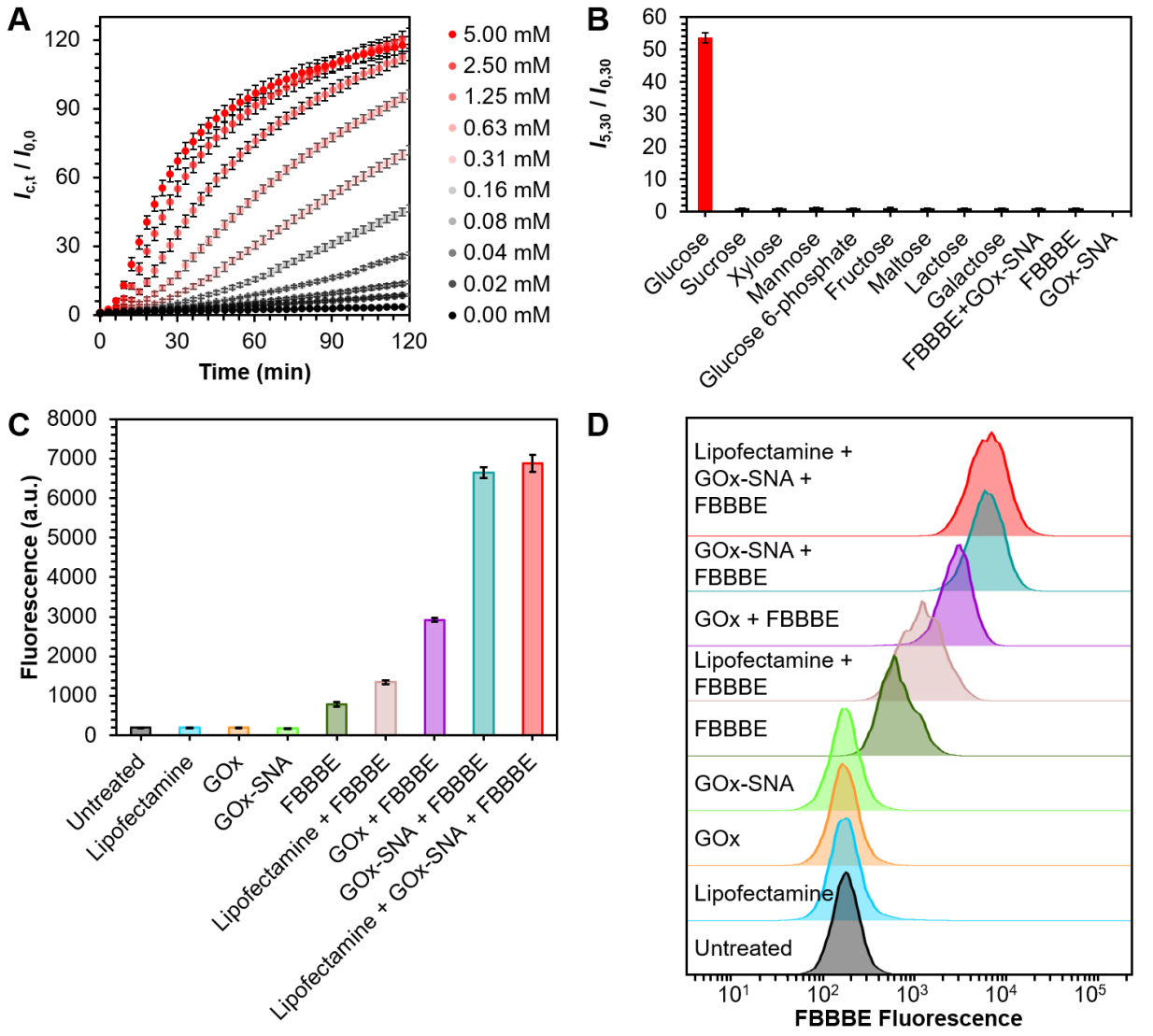

Figure 4.4.1-4. (A) *In vitro* fluorescence response of GOx-SNA to increasing concentrations of glucose. The y-axis shows the observed fluorescence ($I_{c,t}$) for a particular concentration, *c*, of glucose at time, *t*, relative to the fluorescence ($I_{0,0}$) of GOx-SNA at the initial timepoint in the absence of glucose. Over 120-fold fluorescence enhancement is observed in the presence of glucose. (B) *In vitro* selectivity of GOx-SNA against other sugars. (C) Fluorescence of EL4 cells under different treatment conditions. Cells treated with GOx-SNAs and FBBBE fluoresce ~12-fold more compared to cells treated with FBBBE alone. (D) Representative fluorescence histograms corresponding to data in (C).

Modulating intracellular glucose levels impacts the fluorescence detected. GOx-SNA-treated cells exposed to media containing 25 mM glucose show an increase in fluorescence compared to those

exposed to 0 mM glucose (Figure 4.3.3-16). Similarly, increasing glucose uptake by treating cells with 100 nM insulin results in higher fluorescence (Figure 4.3.3-17). In contrast, decreasing glucose uptake by using 10 μM cytochalasin B, a well-known glucose transport inhibitor,[416] results in decreased fluorescence (Figure 4.3.3-18). Taken together, these experiments show that GOx-SNAs can be used as intracellular glucose probes, which going forward, may aid the high throughput screening of antihyperglycemic drugs.

4.5. Conclusion

In summary, I have discussed the development of a powerful new class of intracellular probes based on ProSNAs. Their modular structure allows one to change the protein core and the nucleic acid shell independently and detect analytes using either component as the sensing moiety through binding- or activity-based sensing. The programmable nature of nucleic acids would allow the detection of targets using aptamers, DNAzymes, or hybridization-based probes. The unparalleled specificity of proteins will give rise to probes that are highly selective for their targets. When one takes into account the many proteins that have been developed for sensing analytes in cell lysates or fluorescent proteins that are genetically encoded, the scope of possibilities is enormous, considering that these proteins could be repurposed as exogenous probes for detecting intracellular analytes in live cells and clinical samples.

CHAPTER FIVE

5. Outlook and Future Work

5.1. Summary

The work outlined in this thesis has resulted in the development of a toolbox that can allow researchers and clinicians to study a wide variety of targets (protein, ions, small molecules, etc.) in a wide variety of different milieu (serum, living cells, etc.). In the second chapter, I described the development of a new method of signal transduction for aptamer-target binding, called FIT-aptamers.[378] The advantages of FIT-aptamers outlined in Chapter 2 enabled their employment as the first fluorogenic aptamer probes capable of detecting steroid hormones in clinical serum samples, discussed in Chapter 3.[423] Finally, the quencher-free nature of the FIT-approach allowed the development of a new class of false-positive resistant probes for live cell chemical analysis, presented in Chapter 4.[379] Below, I outline future directions of interest using these developed tools.

5.2. High throughput screening of novel metallo base-pairs

Certain analytes have no known aptamers, small molecule dyes, or proteins for their detection inside of living cells. This deficiency applies to several metal ions. A FIT-based strategy enables the probing of local target-induced conformational changes, a powerful capability that is not possible with conventional fluorophore/quencher or FRET-based methodologies. Future work will leverage this capability for the high-throughput screening of novel metallo-base pairs. Specifically, if a metal is added to a DNA duplex that contains a single base pair mismatch directly adjacent to the FIT-dye, the dye will only turn-on if the metal coordinates the single base pair mismatch. This turn-on is due to the rigidifying of the local environment of the FIT-dye due to metal binding. By testing all combinations of single base pair mismatches (i.e. CT, AG, GT, etc.), a high-throughput screening can be done for several metals. Preliminary experiments have led to

the potential discovery of 13 novel metallo-base pairs, including those mediated by Ag^{+}, Hg^{2+}, and Cu^{2+}. Future work will focus on confirming the metal-DNA coordination through NMR studies and DNA crystallization. These DNA duplexes can potentially serve as recognition elements for probing metal ions intracellularly.

5.3. Expanding scope of recognition to mRNA inside of living cells

Additional future work to expand the library of analytes that can be detected using protein SNAs involves mRNA, the detection, quantification, and tracking of which can enable live-cell genetic analysis. However, the central challenge to reliable mRNA detection is that the majority of SNA-based structures are trapped in the endosome, which renders accurate quantification of cytosolic targets challenging. To address this, aptamer-mediated strategies have been investigated that allow receptor-mediated internalization. By targeting different cell-surface receptors, different uptake pathways can be elicited. Studies have shown that by modifying DNA-based structures with the nucleolin aptamer AS1411, direct cytosolic entry is possible. We have appended the AS1411 aptamer to FIT-based recognition sequences for vimentin mRNA, a known oncogene. This strategy affords 10-fold fluorescence turn-on in solution, with future work testing its feasibility in living cells. Further experiments have focused on microinjecting structures into cells to measure the fluorescence signal generated when cytosolic delivery is maximized.

5.4. Studying events *in vivo*

Ultimately, the most interesting use of a newly developed diagnostic probe is for studying events *in vivo*. To do this, several important considerations must be made. *In vivo* delivery requires the consideration of additional factors compared to cells in culture due to the presence of more

biological barriers. Probes delivered by systemic injection must evade the immune system to avoid rapid clearance before reaching the target site, be stable during circulation, and accumulate in the target region in significant quantities to result in appreciable signal. The majority of structures localize predominantly in the liver and the spleen.[132] This phenomenon offers an opportunity for the imaging of targets present in these organs, but also creates a challenge for studying analytes in organs that are difficult to access such as the brain. In this regard, one promising approach is the local delivery of probes. This strategy has been used for tumor imaging by delivering NanoFlares using an injectable hydrogel directly in the tumor.[74] Alternately, targeting moieties such as aptamers or antibodies can potentially promote tissue-specific uptake.[133,134] Imaging *in vivo* is most effectively done with dyes that emit in the biological optical window (NIR regime).[135] These dyes allow for the signal to be distinguished from tissue autofluorescence, especially important in the analysis of deep tissue. In this light, the study of skin diseases has proven encouraging, as many targets are near the surface and local topical delivery of probes is possible.[6,119] Moreover, multifunctional nanoparticles that combine fluorescence imaging with structural imaging (e.g. magnetic resonance imaging)[112,136,137] can potentially provide more detailed information about diseased tissue *in vivo*. A final consideration is the biocompatibility and the long-term safety of the probes. It is anticipated that advances in probe design can lead to structures that can function as companion diagnostics, such as theranostic platforms for precision medicine, which is a growing area of interest. The versatility of the protein SNA probes that we have developed make us uniquely poised to use them *in vivo*. First, as this new generation of probes no longer require a gold core, a biocompatible and biodegradable core such as a protein makes translation to *in vivo* contexts more attainable. Moreover, the protein SNA structure is expected to exhibit SNA

characteristics that allow analysis of skin samples or access to hard to reach areas like the brain. The versatility of the FIT-approach also allows the use of a palette of dyes, with recent work pushing further towards finding dyes that fluoresce in the NIR regime. Access to a palette of dyes also would enable multiplexed detection, an important capability when trying to understand the interplay between different molecules.

5.5. Selectively releasing nucleic acid-protein conjugates from solid surfaces

Proteins functionalized with biotin modified nucleic acids can be attached to streptavidin coated surfaces. If the protein chosen can be coupled to a colorimetric assay, the selective release of the protein from the surface as a result of a target of interest's presence can be used as a diagnostic assay. In this light, our recent results show that Cas13 enzyme activation via presence of a target nucleic acid of interest can be used to indiscriminately degrade the nucleic acid linkage between proteins and surfaces. Using horseradish peroxidase as the protein core, a colorimetric substrate can be added to the milieu that is detached from the surface. The intensity of color produced is directly proportional to the amount of target that was present to trigger Cas13 activity. This capability has been leveraged by us recently to measure transcripts associated with SARS-CoV-2. Future work aims to look at other nucleic acid targets, or interface this strategy with aptamer-target binding to create a new class of colorimetric probes.

6. References

[1] B. E. Gress, R. J. Waltzer, S. Lüpold, E. M. Droge-Young, M. K. Manier, S. Pitnick, *Proc. R. Soc. B Biol. Sci.* **2014**, *281*, 20132164.

[2] S. R. Adams, M. R. Mackey, R. Ramachandra, S. F. Palida Lemieux, P. Steinbach, E. A. Bushong, M. T. Butko, B. N. G. Giepmans, M. H. Ellisman, R. Y. Tsien, *Cell Chem. Biol.* **2016**, *23*, 1417–1427.

[3] X. Han, A. Aslanian, J. R. Yates, *Curr. Opin. Chem. Biol.* **2008**, *12*, 483–490.

[4] S. Aydin, *Peptides* **2015**, *72*, 4–15.

[5] S.A. Deepak, K.R. Kottapalli, R. Rakwal, G. Oros, K.S. Rangappa, H. Iwahashi, Y. Masuo, G.K. Agrawal, *Curr. Genomics* **2007**, *8*, 234–251.

[6] G. Bao, W. J. Rhee, A. Tsourkas, *Annu. Rev. Biomed. Eng.* **2009**, *11*, 25–47.

[7] R. E. Farrell, in *RNA Methodol.*, Elsevier, **2010**, pp. 241–260.

[8] P.-C. Yang, T. Mahmood, *N. Am. J. Med. Sci.* **2012**, *4*, 429.

[9] C. Cui, W. Shu, P. Li, *Front. Cell Dev. Biol.* **2016**, *4*, DOI 10.3389/fcell.2016.00089.

[10] C. A. Harrington, C. Rosenow, J. Retief, *Curr. Opin. Microbiol.* **2000**, *3*, 285–291.

[11] L. Graham, J. M. Orenstein, *Nat. Protoc.* **2007**, *2*, 2439–2450.

[12] J. W. Lichtman, S. E. Fraser, *Nat. Neurosci.* **2001**, *4*, 1215–1220.

[13] D. J. Stephens, *Science* **2003**, *300*, 82–86.

[14] E. A. Specht, E. Braselmann, A. E. Palmer, *Annu. Rev. Physiol.* **2017**, *79*, 93–117.

[15] F. E. Duncan, E. L. Que, N. Zhang, E. C. Feinberg, T. V. O'Halloran, T. K. Woodruff, *Sci. Rep.* **2016**, *6*, 24737.

[16] A. G. Godin, B. Lounis, L. Cognet, *Biophys. J.* **2014**, *107*, 1777–1784.

[17] A. M. Sydor, K. J. Czymmek, E. M. Puchner, V. Mennella, *Trends Cell Biol.* **2015**, *25*, 730–748.

[18] C. A. Mirkin, R. L. Letsinger, R. C. Mucic, J. J. Storhoff, *Nature* **1996**, *382*, 607–609.

[19] M. R. Jones, N. C. Seeman, C. A. Mirkin, *Science* **2015**, *347*, 1260901–1260901.

[20] M. R. Jones, C. A. Mirkin, *Nature* **2012**, *491*, 42–43.

[21] D. Samanta, A. Iscen, C. Laramy, S. Ebrahimi, K. Bujold, G. Schatz, C. Mirkin, *J. Am. Chem. Soc.* **n.d.**, *141*, 19973–19977.

[22] W. Zhou, R. Saran, J. Liu, *Chem. Rev.* **2017**, *117*, 8272–8325.

[23] R. Stoltenburg, C. Reinemann, B. Strehlitz, *Biomol. Eng.* **2007**, *24*, 381–403.

[24] M. Hollenstein, *Molecules* **2015**, *20*, 20777–20804.

[25] A. D. Ellington, J. W. Szostak, *Nature* **1990**, *346*, 818–822.

[26] N. L. Rosi, D. A. Giljohann, C. S. Thaxton, A. K. R. Lytton-Jean, M. S. Han, C. A. Mirkin, *Science* **2006**, *312*, 1027–1030.

[27] S. L. DeVos, T. M. Miller, *Neurotherapeutics* **2013**, *10*, 486–497.

[28] L. Lannes, S. Halder, Y. Krishnan, H. Schwalbe, *ChemBioChem* **2015**, *16*, 1647–1656.

[29] T. P. Prakash, *Chem. Biodivers.* **2011**, *8*, 1616–1641.

[30] S. Verma, F. Eckstein, *Annu. Rev. Biochem.* **1998**, *67*, 99–134.

[31] A. Grünweller, R. K. Hartmann, *BioDrugs* **2007**, *21*, 235–243.

[32] M. Teplova, G. Minasov, V. Tereshko, G. B. Inamati, P. D. Cook, M. Manoharan, M. Egli, *Nat. Struct. Biol.* **1999**, *6*, 535–539.

[33] B. Vester, J. Wengel, *Biochemistry* **2004**, *43*, 13233–13241.

[34] F. Eckstein, *Nucleic Acid Ther.* **2014**, *24*, 374–387.

[35] N. Farschtschi, D. G. Gorenstein, *Tetrahedron Lett.* **1988**, *29*, 6843–6846.

[36] D. R. Corey, J. M. Abrams, *Genome Biol.* **2001**, *2*, reviews1015.1-reviews1015.3.

[37] F. Pellestor, P. Paulasova, *Eur. J. Hum. Genet.* **2004**, *12*, 694–700.

[38] A. Garg, D. Wesolowski, D. Alonso, K. W. Deitsch, C. Ben Mamoun, S. Altman, *Proc. Natl. Acad. Sci.* **2015**, *112*, 11935–11940.

[39] A. E. Prigodich, P. S. Randeria, W. E. Briley, N. J. Kim, W. L. Daniel, D. A. Giljohann, C. A. Mirkin, *Anal. Chem.* **2012**, *84*, 2062–2066.

[40] E. Kim, J. Yang, J. Park, S. Kim, N. H. Kim, J. I. Yook, J.-S. Suh, S. Haam, Y.-M. Huh, *ACS Nano* **2012**, *6*, 8525–8535.

[41] Y. K. Park, W. Y. Jung, M. G. Park, S. K. Song, Y. S. Lee, H. Heo, S. Kim, *Medchemcomm* **2017**, *8*, 2228–2232.

[42] J. M. Levsky, *J. Cell Sci.* **2003**, *116*, 2833–2838.

[43] G. Ke, C. Wang, Y. Ge, N. Zheng, Z. Zhu, C. J. Yang, *J. Am. Chem. Soc.* **2012**, *134*, 18908–18911.

[44] D. S. Seferos, D. A. Giljohann, H. D. Hill, A. E. Prigodich, C. A. Mirkin, *J. Am. Chem. Soc.* **2007**, *129*, 15477–15479.

[45] D. H. J. Bunka, P. G. Stockley, *Nat. Rev. Microbiol.* **2006**, *4*, 588–596.

[46] Aptagen, **n.d.**

[47] K. Hwang, P. Hosseinzadeh, Y. Lu, *Inorganica Chim. Acta* **2016**, *452*, 12–24.

[48] R. R. Breaker, G. F. Joyce, *Chem. Biol.* **1994**, *1*, 223–229.

[49] G. F. Joyce, *Annu. Rev. Biochem.* **2004**, *73*, 791–836.

[50] H. Peng, X.-F. Li, H. Zhang, X. C. Le, *Nat. Commun.* **2017**, *8*, 14378.

[51] M. Famulok, J. S. Hartig, G. Mayer, *Chem. Rev.* **2007**, *107*, 3715–3743.

[52] D. Bhatia, S. Surana, S. Chakraborty, S. P. Koushika, Y. Krishnan, *Nat. Commun.* **2011**, *2*, 339.

[53] J. C. Politz, E. S. Browne, D. E. Wolf, T. Pederson, *Proc. Natl. Acad. Sci.* **1998**, *95*, 6043–6048.

[54] C. Molenaar, *Nucleic Acids Res.* **2001**, *29*, 89e – 89.

[55] S. Paillasson, M. Van De Corput, R. W. Dirks, H. J. Tanke, M. Robert-Nicoud, X. Ronot, *Exp. Cell Res.* **1997**, *231*, 226–233.

[56] A. Tsuji, H. Koshimoto, Y. Sato, M. Hirano, Y. Sei-Iida, S. Kondo, K. Ishibashi, *Biophys. J.* **2000**, *78*, 3260–3274.

[57] K. Okabe, Y. Harada, J. Zhang, H. Tadakuma, T. Tani, T. Funatsu, *Nucleic Acids Res.* **2011**, *39*, e20–e20.

[58] L. Dahan, L. Huang, R. Kedmi, M. A. Behlke, D. Peer, *PLoS One* **2013**, *8*, e72389.

[59] T. Matsuo, *Biochim. Biophys. Acta - Gen. Subj.* **1998**, *1379*, 178–184.

[60] W. J. Kang, Y. L. Cho, J. R. Chae, J. D. Lee, K.-J. Choi, S. Kim, *Biomaterials* **2011**, *32*, 1915–1922.

[61] L. J. Nielsen, L. F. Olsen, V. C. Ozalp, *ACS Nano* **2010**, *4*, 4361–4370.

[62] Y. Liang, Z. Zhang, H. Wei, Q. Hu, J. Deng, D. Guo, Z. Cui, X.-E. Zhang, *Biosens. Bioelectron.* **2011**, *28*, 270–276.

[63] D. L. Sokol, X. Zhang, P. Lu, A. M. Gewirtz, *Proc. Natl. Acad. Sci.* **1998**, *95*, 11538–11543.

[64] D. Zhao, Y. Yang, N. Qu, M. Chen, Z. Ma, C. J. Krueger, M. A. Behlke, A. K. Chen, *Biomaterials* **2016**, *100*, 172–183.

[65] C. D. Medley, T. J. Drake, J. M. Tomasini, R. J. Rogers, W. Tan, *Anal. Chem.* **2005**, *77*, 4713–4718.

[66] Y. Wu, C. J. Yang, L. L. Moroz, W. Tan, *Anal. Chem.* **2008**, *80*, 3025–3028.

[67] J. Chen, J. Wu, Y. Hong, *Chem. Commun.* **2016**, *52*, 3191–3194.

[68] X.-H. Peng, Z.-H. Cao, J.-T. Xia, G. W. Carlson, M. M. Lewis, W. C. Wood, L. Yang,

Cancer Res. **2005**, *65*, 1909–1917.

[69] P. R. Bohländer, M. L. Abba, F. Bestvater, H. Allgayer, H.-A. Wagenknecht, *Org. Biomol. Chem.* **2016**, *14*, 5001–5006.

[70] Z. Cheglakov, T. M. Cronin, C. He, Y. Weizmann, *J. Am. Chem. Soc.* **2015**, *137*, 6116–6119.

[71] L. Liu, J.-W. Liu, H. Wu, X.-N. Wang, R.-Q. Yu, J.-H. Jiang, *Anal. Chem.* **2018**, *90*, 1502–1505.

[72] C. Wu, S. Cansiz, L. Zhang, I.-T. Teng, L. Qiu, J. Li, Y. Liu, C. Zhou, R. Hu, T. Zhang, C. Cui, L. Cui, W. Tan, *J. Am. Chem. Soc.* **2015**, *137*, 4900–4903.

[73] M. Chen, Z. Ma, X. Wu, S. Mao, Y. Yang, J. Tan, C. J. Krueger, A. K. Chen, *Sci. Rep.* **2017**, *7*, 1550.

[74] L. Qiu, C. Wu, M. You, D. Han, T. Chen, G. Zhu, J. Jiang, R. Yu, W. Tan, *J. Am. Chem. Soc.* **2013**, *135*, 12952–12955.

[75] J. Kim, E. Lee, Y. Y. Kang, H. Mok, *Chem. Commun.* **2015**, *51*, 9038–9041.

[76] F. W. King, W. Liszewski, C. Ritner, H. S. Bernstein, *Stem Cells Dev.* **2011**, *20*, 475–484.

[77] P. J. Santangelo, *Nucleic Acids Res.* **2004**, *32*, e57–e57.

[78] D. P. Bratu, B.-J. Cha, M. M. Mhlanga, F. R. Kramer, S. Tyagi, *Proc. Natl. Acad. Sci.* **2003**, *100*, 13308–13313.

[79] Y. Kam, A. Rubinstein, A. Nissan, D. Halle, E. Yavin, *Mol. Pharm.* **2012**, *9*, 685–693.

[80] S. Kummer, A. Knoll, E. Socher, L. Bethge, A. Herrmann, O. Seitz, *Bioconjug. Chem.* **2012**, *23*, 2051–2060.

[81] S. Kummer, A. Knoll, E. Socher, L. Bethge, A. Herrmann, O. Seitz, *Angew. Chemie Int. Ed.* **2011**, *50*, 1931–1934.

[82] G. Fang, J. Chamiolo, S. Kankowski, F. Hövelmann, D. Friedrich, A. Löwer, J. C. Meier, O. Seitz, *Chem. Sci.* **2018**, *9*, 4794–4800.

[83] F. Hövelmann, I. Gaspar, S. Loibl, E. A. Ermilov, B. Röder, J. Wengel, A. Ephrussi, O. Seitz, *Angew. Chemie - Int. Ed.* **2014**, *53*, 11370–11375.

[84] T. Kubota, S. Ikeda, A. Okamoto, *Bull. Chem. Soc. Jpn.* **2009**, *82*, 110–117.

[85] S. Ikeda, T. Kubota, M. Yuki, A. Okamoto, *Angew. Chemie Int. Ed.* **2009**, *48*, 6480–6484.

[86] I. Oomoto, A. Suzuki-Hirano, H. Umeshima, Y.-W. Han, H. Yanagisawa, P. Carlton, Y. Harada, M. Kengaku, A. Okamoto, T. Shimogori, D. O. Wang, *Nucleic Acids Res.* **2015**, *43*, e126–e126.

[87] S. Ikeda, H. Yanagisawa, A. Nakamura, D. O. Wang, M. Yuki, A. Okamoto, *Org. Biomol.*

Chem. **2011**, *9*, 4199.

[88] T. Kubota, S. Ikeda, H. Yanagisawa, M. Yuki, A. Okamoto, *Bioconjug. Chem.* **2009**, *20*, 1256–1261.

[89] R. Gao, C. Hao, L. Xu, C. Xu, H. Kuang, *Anal. Chem.* **2018**, *90*, 5414–5421.

[90] T. Chen, C. S. Wu, E. Jimenez, Z. Zhu, J. G. Dajac, M. You, D. Han, X. Zhang, W. Tan, *Angew. Chemie - Int. Ed.* **2013**, *52*, 2012–2016.

[91] H. Li, Y. Mu, J. Lu, W. Wei, Y. Wan, S. Liu, *Anal. Chem.* **2014**, *86*, 3602–3609.

[92] E. H. Noh, H. Y. Ko, C. H. Lee, M. S. Jeong, Y. W. Chang, S. Kim, *J. Mater. Chem. B* **2013**, *1*, 4438–4445.

[93] J. Lee, S. Moon, Y. Lee, B. Ali, A. Al-Khedhairy, D. Ali, J. Ahmed, A. Al Salem, S. Kim, *Sensors* **2015**, *15*, 12872–12883.

[94] W. Pan, H. Yang, N. Li, L. Yang, B. Tang, *Chem. - A Eur. J.* **2015**, *21*, 6070–6073.

[95] D. Zheng, D. S. Seferos, D. A. Giljohann, P. C. Patel, C. A. Mirkin, *Nano Lett.* **2009**, *9*, 3258–3261.

[96] J. Huang, L. Ying, X. Yang, Y. Yang, K. Quan, H. Wang, N. Xie, M. Ou, Q. Zhou, K. Wang, *Anal. Chem.* **2015**, *87*, 8724–8731.

[97] P. Wu, K. Hwang, T. Lan, Y. Lu, *J. Am. Chem. Soc.* **2013**, *135*, 5254–5257.

[98] A. Jayagopal, K. C. Halfpenny, J. W. Perez, D. W. Wright, *J. Am. Chem. Soc.* **2010**, *132*, 9789–9796.

[99] W. Zhou, Q. Li, H. Liu, J. Yang, D. Liu, *ACS Nano* **2017**, *11*, 3532–3541.

[100] C. K. K. Choi, C. H. J. Choi, L. Bian, in *Methods Mol. Biol.*, **2017**, pp. 155–164.

[101] H.-Z. Zhu, J.-H. An, Q. Yao, J. Han, X.-T. Li, F.-L. Jiang, G.-P. Chen, L.-N. Peng, Y.-S. Li, J.-G. Sun, Z.-T. Chen, *Molecules* **2014**, *19*, 14710–14722.

[102] L. Yang, Y. Ren, W. Pan, Z. Yu, L. Tong, N. Li, B. Tang, *Anal. Chem.* **2016**, *88*, 11886–11891.

[103] K. Yang, M. Zeng, X. Fu, J. Li, N. Ma, L. Tao, *RSC Adv.* **2015**, *5*, 104245–104249.

[104] S.-R. Ryoo, J. Lee, J. Yeo, H.-K. Na, Y.-K. Kim, H. Jang, J. H. Lee, S. W. Han, Y. Lee, V. N. Kim, D.-H. Min, *ACS Nano* **2013**, *7*, 5882–5891.

[105] Y. Wu, J. Han, P. Xue, R. Xu, Y. Kang, *Nanoscale* **2015**, *7*, 1753–1759.

[106] L.-S. Lin, Z.-X. Cong, J.-B. Cao, K.-M. Ke, Q.-L. Peng, J. Gao, H.-H. Yang, G. Liu, X. Chen, *ACS Nano* **2014**, *8*, 3876–3883.

[107] W. Dai, H. Dong, B. Fugetsu, Y. Cao, H. Lu, X. Ma, X. Zhang, *Small* **2015**, *11*, 4158–4164.

[108] Z. Wu, G. Q. Liu, X. L. Yang, J. H. Jiang, *J. Am. Chem. Soc.* **2015**, *137*, 6829–6836.

[109] Y. Wang, Z. Li, D. Hu, C. T. Lin, J. Li, Y. Lin, *J. Am. Chem. Soc.* **2010**, *132*, 9274–9276.

[110] C.-H. Zhang, H. Wang, J.-W. Liu, Y.-Y. Sheng, J. Chen, P. Zhang, J.-H. Jiang, *ACS Sensors* **2018**, *3*, 2526–2531.

[111] C. Shao, J. Liang, S. He, T. Luan, J. Yu, H. Zhao, J. Xu, L. Tian, *Anal. Chem.* **2017**, *89*, 5445–5452.

[112] C. Wiraja, D. C. Yeo, S. Y. Chew, C. Xu, *J. Mater. Chem. B* **2015**, *3*, 6148–6156.

[113] L. He, D. Q. Lu, H. Liang, S. Xie, C. Luo, M. Hu, L. Xu, X. Zhang, W. Tan, *ACS Nano* **2017**, *11*, 4060–4066.

[114] W. Zhou, D. Li, C. Xiong, R. Yuan, Y. Xiang, *ACS Appl. Mater. Interfaces* **2016**, *8*, 13303–13308.

[115] S. Modi, C. Nizak, S. Surana, S. Halder, Y. Krishnan, *Nat. Nanotechnol.* **2013**, *8*, 459–467.

[116] N. Narayanaswamy, K. Chakraborty, A. Saminathan, E. Zeichner, K. Leung, J. Devany, Y. Krishnan, *Nat. Methods* **2019**, *16*, 95–102.

[117] K. Leung, K. Chakraborty, A. Saminathan, Y. Krishnan, *Nat. Nanotechnol.* **2019**, *14*, 176–183.

[118] S. Thekkan, M. S. Jani, C. Cui, K. Dan, G. Zhou, L. Becker, Y. Krishnan, *Nat. Chem. Biol.* **2019**, *15*, 1165–1172.

[119] C. Y. Tay, L. Yuan, D. T. Leong, *ACS Nano* **2015**, *9*, 5609–5617.

[120] S. Li, L. Xu, W. Ma, X. Wu, M. Sun, H. Kuang, L. Wang, N. A. Kotov, C. Xu, *J. Am. Chem. Soc.* **2016**, *138*, 306–312.

[121] J. S. Paige, K. Y. Wu, S. R. Jaffrey, *Science* **2011**, *333*, 642–646.

[122] J. S. Paige, T. Nguyen-Duc, W. Song, S. R. Jaffrey, *Science* **2012**, *335*, 1194–1194.

[123] W. Song, R. L. Strack, S. R. Jaffrey, *Nat. Methods* **2013**, *10*, 873–875.

[124] O. Köhler, D. V. Jarikote, O. Seitz, *ChemBioChem* **2005**, *6*, 69–77.

[125] S. Tyagi, F. R. Kramer, *Nat. Biotechnol.* **1996**, *14*, 303–308.

[126] W. Zhou, J. Ding, J. Liu, *Org. Biomol. Chem.* **2017**, *15*, 6959–6966.

[127] C.-H. Lu, C.-L. Zhu, J. Li, J.-J. Liu, X. Chen, H.-H. Yang, *Chem. Commun.* **2010**, *46*, 3116.

[128] K. Lee, Y. Cui, L. P. Lee, J. Irudayaraj, *Nat. Nanotechnol.* **2014**, *9*, 474–480.

[129] H.-C. Yeh, J. Sharma, J. J. Han, J. S. Martinez, J. H. Werner, *Nano Lett.* **2010**, *10*, 3106–

3110.

[130] K. Ren, Y. Xu, Y. Liu, M. Yang, H. Ju, *ACS Nano* **2018**, *12*, 263–271.

[131] X. Su, X. Xiao, C. Zhang, M. Zhao, *Appl. Spectrosc.* **2012**, *66*, 1249–1261.

[132] L. K. Chin, C.-H. Lee, B.-C. Chen, *Lab Chip* **2016**, *16*, 2014–2024.

[133] S. Voss, D. M. Krüger, O. Koch, Y.-W. Wu, *Proc. Natl. Acad. Sci.* **2016**, *113*, 14348–14353.

[134] W. E. Briley, M. H. Bondy, P. S. Randeria, T. J. Dupper, C. A. Mirkin, *Proc. Natl. Acad. Sci. U. S. A.* **2015**, *112*, 9591–9595.

[135] D. C. Yeo, C. Wiraja, A. S. Paller, C. A. Mirkin, C. Xu, *Nat. Biomed. Eng.* **2018**, *2*, 227–238.

[136] M. Yu, S. Stott, M. Toner, S. Maheswaran, D. A. Haber, *J. Cell Biol.* **2011**, *192*, 373–382.

[137] C. Bao, J. Conde, J. Curtin, N. Artzi, F. Tian, D. Cui, *Sci. Rep.* **2015**, *5*, 12297.

[138] Y. Chen, P. Li, P.-H. Huang, Y. Xie, J. D. Mai, L. Wang, N.-T. Nguyen, T. J. Huang, *Lab Chip* **2014**, *14*, 626.

[139] T. L. Halo, K. M. McMahon, N. L. Angeloni, Y. Xu, W. Wang, A. B. Chinen, D. Malin, E. Strekalova, V. L. Cryns, C. Cheng, C. A. Mirkin, C. S. Thaxton, *Proc. Natl. Acad. Sci.* **2014**, *111*, 17104–17109.

[140] N. Battich, T. Stoeger, L. Pelkmans, *Nat. Methods* **2013**, *10*, 1127–1133.

[141] X. Tan, T. Chen, X. Xiong, Y. Mao, G. Zhu, E. Yasun, C. Li, Z. Zhu, W. Tan, *Anal. Chem.* **2012**, *84*, 8622–8627.

[142] J. Sanderson, *Understanding Light Microscopy*, Wiley, **2019**.

[143] P. Zhang, T. Beck, W. Tan, *Angew. Chemie Int. Ed.* **2001**, *40*, 402–405.

[144] G. Bunt, F. S. Wouters, *Biophys. Rev.* **2017**, *9*, 119–129.

[145] E. Socher, L. Bethge, A. Knoll, N. Jungnick, A. Herrmann, O. Seitz, *Angew. Chemie Int. Ed.* **2008**, *47*, 9555–9559.

[146] H. Kuhn, V. V. Demidov, J. M. Coull, M. J. Fiandaca, B. D. Gildea, M. D. Frank-Kamenetskii, *J. Am. Chem. Soc.* **2002**, *124*, 1097–1103.

[147] K. Murayama, Y. Kamiya, H. Kashida, H. Asanuma, *ChemBioChem* **2015**, *16*, 1298–1301.

[148] K. Wang, Z. Tang, C. J. Yang, Y. Kim, X. Fang, W. Li, Y. Wu, C. D. Medley, Z. Cao, J. Li, P. Colon, H. Lin, W. Tan, *Angew. Chemie Int. Ed.* **2009**, *48*, 856–870.

[149] A. K. Chen, M. A. Behlke, A. Tsourkas, *Nucleic Acids Res.* **2007**, *35*, e105.

[150] A. K. Chen, M. A. Behlke, A. Tsourkas, *Nucleic Acids Res.* **2008**, *36*, e69–e69.

[151] M. M. Mhlanga, *Nucleic Acids Res.* **2005**, *33*, 1902–1912.

[152] R. M. Dirks, N. A. Pierce, *Proc. Natl. Acad. Sci.* **2004**, *101*, 15275–15278.

[153] P. Yin, H. M. T. Choi, C. R. Calvert, N. A. Pierce, *Nature* **2008**, *451*, 318–322.

[154] F. Hövelmann, I. Gaspar, J. Chamiolo, M. Kasper, J. Steffen, A. Ephrussi, O. Seitz, *Chem. Sci.* **2016**, *7*, 128–135.

[155] S. Kummer, A. Knoll, A. Herrmann, O. Seitz, in *Methods Mol. Biol.*, **2013**, pp. 291–301.

[156] N. Kolevzon, D. Hashoul, S. Naik, A. Rubinstein, E. Yavin, *Chem. Commun.* **2016**, *52*, 2405–2407.

[157] F. Hövelmann, I. Gaspar, A. Ephrussi, O. Seitz, *J. Am. Chem. Soc.* **2013**, *135*, 19025–19032.

[158] F. Hövelmann, L. Bethge, O. Seitz, *ChemBioChem* **2012**, *13*, 2072–2081.

[159] J. Chamiolo, G. Fang, F. Hövelmann, D. Friedrich, A. Knoll, A. Loewer, O. Seitz, *ChemBioChem* **2019**, *20*, 595–604.

[160] A. Okamoto, *Chem. Soc. Rev.* **2011**, *40*, 5815.

[161] X. Min, M. Zhang, F. Huang, X. Lou, F. Xia, *ACS Appl. Mater. Interfaces* **2016**, *8*, 8998–9003.

[162] J. J. Ro, H. J. Lee, B. H. Kim, *Chem. Commun.* **2018**, *54*, 7471–7474.

[163] M. E. Østergaard, P. Cheguru, M. R. Papasani, R. A. Hill, P. J. Hrdlicka, *J. Am. Chem. Soc.* **2010**, *132*, 14221–14228.

[164] A. B. Chinen, C. M. Guan, J. R. Ferrer, S. N. Barnaby, T. J. Merkel, C. A. Mirkin, *Chem. Rev.* **2015**, *115*, 10530–10574.

[165] J. I. Cutler, E. Auyeung, C. A. Mirkin, *J. Am. Chem. Soc.* **2012**, *134*, 1376–1391.

[166] A. E. Prigodich, D. S. Seferos, M. D. Massich, D. A. Giljohann, B. C. Lane, C. A. Mirkin, *ACS Nano* **2009**, *3*, 2147–2152.

[167] C. K. K. Choi, J. Li, K. Wei, Y. J. Xu, L. W. C. Ho, M. Zhu, K. K. W. To, C. H. J. Choi, L. Bian, *J. Am. Chem. Soc.* **2015**, *137*, 7337–7346.

[168] A. Zheng, X. Zhang, Y. Huang, Z. Cai, X. Liu, J. Liu, *RSC Adv.* **2018**, *8*, 6781–6788.

[169] J. Sun, F. Pi, J. Ji, H. Lei, Z. Gao, Y. Zhang, J. D. D. Habimana, Z. Li, X. Sun, *Anal. Chem.* **2018**, *90*, 3099–3108.

[170] P. B. Noble, J. H. Cutts, *Can. Vet. J.* **1967**.

[171] P. Vilela, A. Heuer-Jungemann, A. El-Sagheer, T. Brown, O. L. Muskens, N. R. Smyth,

A. G. Kanaras, *Small* **2018**, *14*, 1703489.

[172] M. Moros, M.-E. Kyriazi, A. H. El-Sagheer, T. Brown, C. Tortiglione, A. G. Kanaras, *ACS Appl. Mater. Interfaces* **2019**, *11*, 13905–13911.

[173] S. Sozer, E. Aptullahoglu, V. Shivarov, A. S. Yavuz, *Int. J. Lab. Hematol.* **2019**, *41*, e95–e98.

[174] N. Li, C. Chang, W. Pan, B. Tang, *Angew. Chemie Int. Ed.* **2012**, *51*, 7426–7430.

[175] Y. Yang, J. Huang, X. Yang, K. Quan, H. Wang, L. Ying, N. Xie, M. Ou, K. Wang, *J. Am. Chem. Soc.* **2015**, *137*, 8340–8343.

[176] C. P. Liang, P. Q. Ma, H. Liu, X. Guo, B. C. Yin, B. C. Ye, *Angew. Chemie - Int. Ed.* **2017**, *56*, 9077–9081.

[177] D. Li, W. Zhou, R. Yuan, Y. Xiang, *Anal. Chem.* **2017**, *89*, 9934–9940.

[178] S. Da Sacco, M. E. Thornton, A. Petrosyan, M. Lavarreda-Pearce, S. Sedrakyan, B. H. Grubbs, R. E. De Filippo, L. Perin, *Stem Cells Transl. Med.* **2017**, *6*, 419–433.

[179] G. K. Zakiryanova, E. Kustova, N. T. Urazalieva, A. Amirbekov, E. T. Baimuchametov, N. N. Nakisbekov, M. R. Shurin, *Immunity, Inflamm. Dis.* **2017**, *5*, 493–502.

[180] Y. Heun, K. Pogoda, M. Anton, J. Pircher, A. Pfeifer, M. Woernle, A. Ribeiro, P. Kameritsch, O. Mykhaylyk, C. Plank, F. Kroetz, U. Pohl, H. Mannell, *Mol. Ther.* **2017**, *25*, 1616–1627.

[181] V. J. AMATYA, A. S. MAWAS, K. KUSHITANI, M. M. MOHI EL-DIN, Y. TAKESHIMA, *Int. J. Oncol.* **2016**, *48*, 1599–1607.

[182] S. R. Harry, D. J. Hicks, K. I. Amiri, D. W. Wright, *Chem. Commun.* **2010**, *46*, 5557.

[183] J. Xue, L. Shan, H. Chen, Y. Li, H. Zhu, D. Deng, Z. Qian, S. Achilefu, Y. Gu, *Biosens. Bioelectron.* **2013**, *41*, 71–77.

[184] M. I. Uddin, A. Jayagopal, A. Wong, G. W. McCollum, D. W. Wright, J. S. Penn, *Nanomedicine Nanotechnology, Biol. Med.* **2018**, *14*, 63–71.

[185] G. Qiao, Y. Gao, N. Li, Z. Yu, L. Zhuo, B. Tang, *Chem. - A Eur. J.* **2011**, *17*, 11210–11215.

[186] W. Pan, T. Zhang, H. Yang, W. Diao, N. Li, B. Tang, *Anal. Chem.* **2013**, *85*, 10581–10588.

[187] C. Bao, J. Conde, J. Curtin, N. Artzi, F. Tian, D. Cui, *Sci. Rep.* **2015**, *5*, 12297.

[188] J. Conde, J. Rosa, J. M. de la Fuente, P. V. Baptista, *Biomaterials* **2013**, *34*, 2516–2523.

[189] W. Pan, Y. Li, M. Wang, H. Yang, N. Li, B. Tang, *Chem. Commun.* **2016**, *52*, 4569–4572.

[190] W. Qiang, W. Li, X. Li, X. Chen, D. Xu, *Chem. Sci.* **2014**, *5*, 3018–3024.

[191] Y. Cheng, S. Zhang, N. Kang, J. Huang, X. Lv, K. Wen, S. Ye, Z. Chen, X. Zhou, L. Ren, *ACS Appl. Mater. Interfaces* **2017**, *9*, 19296–19306.

[192] J. Nam, S. Son, L. J. Ochyl, R. Kuai, A. Schwendeman, J. J. Moon, *Nat. Commun.* **2018**, *9*, 1074.

[193] J. Liu, P. Du, J. Zhang, H. Shen, J. Lei, *Chem. Commun.* **2018**, *54*, 2550–2553.

[194] S. Wang, R. Riahi, N. Li, D. D. Zhang, P. K. Wong, *Adv. Mater.* **2015**, *27*, 6034–6038.

[195] M. R. K. Ali, Y. Wu, Y. Tang, H. Xiao, K. Chen, T. Han, N. Fang, R. Wu, M. A. El-Sayed, *Proc. Natl. Acad. Sci.* **2017**, *114*, E5655–E5663.

[196] Y. Wu, M. R. K. Ali, B. Dong, T. Han, K. Chen, J. Chen, Y. Tang, N. Fang, F. Wang, M. A. El-Sayed, *ACS Nano* **2018**, *12*, 9279–9290.

[197] D. Yin, X. Li, Y. Ma, Z. Liu, *Chem. Commun.* **2017**, *53*, 6716–6719.

[198] R. Riahi, S. Wang, M. Long, N. Li, P.-Y. Chiou, D. D. Zhang, P. K. Wong, *ACS Nano* **2014**, *8*, 3597–3605.

[199] N. Yan, X. Wang, L. Lin, T. Song, P. Sun, H. Tian, H. Liang, X. Chen, *Adv. Funct. Mater.* **2018**, *28*, 1800490.

[200] W. Ma, P. Fu, M. Sun, L. Xu, H. Kuang, C. Xu, *J. Am. Chem. Soc.* **2017**, *139*, 11752–11759.

[201] H. L. Jo, Y. H. Song, J. Park, E.-J. Jo, Y. Goh, K. Shin, M.-G. Kim, K. T. Lee, *Nanoscale* **2015**, *7*, 19397–19402.

[202] S. Wu, H.-J. Butt, *Adv. Mater.* **2016**, *28*, 1208–1226.

[203] M. Alavi, N. Karimi, M. Safaei, *Adv. Pharm. Bull.* **2017**, *7*, 3–9.

[204] S. Han, B. Kang, E. Jang, J. Ki, E. Kim, M. Y. Jeong, Y. M. Huh, H. Y. Son, S. Haam, *Adv. Healthc. Mater.* **2018**, *7*, 1701019.

[205] Z. Wang, K. Zhang, Y. Shen, J. Smith, S. Bloch, S. Achilefu, K. L. Wooley, J.-S. Taylor, *Org. Biomol. Chem.* **2013**, *11*, 3159.

[206] R. Zhang, S. Gao, Z. Wang, D. Han, L. Liu, Q. Ma, W. Tan, J. Tian, X. Chen, *Adv. Funct. Mater.* **2017**, *27*, 1701027.

[207] W. Gao, X. Wei, X. Wang, G. Cui, Z. Liu, B. Tang, *Chem. Commun.* **2016**, *52*, 3643–3646.

[208] X. Shen, Y. Wang, Y. Zhang, J. Ouyang, N. Na, *Adv. Funct. Mater.* **2018**, *28*, 1803286.

[209] Y. Wang, Z. Yu, Z. Zhang, R. Ren, S. Zhang, *Analyst* **2016**, *141*, 2861–2864.

[210] Y. Yuan, S. Wu, F. Shu, Z. Liu, *Chem. Commun.* **2014**, *50*, 1095–1097.

[211] X.-L. Zhang, C. Zheng, S.-S. Guo, J. Li, H.-H. Yang, G. Chen, *Anal. Chem.* **2014**, *86*,

3426–3434.

[212] J. Li, D. Li, R. Yuan, Y. Xiang, *ACS Appl. Mater. Interfaces* **2017**, *9*, 5717–5724.

[213] M. Ou, J. Huang, X. Yang, X. He, K. Quan, Y. Yang, N. Xie, J. Li, K. Wang, *ChemBioChem* **2018**, *19*, 147–152.

[214] J. Li, J. You, Y. Zhuang, C. Han, J. Hu, A. Wang, K. Xu, J.-J. Zhu, *Chem. Commun.* **2014**, *50*, 7107.

[215] P. Kunwar, J. Hassinen, G. Bautista, R. H. A. Ras, J. Toivonen, *ACS Nano* **2014**, *8*, 11165–11171.

[216] I. Díez, R. H. A. Ras, *Nanoscale* **2011**, *3*, 1963.

[217] H. Dong, L. Ding, F. Yan, H. Ji, H. Ju, *Biomaterials* **2011**, *32*, 3875–3882.

[218] C. Chung, Y.-K. Kim, D. Shin, S.-R. Ryoo, B. H. Hong, D.-H. Min, *Acc. Chem. Res.* **2013**, *46*, 2211–2224.

[219] W. Pan, B. Liu, X. Gao, Z. Yu, X. Liu, N. Li, B. Tang, *Nanoscale* **2018**, *10*, 14264–14271.

[220] L. Li, J. Feng, H. Liu, Q. Li, L. Tong, B. Tang, *Chem. Sci.* **2016**, *7*, 1940–1945.

[221] L. Yang, B. Liu, M. Wang, J. Li, W. Pan, X. Gao, N. Li, B. Tang, *ACS Appl. Mater. Interfaces* **2018**, *10*, 6982–6990.

[222] J. Li, J. Zhou, T. Liu, S. Chen, J. Li, H. Yang, *Chem. Commun.* **2018**, *54*, 896–899.

[223] J. Yu, S. He, C. Shao, H. Zhao, J. Li, L. Tian, *Nanoscale* **2018**, *10*, 7067–7076.

[224] X. Liao, H. Ju, *Chem. Commun.* **2015**, *51*, 2141–2144.

[225] K. Ke, L. Lin, H. Liang, X. Chen, C. Han, J. Li, H.-H. Yang, *Chem. Commun.* **2015**, *51*, 6800–6803.

[226] Y. Piao, F. Liu, T. S. Seo, *ACS Appl. Mater. Interfaces* **2012**, *4*, 6785–6789.

[227] Y. Wu, J. A. Phillips, H. Liu, R. Yang, W. Tan, *ACS Nano* **2008**, *2*, 2023–2028.

[228] X. Zhu, H. Zheng, X. Wei, Z. Lin, L. Guo, B. Qiu, G. Chen, *Chem. Commun.* **2013**, *49*, 1276.

[229] L. Chen, H. Zheng, X. Zhu, Z. Lin, L. Guo, B. Qiu, G. Chen, Z.-N. Chen, *Analyst* **2013**, *138*, 3490.

[230] H. Li, M. Eddaoudi, M. O'Keeffe, O. M. Yaghi, *Nature* **1999**, *402*, 276–279.

[231] J. L. C. Rowsell, O. M. Yaghi, *Microporous Mesoporous Mater.* **2004**, *73*, 3–14.

[232] N. Xie, S. Liu, X. Yang, X. He, J. Huang, K. Wang, *Analyst* **2017**, *142*, 3322–3332.

[233] N. Xie, J. Huang, X. Yang, Y. Yang, K. Quan, H. Wang, L. Ying, M. Ou, K. Wang,

Chem. Commun. **2016**, *52*, 2346–2349.

[234] S. Wang, M. Xia, J. Liu, S. Zhang, X. Zhang, *ACS Sensors* **2017**, *2*, 735–739.

[235] L. He, D. Lu, H. Liang, S. Xie, X. Zhang, Q. Liu, Q. Yuan, W. Tan, *J. Am. Chem. Soc.* **2018**, *140*, 258–263.

[236] X. Michalet, *Science* **2005**, *307*, 538–544.

[237] X. Gao, L. Yang, J. A. Petros, F. F. Marshall, J. W. Simons, S. Nie, *Curr. Opin. Biotechnol.* **2005**, *16*, 63–72.

[238] H. Dong, W. Dai, H. Ju, H. Lu, S. Wang, L. Xu, S.-F. Zhou, Y. Zhang, X. Zhang, *ACS Appl. Mater. Interfaces* **2015**, *7*, 11015–11023.

[239] D. Wu, G. Song, Z. Li, T. Zhang, W. Wei, M. Chen, X. He, N. Ma, *Chem. Sci.* **2015**, *6*, 3839–3844.

[240] X. He, T. Zeng, Z. Li, G. Wang, N. Ma, *Angew. Chemie Int. Ed.* **2016**, *55*, 3073–3076.

[241] Y. Shen, Z. Li, G. Wang, N. Ma, *ACS Sensors* **2018**, *3*, 494–503.

[242] S. Modi, S. M. G., D. Goswami, G. D. Gupta, S. Mayor, Y. Krishnan, *Nat. Nanotechnol.* **2009**, *4*, 325–330.

[243] S. Modi, S. Halder, C. Nizak, Y. Krishnan, *Nanoscale* **2014**, *6*, 1144–1152.

[244] S. Halder, Y. Krishnan, *Nanoscale* **2015**, *7*, 10008–10012.

[245] S. Surana, J. M. Bhat, S. P. Koushika, Y. Krishnan, *Nat. Commun.* **2011**, *2*, 340.

[246] A. T. Veetil, K. Chakraborty, K. Xiao, M. R. Minter, S. S. Sisodia, Y. Krishnan, *Nat. Nanotechnol.* **2017**, *12*, 1183–1189.

[247] D. Bhatia, S. Arumugam, M. Nasilowski, H. Joshi, C. Wunder, V. Chambon, V. Prakash, C. Grazon, B. Nadal, P. K. Maiti, L. Johannes, B. Dubertret, Y. Krishnan, *Nat. Nanotechnol.* **2016**, *11*, 1112–1119.

[248] S. Saha, V. Prakash, S. Halder, K. Chakraborty, Y. Krishnan, *Nat. Nanotechnol.* **2015**, *10*, 645–651.

[249] V. Prakash, S. Saha, K. Chakraborty, Y. Krishnan, *Chem. Sci.* **2016**, *7*, 1946–1953.

[250] M. Yang, X. Zhang, H. Liu, H. Kang, Z. Zhu, W. Yang, W. Tan, *Anal. Chem.* **2015**, *87*, 5854–5859.

[251] H. Pei, L. Liang, G. Yao, J. Li, Q. Huang, C. Fan, *Angew. Chemie Int. Ed.* **2012**, *51*, 9020–9024.

[252] K. Ohtsuka, S. Sato, Y. Sato, K. Sota, S. Ohzawa, T. Matsuda, K. Takemoto, N. Takamune, B. Juskowiak, T. Nagai, S. Takenaka, *Chem. Commun.* **2012**, *48*, 4740.

[253] K. Chakraborty, A. Veetil, S. R. Jaffrey, Y. Krishnan, *Annu. Rev. Biochem.* **2016**, *85*,

349–373.

[254] R. Nutiu, Y. Li, *J. Am. Chem. Soc.* **2003**, *125*, 4771–4778.

[255] Y. Yang, J. Huang, X. Yang, K. Quan, N. Xie, M. Ou, J. Tang, K. Wang, *Chem. Commun.* **2016**, *52*, 11386–11389.

[256] C. Wang, Y. Du, Q. Wu, S. Xuan, J. Zhou, J. Song, F. Shao, H. Duan, *Chem. Commun.* **2013**, *49*, 5739.

[257] X. Xu, N. L. Rosi, Y. Wang, F. Huo, C. A. Mirkin, *J. Am. Chem. Soc.* **2006**, *128*, 9286–9287.

[258] F. Huo, A. K. R. Lytton-Jean, C. A. Mirkin, *Adv. Mater.* **2006**, *18*, 2304–2306.

[259] P.-Q. Ma, C.-P. Liang, H.-H. Zhang, B.-C. Yin, B.-C. Ye, *Chem. Sci.* **2018**, *9*, 3299–3304.

[260] Y. Wang, Z. Li, T. J. Weber, D. Hu, C.-T. Lin, J. Li, Y. Lin, *Anal. Chem.* **2013**, *85*, 6775–6782.

[261] Y. Wang, L. Tang, Z. Li, Y. Lin, J. Li, *Nat. Protoc.* **2014**, *9*, 1944–1955.

[262] T.-T. Chen, X. Tian, C.-L. Liu, J. Ge, X. Chu, Y. Li, *J. Am. Chem. Soc.* **2015**, *137*, 982–989.

[263] W. Matuszewski, E. Bandurska-Stankiewicz, D. Wiatr-Bykowska, K. Myszka-Podgórska, U. Kamińska, *Polish Ann. Med.* **2013**, *20*, 154–159.

[264] L. Ma, F. Liu, Z. Lei, Z. Wang, *Biosens. Bioelectron.* **2017**, *87*, 638–645.

[265] J. Zhao, J. Gao, W. Xue, Z. Di, H. Xing, Y. Lu, L. Li, *J. Am. Chem. Soc.* **2018**, *140*, 578–581.

[266] V. C. Özalp, L. J. Nielsen, L. F. Olsen, *ChemBioChem* **2010**, *11*, 2538–2541.

[267] V. C. Özalp, T. R. Pedersen, L. J. Nielsen, L. F. Olsen, *J. Biol. Chem.* **2010**, *285*, 37579–37588.

[268] Z. Tang, P. Mallikaratchy, R. Yang, Y. Kim, Z. Zhu, H. Wang, W. Tan, *J. Am. Chem. Soc.* **2008**, *130*, 11268–11269.

[269] W. Qiang, H. Hu, L. Sun, H. Li, D. Xu, *Anal. Chem.* **2015**, *87*, 12190–12196.

[270] C. Wu, T. Chen, D. Han, M. You, L. Peng, S. Cansiz, G. Zhu, C. Li, X. Xiong, E. Jimenez, C. J. Yang, W. Tan, *ACS Nano* **2013**, *7*, 5724–5731.

[271] Z. Zhao, H. Fan, G. Zhou, H. Bai, H. Liang, R. Wang, X. Zhang, W. Tan, *J. Am. Chem. Soc.* **2014**, *136*, 11220–11223.

[272] K. Deng, Z. Hou, X. Li, C. Li, Y. Zhang, X. Deng, Z. Cheng, J. Lin, *Sci. Rep.* **2015**, *5*, 7851.

[273] Y. Liu, W. Hou, L. Xia, C. Cui, S. Wan, Y. Jiang, Y. Yang, Q. Wu, L. Qiu, W. Tan,

Chem. Sci. **2018**, *9*, 7505–7509.

[274] W. Song, R. L. Strack, N. Svensen, S. R. Jaffrey, *J. Am. Chem. Soc.* **2014**, *136*, 1198–1201.

[275] M. N. Stojanovic, D. M. Kolpashchikov, *J. Am. Chem. Soc.* **2004**, *126*, 9266–9270.

[276] R. L. Strack, W. Song, S. R. Jaffrey, *Nat. Protoc.* **2014**, *9*, 146–155.

[277] C. A. Kellenberger, S. C. Wilson, J. Sales-Lee, M. C. Hammond, *J. Am. Chem. Soc.* **2013**, *135*, 4906–4909.

[278] M. You, J. L. Litke, S. R. Jaffrey, *Proc. Natl. Acad. Sci.* **2015**, *112*, E2756–E2765.

[279] J. L. Litke, M. You, S. R. Jaffrey, in *Methods Enzymol.*, **2016**, pp. 315–333.

[280] G. Pothoulakis, F. Ceroni, B. Reeve, T. Ellis, *ACS Synth. Biol.* **2014**, *3*, 182–187.

[281] W. Q. Ong, Y. R. Citron, S. Sekine, B. Huang, *ACS Chem. Biol.* **2017**, *12*, 200–205.

[282] R. L. Strack, M. D. Disney, S. R. Jaffrey, *Nat. Methods* **2013**, *10*, 1219–1224.

[283] R. L. Strack, S. R. Jaffrey, in *Methods Enzymol.*, **2015**, pp. 129–146.

[284] J. Zhang, J. Fei, B. J. Leslie, K. Y. Han, T. E. Kuhlman, T. Ha, *Sci. Rep.* **2015**, *5*, 17295.

[285] K. D. Warner, M. C. Chen, W. Song, R. L. Strack, A. Thorn, S. R. Jaffrey, A. R. Ferré-D'Amaré, *Nat. Struct. Mol. Biol.* **2014**, *21*, 658–663.

[286] M. Okuda, D. Fourmy, S. Yoshizawa, *Nucleic Acids Res.* **2016**, gkw794.

[287] G. S. Filonov, J. D. Moon, N. Svensen, S. R. Jaffrey, *J. Am. Chem. Soc.* **2014**, *136*, 16299–16308.

[288] D. Shu, E. F. Khisamutdinov, L. Zhang, P. Guo, *Nucleic Acids Res.* **2014**, *42*, e10–e10.

[289] N. Svensen, S. R. Jaffrey, *Cell Chem. Biol.* **2016**, *23*, 415–425.

[290] E. V. Dolgosheina, S. C. Y. Jeng, S. S. S. Panchapakesan, R. Cojocaru, P. S. K. Chen, P. D. Wilson, N. Hawkins, P. A. Wiggins, P. J. Unrau, *ACS Chem. Biol.* **2014**, *9*, 2412–2420.

[291] A. Autour, S. C. Y. Jeng, A. D. Cawte, A. Abdolahzadeh, A. Galli, S. S. S. Panchapakesan, D. Rueda, M. Ryckelynck, P. J. Unrau, *Nat. Commun.* **2018**, *9*, 656.

[292] W. Song, G. S. Filonov, H. Kim, M. Hirsch, X. Li, J. D. Moon, S. R. Jaffrey, *Nat. Chem. Biol.* **2017**, *13*, 1187–1194.

[293] K. D. Warner, L. Sjekloća, W. Song, G. S. Filonov, S. R. Jaffrey, A. R. Ferré-D'Amaré, *Nat. Chem. Biol.* **2017**, *13*, 1195–1201.

[294] I. Shin, J. Ray, V. Gupta, M. Ilgu, J. Beasley, L. Bendickson, S. Mehanovic, G. A. Kraus, M. Nilsen-Hamilton, *Nucleic Acids Res.* **2014**, *42*, e90–e90.

[295] M. Ilgu, J. Ray, L. Bendickson, T. Wang, I. M. Geraskin, G. A. Kraus, M. Nilsen-

Hamilton, *Methods* **2016**, *98*, 26–33.

[296] M. D. E. Jepsen, S. M. Sparvath, T. B. Nielsen, A. H. Langvad, G. Grossi, K. V. Gothelf, E. S. Andersen, *Nat. Commun.* **2018**, *9*, 18.

[297] L. Nguyen, D. A. Davis, *Aquaculture* **2016**, *464*, 331–339.

[298] J. Ouellet, *Front. Chem.* **2016**, *4*, DOI 10.3389/fchem.2016.00029.

[299] A. Chen, M. Yan, S. Yang, *TrAC Trends Anal. Chem.* **2016**, *80*, 581–593.

[300] X. Zheng, R. Peng, X. Jiang, Y. Wang, S. Xu, G. Ke, T. Fu, Q. Liu, S. Huan, X. Zhang, *Anal. Chem.* **2017**, *89*, 10941–10947.

[301] Z. Wang, Y. Luo, X. Xie, X. Hu, H. Song, Y. Zhao, J. Shi, L. Wang, G. Glinsky, N. Chen, R. Lal, C. Fan, *Angew. Chemie Int. Ed.* **2018**, *57*, 972–976.

[302] K. K. Alam, K. D. Tawiah, M. F. Lichte, D. Porciani, D. H. Burke, *ACS Synth. Biol.* **2017**, *6*, 1710–1721.

[303] S. Strauss, P. C. Nickels, M. T. Strauss, V. Jimenez Sabinina, J. Ellenberg, J. D. Carter, S. Gupta, N. Janjic, R. Jungmann, *Nat. Methods* **2018**, *15*, 685–688.

[304] J. Schnitzbauer, M. T. Strauss, T. Schlichthaerle, F. Schueder, R. Jungmann, *Nat. Protoc.* **2017**, *12*, 1198–1228.

[305] C. D. Medley, J. E. Smith, Z. Tang, Y. Wu, S. Bamrungsap, W. Tan, *Anal. Chem.* **2008**, *80*, 1067–1072.

[306] K. Wang, D. Fan, Y. Liu, E. Wang, *Biosens. Bioelectron.* **2015**, *73*, 1–6.

[307] G. Liu, X. Mao, J. A. Phillips, H. Xu, W. Tan, L. Zeng, *Anal. Chem.* **2009**, *81*, 10013–10018.

[308] H. Jo, J. Her, C. Ban, *Biosens. Bioelectron.* **2015**, *71*, 129–136.

[309] Y.-S. Borghei, M. Hosseini, M. Dadmehr, S. Hosseinkhani, M. R. Ganjali, R. Sheikhnejad, *Anal. Chim. Acta* **2016**, *904*, 92–97.

[310] X. Zhang, K. Xiao, L. Cheng, H. Chen, B. Liu, S. Zhang, J. Kong, *Anal. Chem.* **2014**, *86*, 5567–5572.

[311] W. Sheng, T. Chen, R. Kamath, X. Xiong, W. Tan, Z. H. Fan, *Anal. Chem.* **2012**, *84*, 4199–4206.

[312] W. Sheng, T. Chen, W. Tan, Z. H. Fan, *ACS Nano* **2013**, *7*, 7067–7076.

[313] H. Liang, S. Chen, P. Li, L. Wang, J. Li, J. Li, H.-H. Yang, W. Tan, *J. Am. Chem. Soc.* **2018**, *140*, 4186–4190.

[314] L. Li, J. Feng, Y. Fan, B. Tang, *Anal. Chem.* **2015**, *87*, 4829–4835.

[315] Y. Yang, J. Huang, X. Yang, K. Quan, H. Wang, L. Ying, N. Xie, M. Ou, K. Wang, *Anal.*

Chem. **2016**, *88*, 5981–5987.

[316] Y. Yang, J. Huang, X. Yang, X. He, K. Quan, N. Xie, M. Ou, K. Wang, *Anal. Chem.* **2017**, *89*, 5850–5856.

[317] Y. Wu, J. Huang, X. Yang, Y. Yang, K. Quan, N. Xie, J. Li, C. Ma, K. Wang, *Anal. Chem.* **2017**, *89*, 8377–8383.

[318] J. Liu, M. Cui, H. Zhou, W. Yang, *ACS Sensors* **2017**, *2*, 1847–1853.

[319] W. Wang, N. S. R. Satyavolu, Z. Wu, J.-R. Zhang, J.-J. Zhu, Y. Lu, *Angew. Chemie Int. Ed.* **2017**, *56*, 6798–6802.

[320] S. Kim, S.-R. Ryoo, H.-K. Na, Y.-K. Kim, B.-S. Choi, Y. Lee, D.-E. Kim, D.-H. Min, *Chem. Commun.* **2013**, *49*, 8241.

[321] L. Zhang, H. Huang, N. Xu, Q. Yin, *J. Mater. Chem. B* **2014**, *2*, 4935.

[322] H. M. Meng, X. Zhang, Y. Lv, Z. Zhao, N. N. Wang, T. Fu, H. Fan, H. Liang, L. Qiu, G. Zhu, W. Tan, *ACS Nano* **2014**, *8*, 6171–6181.

[323] J.-T. Yi, T.-T. Chen, J. Huo, X. Chu, *Anal. Chem.* **2017**, *89*, 12351–12359.

[324] W.-H. Chen, X. Yu, A. Cecconello, Y. S. Sohn, R. Nechushtai, I. Willner, *Chem. Sci.* **2017**, *8*, 5769–5780.

[325] K. Hwang, P. Wu, T. Kim, L. Lei, S. Tian, Y. Wang, Y. Lu, *Angew. Chemie Int. Ed.* **2014**, *53*, 13798–13802.

[326] L. Cui, R. Peng, T. Fu, X. Zhang, C. Wu, H. Chen, H. Liang, C. J. Yang, W. Tan, *Anal. Chem.* **2016**, *88*, 1850–1855.

[327] S.-F. Torabi, P. Wu, C. E. McGhee, L. Chen, K. Hwang, N. Zheng, J. Cheng, Y. Lu, *Proc. Natl. Acad. Sci.* **2015**, *112*, 5903–5908.

[328] Z. Wu, H. Fan, N. S. R. Satyavolu, W. Wang, R. Lake, J.-H. Jiang, Y. Lu, *Angew. Chemie Int. Ed.* **2017**, *56*, 8721–8725.

[329] P. Zhang, Z. He, C. Wang, J. Chen, J. Zhao, X. Zhu, C.-Z. Li, Q. Min, J.-J. Zhu, *ACS Nano* **2015**, *9*, 789–798.

[330] D. He, X. He, X. Yang, H.-W. Li, *Chem. Sci.* **2017**, *8*, 2832–2840.

[331] F. Chen, M. Bai, Y. Zhao, K. Cao, X. Cao, Y. Zhao, *Anal. Chem.* **2018**, *90*, 2271–2276.

[332] S. F. Bakshi, N. Guz, A. Zakharchenko, H. Deng, A. V. Tumanov, C. D. Woodworth, S. Minko, D. M. Kolpashchikov, E. Katz, *J. Am. Chem. Soc.* **2017**, *139*, 12117–12120.

[333] F. Chen, M. Bai, K. Cao, Y. Zhao, X. Cao, J. Wei, N. Wu, J. Li, L. Wang, C. Fan, Y. Zhao, *ACS Nano* **2017**, *11*, 11908–11914.

[334] Z. Yang, K. Y. Loh, Y.-T. Chu, R. Feng, N. S. R. Satyavolu, M. Xiong, S. M. Nakamata

Huynh, K. Hwang, L. Li, H. Xing, X. Zhang, Y. R. Chemla, M. Gruebele, Y. Lu, *J. Am. Chem. Soc.* **2018**, *140*, 17656–17665.

[335] R. V. Giles, D. G. Spiller, J. Grzybowski, R. E. Clark, P. Nicklin, D. M. Tidd, *Nucleic Acids Res.* **1998**, *26*, 1567–1575.

[336] M. Becker-Hapak, S. S. McAllister, S. F. Dowdy, *Methods* **2001**, *24*, 247–256.

[337] B. Dalby, S. Cates, A. Harris, E. C. Ohki, M. L. Tilkins, P. J. Price, V. C. Ciccarone, *Methods* **2004**, *33*, 95–103.

[338] J. L. Young, D. A. Dean, in *Adv. Genet.*, **2015**, pp. 49–88.

[339] W. J. Rhee, P. J. Santangelo, H. Jo, G. Bao, *Nucleic Acids Res.* **2008**, *36*, e30–e30.

[340] C. Tuerk, L. Gold, *Science* **1990**, *249*, 505–510.

[341] A. D. Keefe, S. Pai, A. Ellington, *Nat. Rev. Drug Discov.* **2010**, *9*, 537–550.

[342] E. N. Brody, L. Gold, *Rev. Mol. Biotechnol.* **2000**, *74*, 5–13.

[343] T. M. Wickramaratne, V. C. Pierre, *Bioconjug. Chem.* **2015**, *26*, 63–70.

[344] J. Liu, Z. Cao, Y. Lu, *Chem. Rev.* **2009**, *109*, 1948–1998.

[345] N. Hamaguchi, A. Ellington, M. Stanton, *Anal. Biochem.* **2001**, *294*, 126–131.

[346] S. Modi, S. M. G., D. Goswami, G. D. Gupta, S. Mayor, Y. Krishnan, *Nat. Nanotechnol.* **2009**, *4*, 325–330.

[347] W. Zhou, J. Ding, J. Liu, *Biosens. Bioelectron.* **2017**, *87*, 171–177.

[348] Z. Wang, J. Heon Lee, Y. Lu, *Chem. Commun.* **2008**, 6005.

[349] S. J. Leavesley, T. C. Rich, *Cytom. Part A* **2016**, *89*, 325–327.

[350] Y. Miyake, H. Togashi, M. Tashiro, H. Yamaguchi, S. Oda, M. Kudo, Y. Tanaka, Y. Kondo, R. Sawa, T. Fujimoto, T. Machinami, A. Ono, *J. Am. Chem. Soc.* **2006**, *128*, 2172–2173.

[351] O. US EPA, *Drink. Water Contam.* **2013**, DOI EPA 816-F-09-004.

[352] J. Kondo, Y. Tada, T. Dairaku, Y. Hattori, H. Saneyoshi, A. Ono, Y. Tanaka, *Nat. Chem.* **2017**, *9*, 956–960.

[353] O. P. Schmidt, G. Mata, N. W. Luedtke, *J. Am. Chem. Soc.* **2016**, *138*, 14733–14739.

[354] N. G. Walter, D. A. Harris, M. J. B. Pereira, D. Rueda, *Biopolymers* **2002**, *61*, 224–242.

[355] D. Song, T. G. W. Graham, J. J. Loparo, *Nat. Commun.* **2016**, *7*, 10976.

[356] J. M. Benevides, G. J. Thomas, *Biochemistry* **2005**, *44*, 2993–2999.

[357] T. D. BRADRICK, *RNA* **2004**, *10*, 1459–1468.

[358] M. Kaul, C. M. Barbieri, D. S. Pilch, *J. Mol. Biol.* **2005**, *346*, 119–134.

[359] D. Fourmy, S. Yoshizawa, J. D. Puglisi, *J. Mol. Biol.* **1998**, *277*, 333–345.

[360] M. Zeraati, D. B. Langley, P. Schofield, A. L. Moye, R. Rouet, W. E. Hughes, T. M. Bryan, M. E. Dinger, D. Christ, *Nat. Chem.* **2018**, *10*, 631–637.

[361] I. V. Nesterova, E. E. Nesterov, *J. Am. Chem. Soc.* **2014**, *136*, 8843–8846.

[362] G. MacBeath, *Nat. Genet.* **2002**, *32*, 526–532.

[363] S. Selvarajah, O. H. Negm, M. R. Hamed, C. Tubby, I. Todd, P. J. Tighe, T. Harrison, L. C. Fairclough, *Mediators Inflamm.* **2014**, *2014*, 1–12.

[364] A. Onopiuk, A. Tokarzewicz, E. Gorodkiewicz, in *Adv. Clin. Chem.*, **2015**, pp. 57–69.

[365] E. Heyduk, T. Heyduk, *Anal. Chem.* **2005**, *77*, 1147–1156.

[366] L. C. Bock, L. C. Griffin, J. A. Latham, E. H. Vermaas, J. J. Toole, *Nature* **1992**, *355*, 564–566.

[367] D. M. Tasset, M. F. Kubik, W. Steiner, *J. Mol. Biol.* **1997**, *272*, 688–698.

[368] M. K. Horne III, P. K. Merryman, A. M. Cullinane, K. Nghiem, H. R. Alexander, *Am. J. Hematol.* **2007**, *82*, 815–820.

[369] K. E. Brummel-Ziedins, R. L. Pouliot, K. G. Mann, *J. Thromb. Haemost.* **2004**, *2*, 281–288.

[370] L. Wang, M. Tran, E. D'Este, J. Roberti, B. Koch, L. Xue, K. Johnsson, *Nat. Chem.* **2020**, *12*, 165–172.

[371] H. Kobayashi, M. Ogawa, R. Alford, P. L. Choyke, Y. Urano, *Chem. Rev.* **2010**, *110*, 2620–2640.

[372] K. J. Bruemmer, S. W. M. Crossley, C. J. Chang, *Angew. Chemie Int. Ed.* **2020**, *59*, 13734–13762.

[373] A. E. Palmer, R. Y. Tsien, *Nat. Protoc.* **2006**, *1*, 1057–1065.

[374] S. B. Ebrahimi, D. Samanta, C. A. Mirkin, *J. Am. Chem. Soc.* **2020**, *142*, 11343–11356.

[375] D. Samanta, S. B. Ebrahimi, C. A. Mirkin, *Adv. Mater.* **2020**, *32*, 1901743.

[376] R. Nutiu, Y. Li, *J. Am. Chem. Soc.* **2003**, *125*, 4771–4778.

[377] J. Zhou, J. Rossi, *Nat. Rev. Drug Discov.* **2017**, *16*, 181–202.

[378] S. B. Ebrahimi, D. Samanta, H. F. Cheng, L. I. Nathan, C. A. Mirkin, *J. Am. Chem. Soc.* **2019**, *141*, 13744–13748.

[379] D. Samanta, S. B. Ebrahimi, C. D. Kusmierz, H. F. Cheng, C. A. Mirkin, *J. Am. Chem. Soc.* **2020**, *142*, 13350–13355.

[380] R. A. Quax, L. Manenschijn, J. W. Koper, J. M. Hazes, S. W. J. Lamberts, E. F. C. van Rossum, R. A. Feelders, *Nat. Rev. Endocrinol.* **2013**, *9*, 670–686.

[381] T. Rhen, J. A. Cidlowski, *N. Engl. J. Med.* **2005**, *353*, 1711–1723.

[382] A. F. Turcu, J. Rege, R. J. Auchus, W. E. Rainey, *Nat. Rev. Endocrinol.* **2020**, *16*, 284–296.

[383] A. J. Steckl, P. Ray, *ACS Sensors* **2018**, *3*, 2025–2044.

[384] D. H. Chace, *Chem. Rev.* **2001**, *101*, 445–478.

[385] R. Liu, S. Zhang, C. Wei, Z. Xing, S. Zhang, X. Zhang, *Acc. Chem. Res.* **2016**, *49*, 775–783.

[386] J. Shen, Y. Li, H. Gu, F. Xia, X. Zuo, *Chem. Rev.* **2014**, *114*, 7631–7677.

[387] S. M. Borisov, O. S. Wolfbeis, *Chem. Rev.* **2008**, *108*, 423–461.

[388] R. L. Biltonen, N. Langerman, in *Methods Enzymol.*, **1979**, pp. 287–318.

[389] K.-A. Yang, R. Pei, D. Stefanovic, M. N. Stojanovic, *J. Am. Chem. Soc.* **2012**, *134*, 1642–1647.

[390] M. Zuker, *Nucleic Acids Res.* **2003**, *31*, 3406–3415.

[391] R. A. Prough, B. J. Clark, C. M. Klinge, *J. Mol. Endocrinol.* **2016**, *56*, R139–R155.

[392] C. J. ODDIE, J. P. COGHLAN, B. A. SCOGGINS, *J. Clin. Endocrinol. Metab.* **1972**, *34*, 1039–1054.

[393] J. P. Holst, S. J. Soldin, R. E. Tractenberg, T. Guo, P. Kundra, J. G. Verbalis, J. Jonklaas, *Steroids* **2007**, *72*, 71–84.

[394] S. J. Webb, T. E. Geoghegan, R. A. Prough, K. K. Michael Miller, *Drug Metab. Rev.* **2006**, *38*, 89–116.

[395] M. Kovac, L. Risch, S. Thiel, M. Weber, K. Grossmann, N. Wohlwend, T. Lung, D. Hillmann, M. Ritzler, S. Bigler, F. Ferrara, T. Bodmer, K. Egli, M. Imperiali, S. Heer, Y. Salimi, H. Renz, P. Kohler, P. Vernazza, C. R. Kahlert, M. Paprotny, M. Risch, *Diagnostics* **2020**, *10*, 593.

[396] K. M. Dean, A. E. Palmer, *Nat. Chem. Biol.* **2014**, *10*, 512–523.

[397] A. M. Valm, S. Cohen, W. R. Legant, J. Melunis, U. Hershberg, E. Wait, A. R. Cohen, M. W. Davidson, E. Betzig, J. Lippincott-Schwartz, *Nature* **2017**, *546*, 162–167.

[398] S. Park, A. Aalipour, O. Vermesh, J. H. Yu, S. S. Gambhir, *Nat. Rev. Mater.* **2017**, *2*, 17014.

[399] M. Schäferling, *Angew. Chemie Int. Ed.* **2012**, *51*, 3532–3554.

[400] K. J. Bruemmer, S. W. M. Crossley, C. J. Chang, *Angew. Chemie Int. Ed.* **2020**, *59*,

13734–13762.

[401] G. N. Konstantinou, in *Methods Mol. Biol.*, **2017**, pp. 79–94.

[402] E. C. Greenwald, S. Mehta, J. Zhang, *Chem. Rev.* **2018**, *118*, 11707–11794.

[403] T. Nolan, R. E. Hands, S. A. Bustin, *Nat. Protoc.* **2006**, *1*, 1559–1582.

[404] B. J. Trask, *Nat. Rev. Genet.* **2002**, *3*, 769–778.

[405] J. D. Brodin, A. J. Sprangers, J. R. McMillan, C. A. Mirkin, *J. Am. Chem. Soc.* **2015**, *137*, 14838–14841.

[406] C. D. Kusmierz, K. E. Bujold, C. E. Callmann, C. A. Mirkin, *ACS Cent. Sci.* **2020**, *6*, 815–822.

[407] T.-T. Chen, X. Tian, C.-L. Liu, J. Ge, X. Chu, Y. Li, *J. Am. Chem. Soc.* **2015**, *137*, 982–989.

[408] Z. Liu, J. Zhao, R. Zhang, G. Han, C. Zhang, B. Liu, Z. Zhang, M.-Y. Han, X. Gao, *ACS Nano* **2018**, *12*, 3629–3637.

[409] J. Conde, N. Oliva, N. Artzi, *Proc. Natl. Acad. Sci. U. S. A.* **2015**, *112*, E1278–E1287.

[410] B. D. Wilson, A. A. Hariri, I. A. P. Thompson, M. Eisenstein, H. T. Soh, *Nat. Commun.* **2019**, *10*, 5079.

[411] L. Bethge, D. V. Jarikote, O. Seitz, *Bioorg. Med. Chem.* **2008**, *16*, 114–125.

[412] R. A. S. Nascimento, R. E. Özel, W. H. Mak, M. Mulato, B. Singaram, N. Pourmand, *Nano Lett.* **2016**, *16*, 1194–1200.

[413] G. W. Cline, K. F. Petersen, M. Krssak, J. Shen, R. S. Hundal, Z. Trajanoski, S. Inzucchi, A. Dresner, D. L. Rothman, G. I. Shulman, *N. Engl. J. Med.* **1999**, *341*, 240–246.

[414] A. Rabin-Court, M. R. Rodrigues, X.-M. Zhang, R. J. Perry, *PLoS One* **2019**, *14*, e0218126.

[415] D. Leto, A. R. Saltiel, *Nat. Rev. Mol. Cell Biol.* **2012**, *13*, 383–396.

[416] R. D. Estensen, P. G. W. Plagemann, *Proc. Natl. Acad. Sci.* **1972**, *69*, 1430–1434.

[417] N. C. Abascal, L. Regan, *Open Biol.* **2018**, *8*, 180113.

[418] N. Krall, F. P. da Cruz, O. Boutureira, G. J. L. Bernardes, *Nat. Chem.* **2016**, *8*, 103–113.

[419] J. Choi, S. Kim, T. Tachikawa, M. Fujitsuka, T. Majima, *J. Am. Chem. Soc.* **2011**, *133*, 16146–16153.

[420] N. Nakatsuka, K.-A. Yang, J. M. Abendroth, K. M. Cheung, X. Xu, H. Yang, C. Zhao, B. Zhu, Y. S. Rim, Y. Yang, P. S. Weiss, M. N. Stojanović, A. M. Andrews, *Science* **2018**, *362*, 319–324.

[421] K. B. Daniel, A. Agrawal, M. Manchester, S. M. Cohen, *ChemBioChem* **2013**, *14*, 593–598.

[422] H. G. Hers, L. Hue, *Annu. Rev. Biochem.* **1983**, *52*, 617–653.

[423] S. B. Ebrahimi, D. Samanta, B. E. Partridge, C. D. Kusmierz, H. F. Cheng, A. A. Grigorescu, J. L. Chávez, P. A. Mirau, C. A. Mirkin, *Angew. Chemie Int. Ed.* **2021**, *n/a*, DOI https://doi.org/10.1002/anie.202103440.